UNIVERSITÄT DUISBURG ESSEN

Offen im Denken

TECHNISCHE UNIVERSITÄT BERLIN

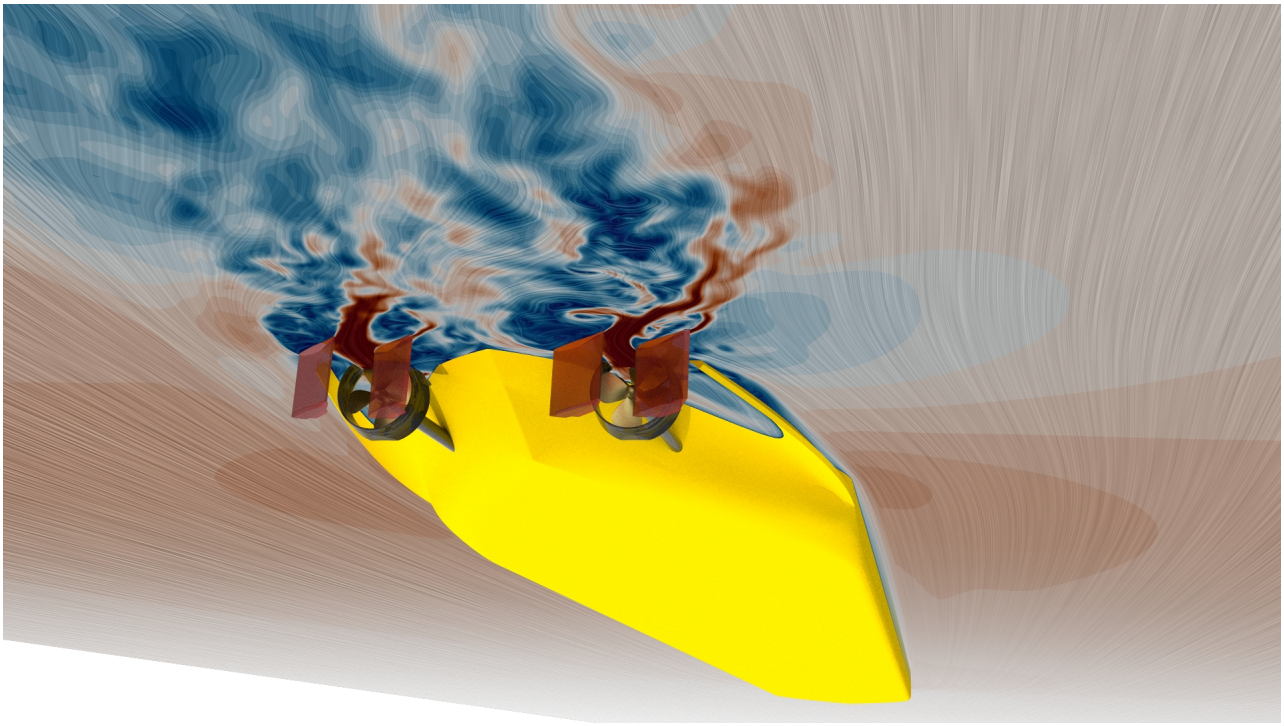
28th Numerical Towing Tank Symposium

NuTTS'26

19th – 21th October 2026

Mülheim/Ruhr, Germany

Proceedings



Udo Lantermann, Andreas Peters, Bettar Ould el Moctar (Eds.)

List of Extended Abstracts

P01	Guillermo Chillcce, Lahbib Zentari	On the Prediction of the Turning Circle Manoeuvre for an Inland Waterway Ship
P02	Jun Hyeok Lee, Chang Hyuk Ji, Hyung Taek Ahn	Development of an ALE-Based RANS Method for Rotating-Arm Simulation of the BB2 Submarine
P03	Ivan Sulovsky, Andro Bakica, Hrvoje Jasak, Jasna Prpić-Oršić	CFD simulations of zigzag manoeuvres using a simplified propeller representation
P04	Jakob Rzeszutko, Lahbib Zentari, Bettar Ould el Moctar	Comparison of Direct and Indirect System Identification for Hydrodynamic Derivatives of an Inland Waterway Ship in Deep and Shallow Water
P05	Mahmoud Amer, Jens Neugebauer, Frédéric Kracht	Data-Driven Identification of Ship Manoeuvring Dynamics Using SINDy: Forward Greedy Selection and Sequential Backward Elimination for Model-Structure Identification
P06	Thibault Maubert, Adam Persson	Actuator Line Method for Wind Assisted Ship Modelling
P07	Abdoul-Malik Bakari, Rui Lopes, Alex Shiri, Arash Eslamdoost	Hydrodynamic Analysis of a Wind-Assisted Ship's Rudder
P08	Saeed Hosseinzadeh, Muhammed Talha Ozdenoglu, Tahsin Tezdogan, Joseph Banks, Dominic Taunton, Stephen Turnock	Experimental and numerical analysis of the wave-making resistance of a self-propelled KCS at drift
P09	Adwaith Nath, Heather Peng, Ayhan Akinturk, Wei Qiu	Numerical Investigation of Propeller Loads during Steady Turning Maneuver of the ONR Tumblehome
P10	Nils Lundqvist, Alex Shiri, Arash Eslamdoost	Numerical and Experimental Analysis of a Hydrofoil Performance in Waves
P11	Etienne Fichers, Benoit Mallol	CFD modeling of surf-riding and broaching dynamic instabilities for the ONRT vessel subject to stern-quartering wave conditions
P12	Anton Turk, Zoran Čarija, Jakov Čarija, Jasna Prpić-Oršić	Progressive development of a CFD framework for parametric rolling and the identification of green water as the dominant saturation mechanism
P13	Joshua Patrick Davidson, Pal Schmitt, Christian Windt, Gabriel Barajas, Javier L. Lara	Nonlinear potentialFreeSurfaceFoam
P14	Mazyar Dawoodian, Sasan Rezaee, Bettar Ould el Moctar	Echo-Driven Modulation of Laser-Induced Cavitation Bubbles in Cylindrical Confinement
P15	Gohar Moloudi, Mazyar Dawoodian, Sasan Rezaee, Bettar Ould el Moctar	Interaction between reflected shock waves and laser-induced cavitation bubbles near a solid boundary
P16	Raul Bajimaya, Stephen Watson	Modelling cavitation of lifting surfaces for use during preliminary design
P17	Yoshihisa Okada, Manaka Isobe, Mai Kishikawa, Kenji Mokuo	Investigation of Simplified Bulbous Bow Shapes for Small Cargo Ship
P18	Manaka Isobe, Yoshihisa Okada, Mai Kishikawa, Kenji Mokuo	Research of a Hybrid Bulbous Bow for Small Cargo Ships by CFD

P19	Morteza Feizbakhsh, Nikolai Kornev	A Zonal URANS-SLH Hybrid Approach for Accurate Prediction of Ship Resistance and Stern Wake
P20	Hasan Ozturk, Tahsin Tezdogan, Kang Ren, Stephen Turnock	Extension of Granville's Similarity Law for Heterogeneous Hull Roughness
P21	Antoine Monot, Christophe Friess, Emmanuel Guilmineau, Michel Visonneau, Jeroen Wackers	Improving Hybrid RANS/LES Simulation of Ship Flows through Turbulence Forcing
P22	Melissa Böhm, Lahbib Zentari, Bettar Ould el Moctar, Benjamin Friedhoff	Numerical and Experimental Investigation of Inland Waterway Ship–Bank Interaction Using Scale-Resolving Simulation
P23	Andreas Peters, Simon Tödter, Mohammad Zehab Ud Din, Bettar Ould el Moctar	Numerical and Experimental Investigation of Phase-Transition During Sloshing Impacts
P24	Sergio Ribeiro e Silva, Giacomo Fatano	Hydrodynamic Analysis of a Hybrid Wave Energy Converter–Floating Offshore Wind Turbine Farm Using a 3D Boundary Element Method: Workflow Development and Numerical Challenges
P25	Auke van der Ploeg	Partly implicit coupling of sub grids and across interfaces
P26	Alper Yildirim, Robert Mutton, Batuhan Aktas, Mehmet Atlar	Rapid Prediction of Marine Propeller Performance Using Artificial Neural Networks
P27	Daniel Akinmulewo, Florian Sprenger	A Representation Learning Framework for Efficient Exploration of Ship Hull Design Spaces
P28	Ivan Zeman, Luuk Halsema, Perry van Oossanen	High-Fidelity Optimization of Generic Hull Forms and Energy Saving Devices
P29	Henry Hallam, Joseph Banks, Stephen Turnock	Use of a Computationally Lightweight Analysis Approach for Early Stage AUV Hull Form Optimisation

List of Participants

Hyung Taek Ahn	University of Ulsan
Daniel Akinmulewo	University of Rostock
Giuseppe Ambrogi	Sanlorenzo Spa
Mahmoud Amer	University of Duisburg-Essen
Cagri Aydin	Damen Research, Development & Innovation B.V.
Raul Bajimaya	QinetiQ
Abdoul-Malik Bakari	Chalmers University of Technology
Volker Bertram	VB Conferences
Gabriele Bigini	Van Oossanen
Melissa Böhm	Federal Waterways Engineering and Research Institute
Zoran Carija	University of Rijeka
Ji Changhyuk	University of Ulsan
Guillermo Chillcce	DLR
Mazyar Dawoodian	Technische Universität Berlin
Bettar el Moctar	Technische Universität Berlin
Arash Eslamdoost	Chalmers University of Technology
Giacomo Fatano	Instituto Superior Tecnico
Morteza Feizbakhsh	University of Rostock
Etienne Fichers	Cadence Design Systems
Erlend Liavåg Grotle	Kongsberg Maritime AS
Henry Hallam	University of Southampton
Manaka Isobe	Nakashima Propeller Co., Ltd.
Lee Jun Hyeok	University of Ulsan
Udo Lantermann	University of Duisburg-Essen
Nils Lundqvist	Chalmers University of Technology
Thibault Maubert	ENS Paris Saclay
Gohar Moloudi	University of Duisburg-Essen
Adwaith Nath	Memorial University of Newfoundland
Jens Neugebauer	University of Duisburg-Essen
Yoshihisa Okada	NAKASHIMA PROPELLER Co.,Ltd.
Wout Opdam	Wärtsilä Netherlands B.V.
Muhammed Talha Ozdenoglu	University of Southampton
Hasan Ozturk	University of Southampton
Adam Persson	RISE Research Institutes of Sweden
Andreas Peters	University of Duisburg-Essen
Sara Rasori	Sanlorenzo Spa
Seemontini RoyChoudhury	Kongsberg Maritime Sweden AB
Jakob Rzeszutko	Technische Universität Berlin
Pal Schmitt	Queen's University of Belfast
Ivan Sulovsky	University of Rijeka
Anton Turk	University of Rijeka
Stephen Turnock	University of Southampton
Auke van der Ploeg	MARIN
Stijn Vervoordeldonk	Damen Research, Development & Innovation B.V.
Jeroen Wackers	Centrale Nantes / CNRS
Alper Yildirim	University of Strathclyde
Ivan Zeman	Van Oossanen Naval Architects
Lahbib Zentari	Federal Waterways Engineering and Research Institute

28th Numerical Towing Tank Symposium (NuTTS)
19-21 October 2026 - Mülheim an der Ruhr, Germany

On the Prediction of the Turning Circle Manoeuvre for an Inland Waterway Ship

Guillermo Chillcce[1] and **Lahbib Zentari**[2]

[1]DLR, Institute of Maritime Technology and Propulsion Systems, Kiel, Germany
[2]Bundesanstalt für Wasserbau (BAW), Karlsruhe, Germany

1 Introduction

Accurate prediction of ship manoeuvring performance is essential for inland waterway operations, where complex propulsion systems and shallow water effects present unique challenges. The turning circle manoeuvre constitutes a standard test for assessing a ship's manoeuvrability, yielding essential parameters such as advance, transfer, tactical diameter, and turning radius that characterise a ship's ability to change course. For inland waterway ships operating on the Rhine River, this assessment is particularly demanding due to their complex propulsion configurations, typically featuring ducted propellers and twin rudders, combined with significant shallow water effects.

While traditional model tests in towing tanks or manoeuvring basins have been the primary means of evaluating ship manoeuvrability, these experimental approaches are costly and time-consuming, particularly for large-scale or parametric studies. Computational Fluid Dynamics (CFD) has emerged as a promising alternative, offering detailed flow analysis capabilities at potentially reduced costs. Recent studies have demonstrated CFD's capability to predict seagoing ship manoeuvring characteristics with reasonable accuracy, even in extreme shallow water conditions Döscher et al. (2026). However, the reliability of CFD for inland waterway ships with ducted propellers and twin rudders remains insufficiently explored in the literature.

This study evaluates CFD-based prediction of the turning circle manoeuvre for a 135 m cargo ship with ducted propellers and twin rudders, at model scale. The numerical approach employs the k–ω SST turbulence model with a 3-degree-of-freedom motion model. Two propeller modelling techniques are compared: steady-state Moving Reference Frame (MRF) and transient Rigid Body Motion (RBM). The primary objectives of this study are to assess the reliability of CFD for predicting the turning circle manoeuvre of an inland waterway ship that features a complex propulsion system. Furthermore, to evaluate the impact of different propeller and rudder modelling approaches on prediction accuracy, and to quantify the computational cost associated with high-fidelity CFD simulations of ship manoeuvring.

2 Test Case

The considered test case in this study is the inland waterway ship benchmark introduced by Mucha et al. (2017), at a scale of $\lambda = 16$. It represents a typical 135 m long cargo ship routinely navigating the Rhine River. The main particulars are detailed in Table 1. This ship is equipped with a complex propulsion system, including ducted propellers and twin fish-tail rudders, designed to provide maximum manoeuvrability in confined inland waterways.

Table 1: Main dimensions of the testcase and its appendages under design loading conditions, in both full-scale and model-scale, based on Mucha (2017).

Description	**Symbol**	**Unit**	**Full scale**	**Model scale**
Scale factor	λ	–	1	16
Length of waterline	L_{WL}	m	134.42	8.4013
Length between perpendiculars	L_{PP}	m	135.00	8.4375
Breadth	B	m	11.44	0.7150
Draft	T	m	3.5	0.2188
Wetted surface	S_W	m^2	2376.1	9.2817
Volumetric displacement	∇	m^3	4992	1.2187
Block coefficient	C_B	–	0.92	0.92
Number of propeller blades	Z	–	4	4
Propeller diameter	D_P	m	1.6	0.1

The turning circle manoeuvre was simulated under the conditions specified in Table 2. The initial speed, U_0, corresponds to a Froude number of 0.06, which is typical for inland waterway operations. The rudder deflection angle, δ, was set to 40°, with a rotation rate of $80\,^\circ\,\mathrm{s}^{-1}$. The propeller rotation rate was 12 rps, and the water depth condition was set to $h/T = 2.75$, representing shallow water effects.

Table 2: Turning circle manoeuvre conditions.

Parameter	Value
Initial speed, U_0	$0.556\,\mathrm{m\,s}^{-1}$
Froude number, Fr	0.06
Rudder deflection, δ	40°
Propeller rotation rate, n	12 rps
Water depth condition, h/T	2.75
Number of propeller blades	4

3 Numerical procedure

The numerical simulations were performed with the commercial solver Simcenter STAR-CCM+, see Siemens (2023).

The numerical procedure was based on the solution of the Reynolds–averaged Navier–Stokes (RANS) equations, closed with the k–ω SST turbulence model proposed by Menter (1994). This model was chosen for its ability to capture both near-wall and free-shear flow behaviour, which is essential for predicting the complex flow field around the hull, propellers and rudders during manoeuvring. The free surface was modelled as a flat, undeformable surface (double-body approach). This is a reasonable approximation for low-Froude-number manoeuvres (Fr = 0.06), where free-surface deformation is negligible, see Chillcce et al. (2025). The ship motion was modelled with three degrees of freedom (DoF), namely surge, sway and yaw, while trim and sinkage were neglected. Second-order schemes were used for both the spatial and the temporal discretisation, and pressure–velocity coupling was handled with the SIMPLE algorithm.

The computational domain was designed to be compact while leaving sufficient space for the flow field around the ship to develop. The domain had a total length of $4.2L_{pp}$ and a width of $3.8L_{pp}$, and its depth corresponded to the prescribed water depth h. A schematic of the domain is shown in Figure 1. A no-slip condition was applied to the hull and the bottom boundary. The front and side boundaries were defined as velocity inlets with zero velocity, and the rear

boundary as a pressure outlet. The top boundary was modelled as a symmetry plane, consistent with the double-body assumption.

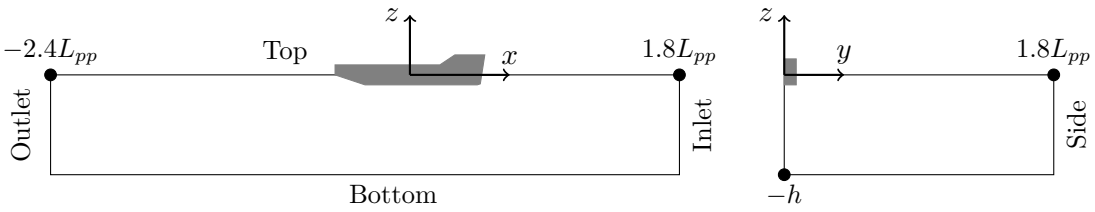


Fig. 1: Schematic of the numerical domain for the turning circle manoeuvre simulations.

Figure 2 shows the surface mesh, with colours distinguishing the hull, rudders, ducts and propellers. The computational domain consisted of seven regions: four rudder regions, two propeller regions and one main region containing the hull. The propeller and rudder regions were discretised with polyhedral control volumes to improve the flow resolution around the propulsive and steering devices, whereas the main region was discretised with tetrahedral control volumes to keep the cell count low. The final mesh comprised approximately 9 million control volumes, with local refinement at the stern to resolve the flow features around the propulsive and steering devices. The mesh details are summarised in Table 3.

Table 3: Mesh details for the numerical domain.

Region	Number of Cells
Total domain	9,000,000
Propeller (each)	330,000
Rudder (each)	220,000

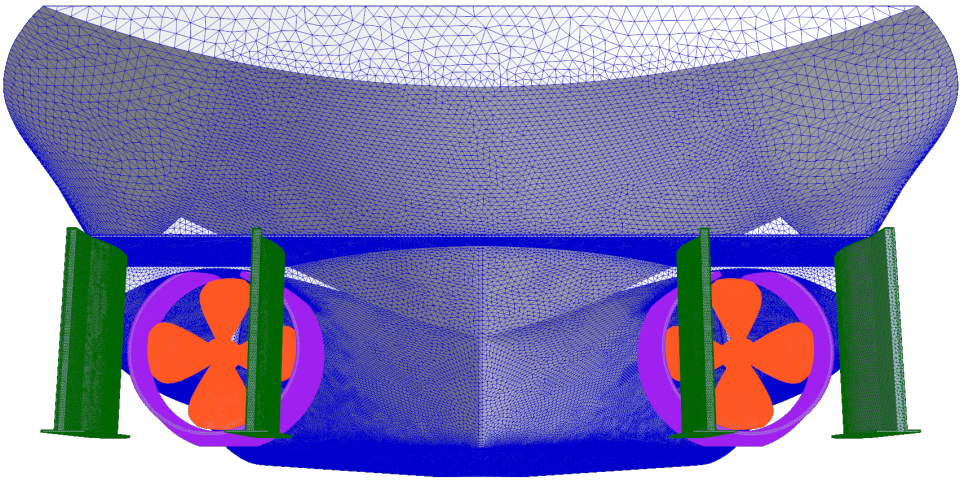


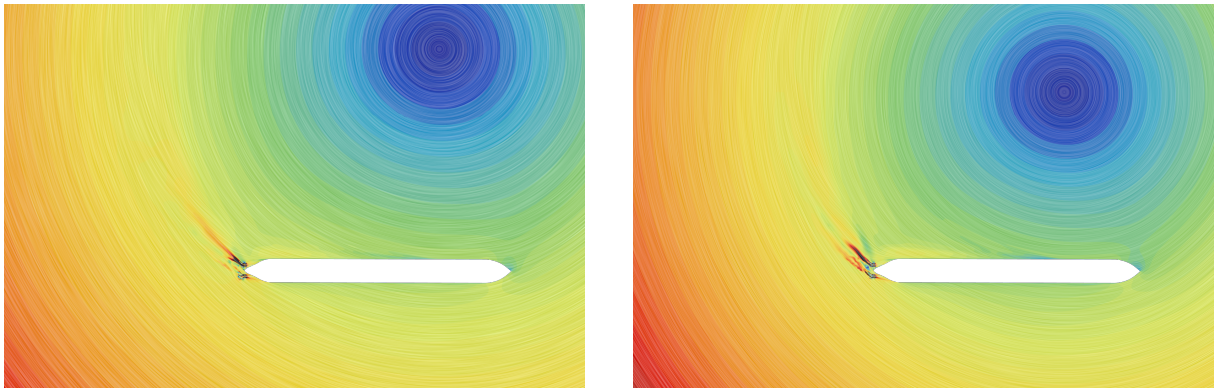
Fig. 2: Computational surface mesh of hull, propellers, ducts, and rudders.

The main objective of this study was to compare propeller modelling techniques and to assess their influence on the accuracy of numerical turning circle manoeuvres of inland waterway ships. For this purpose, two approaches were considered: the Moving Reference Frame (MRF) method and the Rigid Body Motion (RBM) method. The MRF method keeps the propeller geometry fixed and accounts for its rotation by solving the flow equations in a rotating reference frame within the propeller region, so that only time-averaged flow features are captured. This approach is computationally efficient but cannot resolve the transient interaction between the propeller

blades and the surrounding flow. The RBM method, in contrast, physically rotates the propeller mesh at each time step and therefore resolves blade-passing effects and the unsteady propeller–rudder–hull interaction, albeit at a considerably higher computational cost. The rudders were modelled as static rudders, fixed at a deflection angle of 40°.

4 Results

The primary objective was to capture the steady turning radius and the steady-state quantities. Thus, the initial conditions start with the rudders already deflected by 40° to the port side. For this condition, two different propeller modelling approaches were compared: the Moving Reference Frame (MRF) and the Rigid Body Motion (RBM). Figure 3 shows the velocity magnitude in ship-fixed coordinate system when the ship has reached steady-state condition. As seen, the rotation simulation with propeller RBM produces a shorter rotation radius.



(a) MRF approach. (b) RBM approach.

Fig. 3: Velocity magnitude in ship-fixed coordinate system on a horizontal plane passing the propeller axis or rotations.

The computed steady-state manoeuvring parameters are compared with the measured data in Table 4. The turning radius, non-dimensionalised by L_{pp}, was determined via regression analysis of the last 20 % of the time record. The measured turning radius was $0.66L_{pp}$. The RBM propeller simulation reproduced this value ($R = 0.66L_{pp}$), whereas the MRF propeller simulation overpredicted the turning radius by 26 % ($R = 0.83L_{pp}$). This discrepancy highlights the importance of accurately modelling transient hull–propeller–flow interactions, particularly when the numerical domain is moving. While the MRF approach has yielded good results in earlier studies with stationary numerical domains such as Zentari et al. (2026), the combined complexity of a moving domain and oblique flow reduces its accuracy.

Table 4: Comparison of measured and calculated parameters during steady-state turning at rudder angle 40° port side. The steady rotation radius were non-dimensionalised by L_{pp}.

Parameter	Unit	EFD	MRF	RBM
Steady-state speed	m/s	0.16	0.19	0.17
Rotation rate	°/s	1.77	1.58	1.77
Steady-state radius	-	0.66	0.83	0.66
Drift angle	°	18.69	16.52	18.63

The thrust histories for the port and starboard propellers are presented in Figure 4 for both MRF and RBM approaches. The RBM approach captured the transient fluctuations in thrust, while the MRF approach provided a time-averaged solution. The wake fields behind the propellers for the MRF and RBM approaches are presented in Figure 5. The RBM approach resolves

the time-dependent interactions between the propeller and the surrounding flow, resulting in a more physically realistic wake field. In contrast, the MRF approach provides a time-averaged solution. The wake field for the RBM approach shows distinct vortex structures that are not present in the MRF wake field, which affects the flow into the rudders and, consequently, the forces generated.

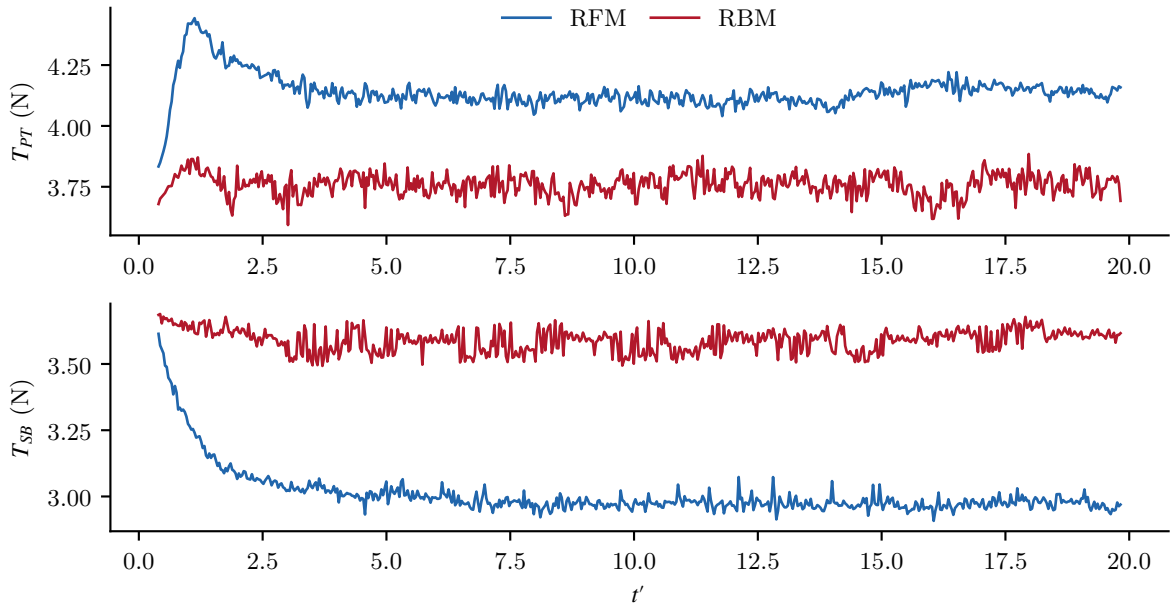
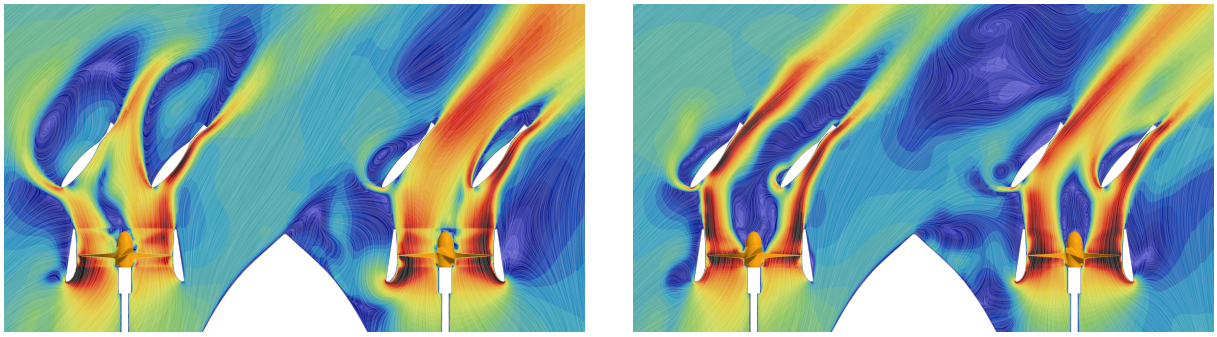


Fig. 4: Thrust history for port and starboard propellers with MRF and RBM approaches.



(a) MRF approach.

(b) RBM approach.

Fig. 5: Wake fields behind the propellers for the MRF and RBM approaches.

4.1 Computational Cost

The computational cost for different modelling approaches is presented in Table 5. All simulations were performed on 2 nodes (128 cores each) of a high-performance computing (HPC) cluster with AMD EPYC 7702 processors. The static rudder simulations with the MRF propeller model required approximately 9 min of wall-clock time per second of physical time, while the transient rudder simulations with the RBM propeller model required approximately 11 min of wall-clock time per second of physical time. The computational cost increased significantly when a smaller time step was used for the RBM approach, with a time step of 0.001 s resulting in a total wall-clock time of approximately 16 days for a 300 s simulation.

Table 5: Computational cost for different modelling approaches.

Method	Time Step	Wall-Time/Simulation s	Simulation time	Total wall time
MRF	0.01 s	8.12 min	300 s	40.6 h
RBM	0.01 s	9.3 min	300 s	46.5 h
RBM	0.001 s	77.4 min	300 s	~16 days

5 Conclusion and Future Work

The present study evaluated the capability of CFD to predict the turning circle manoeuvre of an inland waterway ship in moderately shallow water. Given the low speed of the ship, the double-body approach proved sufficient, which considerably reduced the computational effort. The choice of propeller model, on the other hand, had a decisive influence on the results. The RBM approach proved to be the most accurate, capturing the measured steady turning radius, whereas the MRF approach overpredicted it by 26 %. Although the MRF approach performs well in stationary domains, the combination of domain motion and cross-flow appears to reduce its accuracy. In terms of computational cost, the RBM approach also proved efficient, increasing the total computing time by only about 15 %. Considering the substantial gain in accuracy, the RBM approach is recommended for such analyses. In future work, the present approach will be extended to other typical manoeuvres and to shallower water depths.

Acknowledgements

The authors thank the Development Centre for Ship Technology and Transport Systems (DST), Duisburg, for conducting the model tests.

References

Chillcce, G., Zentari, L., Van Hoydonck, W., Bedos, A., Ley, J., Gornicz, T., Yang, Y., Oud, G., Tenzer, M., Rzeszutko, J., el Moctar, O., 2025. Numerical calculation of hydrodynamic forces on inland waterway vessels during circular motion in shallow and extreme shallow waters. Ocean Engineering 318, 120095. doi:10.1016/j.oceaneng.2024.120095.

Döscher, M., Böttner, C.U., Abdel-Maksoud, M., 2026. Experimental and numerical investigation of free-running turning manoeuvres in extreme shallow water. Ocean Engineering 363, 126686. doi:10.1016/j.oceaneng.2026.126686.

Menter, F.R., 1994. Two-equation eddy-viscosity turbulence models for engineering applications. AIAA Journal 32, 1598–1605.

Mucha, P., 2017. On Simulation-based Ship Maneuvering Prediction in Deep and Shallow Water. Ph.D. thesis. Universität Duisburg-Essen. Duisburg.

Mucha, P., el Moctar, O., Dettmann, T., Tenzer, M., 2017. Inland waterway ship test case for resistance and propulsion prediction in shallow water. Ship Technology Research 64, 106–113. doi:10.1080/09377255.2017.1349723.

Siemens, 2023. Simcenter STAR-CCM+ 2310 User Guide.

Zentari, L., Chillcce, G., Rzeszutko, J., el Moctar, O., 2026. Drift angle prediction of an inland waterway ship during quasi-steady turning maneuver using Bayesian optimization and CFD. Ocean Engineering 367, 127668. doi:https://doi.org/10.1016/j.oceaneng.2026.127668.

Development of an ALE-Based RANS Method for Rotating-Arm Simulation of the BB2 Submarine

Jun Hyeok Lee, Chang Hyuk Ji, Hyung Taek Ahn*
School of Naval Architecture and Ocean Engineering, University of Ulsan, Ulsan, Korea
* Corresponding author: htahn@ulsan.ac.kr

1 Introduction

Predicting submarine and underwater-vehicle manoeuvrability requires estimates of side force and yaw moment during turns. Local inflow velocity and drift angle vary along the turning hull, while cross-flow separation and appendage vortices affect the loads (Holloway et al., 2015; Fureby et al., 2016). Rotating-arm tests provide rotational hydrodynamic loads and manoeuvring derivatives but require dedicated facilities (Jeong et al., 2016). Numerical rotating-arm simulations complement these tests and resolve local flow structures; steady-turn CFD and rotating-arm measurements have also been reported for SUBOFF (Toxopeus et al., 2012; Zhao et al., 2023).

Rotating-arm CFD can use a single rotating reference frame (SRF) or an arbitrary Lagrangian–Eulerian (ALE) formulation (Limache and Cliff, 2000; Mader and Martins, 2011). In steady SRF, the body and mesh remain fixed in rotating coordinates, with rotational inertial terms included, enabling efficient prediction of steady loads at a constant turn rate. Variable turn rates require an unsteady reference-frame formulation. ALE directly represents body and mesh motion in an inertial frame and readily accommodates unsteady motion, at the cost of physical-time integration and careful treatment of mesh-motion conservation. Submarine applications include steady RANS with rotational source terms (Zhang et al., 2013) and dynamic-mesh URANS (Pan et al., 2015).

Future CFD coupling with six-degree-of-freedom (6DOF) motion, involving simultaneous changes in translation and rotation, requires consistent treatment of hydrodynamic loads and body dynamics. CFD-derived hydrodynamic derivatives have been incorporated into 6DOF models of underwater tow-fish (Go et al., 2016; Go and Ahn, 2019). These studies exemplify derivative-based motion prediction, distinct from direct coupling of flow and rigid-body dynamics through moving meshes (Kim et al., 2018; Carrica et al., 2021). Here, an ALE method is developed as a common framework for rotating-arm and future free-running simulations, with particular attention to the geometric conservation law (GCL), boundary conditions and load transformations.

The target application is the BB2 submarine, developed from the work of Joubert (2006). Available BB2 studies include free-running and underwater planar motion mechanism (PMM) experiments (Overpelt et al., 2015; Kim et al., 2023) and rotating-arm CFD comparisons (Toxopeus et al., 2022). Before three-dimensional BB2 calculations, the two-dimensional NACA0012 airfoil is used to assess the kinematics and load predictions of the RANS-based ALE method. The side-force sign and linear trend with turn rate are compared with quasi-steady thin-airfoil theory, while differences from steady SRF solutions and time-step sensitivity are examined to establish a basis for three-dimensional extension. This paper focuses on the two-dimensional assessment; results from the ongoing three-dimensional BB2 rotating-arm study are planned for presentation at the symposium.

2 Numerical method

2.1 Governing equations and discretisation

The in-house solver ULSAN3d discretises the incompressible RANS equations using a cell-centered finite-volume method on unstructured meshes. Related studies include a node-centered hybrid-mesh method (Kallinderis and Ahn, 2005) and a reconstruction-based cell-centered method (Lee and Ahn, 2018). With reference length L_{ref} and velocity U_{ref}, the Reynolds number is $Re = U_{\mathrm{ref}} L_{\mathrm{ref}}/\nu$. Pressure–velocity coupling uses artificial compressibility (Chorin, 1967). The mean-flow equations for a two-dimensional cell V_i undergoing rigid-body motion are

$$\frac{\partial}{\partial \tau}\int_{V_i} \mathbf{Q}\ \mathrm{d}V + \mathbf{M}\frac{\mathrm{d}}{\mathrm{d}t}\int_{V_i} \mathbf{Q}\ \mathrm{d}V + \oint_{\partial V_i} (\mathbf{F}_n^c - \mathbf{F}_n^v)\ \mathrm{d}A = \int_{V_i} \mathbf{S}\ \mathrm{d}V \tag{1}$$

The state vector, physical-time coefficient matrix and convective flux in Eq. (1) are

$$\mathbf{Q} = \begin{pmatrix} p \\ u \\ v \end{pmatrix}, \quad \mathbf{M} = \mathrm{diag}(0,1,1), \quad \mathbf{F}_n^c = \begin{pmatrix} \beta(u_n - \sigma) \\ u(u_n - \sigma) + pn_x \\ v(u_n - \sigma) + pn_y \end{pmatrix} \tag{2}$$

Here, $u_n = \mathbf{u} \cdot \mathbf{n}$ and $\sigma = \mathbf{u}_g \cdot \mathbf{n}$, where $\mathbf{u}_g$ is the mesh velocity. The artificial-compressibility parameter $\beta > 0$ is spatially uniform. The GCL for rigid-body rotation gives a zero net mesh-volume flux, so the integrated continuity residual equals that obtained using βu_n. The viscous flux $\mathbf{F}_n^v$ uses the effective viscosity $\nu + \nu_t$.

Convection is discretised with Roe-type flux-difference splitting and second-order unlimited reconstruction using weighted least-squares gradients. The principal $Re = 10^6$ results evaluate Roe dissipation using inertial-frame velocity; the diagnostics in Section 3.3 use relative-velocity dissipation and a momentum-residual correction. ALE uses BDF1 dual-time stepping, while steady SRF uses pseudo-transient continuation. Turbulence closure is provided by the fully turbulent SA-neg model (Spalart and Allmaras, 1992; Allmaras et al., 2012).

2.2 Rigid-body motion and geometric conservation

A GCL-preserving ALE scheme for strongly coupled flow–structure interaction was developed by Ahn and Kallinderis (2006). Here, the body and entire mesh rotate at constant angular velocity about a fixed centre $\mathbf{x}_p$. Using the reference position $\mathbf{X}$ and rotation matrix $\mathbf{T}(\theta)$, the geometry is constructed directly as

$$\mathbf{x} = \mathbf{x}_p + \mathbf{T}(\theta)\big(\mathbf{X} - \mathbf{x}_p\big), \qquad \mathbf{u}_g = \dot{\theta}\, \mathbf{e}_z \times \big(\mathbf{x} - \mathbf{x}_p\big) \tag{3}$$

Cell volumes and face lengths remain constant, reducing the GCL to $\sum_f s_{if}\, \sigma_f A_f = 0$. Evaluating the linear rigid-rotation velocity at each straight-face midpoint satisfies this relation in exact arithmetic. Identical face mesh velocities are used for the mean-flow and SA equations. The wall velocity follows the body, while the far-field fluid is stationary in the inertial frame. Wall distances are preserved during rigid motion, and SA production uses absolute vorticity.

2.3 Rotating-frame reference solution and load definitions

SRF uses a fixed mesh with relative velocity $\mathbf{w}_B$ as the unknown. Subscripts I and B denote inertial-frame and body-frame components, respectively. For constant angular velocity, the velocity transformation and rotational inertial terms are

$$\mathbf{w}_B = \mathbf{T}^T(\mathbf{u}_I - \boldsymbol{\Omega}_I \times \mathbf{r}_I), \qquad \mathbf{r}_I = \mathbf{x} - \mathbf{x}_p \tag{4}$$

$$\mathbf{S}_{\mathrm{rot}} = -2\boldsymbol{\Omega}_B \times \mathbf{w}_B - \boldsymbol{\Omega}_B \times (\boldsymbol{\Omega}_B \times \mathbf{r}_B) \tag{5}$$

Here, $\mathbf{r}_B = \mathbf{T}^T \mathbf{r}_I$, and the source in Eq. (1) is zero in ALE and $\big(0, S_{\mathrm{rot},x}, S_{\mathrm{rot},y}\big)^T$ in SRF. The far-field and wall conditions are $\mathbf{w}_{\infty,B} = -\boldsymbol{\Omega}_B \times \mathbf{r}_B$ and $\mathbf{w}_B = 0$, respectively (Limache and Cliff, 2000). Absolute vorticity in SRF is $\nabla_B \times \mathbf{w}_B + 2\boldsymbol{\Omega}_B$. Surface pressure and viscous stresses are integrated, and the resulting force is projected onto the body axes. For tangential velocity $U_{\mathrm{ref}} = \Omega R$ at the reference point, the side-force coefficient and nondimensional turn rate are defined as

$$C_Y = \frac{Y}{1/2\rho U_{\mathrm{ref}}^2 c}, \qquad r' = \frac{\Omega c}{U_{\mathrm{ref}}} = \frac{c}{R} \tag{6}$$

Here, Y is the dimensional side force and C_Y its nondimensional coefficient. The definition $r' = c/R$ corresponds to L/R used in rotating-arm tests.

Steady SRF solutions were warm-started sequentially at Re=10^5, 3×10^5 and 10^6. At Re=10^6, ALE was initialised from the transformed steady SRF field and advanced for two revolutions at 698 steps/rev. Two further revolutions at 1,396 steps/rev were then computed from that endpoint to assess time-step sensitivity. All two-dimensional calculations used 16 MPI ranks.

The selected $r' = 0.18$ lies within the experimental range $0.143 \le L/R \le 0.25$ of Jeong et al. (2016). Their loads were not used for direct validation because the geometry and flow conditions differ.

3 NACA0012 rotating-arm calculations

3.1 Geometry, meshes and operating conditions

The NACA0012 extends from the leading edge $(0,0)$ to the trailing edge $(1,0)$, with the mid-chord $\mathbf{x}_b = (0.5,0)$ as the body reference point. The $+x$ axis points towards the trailing edge, $+y$ points upwards and $\Omega > 0$ denotes counter-clockwise rotation. With the turn centre at $\mathbf{x}_p = (0.5, -R)$, the inward side-force coefficient is $-C_Y$, and the body initially travels towards the leading edge, in the $(-x)$ direction. Since $c = U_{\mathrm{ref}} = 1, \Omega = r'$.

Figure 1 shows the semicircular domain mesh, and Fig. 2 shows the airfoil region. Initial checks used a circular domain of radius $50c$ about the mid-chord, with 72,890 triangular cells at Re=10^5. Quantitative comparisons used an approximately 180° semicircular domain for $r' = 0.18$, centred at the corresponding turn centre $(0.5, -5.5556)$, with outer-arc radius $30c$. Meshes with 55,341 and 275,169 cells were used for the Re=10^5 diagnostics and Re=10^6 principal results, respectively. At $r' = 0.05$ and 0.10, the mesh was retained and only the turn centre was moved. The static lift slope was obtained from steady $\alpha = \pm 2°$ solutions on a full circular mesh with 280,134 cells. At Re=10^6, $y^+_{\max}$ was below unity, but no grid-convergence study was performed.

Table 1 Principal computational conditions and comparison objectives

Case	Cells	Re	r'	Formulation and conditions
Steady reference	275,169	10^6	0.05, 0.10, 0.18	Steady SRF
Moving mesh	275,169	10^6	0.18	ALE BDF1 698 steps/rev × 2 revolutions → 1,396 steps/rev × 2 revolutions
Static lift slope	280,134	10^6	0	Fixed mesh, $\alpha = \pm 2°$
Operator diagnostics	55,341	10^5	0.18	SRF and baseline/corrected ALE BDF1, 698 steps/rev, 1 revolution

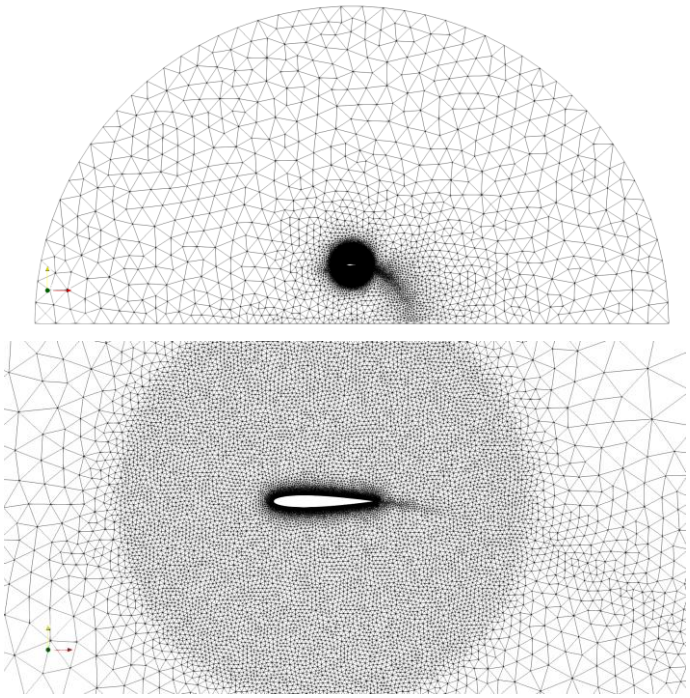


Fig. 1 Overall mesh of the semicircular domain (top). Fig. 2 Close-up of the triangular mesh around NACA0012 (bottom), showing near-airfoil refinement and gradual coarsening towards the outer domain.

3.2 Side-force trends and thin-airfoil comparison

Figure 3 visualises pressure and curved streamlines around the airfoil. The lower pressure beneath the airfoil is qualitatively consistent with an inward side force in the present coordinates. Rotating-arm flow has a chordwise variation in local inflow angle, unlike straight-ahead flow at uniform incidence. The figure illustrates the flow structure; the quantitative comparisons below use integrated loads.

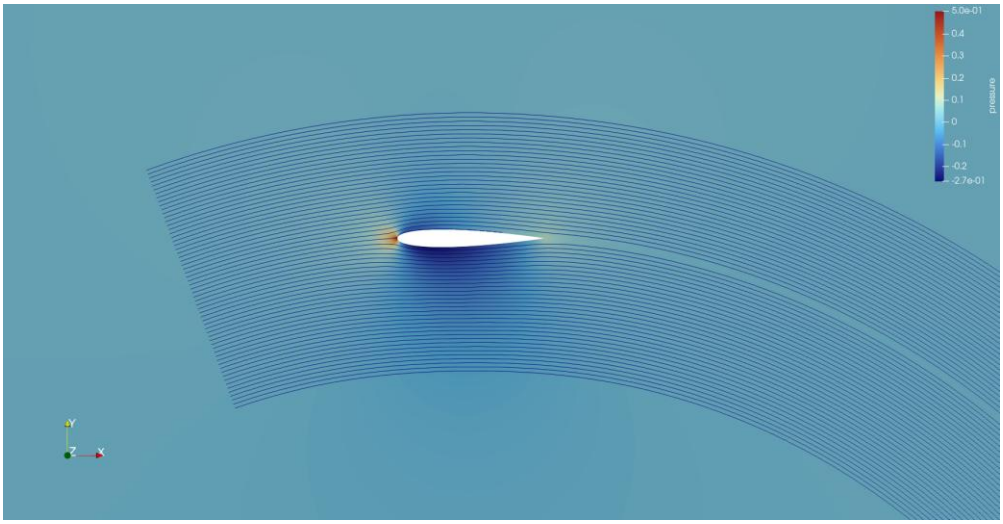


Fig. 3 Pressure distribution and streamlines around NACA0012, showing curved streamlines and pressure asymmetry between the upper and lower surfaces.

Table 2 Side force versus turn rate and comparison with thin-airfoil theory

r'	**SRF** $-C_Y$	**Thin-airfoil** $(\pi/2)r'$	**SRF effective coefficient** $-C_Y/r'$
0.05	0.06339	0.07854	1.2678
0.10	0.12560	0.15708	1.2560
0.18	0.22818	0.28274	1.2677

At $Re = 10^6$, the steady SRF inward side-force coefficient $-C_Y$ increased with turn rate, as shown in Table 2. A linear fit to the three points, including an intercept, gives

$$-C_Y \simeq -5.35 \times 10^{-4} + 1.2690r' \tag{7}$$

The chordwise variation in relative inflow angle produces an effect analogous to effective camber on a symmetric airfoil, proportional to $c/R = r'$. At small turn rates, the inward side force is therefore expected to vary approximately linearly with turn rate.

For a symmetric thin airfoil attached to the rotating arm at mid-chord, the inviscid small-curvature approximation gives $-C_Y = (\pi/2)r'$ (Winckelmans et al., 2026). The computed slope, 1.2690, is 19.2% below the theoretical value of 1.5708, but the sign, linear trend and order of magnitude agree. The static lift slope $C_{l_\alpha} = 6.0175\ \mathrm{rad}^{-1}$ is only 4.2% below 2π and cannot alone explain the turning-slope difference.

The effects of finite thickness, viscous RANS-SA modelling, finite turn rate, mesh resolution and far-field boundaries have not yet been separated. This comparison therefore checks physical trends and does not establish quantitative validation or grid independence.

3.3 Comparison of steady SRF and ALE solutions

Mader and Martins (2011) reported Euler-based stability derivatives, including NACA0012. Their conditions differ from the present viscous RANS-SA calculations. We therefore use SRF solutions with identical geometry, mesh and turn rate as an internal reference.

At $r' = 0.18$, ALE initialised from the steady SRF field at 698 steps/rev differed from SRF by 0.64% at the first step and reached $C_Y = -0.241218$ at the end of the second revolution. In the subsequent 1,396-steps/rev calculation, the side-force coefficient varied by 5.72×10^{-8} over the second revolution, while the difference between the first- and second-revolution endpoints was 4.38×10^{-8}, indicating phase invariance and periodic closure. Halving the time step changed the endpoint by approximately 0.06%; nevertheless, the magnitude of the ALE endpoint $C_Y = -0.24136$ exceeded the steady SRF value of -0.22818 by 5.78%.

Operator diagnostics at Re=10^5 on the 55,341-cell mesh removed terms predicted by the coordinate transformation from the momentum residual. The remainder was normalised by the larger of the predicted residual RMS and the RMS of the centrifugal scale $\Omega^2|\mathbf{r}|$. Relative-velocity Roe dissipation and a convective-residual correction reduced this measure from 7.46 to 0.016 near the wall and from 2.99 to 0.00819 over the full domain. The side-force difference from SRF decreased from 1.24% to 0.48% at the first step and from 8.67% to 5.62% after one revolution, but drift remained. A separate convection correction reduced the SA operator mismatch by about 1,000-fold, yet changed the endpoint C_Y by only 3×10^{-7}, indicating that this mismatch was not dominant. Further work will isolate unsteady SRF integration, BDF/coordinate-transformation consistency and mesh effects.

Satisfying the GCL and obtaining repeatable loads do not alone establish discrete equivalence between the two formulations. The consistency of time discretisation and coordinate transformation therefore remains a separate verification task.

4 Preparation for three-dimensional BB2 simulations

Three-dimensional BB2 results are not yet available. Prism–tetrahedron–pyramid meshes and solver capabilities are being assessed using PETSc DMPlex, artificial compressibility, Roe-type fluxes and SA-neg. Boundary-layer prisms and boundary conditions will first be checked with a short-span three-dimensional NACA0012 case. Subsequent stages comprise fixed-mesh, straight-ahead calculations of a BB2 bare-hull half-model at reduced Reynolds number, followed by appendage inclusion. Turning breaks symmetry, requiring the full model for rotating-arm simulations.

Remaining work includes the outer domain for circular motion, three-dimensional ALE rigid-body motion, iterative linear solvers and wall-distance evaluation. BB2 rotating-arm calculations will follow. This paper reports the development path and constraints of the three-dimensional extension. Dynamic mesh smoothing (Ahn et al., 2010) provides a reference for future deforming-mesh applications; the present two-dimensional method rigidly rotates the entire mesh without internal deformation.

The present scope covers the RANS moving-mesh method and preparation for three-dimensional application. Scale-resolving simulations and wall modelling will follow establishment of the three-dimensional moving-mesh capability.

5 Conclusions

Inertial-frame ALE rotating-arm motion was implemented in the in-house unstructured solver ULSAN3d. The NACA0012 side force acted towards the turn centre and varied approximately linearly with turn rate. Its slope, 1.2690, was about 19% below quasi-steady thin-airfoil theory. At $Re = 10^6$ and $r' = 0.18$, ALE loads exhibited periodic closure and low time-step sensitivity, but their magnitude exceeded the steady SRF value by 5.78%. Consistency corrections at $Re = 10^5$ reduced operator mismatch and load differences but did not eliminate drift.

The results establish repeatable body-fixed loads; full SRF–ALE equivalence and grid independence remain unproven. Next steps are three-dimensional hybrid-mesh assessment, staged fixed-mesh BB2 tests, ALE implementation and computational-efficiency improvements toward BB2 rotating-arm simulations.

Acknowledgements

This research was supported by Korea Institute for Advancement of Technology (KIAT) grant funded by the Korea Government (MOTIR) (RS-2026-25505686, The Competency Development Program for Industry Specialist).

References

1. Ahn, H. T., & Kallinderis, Y. (2006). Strongly coupled flow/structure interactions with a geometrically conservative ALE scheme on general hybrid meshes. Journal of Computational Physics, 219(2), 671–696.
2. Ahn, H. T., Branets, L., & Carey, G. F. (2010). Moving boundary simulations with dynamic mesh smoothing. International Journal for Numerical Methods in Fluids, 64(8), 887–907.
3. Allmaras, S. R., Johnson, F. T., & Spalart, P. R. (2012). Modifications and clarifications for the implementation of the Spalart–Allmaras turbulence model. Proceedings of ICCFD7, ICCFD7-1902.
4. Carrica, P. M., Kerkvliet, M., Quadvlieg, F., & Martin, J. E. (2021). CFD simulations and experiments of a submarine in turn, zigzag, and surfacing maneuvers. Journal of Ship Research, 65(4), 293–308.
5. Chorin, A. J. (1967). A numerical method for solving incompressible viscous flow problems. Journal of Computational Physics, 2(1), 12–26.
6. Fureby, C., et al. (2016). Experimental and numerical study of a generic conventional submarine at 10° yaw. Ocean Engineering, 116, 1–20.
7. Go, G., Lee, E., Ahn, H. T., Kim, S., Chun, S. Y., Kim, J. S., & Lee, B. H. (2016). 6DOF simulation and determination of hydrodynamic derivatives of underwater tow-fish using CFD. Journal of the Society of Naval Architects of Korea, 53(4), 315–328.
8. Go, G., & Ahn, H. T. (2019). Hydrodynamic derivative determination based on CFD and motion simulation for a tow-fish. Applied Ocean Research, 82, 191–209.
9. Holloway, A. G. L., Jeans, T. L., & Watt, G. D. (2015). Flow separation from submarine shaped bodies of revolution in steady turning. Ocean Engineering, 108, 426–438.
10. Jeong, J.-H., Han, J.-H., Ok, J., Kim, H.-D., Kim, D.-H., Shin, Y.-K., & Lee, S.-K. (2016). Prediction of hydrodynamic coefficients for underwater vehicle using rotating arm test. Journal of Ocean Engineering and Technology, 30(1), 25–31.
11. Joubert, P. N. (2006). Some Aspects of Submarine Design, Part 2: Shape of a Submarine 2026. DSTO-TR-1920.
12. Kallinderis, Y., & Ahn, H. T. (2005). Incompressible Navier–Stokes method with general hybrid meshes. Journal of Computational Physics, 210(1), 75–108.
13. Kim, H., Ranmuthugala, D., Leong, Z. Q., & Chin, C. (2018). Six-DOF simulations of an underwater vehicle undergoing straight line and steady turning manoeuvres. Ocean Engineering, 150, 102–112.
14. Kim, D.-H., et al. (2023). Experimental study of the hydrodynamic maneuvering coefficients for a BB2 generic submarine using the planar motion mechanism. Ocean Engineering, 271, 113428.
15. Lee, E., & Ahn, H. T. (2018). A reconstruction-based cell-centered high-order finite volume method for incompressible viscous flow simulation on unstructured meshes. Computers & Fluids, 170, 187–196.
16. Limache, A. C., & Cliff, E. M. (2000). Aerodynamic sensitivity theory for rotary stability derivatives. Journal of Aircraft, 37(4), 676–683.
17. Mader, C. A., & Martins, J. R. R. A. (2011). Computation of aircraft stability derivatives using an automatic differentiation adjoint approach. AIAA Journal, 49(12), 2737–2750.
18. Overpelt, B., Nienhuis, B., & Anderson, B. (2015). Free running manoeuvring model tests on a modern generic SSK class submarine (BB2). Pacific International Maritime Conference.
19. Pan, Y.-C., Zhou, Q.-D., & Zhang, H.-X. (2015). Numerical simulation of rotating arm test for prediction of submarine rotary derivatives. Journal of Hydrodynamics, 27(1), 68–75.
20. Spalart, P. R., & Allmaras, S. R. (1992). A one-equation turbulence model for aerodynamic flows. AIAA Paper 92-0439.
21. Toxopeus, S. L., et al. (2012). Collaborative CFD exercise for a submarine in a steady turn. Proceedings of OMAE 2012, OMAE2012-83573, 761–772.
22. Toxopeus, S. L., Kerkvliet, M., Vogels, R., Quadvlieg, F., & Nienhuis, B. (2022). Submarine hydrodynamics for off-design conditions. Journal of Ocean Engineering and Marine Energy, 8, 499–511.
23. Winckelmans, G., Rochefort, P., Villeneuve, T., Trigaux, F., Duponcheel, M., & Dumas, G. (2026). Improved modeling of flow curvature effects and actuator line method with aerodynamic moment, with application to vertical-axis turbines. Wind Energy Science, 11, 3615–3651. https://doi.org/10.5194/wes-11-3615-2026
24. Zhang, J. T., Maxwell, J. A., Gerber, A. G., Holloway, A. G. L., & Watt, G. D. (2013). Simulation of the flow over axisymmetric submarine hulls in steady turning. Ocean Engineering, 57, 180–196.
25. Zhao, B., et al. (2023). Hydrodynamic coefficients of the DARPA SUBOFF AFF-8 in rotating arm maneuver—Part II: Test results and discussion. Ocean Engineering, 268, 113466.

CFD simulations of zigzag manoeuvres using a simplified propeller representation

Ivan Sulovsky[1*], Andro Bakica[2], Hrvoje Jasak[3], Jasna Prpić-Oršić[1]

[1]Faculty of Engineering, University of Rijeka, Croatia
[2] Faculty of Maritime studies, University of Split, Croatia
[3] University of Cambridge, United Kingdom

(ivan.sulovsky@uniri.hr, abakica@pfst.hr, h.jasak@wikki.co.uk, jasna.prpic.orsic@uniri.hr)

1 Introduction

Ship manoeuvering is an integral part in a ship design spiral, often assessed by empirical or semi-empirical methods due to computational or model tests related costs. In this paper, zigzag manoeuvres in calm water are conducted on a KVLCC2 hull benchmark model through CFD-RANS approach with free surface. Numerical simulations are performed using OpenFOAM, an open-source toolbox for solving fluid dynamics problems. Furthermore, simulations are performed on a specialized OpenFOAM extension *Naval Hydro Pack*, suitable for various assessments in the domain of ship hydrodynamics (Vukčević et al., 2017). In the simulations, propeller is modelled as a simplified actuator disk (AD) model (Bakica et al., 2019) in order to preserve computational efficiency. The aim of this paper is to evaluate the suitability of the actuator disk model for manoeuvring simulations, and to compare the results against experimental data and against other numerical approaches reported in the literature.

2 Experimental Setup

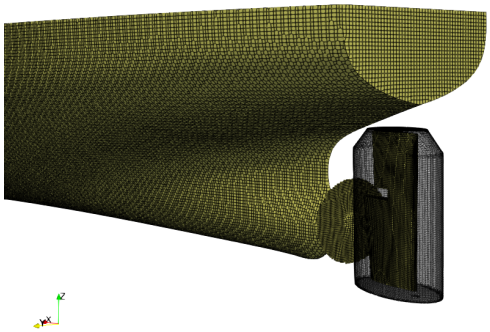
The free-running model tests (FRMT) used here for comparison were carried out at MARIN, Netherlands, where the hull was tested in calm water and in waves (SIMMAN, 2008). The present study considers the calm water 10/10 and 20/20 zigzag manoeuvres. The simulations are performed at model scale $\lambda = 45.7$, consistent with the experimental campaign. The main particulars of the hull are given in Table 1. The ship is fitted with a single fixed-pitch propeller and a horn rudder, and the manoeuvres are initiated from the self-propulsion point at the model approach speed corresponding to a Froude number of 0.142.

Table 1: Main particulars of the KVLCC2 in model scale ($\lambda = 45.7$)

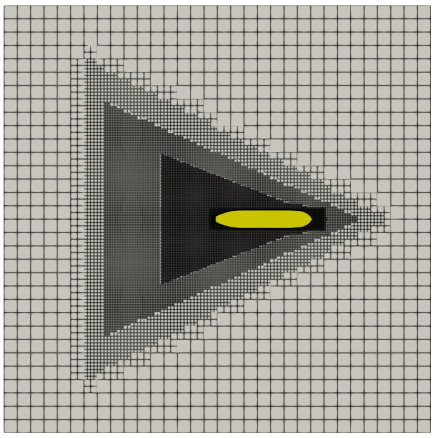
Parameter	Symbol	Value
Length between perpendiculars	L_{pp} (m)	7.0
Beam	B (m)	1.1688
Draft	T (m)	0.455
Block coefficient	C_B (-)	0.8098
Displacement	∇ (m^3)	3.2724
Design (approach) speed	U_0 (m/s)	1.1702
Propeller revolution rate	n (rps)	9.9
Propeller diameter	D (m)	0.204

3 Numerical model

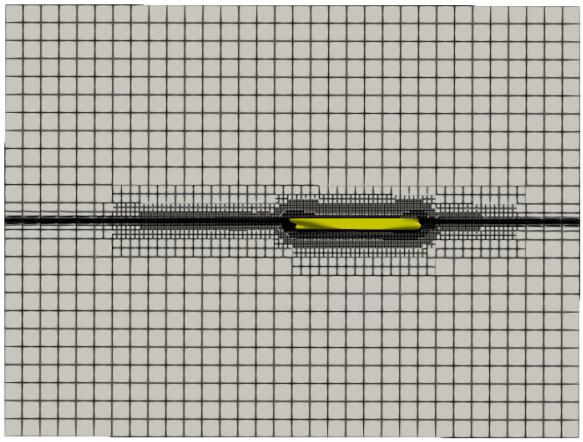
The incompressible RANS equations are solved with the finite volume method on a collocated, unstructured grid. Convective and diffusive terms are discretized with second-order accurate schemes, with bounded interpolation applied to the convective fluxes to preserve stability during the large rudder and hull motions. Temporal discretization is set to first order during approach part while the zigzag manoeuvres are solved using second-order accurate backward scheme. Turbulence closure is achieved using a k-ω SST two-equation eddy-viscosity model. The free surface is captured with the Ghost Fluid Method, which treats the interface as a sharp discontinuity and imposes the jump conditions directly (Vukčević et al., 2017). Ship motions during the manoeuvre are resolved with a dynamic 6DoF mesh motion with only rudder being encapsulated by overset domain. The propeller action is introduced through the actuator disk as a face-based pressure jump. The computational mesh in the aft region and corresponding cross-sections are shown in Figure 1.



(a) Aft region with rudder encapsulated by the overset domain



(b) Cross horizontal view at $z = 0$



(c) Cross vertical view at $y = 0$

Figure 1: KVLCC2 computational mesh: aft region and cross-sections

4 Results and Discussion

Prior to the manoeuvers, the self-propulsion point at an approach speed U_0 was established using a PID controller on the actuator disk loading (Đurašević et al., 2023). The predicted propeller revolution rate agrees well with the experiment, deviating by approximately 4.7%. This confirms that the propulsion setup reproduces the correct operating point of the propeller and provides a consistent basis for the manoeuvring simulations that follow. Figure 2 shows the 10/10 zigzag manoeuvre initiated to portside. The computed yaw angle follows the experimental trend closely, with the first overshoot angle captured within approximately 5% and the second within about 10% (Table 2). The peak yaw rate and drift angle agree with the measurements to within roughly 9% and 4%, respectively. The largest deviations appear in the timing of the response, with the computed overshoot instants reached somewhat earlier than in the experiment. In the 20/20 zigzag initiated to starboard, Figure 4, the larger rudder angle produces a stronger yaw response that is again well reproduced. The overshoot angles agree to within about 10% and the peak drift angles to within 5%, while the second rudder execute time and the first overshoot instant show the largest timing differences. Overall, both manoeuvres are captured with reasonable accuracy across the reported parameters.

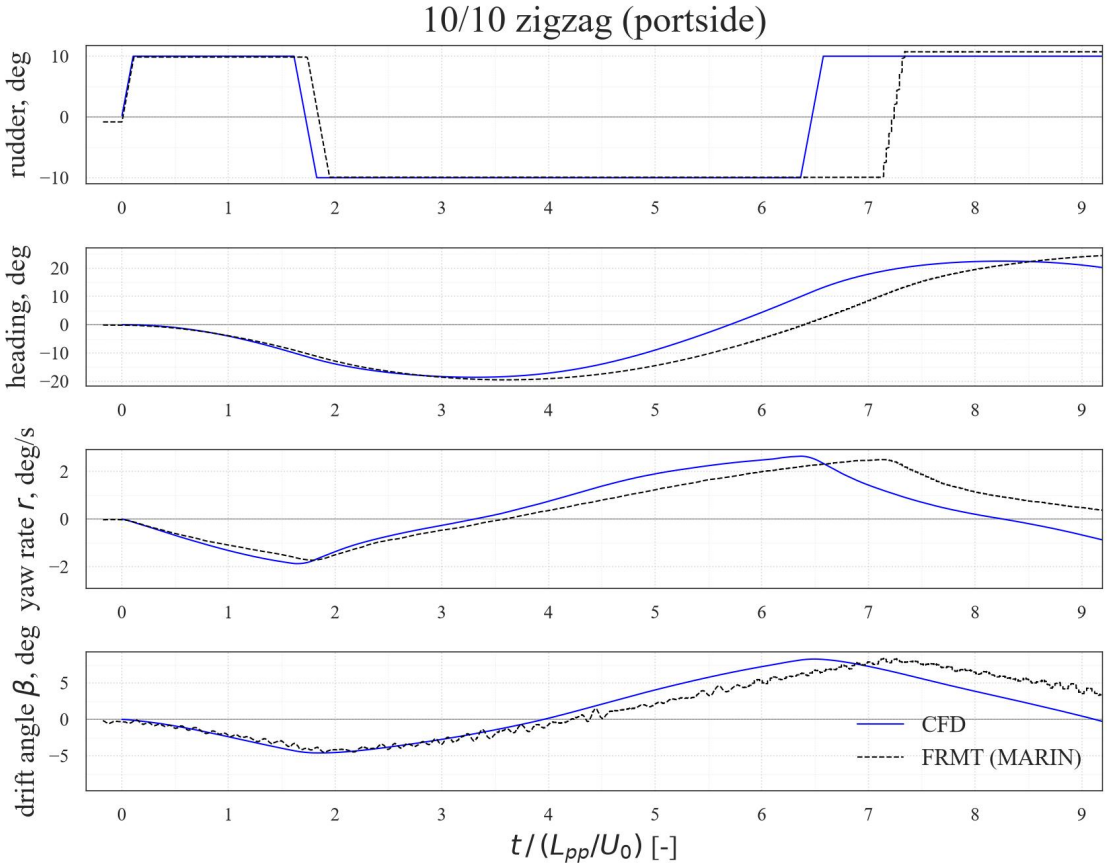


Figure 2: Time histories of rudder angle, heading, yaw rate and drift angle for the 10/10 zigzag manoeuvre.

The surge and sway velocities in a horizontal body-fixed system are given in Figure 3:

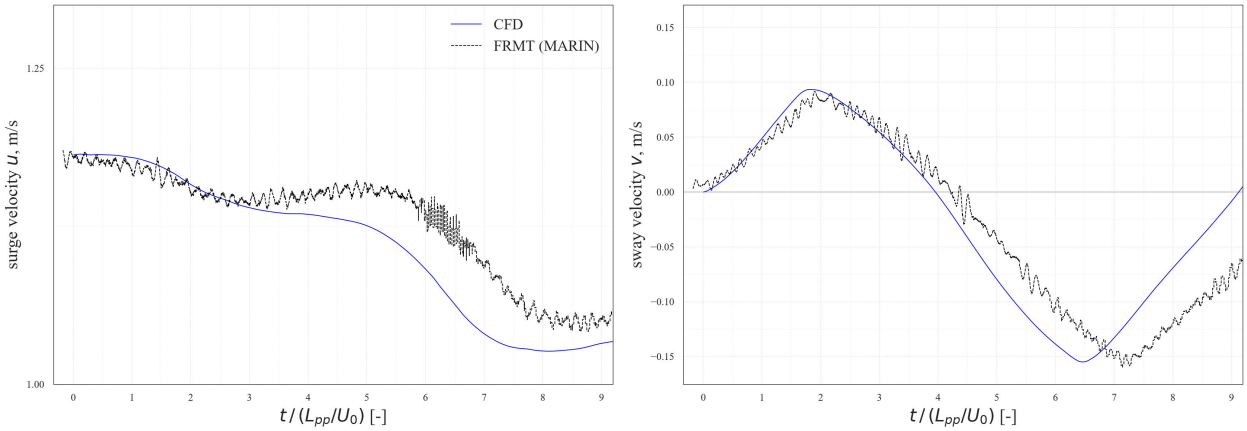


Figure 3: Surge and sway velocities for the 10/10 zigzag manoeuvre (portside).

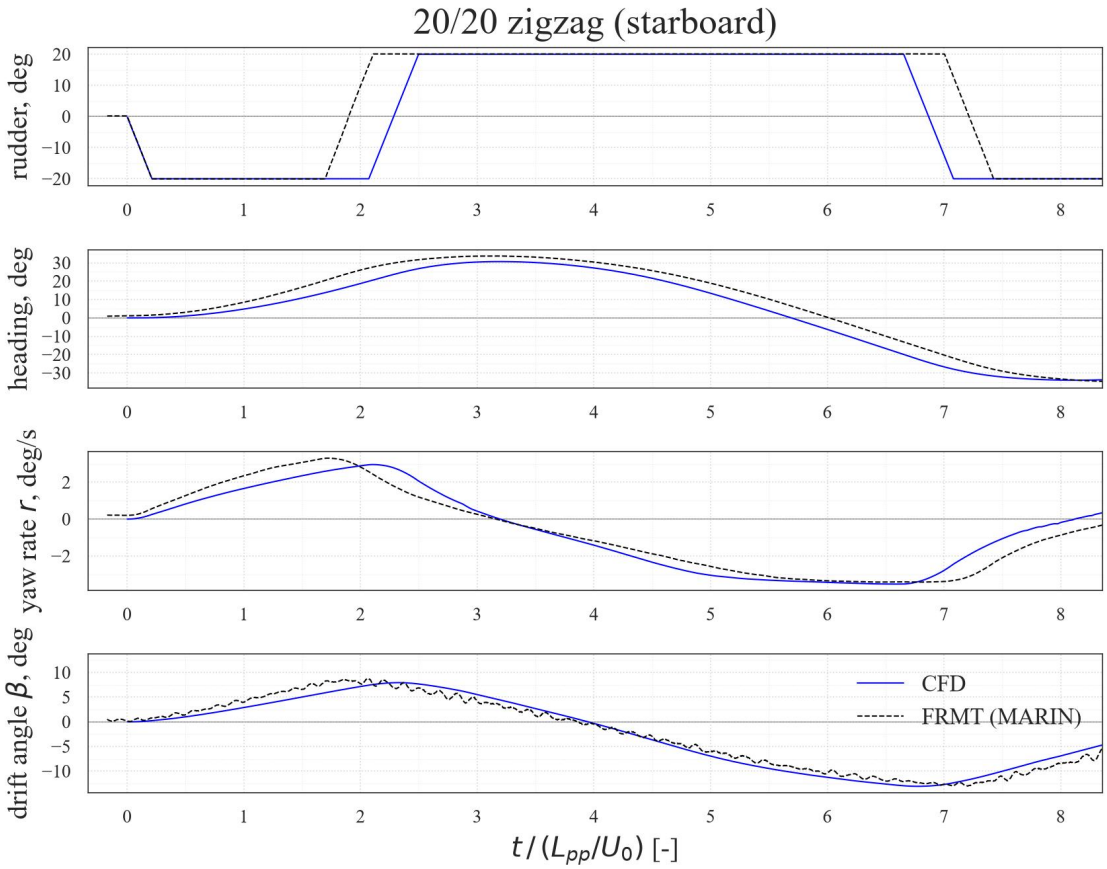


Figure 4: Time histories of rudder angle, heading, yaw rate and drift angle for the 20/20 zigzag manoeuvre.

As with the previous manoeuvre, the velocities are given accordingly in Figure 5:

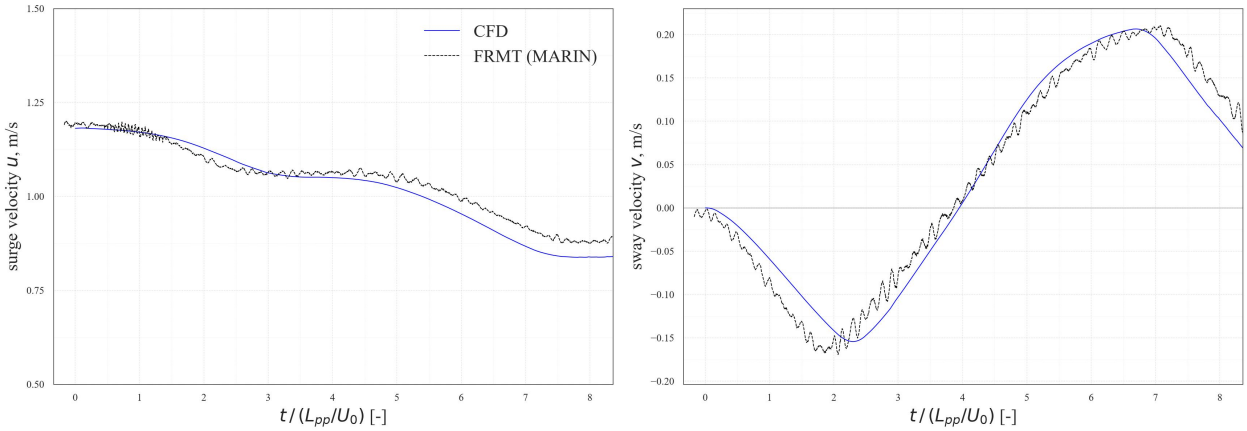


Figure 5: Surge and sway velocities for the 20/20 zigzag manoeuvre (starboard).

Comparison of manoeuvring parameters between free-running model tests and CFD for the 10/10 and 20/20 zigzag manoeuvres are given in Table 2. Due to computational constraints, the numerical results reach up to the second overshoot angle. The comparison error is defined as $E = ((\text{FRMT} - \text{CFD})/\text{FRMT}) \times 100$.

Table 2: Manoeuvring parameters between free-running model tests and CFD for the 10/10 and 20/20 zigzag manoeuvres.

		10/10 zigzag			20/20 zigzag		
Parameter	Unit	FRMT	CFD	E (%)	FRMT	CFD	E (%)
ψ_{OS1}	deg	19.50	18.57	5	33.7	30.3	10.08
ψ_{OS2}	deg	22.48	25.02	10.15	35.2	34	2.94
t_2	s	10.19	9.42	7.5	9.96	12.17	22.1
t_3	s	41.94	37.46	10.6	41.23	39.17	5
t_{OS1}	s	21.08	18.2	13.6	17.97	20.8	15.74
t_{OS2}	s	53.97	48.25	10.59	49.12	47.16	3.99
r_1	deg/s	1.72	1.87	8.56	3.34	3.0	10.18
r_2	deg/s	2.51	2.65	5.57	3.4	3.56	4.7
β_1	deg	4.43	4.6	3.83	8.3	8.0	3.61
β_2	deg	8.18	8.27	1.1	12.51	13.06	4.39

The discrepancies are consistent with the known limitations of the actuator disk used for manoeuvring simulations (Sadat et al., 2014; Kim et al., 2021). Part of this deviation may be associated with the simplified propeller representation.The AD model imposes a distributed axial load and does not reproduce the tangential and lateral action of a rotating propeller, which can influence the flow into the rudder and, in turn, the yaw checking behaviour. Also, as stated by Chen et al. (2022), the inflow velocity towards the rudder may be overpredicted by the actuator disk, which in turn produces a stronger rudder normal force.

5 Conclusions and Future Work

A CFD-RANS approach with a free surface and an actuator disk propeller model was applied to 10/10 and 20/20 zigzag manoeuvres of the KVLCC2 hull. The self-propulsion point was reproduced with a revolution rate deviation of about 4.7%, and both manoeuvres followed the experimental trends, with overshoot angles, yaw rates and drift angles generally predicted within about 10%. The larger deviations were confined mainly to the response timing. These remaining differences may be linked in part to the simplified propeller representation, which omits the tangential and lateral propeller action, although a conclusive confirmation is not possible from the present results. Future work will involve modelling the zigzag manoeuvres using a hybrid propeller model (Đurašević et al., 2023) to isolate the influence of propeller modelling fidelity on the manoeuvring response of single-screw ships.

Acknowledgments

This work was supported by the Croatian Science Foundation under project IP-2022-10-2821 and funded by the European Union – NextGenerationEU – VEDRO– PU-17 uniri-iz-25-10.

References

A. Bakica, I. Gatin, V. Vukčević, H. Jasak, and N. Vladimir. Accurate assessment of ship-propulsion characteristics using CFD. *Ocean Engineering*, 175:149–162, 2019. ISSN 0029-8018. doi: 10.1016/j.oceaneng.2018.12.043.

C. Chen, L. Zou, Z. Zaojian, and H. Guo. Assessment of CFD-Based Ship Maneuvering Predictions Using Different Propeller Modeling Methods. *Journal of Marine Science and Engineering*, 10(8), 2022. ISSN 2077-1312. doi: 10.3390/jmse10081131. URL `https://www.mdpi.com/2077-1312/10/8/1131`.

I. Kim, C. Kim, S.Kim, D. Ko, S. Moon, H. Park, J. Kwon, and B. Jin. Estimation of the manoeuvrability of the KVLCC2 in calm water using free running simulation based on CFD. *International Journal of Naval Architecture and Ocean Engineering*, 13:466–477, 2021. ISSN 2092-6782. doi: https://doi.org/10.1016/j.ijnaoe.2021.05.004. URL `https://www.sciencedirect.com/science/article/pii/S2092678221000303`.

H. Sadat, P. Wu, and F.Stern. CFD simulations of KVLCC2 maneuvering with different propeller modeling. In *Verification and Validation of Ship Maneuvering Simulation Method Workshop*, 12 2014.

SIMMAN. Preprints of workshop proceeding. *SIMMAN 2008, Copenhagen*, 2008.

S. Đurašević, I. Gatin, T. Uroić, and H. Jasak. Hydrodynamic performance of a full-scale ship with a Pre-Swirl Duct: A numerical study with partially rotating grid method. *Ocean Engineering*, 283:1–23, 2023. doi: 10.1016/j.oceaneng.2023.115049.

V. Vukčević, H. Jasak, and I.Gatin. Implementation of the Ghost Fluid Method for free surface flows in polyhedral Finite Volume framework. *Computers & Fluids*, 153:1–19, 2017. ISSN 0045-7930. doi: 10.1016/j.compfluid.2017.05.003.

28th Numerical Towing Tank Symposium (NuTTS)
19–21 October 2026 – Mülheim a. d. Ruhr, Germany

Comparison of Direct and Indirect System Identification for Hydrodynamic Derivatives of an Inland Waterway Ship in Deep and Shallow Water

Jakob Rzeszutko[1], **Lahbib Zentari**[2], **Ould el Moctar**[1]
[1]Technical University of Berlin (TUB), Germany
[2]Federal Waterways Engineering and Research Institute (BAW), Germany
jakob.rzeszutko@baw.de

1 Introduction

In recent years, Germany's waterways have experienced prolonged periods of extremely shallow water, severely affecting the inland shipping industry. Navigation on the Rhine was temporarily suspended in 2018, 2022, and most recently in 2026. Several tools are available to investigate the hydrodynamics of inland waterway ships under such extreme shallow water conditions. Captive maneuvering tests at model scale allow the hydrodynamic parameters to be determined directly, as demonstrated experimentally by Mucha et al. (2017) and Bedos and Tonelli (2022) and numerically by Zentari et al. (2022), Chillcce et al. (2025a), and Rzeszutko et al. (2025b). Free-running maneuvering tests, in contrast, are available at both model and full scale; Mucha et al. (2019) presented zig-zag maneuvers for an inland waterway ship in model scale. Both types of maneuvering test can be conducted experimentally or numerically. To describe the hydrodynamics of an inland waterway ship under operating conditions, maneuvering models are developed whose so-called hydrodynamic coefficients are obtained by regression analysis, following Abkowitz (1964). Two system identification methods are employed to determine these coefficients: the direct and the indirect approach. Direct system identification is applied to captive model tests and is well established, as shown by Rzeszutko et al. (2025a) and Chillcce (2025b). Indirect system identification is applied to free-running tests, as shown by Chillcce and El Moctar (2023). In the present work, we highlight the key differences between the two methodologies and provide a systematic analysis of the determination of hydrodynamic coefficients by direct and indirect system identification for a typical inland waterway ship in deep and shallow water. We aim to demonstrate that the differences arising in the solution of the equations of motion depend strongly on the quality and quantity of the available data.

2 Methodology

2.1 Coordinate System

Fig. 1 shows a sketch of the Cartesian coordinate system, illustrating the inertial and ship-fixed reference frames in three degrees-of-freedom. The inertial reference frame O_O is defined by a longitudinal axis x_O, a lateral axis y_O, and a vertical axis z_O pointing upwards. We use the symbol ψ to describe the orientation of the ship-fixed frame relative to the inertial reference frame. The ship-fixed reference frame S is located amidships, with its longitudinal axis x, lateral axis y, and a vertical axis z pointing upwards. Along these axes, the longitudinal and sway hydrodynamic forces X and Y, velocities u and v, and accelerations $\dot{u}$ and $\dot{v}$ are defined, respectively. Around the z-axis, the hydrodynamic yaw moment N, yaw rate r, and yaw acceleration $\dot{r}$ are defined. Additional parameters used to describe the ship's kinematics and configuration include the longitudinal center of gravity x_G, the ship speed vector $\mathbf{U}$, the drift angle β, and the rudder angle δ.

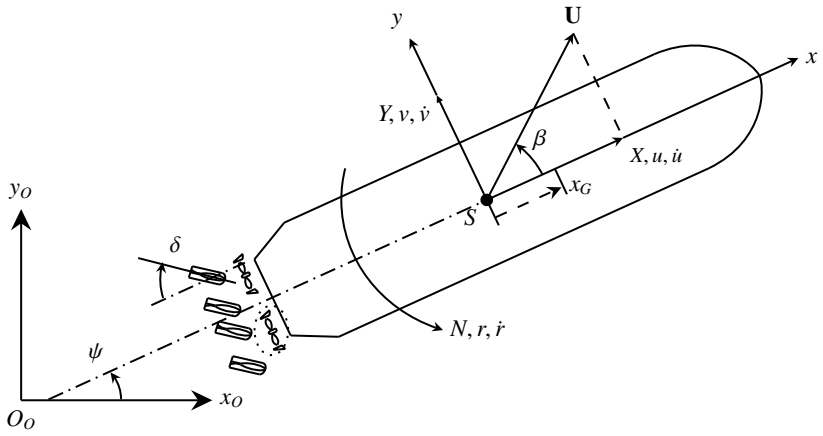


Fig. 1: Sketch of the Cartesian coordinate system with an inertial O_O and ship-fixed S reference frame in three degrees-of-freedom.

2.2 Test Case

Our test case is a typical inland waterway ship, introduced by Mucha et al. (2017), at a model scale factor λ of 1 : 16, as shown in Fig. 2. The principal dimensions are provided in Tab. 1. The water density ρ is assumed constant at 1000 kg·m^{-3}.



Fig. 2: Perspective of the rendered inland waterway ship.

Table 1: Principal dimensions of the *inland waterway ship*, reproduced from Mucha et al. (2017).

Description	**Parameter**	**Unit**	**Full scale**	**Model scale**
Scale factor	λ	–	1	16
Length between perpendiculars	L_{PP}	m	135.00	8.438
Breadth	B	m	11.44	0.715
Draft	T	m	3.50	0.219
Mass	m	t	4974.10	1.214
Longitudinal center of gravity	x_G	m	−0.1718	−0.010 74
Block coefficient	C_B	–	0.92	0.92

2.3 Mathematical Maneuvering Model

The equation of motion in three degrees-of-freedom is given in Eq. (1). Here, the added mass coefficients ($X_{\dot{u}}$, $Y_{\dot{v}}$, $Y_{\dot{r}}$, $N_{\dot{v}}$, $N_{\dot{r}}$) are incorporated into the left-hand side of the equations. The utilized added mass coefficients are provided by El Moctar et al. (2022) for the investigated water depths.

$$\begin{aligned} m\left(\dot{u} - vr - x_G r^2\right) - X_{\dot{u}}\dot{u} &= X\left(u, v, r, \delta\right) \\ m\left(\dot{v} - ur - x_G \dot{r}\right) - Y_{\dot{v}}\dot{v} - Y_{\dot{r}}\dot{r} &= Y\left(u, v, r, \delta\right) \\ mx_G\left(\dot{v} + ur\right) + I_{zz}\dot{r} - N_{\dot{v}}\dot{v} - N_{\dot{r}}\dot{r} &= N\left(u, v, r, \delta\right) \end{aligned} \tag{1}$$

An Abkowitz-based mathematical maneuvering model, given in Eq. (2) by Chillcce and El Moctar (2023), models the longitudinal force X, sway force Y, and yaw moment N using hydrodynamic coefficients (e.g., X_u, X_{uu}) as functions of the kinematic quantities and rudder angle.

$$
\begin{aligned}
X(u,v,r,\delta) &= X_u u + X_{uu} u^2 + X_{vv} v^2 + X_{rr} r^2 + X_{dd} \delta^2 \\
&\quad + X_{vr} vr + X_{vvvv} v^4 + X_{vvrr} v^2 r^2 + X_{udd} u\delta^2 + X_{dddd} \delta^4 \\
Y(u,v,r,\delta) &= Y_0 + Y_v v + Y_r r + Y_d \delta + Y_{vvv} v^3 + Y_{rrr} r^3 \\
&\quad + Y_{vvr} v^2 r + Y_{vrr} v r^2 + Y_{ddd} \delta^3 + Y_{ud} u\delta + Y_{uddd} u\delta^3 \\
N(u,v,r,\delta) &= N_0 + N_v v + N_r r + N_d \delta + N_{vvv} v^3 + N_{rrr} r^3 \\
&\quad + N_{vvr} v^2 r + N_{vrr} v r^2 + N_{ddd} \delta^3 + N_{ud} u\delta + N_{uddd} u\delta^3
\end{aligned}
\tag{2}
$$

The hydrodynamic forces, kinematic parameters, and other quantities are normalized using Prime System I, adapted from Chillcce and El Moctar (2023), at a reference ship speed U_0 of $0.556\,\mathrm{m{\cdot}s^{-1}}$. These normalized variables are denoted by an apostrophe $(\cdot)'$ in the following sections.

2.4 System Identification

System identification determines the hydrodynamic coefficients in Eq. (2) from measured data. Because the polynomial model is linear in its coefficients, the identification reduces to a linear regression problem for each degree of freedom $j \in \{X, Y, N\}$. Collecting the regressors into the vector φ_j and the unknown coefficients into the vector θ_j, the model reads $j' = \varphi_j^\top \theta_j$. Evaluating this relation for M samples yields the overdetermined linear system $\mathbf{A}_j \theta_j = \mathbf{b}_j$, in which the design matrix $\mathbf{A}_j$ contains the regressors evaluated at every sample and the observation vector $\mathbf{b}_j$ contains the corresponding measured quantities. The two identifications differ only in the origin of these observations. Direct System Identification measures the hydrodynamic forces themselves in constrained model tests, whereas Indirect System Identification infers them from the motion of the free-running ship through the equations of motion. In both cases the system is solved for each degree of freedom and water depth separately.

Direct System Identification relies on captive tests, in which the model is guided through prescribed steady states (propulsion, drift, rudder, rotating arm, and combined rotating arm with drift) while the resulting forces and moments are measured experimentally or numerically by Computational Fluid Dynamics (CFD). Because every captive condition is steady, the non-dimensional accelerations vanish ($\dot{u}' = \dot{v}' = \dot{r}' = 0$) and the inertial and added-mass terms of Eq. (1) drop out, so the measured forces are balanced by the hydrodynamic model alone and directly form the observation vector $\mathbf{b}_j = [\, j'_k \,]$. The coefficient vector then follows from ordinary least squares in Eq. (3), solved by singular-value decomposition to preserve conditioning in the near-collinear captive subsets.

$$
\hat{\theta}_j = \arg\min_{\theta_j} \left\| \mathbf{A}_j \theta_j - \mathbf{b}_j \right\|_2^2 \tag{3}
$$

Indirect System Identification draws on free-running maneuvering measurements (turning circles, zig-zag maneuvers), in which the hydrodynamic forces are not directly observable but are implicitly present in the measured motion. Following the equation-error approach, the equations of motion in Eq. (1) are enforced pointwise at every time step, which avoids both mass-matrix inversion and time integration. The required non-dimensional velocities and accelerations are obtained per record by Savitzky–Golay smoothing and differentiation of the measured states. Each sample then contributes one row to the system in Eq. (4).

$$
\begin{aligned}
(m' - X_{\dot{u}})\,\dot{u}' - m'\left(v' r' + x'_G\, r'^2\right) &= b_X \\
(m' - Y_{\dot{v}})\,\dot{v}' + (m' x'_G - Y_{\dot{r}})\,\dot{r}' + m'\,u' r' &= b_Y \\
(m' x'_G - N_{\dot{v}})\,\dot{v}' + (I'_{zz} - N_{\dot{r}})\,\dot{r}' + m' x'_G\,u' r' &= b_N
\end{aligned}
\tag{4}
$$

This formulation gathers all known rigid-body and added-mass contributions on the left-hand side, so that the right-hand side isolates the residual hydrodynamic force components in surge, sway, and yaw (b_X, b_Y, b_N), which serve as the observations. Because the regressors of a single maneuver are strongly correlated, an unconstrained least-squares solution is prone to physically implausible coefficients, and the final coefficients are therefore determined by the bounded elastic-net regression Eq. (5) proposed in Chillcce and El Moctar (2023). The bound vectors $\theta_j^{\min}$ and $\theta_j^{\max}$ constrain each coefficient to its physically admissible sign, while the two regularization terms prevent overfitting. The L_1 penalty, weighted by λ, promotes sparsity in the coefficient vector, and the L_2 penalty, weighted by α, stabilizes the estimates of highly collinear regressors.

$$
\hat{\theta}_j = \arg\min_{\theta_j^{\min} \le \theta_j \le \theta_j^{\max}} \left\| \mathbf{A}_j \theta_j - \mathbf{b}_j \right\|_2^2 + \lambda \|\theta_j\|_1 + \alpha \|\theta_j\|_2^2. \tag{5}
$$

3 Results and Discussion

Figure 3 compares the hydrodynamic coefficients from Eq. (2) obtained by direct and indirect system identification in shallow ($h/T = 1.2$) and deep water ($h/T = 3.0$). The coefficients are plotted on a symmetric-logarithmic axis to compare their orders of magnitude. The direct method estimated the coefficients from numerical steady captive tests at the reference speed $U_0 = 0.556\,\mathrm{m{\cdot}s^{-1}}$, while the indirect method used three 35°/5° zig-zag maneuvers per water depth by Mucha et al. (2019). The coefficients X'_u, Y'_r, Y'_δ, N'_v, N'_r, and N'_δ shared the same sign in every case, and both methods reproduced the expected shallow water amplification, with the magnitudes at $h/T = 1.2$ exceeding those at $h/T = 3.0$. The linear coefficients differed only slightly in magnitude, except for Y'_v, which vanished in the indirect models. However, some of the non-linear coefficients disagreed in magnitude and sign, showing that the indirect system identification did not always reproduce the physical behavior of the ship. The L_1 penalty and the physical sign bounds of the indirect regression additionally drove X'_{vv}, Y'_v, Y'_{vvv}, $Y'_{\delta\delta\delta}$, N'_{rrr}, and $N'_{\delta\delta\delta}$ to zero, indicating that the zig-zag data did not constrain these terms.

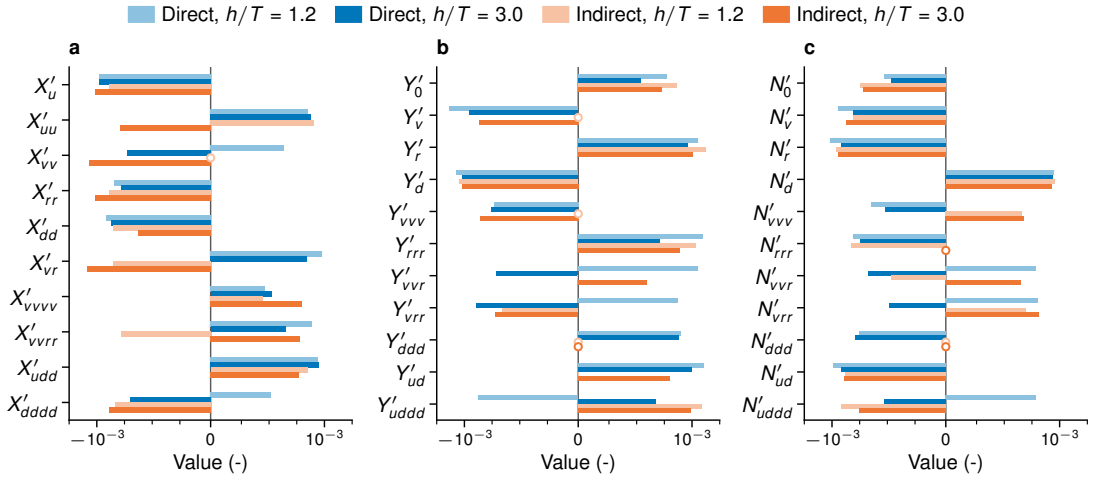


Fig. 3: Comparison of the hydrodynamic coefficients of the surge X' (a), sway Y' (b), and yaw N' (c) equations, identified by the direct and indirect method in shallow ($h/T = 1.2$) and deep water ($h/T = 3.0$).

Figure 4 compares the two identified models in the force domain by evaluating the maneuvering model of Eq. (2) along single-variable sweeps of the rudder angle (a–c) and the non-dimensional yaw rate (d–f). The panels show the resulting hydrodynamic forces at model scale, namely the surge force X Fig. 4 (a,d), the sway force Y Fig. 4 (b,e), and the yaw moment N Fig. 4 (c,f). Near the origin of both sweeps, all four models nearly coincided, confirming that both identification methods captured the linear behavior consistently at both water depths. The surge force in (a) was qualitatively consistent across all cases, with the indirect models predicting larger quantities. In (b) and (c), the higher-order terms dominated and the predictions diverged. In the rudder sweep, the agreement held up to approximately $|\delta| = 25°$, close to the largest rudder angle excited by the 35°/5° zig-zag maneuver. Beyond this angle, the direct deep water model developed in sway and yaw through its cubic rudder coefficients, while the indirect models continued to grow monotonically. In the yaw rate sweep in (d), both models reproduced the shallow water amplification, with the forces and moments at $h/T = 1.2$ exceeding those at $h/T = 3.0$ throughout. The sway force (e) showed a pronounced cubic yaw rate dependence in shallow water, on which both agreed closely, whereas in yaw (f) the direct shallow water moment reached roughly twice the indirect prediction at $|r'| = 1$. The differences between the two approaches showed that the regression was limited to the available data. For indirect system identification, no rudder angles of $|\delta| = 35°$ were available, so maneuvers beyond this range could only be extrapolated.

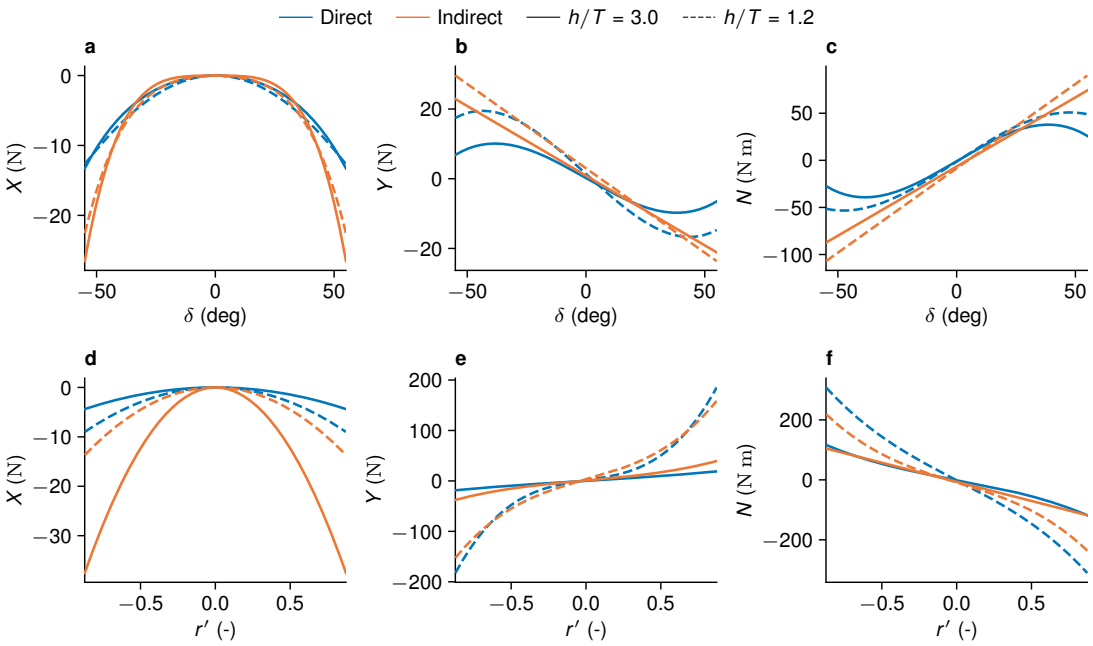


Fig. 4: Hydrodynamic forces evaluated with the identified coefficient sets along a rudder-angle sweep (a–c) and a yaw rate sweep (d–f) at the reference speed U_0, showing the surge force X, sway force Y, and yaw moment N for the direct and indirect method in shallow ($h/T = 1.2$) and deep water ($h/T = 3.0$).

Figure 5 compares the simulated rudder angle δ and heading angle ψ with the measured run in shallow water (a) and deep water (b). Both identified models were validated in the time domain against a free-running $\pm 35°/5°$ zig-zag measurement. In shallow water, both system identifications overpredicted the overshoot angles. In addition, the simulated ship response showed a growing time shift until the heading angle was reached. The overshoot angles exceeded the measurement by up to 5.04° for the direct identification and by up to 3.63° for the indirect identification. The indirect model therefore reproduced the measured overshoot angles more closely. In contrast, the direct model followed the maneuver more closely. In deep water, both system identifications showed even larger overshoot deviations of approximately 7.15° to 8.16°. Both simulations oscillated with a slightly longer period than the measurement. Consequently, both simulations accumulated a growing phase lag over successive rudder executions. The close agreement of the indirect model must, however, be interpreted with care. This model was identified from repeat runs of the same maneuver. It therefore demonstrated internal consistency rather than independent predictive capability.

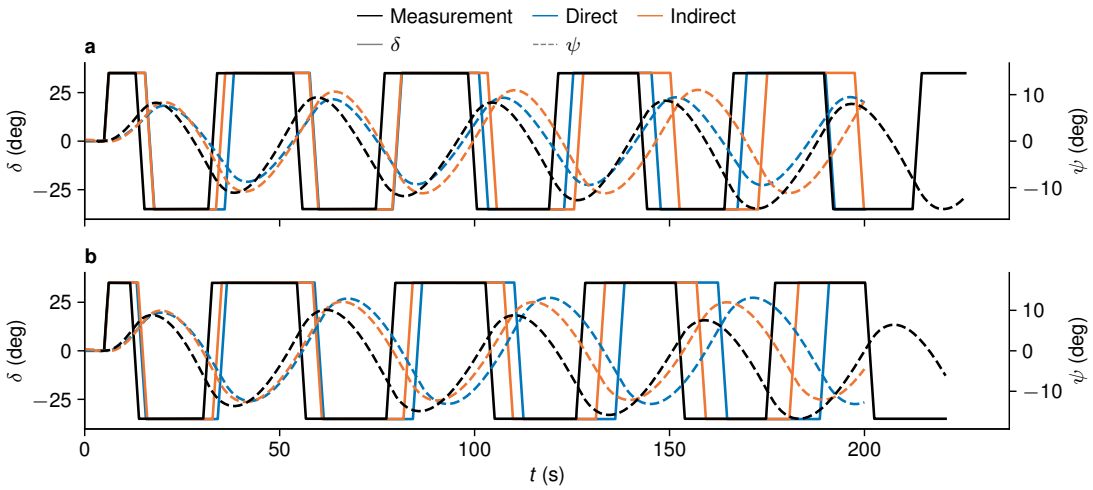


Fig. 5: Comparison of the simulated and measured $\pm 35°/5°$ zig-zag maneuver, showing the rudder angle δ and heading ψ for the direct and indirect method against a free-running measurement in shallow $h/T = 1.2$ (a) and deep water $h/T = 3.0$ (b).

4 Conclusions

This work compared the direct and indirect system identification of Abkowitz-type hydrodynamic coefficients for a typical inland waterway ship in shallow ($h/T = 1.2$) and deep water ($h/T = 3.0$), using steady captive tests and repeated 35°/5° zig-zag maneuvers, respectively. The linear derivatives were the most robustly identified: both methods agreed in sign and reproduced the expected shallow water amplification. In contrast, the higher-order coefficients scatter widely, indicating that a single maneuver type did not sufficiently excite the corresponding states to constrain them. In time-domain validation, both models reproduced measured heading overshoots in deep water. However, in shallow water, only the indirect model closely matched the measurements. Identified through repeat runs of the validation maneuver, the model demonstrated internal consistency rather than independent predictive capability. The differences between the two routes thus depended primarily on the quality and quantity of the underlying data, and future work should validate both models against independent maneuvers and perform the indirect identification with additional maneuver types.

Acknowledgements

The results presented in this paper originated from a joint research project between the *Federal Waterways Engineering and Research Institute* (BAW) and the *Autonomous and Energy-efficient Maritime Technologies* of the *Technical University of Berlin* (TUB). The work presented was funded by the *Federal Waterways Engineering and Research Institute* (BAW).

References

Abkowitz, M. A. (1964). Ship hydrodynamics - steering and manoeuvrability. *Hydro- and Aerodynamics Laboratory*, Report No. Hy-5.

Bedos, A.; Tonelli, R. (2022). An Extensive Experimental Investigation of Shallow- and Confined-Water Effects on the Manoeuvring Forces of a 110m Inland Ship. *Proceedings of the 6th International Conference on Ship Manoeuvring in Shallow and Confined Water (MASHCON)* **6**, 1–9.

Chillcce, G.; El Moctar, O. (2023). Data-driven system identification of hydrodynamic maneuvering coefficients from free-running tests. *Physics of Fluids* **35**(5), 057122. DOI: 10.1063/5.0148219.

Chillcce, G.; Zentari, L.; Van Hoydonck, W.; Bedos, A.; Ley, J.; Gornicz, T.; Yang, Y.; Oud, G.; Tenzer, M.; Rzeszutko, J.; El Moctar, O. (2025). Numerical calculation of hydrodynamic forces on inland waterway ships during circular motion in shallow and extreme shallow waters. *Ocean Engineering* **318**, 120095. DOI: 10.1016/j.oceaneng.2024.120095.

Chillcce, G. (2025). Mathematical models for ship manoeuvring under realistic environmental conditions. *Ship Technology Research* **0**(0), 1–17. DOI: 10.1080/09377255.2025.2513760.

El Moctar, O.; Lantermann, U.; Chillcce, G. (2022). An efficient and accurate approach for zero-frequency added mass for maneuvering simulations in deep and shallow water. *Applied Ocean Research* **126**, 103259. DOI: 10.1016/j.apor.2025.103259.

Mucha, P.; El Moctar, O.; Dettmann, T.; Tenzer, M. (2017). Inland waterway ship test case for resistance and propulsion prediction in shallow water. *Ship Technology Research* **64**(2), 106–113. DOI: 10.1080/09377255.2017.1349723.

Mucha, P.; Dettmann, T.; Ferrari, V.; El Moctar, O. (2019). Experimental investigation of free-running ship manoeuvers under extreme shallow water conditions. *Ocean Engineering* **83**, 155–162. DOI: 10.1016/j.apor.2018.09.008.

Rzeszutko, J.; Zentari, L.; El Moctar, O. (2025). Mathematical modeling of propulsion forces in shallow waters. *Applied Ocean Research* **154**, 104417. DOI: 10.1016/j.apor.2025.104417.

Rzeszutko, J.; Zentari, L.; Tenzer, M.; Chillcce, G.; El Moctar, O. (2025). Numerical and experimental investigation of rudder-induced hydrodynamic forces on an inland waterway ship in deep and shallow waters. *Physics of Fluids* **37**(10), 105164. DOI: 10.1063/5.0293128.

Zentari, L.; El Moctar, O.; Lassen, J.; Hallmann, R.; Schellin, T. E. (2022). Experimental and numerical investigation of shallow water effects on resistance and propulsion of coupled pusher-barge convoys. *Applied Ocean Research* **121**, 103048. DOI: 10.1016/j.apor.2022.103048.

Data Driven Identification of Ship Manoeuvring Dynamics Using SINDy Forward Greedy Selection and Sequential Backward Elimination for Model Structure Identification

Mahmoud Amer[1], **Jens Neugebauer**[1], **Frédéric Kracht**[2]

1 University of Duisburg-Essen, Duisburg, Germany

2 Development Centre for Ship Technology and Transport Systems (DST), Duisburg, Germany

Corresponding author: mahmoud.amer@uni-due.de

Introduction

A manoeuvring model must capture the ship's response to rudder and propeller commands without becoming unnecessarily complex. We compared forward greedy selection and sequential backward elimination within the Sparse Identification of Nonlinear Dynamics (SINDy) framework, using ridge regression to estimate the coefficients of each trial model. The selected surge, sway and yaw acceleration models contained 18, 16 and 13 active terms, with validation R^2 values of 0.9016, 0.9465 and 0.9646, respectively. Separate simulations reproduced the main features of the measured manoeuvres, although some positional drift remained in some turning cases.

SINDy expresses nonlinear dynamics as a sparse combination of candidate functions [1]. The formulation can also include control inputs [2], allowing rudder angle and propeller rate to enter the equations alongside the ship states. We applied this approach to the Ernst Kramer manoeuvre dataset and examined how the selected terms relate to the four-quadrant Reference model [3].

Ship manoeuvring identification has been approached through both prescribed physical models and methods that discover the equations from data. The modular MMG method provides an established physical framework [4]. Chillcce and el Moctar [5] estimated the coefficients of an Abkowitz-type force model from free-running tests, with constraints based on physical properties. Hasan [6] used the WyNDA observer framework to identify model structures and parameters, while Ma et al. [7] combined forward-greedy SINDy and ridge regression with LSTM residual correction. Here, we focus on how the direction of the structure search affects model accuracy and complexity, and how the resulting acceleration fits relate to integrated manoeuvring behaviour.

Data and Methods

Dataset and Candidate Functions

The dataset consists of turning-circle and zigzag trials in the horizontal plane. We describe the motion using body-fixed surge velocity u, sway velocity v and yaw rate r, with rudder angle δ and propeller rate n as inputs. Each acceleration was fitted separately to its sensor-derived target. For target q, the regression is written as

$$y_q = {\theta_q}^T \xi_q + \varepsilon_q, \quad q \in \{u, v, r\} \quad (1)$$

In this expression, y_q is the acceleration target, θ_q is the vector of candidate functions, ξ_q contains their coefficients and ε_q is the residual. The libraries include state polynomials, signed damping functions, state–control interactions and current-dependent terms. They also contain functions restricted to one rudder direction and terms drawn from the four-quadrant model. Propeller lags and moving averages were available for surge and sway. The surge, sway and yaw libraries contained 128 candidate functions. After preprocessing and alignment of the history-dependent features, yaw, surge and sway each had 827,189 training samples and 248,232 validation samples. These are samples from time series, so they should not be interpreted as independent manoeuvres.

Preprocessing and Regression

We used a fixed split between training and validation data. Median filtering was applied to both the training regressors and the training acceleration targets. The validation signals received no additional smoothing. Feature scales were calculated from the training data and then applied unchanged to the validation data.

Before fitting, each library column was divided by its root-mean-square value in the training data. Denoting this scale by s_j gives $\tilde{\Theta}_j = \Theta_j / s_j$ and $\beta_j = s_j \xi_j$, where β_j is the coefficient of the scaled feature. The coefficient in the original units is therefore $\xi_j = \beta_j / s_j$. Scaling limits the influence of differences in feature magnitude on the regularization penalty. For a selected set of terms S, the coefficients were estimated by ridge regression [8]:

$$\hat{\beta}_S = \arg\min_{\beta} \{\|y_{tr} - \tilde{\Theta}_{tr,S}\beta\|_2^2 + \alpha\|\beta\|_2^2\} \quad (2)$$

The coefficients were refitted and the ridge parameter retuned whenever the selected terms changed. Ridge regularization reduces the sensitivity of coefficient estimates to correlated regressors [8]. Sparsity was introduced by adding or removing terms from the library.

Model Selection and Evaluation

Forward selection began with an empty model and added one best performance term at a time. Backward elimination began with the full library and removed one worst performance term at a time. The coefficients were refitted for each trial change before the next step was accepted. The backward search therefore passed through large models before reaching the range allowed for final selection. We limited the final models to at most 18 active terms; models with fewer terms remained eligible.

Balancing fit against model size is also central to SINDy model selection using information criteria [10]. In this study, we used an empirical score that combines normalized validation root-mean-square error with a fixed penalty for each active term:

$$J = \frac{RMSE_{val}}{\sigma_{val}} + 0.002\,k \quad (3)$$

Here, σ_{val} is the standard deviation of the validation target, and k counts coefficients whose scaled magnitude exceeds the activity threshold. Prediction accuracy was evaluated on the same validation samples using

$$R^2 = 1 - \frac{SSE}{SST}, \quad RMSE = \sqrt{\frac{SSE}{N}} \quad (4)$$

SSE denotes the sum of squared prediction errors, SST the sum of squared deviations from the validation mean, and N the number of validation samples. When σ_{val} is calculated with the population definition, normalized RMSE equals the square root of $1 - R^2$. An additional term is therefore favoured only when its reduction in normalized error compensates for the increase in the complexity penalty.

All metrics reported here refer to the fixed validation set used during model selection. Because this set guided both term selection and hyperparameter tuning, the scores describe selection performance. We compared the two search directions using the same feature configuration within each target. The reported models came from the accepted search paths; individual subsets evaluated in diagnostic trials are separate from those paths. The search is greedy and does not establish a global optimum over all possible subsets.

Results

Acceleration Models

Table 1 summarizes the matched forward and backward runs. The three selected models, shown in bold, contain 47 active coefficients in total. Within each target, both searches used the same candidate library and history settings.

Table 1 Validation of acceleration metrics for matched search directions

Target	Search	K	R^2	RMSE	J
Surge	**Forward**	**18**	**0.9016**	**1.3866×10^{-3}**	**0.3496**
Surge	Backward	18	0.8966	1.4216×10^{-3}	0.3575
Sway	Forward	12	0.9406	2.0296×10^{-3}	0.2677
Sway	**Backward**	**16**	**0.9465**	**1.9258×10^{-3}**	**0.2632**
Yaw	Forward	11	0.9640	5.9028×10^{-5}	0.2117
Yaw	**Backward**	**13**	**0.9646**	**5.8585×10^{-5}**	**0.2143**

RMSE units: m/s^2 for surge and sway; rad/s^2 for yaw.

For surge, forward selection gave a higher R^2 than backward elimination at the same 18-term limit. For sway, the backward model used four more terms, but the reduction in prediction error was large enough to improve J as well. The yaw results show a smaller trade-off. The 13-term backward model had slightly higher R^2 and lower RMSE, whereas the 11-term forward model had the lower J. Selecting the backward yaw model therefore favours the small gain in accuracy over the reduction in model size.

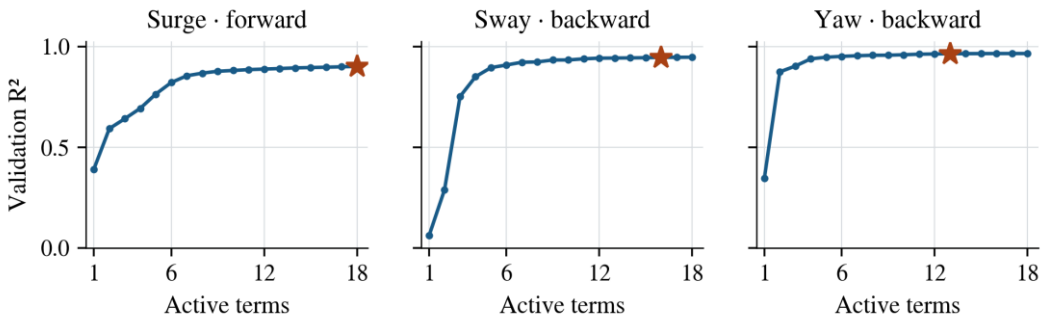


Figure 1 Validation R^2 along accepted supports with 1–18 active terms. Stars mark the retained models. Backward histories are plotted in increasing term count for comparison, although the search proceeds by deletion.

Figure 1 shows that the first few terms account for most of the improvement in R^2, with smaller gains as the models grow. Larger sway and yaw models along the accepted paths can achieve higher R^2 than the selected models, but the penalty favours a more compact representation. Correlated functions can replace one another, so changing the search direction can also change the selected terms. Both fit and model size are needed to interpret the result of the search.

The equations also differ in the input information they require. Surge includes a 10 s propeller lag and a signed damping term based on current-relative velocity. Sway includes moving-average propeller terms and interactions specific to the rudder direction. The selected yaw model uses state damping and propeller–rudder interactions without lag terms. Implementing functions with input history requires stored past values and consistent initialization, an additional cost that the number of active terms alone does not describe.

Manoeuvre Simulations

We also examined simulation examples for zigzag and turning circles runs, comparing GPS measurements with a SINDy-based simulator and the Reference model [3]. Figure 2 presents one zigzag run and the more demanding 45° starboard turn. At each time, the position error is the two-dimensional distance between the simulated position and the GPS measurement.

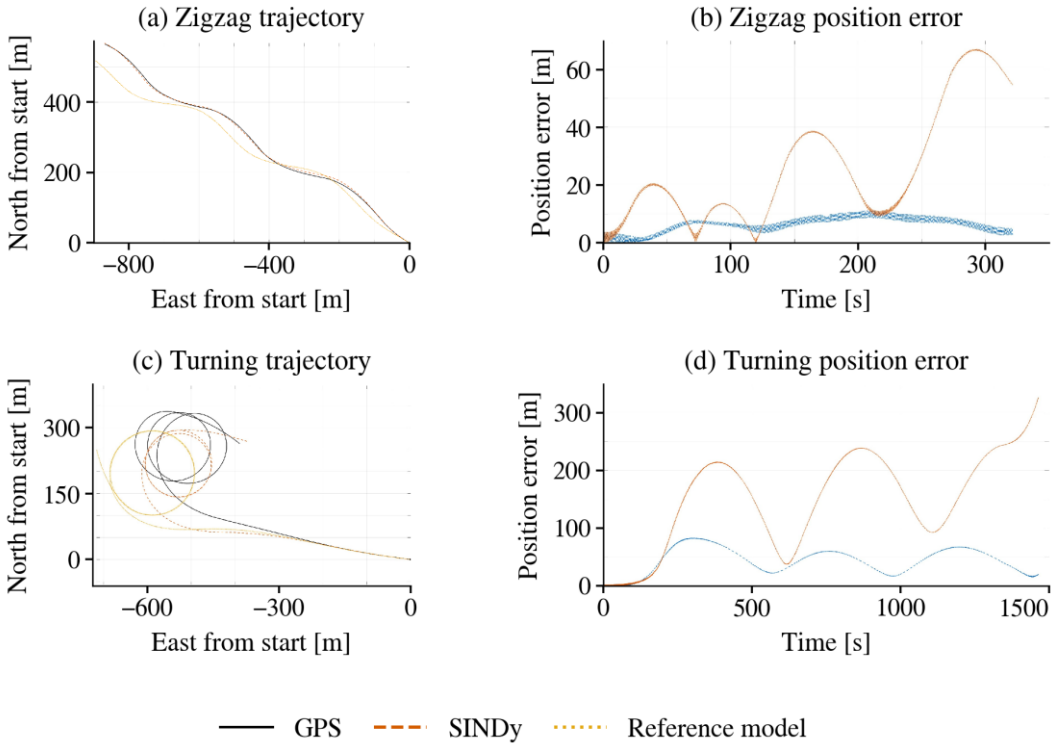


Figure 2 Representative simulator comparisons. Upper row: zigzag run ZZ_35_10. Lower row: turning run TCM_45SB. In the error panels, blue denotes SINDy and orange the Reference model. Both position errors are relative to GPS.

Zigzag tests reveal the response to steering reversals, while turning tests show the effects of sustained sway–yaw coupling on the ship's path. Assessing the integrated motion is also part of the validation of identified force models in [5]. This assessment matters because without MPC, small acceleration errors can accumulate rapidly during a manoeuvre in both velocity and trajectory.

In the zigzag run shown in Figure 2, the SINDy simulation follows the measured path closely and the position error remains relatively small. The second zigzag run reproduces the alternating response but develops a growing positional offset. During the 35° starboard turn, the SINDy loop is closer to the measured trajectory than the Reference model loop, although drift is still visible. In the 45° turn, the simulated loop is too small and the position error oscillates over successive turns. The comparison therefore shows appreciable differences in accuracy between maneuvers.

These examples provide a qualitative view of the simulator's behaviour and do not constitute an independent numerical test of the acceleration models in Table 1. Velocity, heading and position need to be examined together, since a persistent yaw or sway error can produce a substantial displacement. During repeated turns, the relative phase of the trajectories can also affect the position error, making the full time history more informative than the final error alone.

Discussion

The surge equation, for example, contains v^2, r^2 and $(v^2r^2/U^2)\mathrm{sgn}(u)$, which have counterparts in the Reference model under forward-motion conditions [3]. The term $U^2\delta^2$ restricted to one rudder direction has the same speed and angle dependence only while that restriction is active. A raw δ^2 term omits the speed factor. The equations also contain propeller lag, current-dependent terms and state–control products, giving it additional empirical flexibility beyond the reference basis.

The sway equation includes v^3, vr^2, v^2r, uv, $u^2\delta$ and $n\delta^3$, together with functions for rudder direction and propeller history. Some resemble terms in the Reference model after appropriate speed scaling or the small-sway approximation $U \approx u$. The raw cubic state terms, however, do not contain the inverse-speed factors in the reference expressions [3]. The yaw equation includes r, $r|r|$, uv, ur, $v|r|$, $u^2\delta$ terms for each rudder direction and propeller–rudder interactions. Terms such as $r|r|$ and $\delta|\delta|$ provide further empirical flexibility. Similarity of these functions alone does not show that the original hydrodynamic coefficients have been recovered [3].

Chillcce and el Moctar [5] estimated coefficients within prescribed force equations and imposed physical constraints. In our approach, term selection acts on explicit acceleration equations. Converting force and moment balances into this form mixes contributions through the inertia and added-mass matrix [3,5]. Correlated features and ridge regularization can also redistribute the fitted coefficient magnitudes [8]. A direct comparison of coefficients is therefore meaningful only after matching the normalization, coordinate convention, operating quadrant and equation transformation.

Conclusions

Both searches produced compact models with high validation R^2, but the preferred direction depended on the motion component and the selection criterion. Forward selection performed better for surge, backward elimination for sway, and the yaw comparison involved a small gain in accuracy at the cost of two additional terms. The simulation examples show why this comparison must extend beyond acceleration fit. Independent manoeuvre tests are needed to establish how well the selected equations predict integrated motion and where the remaining trajectory drift can be reduced.

References

[1] Brunton, S. L., Proctor, J. L. and Kutz, J. N. (2016). Discovering governing equations from data by sparse identification of nonlinear dynamical systems. Proceedings of the National Academy of Sciences, 113(15), 3932–3937. doi:10.1073/pnas.1517384113.

[2] Brunton, S. L., Proctor, J. L. and Kutz, J. N. (2016). Sparse Identification of Nonlinear Dynamics with Control (SINDYc). arXiv:1605.06682. doi:10.48550/arXiv.1605.06682.

[3] Yang, Y. and el Moctar, O. (2025). A four-quadrant model for ship maneuvering in forward and backward motions. Applied Ocean Research, 164, 104779. doi:10.1016/j.apor.2025.104779.

[4] Yasukawa, H. and Yoshimura, Y. (2015). Introduction of MMG standard method for ship maneuvering predictions. Journal of Marine Science and Technology, 20, 37–52. doi:10.1007/s00773-014-0293-y.

[5] Chillcce, G. and el Moctar, O. (2023). Data-driven system identification of hydrodynamic maneuvering coefficients from free-running tests. Physics of Fluids, 35, 057122. doi:10.1063/5.0148219.

[6] Hasan, A. (2025). Discovering ship maneuvering models from data. Journal of Marine Science and Technology, 30, 255–267. doi:10.1007/s00773-024-01045-9.

[7] Ma, D., Ji, C. and Li, S. (2026). Hybrid modeling of ship maneuvering motion via physics-based parameter identification and data-driven residual correction. Ocean Engineering, 363, 126546. doi:10.1016/j.oceaneng.2026.126546.

[8] Hoerl, A. E. and Kennard, R. W. (1970). Ridge regression: Biased estimation for nonorthogonal problems. Technometrics, 12(1), 55–67. doi:10.1080/00401706.1970.10488634.

[9] Guyon, I. and Elisseeff, A. (2003). An introduction to variable and feature selection. Journal of Machine Learning Research, 3, 1157–1182. https://www.jmlr.org/papers/v3/guyon03a.html

[10] Mangan, N. M., Kutz, J. N., Brunton, S. L. and Proctor, J. L. (2017). Model selection for dynamical systems via sparse regression and information criteria. Proceedings of the Royal Society A, 473, 20170009. doi:10.1098/rspa.2017.0009.

[11] Cawley, G. C. and Talbot, N. L. C. (2010). On over-fitting in model selection and subsequent selection bias in performance evaluation. Journal of Machine Learning Research, 11, 2079–2107. https://www.jmlr.org/papers/v11/cawley10a.html

Actuator Line Method for Wind-Assisted Ship Modelling

Thibault Maubert[1,2] and Adam Persson, adam.persson@ri.se[2]

[1]ISAE Supaero, Toulouse University, France
[2]RISE Research Institutes of Sweden, Maritime Department, Sweden

Introduction

Economic and environmental imperatives drive the need to reduce fuel consumption in commercial shipping, increasing the use of wind propulsion systems. An important challenge is the prediction of aerodynamic interaction between wind propulsion units, and with the vessel's superstructure/hull. Lacking accurate and low-cost alternative methods, current evaluations often rely on costly Computational Fluid Dynamics (CFD).

Adapting wind energy methods [1], such as the Actuator Line Method (ALM), could help overcome this challenge. Similar to Kramer [2], the present approach uses CFD for the viscous flow around the ship while the wind propulsion system (WPS) is represented by a reduced-order model, coupled through body-force terms. Resolving the WPS boundary layer is thereby avoided, while the influence of the WPS on the bulk flow is retained, permitting analysis of interaction.

This study evaluates how details of the ALM implementation affect the prediction, identifying strengths and limitations. Specifically, the velocity sampling strategy, the body-force injection technique and the mesh refinement around the wings are investigated, and the method is complemented with a correction for three-dimensional effects. The predictions are compared to fully resolved RANS CFD simulations.

Actuator Line Method and equations

The method operates in three main steps: extracting the fluid velocity at the theoretical location of the object, calculating the resulting aerodynamic forces from 2D polars, and injecting these forces back into the fluid domain as body forces. This sequence is updated at every time-step of the STAR-CCM+ simulation.

Wing discretisation

The present study concerns multiple wings and their aerodynamic interactions. Because the incoming airflow can vary significantly from the bottom to the top of a wing, the model must capture these vertical flow gradients. To this end, each wing is discretised into multiple horizontal strips along its span, with the possibility of assigning a distinct aerodynamic profile to each strip (Fig.1). Rather than treating the wing as a single entity, the ALM procedure is applied locally: the solver evaluates the velocity vector (magnitude and direction) around the quarter-chord line of each strip, deduces the local forces from the assigned polar, and injects the corresponding body forces around the same line. The flow distribution over the wing is thereby represented.

Velocity sampling

The first step is the determination of the local velocity magnitude and direction. For this purpose, a sampling line (sensor ring, SR, shown in red in Fig. 2) is defined within STAR-CCM+ for each strip, following the LineAverage technique of [3]. This line is centred on the quarter-chord point and lies in the 2D plane of the strip's profile. By default, its radius r_{SR} is set equal to the local chord length c. The reference velocity magnitude and direction used for the subsequent calculations are obtained by averaging the flow field along this line.

The primary objective is to estimate the undisturbed (free-stream) wind angle. Because the flow is strongly distorted in the immediate vicinity of the wing, this theoretical undisturbed velocity

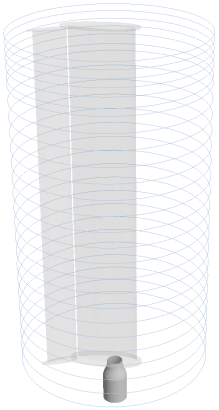


Figure 1: Wing discretisation

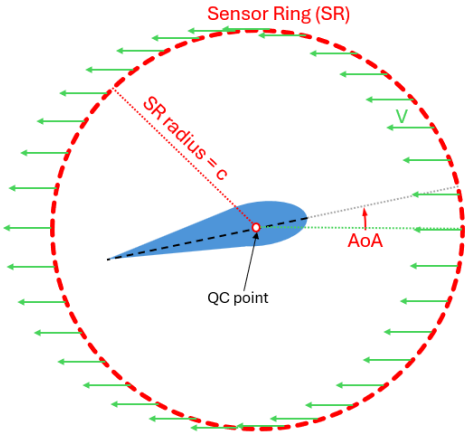


Figure 2: Sensor ring and sampled quantities

cannot be sampled directly. Instead, by averaging the flow around the strip, the method aims to cancel the leading-edge upwash against the trailing-edge downwash. The radius of the sampling line is therefore a crucial parameter: it must be selected such that these two phenomena balance, yielding the correct theoretical angle of attack (AoA). The geometric AoA α_{geo} is the angle between the chord of the strip and the sampled wind direction.

Correction/modelling of 3D finite span effects

Since the strips are evaluated with two-dimensional polars $C_l(\alpha)$ and $C_d(\alpha)$, the finite span of the wing is not accounted for. An empirical tip-loss factor is employed to provide a smooth initial condition for a subsequent lifting-line correction.

Empirical tip-loss factor. The lift of strip i at height z_i is scaled by

$$F_i = 1 - f\,(1 - F_i^{\text{3D}}), \qquad F_i^{\text{3D}} = \frac{2}{\pi}\arccos\Big[\exp(-\beta\, s_i)\Big], \qquad s_i = \tfrac{1}{2} - \Big|\tfrac{z_i}{b} - \tfrac{1}{2}\Big|, \tag{1}$$

where b denotes the span, s_i the normalised distance to the nearest tip, β a shape parameter and $f \in [0,1]$ a blending factor, $f = 1$ corresponding to the full correction and $f = 0$ to the two-dimensional lift. Equation (1) is of the form of the Prandtl tip-loss function of blade-element momentum theory; it enforces a vanishing circulation at a free tip but does not contain information on the actual load distribution.

Lifting-line correction. According to Helmholtz' theorems, a spanwise variation of the bound circulation $\Gamma(z)$ is shed as a vortex sheet of strength $-\mathrm{d}\Gamma/\mathrm{d}z$. For a straight lifting line and a planar wake, the velocity induced by this sheet on the line is obtained from the Biot–Savart law as the Cauchy principal value

$$w(z) = \frac{1}{4\pi}\,\mathrm{PV}\!\int_0^b \frac{\mathrm{d}\Gamma/\mathrm{d}z'}{z - z'}\,\mathrm{d}z', \qquad \alpha_{\text{ind}}(z) = \arctan\frac{w(z)}{U(z)}, \qquad \alpha_{\text{eff}} = \alpha_{\text{geo}} - \alpha_{\text{ind}}, \tag{2}$$

which constitutes Prandtl's lifting-line equation. With the circulation given by the Kutta–Joukowski theorem, $\Gamma = L'/(\rho U)$, and $L' = \frac{1}{2}\rho U^2 c\, C_l(\alpha_{\text{eff}})$, Eq. (2) represents a non-linear integro-differential equation for $\Gamma(z)$. The induced angle reduces the effective incidence and rotates the sectional force by α_{ind}, whereby part of the lift is converted into induced drag.

Discrete implementation. The circulation $\Gamma_i = L'_i/(\rho U_i)$ is provided by the strips at the stations z_i, with U_i being sampled on the sensor ring. The derivative $\mathrm{d}\Gamma/\mathrm{d}z$ is approximated by central differences (one-sided at the end stations) and the integral by the trapezoidal rule. The singular self-term is replaced by the mean of the two neighbouring values (a linear extrapolation

at the end stations), which is a first-order approximation of the principal value, exact for a linear integrand and consistent with the quadrature. The coupling with the polars is resolved by a fixed-point iteration synchronised with the flow solver, the induced angle being relaxed at each update according to

$$\alpha_{\mathrm{ind},i}^{n+1} = \alpha_{\mathrm{ind},i}^{n} + r_\ell(\tilde{\alpha}_{\mathrm{ind},i}^{n+1} - \alpha_{\mathrm{ind},i}^{n}), \qquad 0 \le r_\ell \le 1, \tag{3}$$

where $\tilde{\alpha}_{\mathrm{ind},i}$ denotes the unrelaxed evaluation of Eq. (2). The relaxation is required to damp the feedback between the non-linear polars and U_i, which already contains the induction resolved by the RANS solution. Two aspects distinguish the implementation from the continuous theory. First, the velocity entering Eq. (2) is the sampled U_i rather than a uniform free stream; since U_i already contains part of the trailing-vortex induction resolved by the flow solver, the separation between resolved and modelled induction is not made explicit in the present implementation. Second, Eqs. (1) and (2) describe the same mechanism and are therefore not applied simultaneously: the computation is initialised with $f = 1$, which provides the initial condition referred to above. To ensure that the solution is governed by the lifting line, f is gradually reduced to zero.

Force calculation

Once $\alpha_{\mathrm{eff},i}$ and U_i have been determined, the sectional coefficients C_l and C_d are obtained from the polar of the profile assigned to the strip, which is derived from two-dimensional CFD. The sectional forces per unit span are given by

$$L_i' = \tfrac{1}{2}\,\rho\,U_i^2\,c_i\,F_i\,C_l(\alpha_{\mathrm{eff},i})\,, \qquad D_i' = \tfrac{1}{2}\,\rho\,U_i^2\,c_i\,C_d(\alpha_{\mathrm{eff},i})\,, \tag{4}$$

where ρ is the air density, c_i the local chord and F_i the tip-loss factor of Eq. (1); the forces on a strip of height h_i follow as $L_i = L_i' h_i$ and $D_i = D_i' h_i$. The drag is aligned with the local effective wind direction, i.e. the sampled direction rotated by $\alpha_{\mathrm{ind},i}$, and the lift is normal to it. The momentum source is the reaction $-(L_i', D_i')$, distributed over the strip volume by the Gaussian kernel described below. For comparison with the fully resolved simulations, the reported forces are projected onto the far-field apparent-wind axes.

Injection

The forces are introduced into the simulation as body forces, which must be smeared over a volume for numerical stability. Of the smearing strategies discussed in [4], isotropic and anisotropic Gaussian kernels were evaluated. In both cases the force per unit span of a strip is distributed in the plane of the strip by a normalised Gaussian centred on the quarter-chord point and applied uniformly over the strip height; the anisotropic kernel has widths β_c along and β_t normal to the chord. For the isotropic kernel, $\beta_c = \beta_t$.

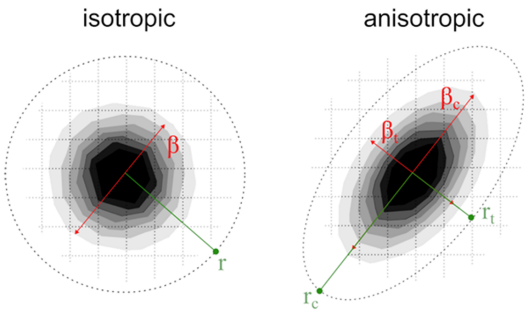


Figure 3: Smearing kernels, from [4]

The isotropic kernel does not require alignment with the sheeting angle of the wing but, for a given projection area, distributes the force over a wider lateral region than is observed for a real profile, whose loads are concentrated near the leading edge. Following initial tests, anisotropic smearing with $\beta_t = 0.1\,c$ and $\beta_c = 0.2\,c$ was adopted for the results presented below.

Test case

In order to evaluate how the method can be applied in practice, an industrially relevant but open test case was selected, the SWOPPII vessel. This is a coneptual 88.3 m general cargo vessel design, adapted for wind propulsion [5]. In the SWOPPII configuration, it is equipped with four 182 m^2 two-element wings, as shown in Fig. 4. The wings consist of a main element and a flap, both with symmetric NACA 4-series sections and a chord length and thickness-to-chord ratio of 4 m and 22 % for the main element and 2 m and 15 % for the flap. For the aerodynamic simulations a twisted, atmospheric boundary layer wind profile is used, with reference wind conditions at 10 m height equal to $\beta_{AW,10} = 70°$ and $V_{AW,10} = 8.5$ m/s.

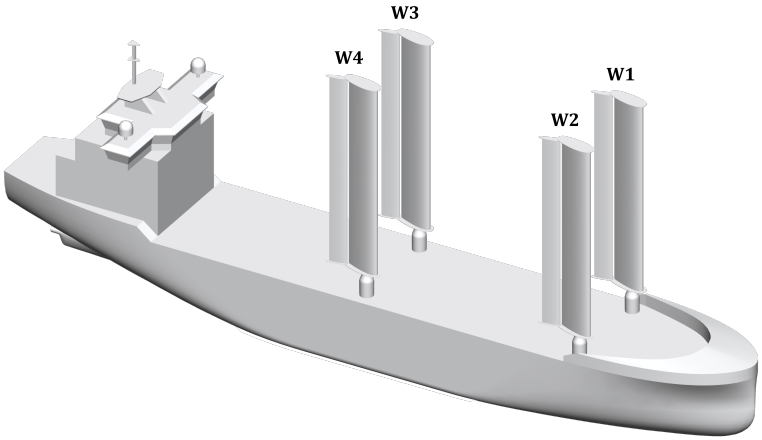


Figure 4: Isometric view of the SWOPPII test case

Verification study

To assess the influence of the principal method parameters on the fidelity of the ALM simulation, a fully resolved CFD simulation was established as reference. This set-up was designed such that the aerodynamic forces acting on a single 2-metre section at mid-span, where the flow is predominantly two-dimensional, could be isolated and extracted. The fully resolved reference comprises 25.6 million cells and the ALM mesh 13.2 million cells. Following [4], the ALM results are compared with this reference in terms of the AoA and local speed sampled at the mid-span section and in terms of the global forces.

In a first step, the AoA and wind velocity sampled at the mid-span section were compared with the reference for several sensor-ring radii, whereby a suitable radius was identified; the aerodynamic forces computed from the 2D polar at the sampled conditions were verified against the section forces of the reference.

In a second step, the smearing widths β_c and β_t were examined. A more concentrated force distribution approaches the physical situation, which is characterised by rapidly dissipating local accelerations; excessive concentration, however, increases the numerical instability until the solver diverges under the resulting gradients. The values adopted here represent a compromise.

In a third step, the mesh refinement around the wings was examined. Besides the standard cylindrical region around each wing, a D-shaped region aligned with the far-field apparent wind, consisting of the cylinder and a rectangular extension along the wake, was tested. Since it resolves the wake of each wing up to its neighbours, it was found to improve the prediction of the interaction effects and was adopted for the results below.

Following these checks, the force predictions of the ALM were compared with those of the fully resolved RANS simulations. In addition, the distribution of the forces between the wings and their relative ranking were assessed.

Results

The analysis of the impact of the SR radius on the AoA and local speed supports the standard ratio $r_{SR}/c = 1$ of the line-averaging technique [3], which is also used as reference setting in [4]. As shown in Fig. 6, the local speed is insensitive to the radius above $r_{SR}/c \approx 1$. The selection therefore rests on the AoA (Fig. 5): for smaller rings the sampled AoA falls below the reference value, whereas for larger rings it extends into the wake of the neighbouring wings. The closest agreement is obtained for r_{SR}/c between 1 and 1.2, and the standard value 1 was retained.

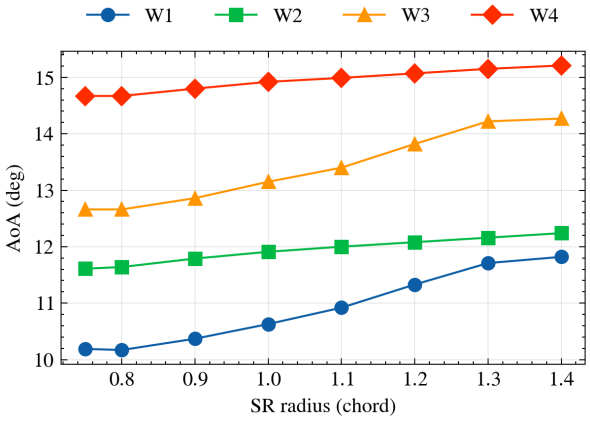


Figure 5: Dependence of the AoA on the SR radius

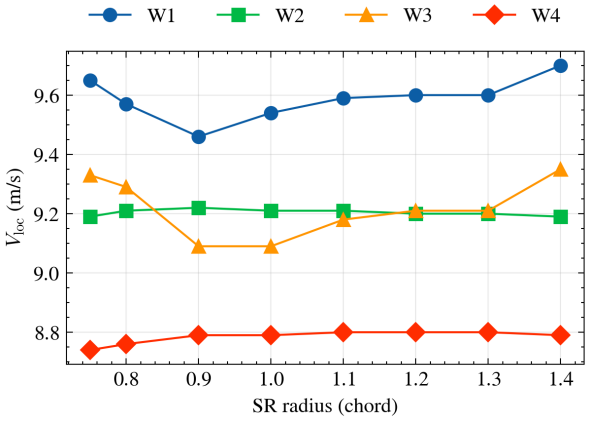


Figure 6: Dependence of the local speed on the SR radius

With $r_{SR}/c = 1$, the lifting-line correction with $f \to 0$, and force smearing widths of $\beta_c = 0.2\,c$ and $\beta_t = 0.1\,c$, the ALM yields the results of Table 1. The lift is predicted within -2.8 to $+7.1\,\%$ per wing and within $1\,\%$ in total, whereas the drag is over-predicted on every wing, by $+28$ to $+88\,\%$ ($+43\,\%$ in total). The drag deviation is largest on W2 and W4, the upstream wings, which benefit from the upwash induced by the downstream wings W1 and W3 and therefore have the lowest drag in the reference simulation; the drag distribution between the wings is thereby flattened, indicating that this beneficial interaction is only partly captured. The relative ordering of lift, drag and lift-to-drag ratio is nevertheless reproduced ($\tau = 1$). Table 2 gives the projection onto the ship axes at $\beta_{AW,10} = 70°$. The total thrust agrees to $-0.6\,\%$, since the drag error enters the thrust with the factor $\cos\beta_{AW,10}$, whereas the side force is over-predicted by $+10.9\,\%$. The thrust ordering of the closely loaded wings W1 and W3 is reversed by the ALM ($\tau = 0.67$); the ordering of side force and thrust-to-side-force ratio are preserved.

Table 1: Lift and drag, RANS versus ALM. Δ = (ALM − RANS)/RANS. Kendall's rank correlation τ compares how the ordering is predicted by the two methods ($\tau = 1$: identical order).

	Lift L [N]			Drag D [N]			L/D [–]	
Wing	RANS	ALM	Δ [%]	RANS	ALM	Δ [%]	RANS	ALM
W1	6183	6621	+7.1	992	1295	+30.5	6.2	5.1
W2	7444	7607	+2.2	355	612	+72.4	21.0	12.4
W3	6749	6694	−0.8	1301	1663	+27.8	5.2	4.0
W4	8127	7901	−2.8	502	943	+87.8	16.2	8.4
Total	28503	28823	+1.1	3150	4513	+43.3	9.0	6.4
Kendall τ		1.00			1.00			1.00

Table 2: Thrust and side force per wing at an apparent wind angle $\beta_{AW,10} = 70°$, $T = L\sin\beta_{AW,10} - D\cos\beta_{AW,10}$ (positive forward) and $S = L\cos\beta_{AW,10} + D\sin\beta_{AW,10}$ (positive to leeward). Share denotes each wing's fraction of the total thrust. Kendall's τ as in Table 1.

	Thrust T [N]			Share [%]		Side force S [N]			T/S [–]	
Wing	RANS	ALM	Δ [%]	RANS	ALM	RANS	ALM	Δ [%]	RANS	ALM
W1	5471	5779	+5.6	21.3	22.6	3047	3481	+14.3	1.80	1.66
W2	6874	6939	+0.9	26.7	27.2	2880	3177	+10.3	2.39	2.18
W3	5897	5722	−3.0	22.9	22.4	3531	3852	+9.1	1.67	1.49
W4	7465	7102	−4.9	29.0	27.8	3251	3588	+10.4	2.30	1.98
Total	25707	25541	−0.6	100	100	12709	14099	+10.9	2.02	1.81
Kendall τ		0.67		0.67			1.00		1.00	

Conclusion

In the present study, the ALM was combined with a lifting-line correction that estimates the induced angle section by section. The total lift and thrust of the four-wing configuration are predicted within 1 % of the fully resolved simulation, and the ordering of the wings by lift, drag, lift-to-drag ratio and side force is reproduced. The drag, however, is over-predicted on every wing, most strongly on the upstream wings that operate in the upwash of their neighbours, which is consistent with an under-prediction of the beneficial interaction effects. Since the drag deviation varies by a factor of three between the wings, it cannot be removed by a constant correction; at the apparent wind angle considered it affects the side force (+11 %) far more than the thrust, and it reverses the thrust ordering of two closely loaded wings. The consistency of the lifting-line coupling with the sampled velocity, in particular the treatment of the induction already resolved by the flow solver and the choice of the collocation point, is therefore identified as the principal subject of further development. However, the relatively good agreement obtained for lift and thrust supports the suitability of the method for interaction studies of wind-assisted ships, particularly in a concept design phase. The simulation time is approximately reduced by a factor of about two using the Actuator Line Method. Moreover, the wings are not meshed, so that a change of sheeting angle or wing position requires no remeshing, which is a key advantage for wing trim optimisation and interaction studies.

Acknowledgements

This project was funded by Dr. Hugo Hammars Fond för Sjöfartsteknisk Forskning and Dr. Hugo Hammars Fond för Internationell Forskning inom Sjöfarten.

References

[1] Jens Nørkær Sørensen and Wen Zhong Shen. "Numerical Modeling of Wind Turbine Wakes". In: *Journal of Fluids Engineering* 124 (June 2002), pp. 393–399.

[2] Jarle Vinje Kramer and Sverre Steen. "Actuator Line for Wind Propulsion Modelling". In: *Proceedings of the 25th Numerical Towing Tank Symposium (NuTTS)*. Ericeira, Portugal, Oct. 2023.

[3] Eva Jost et al. "Extracting the angle of attack on rotor blades from CFD simulations". In: *Wind Energy* 21.10 (2018), pp. 807–822. DOI: 10.1002/we.2196.

[4] Pier Francesco Melani et al. "An insight into the capability of the actuator line method to resolve tip vortices". In: *Wind Energy Science* 9 (Mar. 2024).

[5] S. Kontos et al. "Seakeeping and manoeuvring simulations for wind-powered vessels at the design stage". In: *Proceedings of the RINA International Conference Wind Propulsion 2024*. 22–23 October 2024. London, UK: The Royal Institution of Naval Architects, Oct. 2024.

Hydrodynamic Analysis of a Wind-Assisted Ship's Rudder

Abdoul-Malik Bakari[1*], Rui Lopes[3], Alex Shiri[2] and Arash Eslamdoost[1]

[1]Chalmers University of Technology, Sweden. [2]RISE SSPA Maritime Center, Sweden. [3]Kongsberg Maritime Sweden AB, Sweden.

bakari@chalmers.se

1 Introduction

The maritime industry has proposed a range of solutions to mitigate its contribution to global warming, and Wind-Assisted Ship Propulsion (WASP) has emerged as a particularly promising approach (Chou et al., 2021). Depending on the sail configuration and operating conditions, wind propulsion systems can reduce a vessel's fuel consumption by approximately 10% to 30% by providing supplementary propulsive power (Ammar and Seddiek, 2022; Ouchi et al., 2013). Accurately predicting WASP performance is nonetheless complex, since it requires a thorough understanding of the coupled aerodynamic and hydrodynamic interactions that govern the ship's behaviour. When a WASP vessel is sailing, the lateral aerodynamic force generated by the sails must be balanced by hydrodynamic forces from the hull, propeller, and rudder. This lateral force leads to a leeway angle and the corresponding heel angle of the vessel (Kramer et al., 2022). Understanding the influence of leeway and heel angle on the hydrodynamic behaviour of the hull, propeller, and rudder is therefore essential for reliable prediction of WASP performance.

The objective of the present work is to analyse the forces acting on the rudder under different leeway angles and sail-thrust conditions, together with the resulting side forces on the ship. This analysis neglects the heel angle. The study is carried out using Computational Fluid Dynamics (CFD), and the propeller is modeled using the Blade Element Method. Two-dimensional simulations determine the lift and drag coefficients of the blade sections, while self-propulsion simulations (hull, rudder, and propeller together) use the double-body method; thus, the free surface is not considered. Numerical uncertainty is quantified through a systematic grid convergence study.

2 Computational Methods

This study is carried out on the JoRes1 tanker (JoRes Project, 2023), a single-screw vessel with an asymmetric hull. The main particulars of the hull are listed in Table 1. The numerical study consists of two parts. In the first part, two-dimensional simulations of the propeller blade sections are carried out over a range of angles of attack and Reynolds numbers using the Reynolds-Averaged Navier–Stokes (RANS) equations, in order to determine the lift and drag coefficients of each section as functions of flow speed and angle of attack. These coefficients are subsequently used to model the propeller with the Blade Element Method, an approach widely adopted for propellers and wind turbines owing to its accuracy (Branlard, 2017). The domain size and boundary conditions for each blade section follow Shang and Horrillo (2021), with a domain extent of 27 chord lengths. The Reynolds numbers investigated ranged from 50×10^3 to 600×10^3, while the angles of attack ranged from 0° to 10°. The resulting drag (C_D) and lift (C_L) coefficients are then used as input to the Blade Element Method propeller model in the self-propulsion simulations.

In the second part, a three-dimensional double-body simulation of the hull–propeller–rudder configuration is carried out using the RANS equations, for drift angles and rudder angles ranging from 0° to 9°, and for three sail-assist conditions corresponding to 0%, 30%, and 50% sail thrust. The blade element method is used to model the propeller in this part, since it has been shown to represent propeller operating conditions with reasonable accuracy in ship propulsion applications (Gaggero et al., 2017). No sail geometry was modeled directly. Instead, the sail contribution was represented indirectly by reducing the propeller thrust while maintaining a constant inflow speed. A PID controller regulates the propeller rotation rate so that the desired sail-thrust condition is reached and maintained throughout the simulation. This part of the study analyses the resulting hydrodynamic side forces on the hull–propeller–rudder system and the corresponding rudder force components.

All simulations were performed with Simcenter STAR-CCM+ (version 2024.10.1), which discretises the governing transport equations using the finite volume method. Pressure–velocity coupling was han-

dled with a segregated solver based on the SIMPLE algorithm. The two-dimensional blade-section cases were run under steady-state conditions, while the three-dimensional self-propulsion simulations were run under unsteady conditions. Both the two-dimensional blade-section computations and the self-propulsion simulations were conducted at model scale, using a geometric scale ratio of $1/26$ relative to the full-scale vessel. The propeller has a diameter of 6.5 m at full scale and has four blades.

For the two-dimensional propeller blade-section simulations, a finite volume-based solver together with the SIMPLE algorithm for coupling the segregated velocity and pressure fields was used, with the turbulence modeled by the Spalart–Allmaras (S-A) model and the Gamma transition model. The S-A model is a widely used, computationally efficient one-equation turbulence model developed specifically for aerodynamic and aerospace applications, and it was applied to each blade section across the full range of Reynolds numbers and angles of attack considered. To adequately resolve the near-wall flow and boundary layer, a wall-resolved approach was adopted, with the mesh designed to maintain $y^+ < 1$ along the blade surfaces throughout the simulations. The boundary layer thickness ranged from approximately 1.2 mm to 0.6 mm, with the number of prism layers ranging between 19 and 31.

For the self-propulsion case, the computational domain size follows the ITTC guidelines (ITTC, 2014), with the inlet placed two L_{pp} upstream of the hull and the outlet located three L_{pp} downstream of the aft perpendicular. The boundary conditions are illustrated in Figure 1: velocity-inlet conditions were prescribed at the inlet and bottom boundaries, with the top boundary treated as a symmetry plane; a pressure-outlet condition was applied at the outlet, and the hull and rudder surfaces were treated as no-slip walls. Self-propulsion was simulated at a constant Froude number of 0.165, with drift angles from 0° to 9° achieved by rotating the hull while keeping the flow direction fixed. Positive drift angles are defined by rotating the bow to port, and positive rudder angles follow the same rotational convention. All hull, propeller, and rudder surfaces were assumed hydrodynamically smooth, with no roughness applied. Since the simulations are carried out in fresh water, the density and kinematic viscosity are set to 999 kg/m^3 and 1.1882×10^{-6} m^2/s, respectively. Thus, the hull Reynolds number is $Re = 8.376 \times 10^6$.

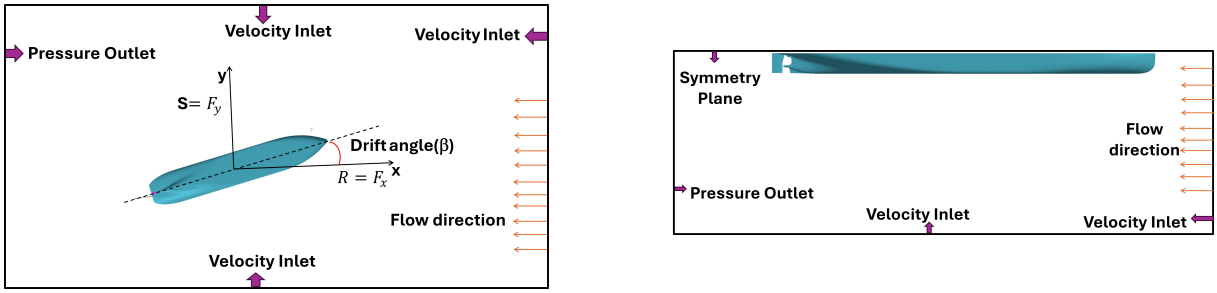


Fig. 1: Boundary conditions used for the self-propulsion simulations.

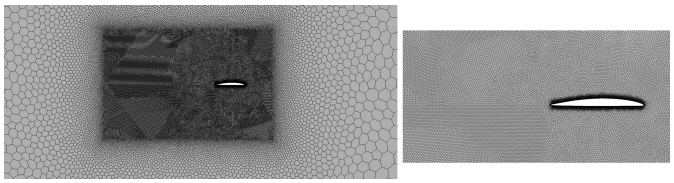
The two-dimensional blade-section simulations were meshed using the automated two-dimensional Mesh Operation in STAR-CCM+, generating a polygonal mesh for each section, as shown for one example in Figure 2a. The resulting meshes comprised, on average, approximately 30,000 cells per blade section.

Table 1: Full-scale and model-scale particulars of the JoRes1 tanker

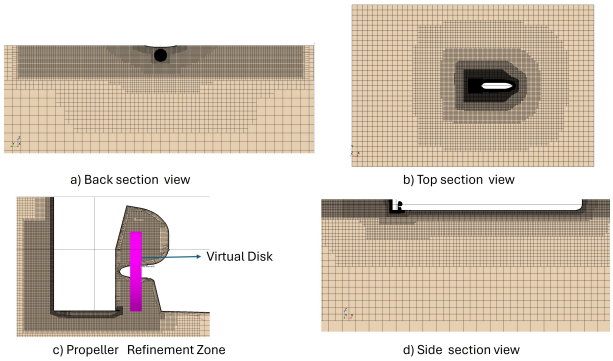
Parameter	Full scale	Model scale
Length between perpendiculars L_{pp} (m)	178.50	6.86
Breadth B (m)	32.26	1.24
Draught at fore perpendicular T_{FP} (m)	10.56	0.406
Draught at aft perpendicular T_{AP} (m)	10.38	0.399
Draught at midship T_M (m)	10.47	0.402
Wetted surface area S (m^2)	8337.10	12.68
Displaced volume ∇ (m^3)	46648	2.86

The three-dimensional computational domain was discretised using the STAR-CCM+ automated mesh generator, producing an unstructured trimmed-cell (hexahedral) mesh with local refinement around the hull and rudder, complemented by prism layers along the surfaces to resolve the boundary layer. The resulting mesh, shown in Figure 2b, comprised approximately 12 million cells at model scale. A wall-

resolved approach with $y^+ < 1$ was adopted throughout, in conjunction with the k-ω SST turbulence model. The boundary layer thickness on the hull was estimated at approximately 0.0997 m, resolved with 33 prism layers. A grid convergence study was carried out for both 2D and 3D simulations to quantify the numerical uncertainty using three additional grids.



(a) **2D mesh for the propeller cross section simulation**



(b) **3D domain mesh**

Fig. 2: Mesh configurations: (a) 2D sectional mesh and (b) 3D computational domain mesh.

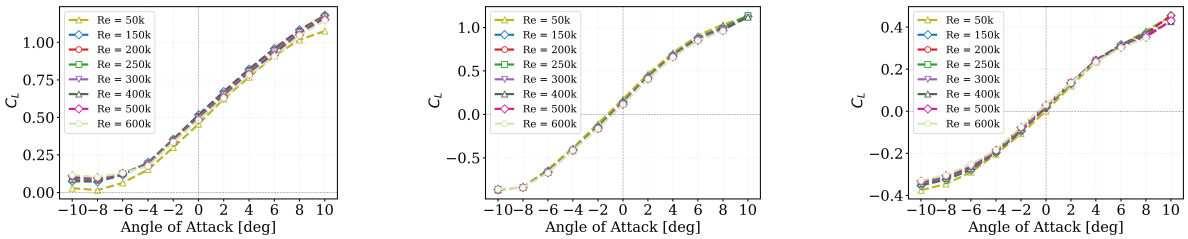
2.1 Propeller Model Construction using the Blade Element Method

The lift and drag forces acting on the propeller blade are essential for generating thrust and torque, and setting up the Blade Element Method requires detailed lift and drag coefficients at different angles of attack for each blade section. The lift and drag forces on each blade section are non-dimensionalised using the local chord length, section relative velocity, and fluid density, defined as

$$C_L = \frac{L}{\frac{1}{2}\rho V^2 c} \tag{1}$$

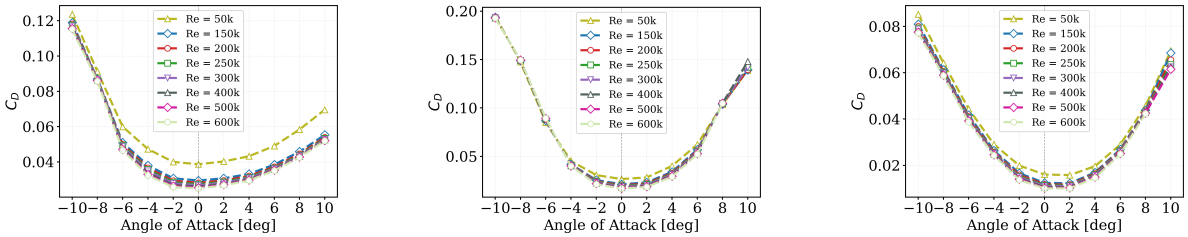
$$C_D = \frac{D}{\frac{1}{2}\rho V^2 c} \tag{2}$$

where L and D are the section lift and drag forces, ρ is the fluid density, V is the local relative inflow velocity at the blade section, and c is the local chord length of the blade section. Figures 3 and 4 show the lift coefficient and the drag coefficient against the angle of attack for three representative sections, located at $r/R = 0.40$, 0.70, and 0.90. The C_D generally decreases with increasing Reynolds number, although the magnitude of this decrease differs between sections, whereas C_L increases as the Reynolds number increases. These results are used as input to the Blade Element Method propeller model in STAR-CCM+ and are subsequently applied in the self-propulsion simulations.



(a) $r/R = 0.40$ (b) $r/R = 0.70$ (c) $r/R = 0.90$

Fig. 3: Lift coefficient at the radial blade sections $r/R = 0.40$, 0.70, and 0.90.



(a) $r/R = 0.40$ (b) $r/R = 0.70$ (c) $r/R = 0.90$

Fig. 4: Drag coefficient at the radial sections $r/R = 0.40$, 0.70, and 0.90.

3 Results and Discussion

3.1 Numerical uncertainty analysis

The grid convergence study was carried out following the procedure of Eça and Hoekstra (2014). Numerical uncertainty was estimated for representative cases from both the propeller cross-section and self-propulsion simulations. For the propeller cross-section, the uncertainty analysis was conducted for the blade section at $r/R = 0.6$ and $Re = 400{,}000$ with zero attack angle, using a grid of approximately 30,000 cells. As shown in Table 2, the resulting uncertainties in the lift and drag coefficients were 4.3% and 8.3%, respectively. For the self-propulsion simulations, Table 3 presents the uncertainty estimates for a representative case with a drift angle of 9° and a rudder angle of 9°, evaluated on the second-finest grid level, containing approximately 12 million cells. The uncertainty in the total resistance coefficient was around 7.1%, while the uncertainties in the side-force coefficient and rudder lift coefficient were 5.9% and 7.4%, respectively. These uncertainty levels are considered reasonable.

Table 2: Coefficients for Normalized radius $r/R = 0.6$ section with Re = 400k

Grid		Coefficients	
Case	Cells number	C_L	C_D
1	9248	0.4083	0.01886
2	16704	0.4044	0.01831
3	30465	0.4027	0.01822
4	118028	0.3979	0.01811
U_2 (%)		4.3	8.3

Table 3: Coefficients for different grid resolutions, Drift angle 9° and Rudder angle 9°

Grid		Coefficients $\times 10^{-3}$		
Case	Cells number	C_R	C_S	C_{LR}
1	2.37M	4.700	8.333	61.701
2	5.05M	4.690	8.336	62.085
3	11.96M	4.748	8.386	63.071
4	30.10M	4.772	8.447	63.488
U_2 (%)		7.1	5.9	7.4

3.2 Rudder and side forces

Leeway angles induced by the sails affect the hull hydrodynamics, and in particular the propeller–hull–rudder interaction; as a result, the forces acting on the rudder vary with the combination of leeway angle and sail thrust. The lift and drag forces on the rudder are non-dimensionalised using the rudder's reference area, speed, and fluid density, defined as

$$C_{LR} = \frac{F_{LR}}{\frac{1}{2}\rho V^2 S_R} \tag{3}$$

$$C_{DR} = \frac{F_{DR}}{\frac{1}{2}\rho V^2 S_R} \tag{4}$$

where F_{LR} and F_{DR} are the rudder lift and drag forces, ρ is the fluid density, V is the reference (model) speed, and S_R is the rudder's wetted reference area. The side force acting on the hull is non-dimensionalised using the hull's reference wetted area, forward speed, and fluid density, defined as

$$C_S = \frac{F_S}{\frac{1}{2}\rho V^2 S_H} \tag{5}$$

where F_S is the side force acting on the hull, and S_H is the hull's wetted reference area.

Figures 5 and 6 show the rudder lift (C_{LR}) and drag (C_{DR}) coefficients for different drift and rudder angles. Combining a drift angle with a rudder angle of opposite sign (e.g., drift 9°, rudder −9°) generates a large rudder force. Increasing sail thrust reduces the lift while increasing the drag force produced by the rudder, thereby reducing rudder efficiency. For drift 9°/rudder −9°, as sail thrust increases from 0% to 50% (i.e., the propeller unloads by 50%), the rudder lift coefficient drops from approximately 0.3 to 0.2, a reduction of roughly 30%, while the drag coefficient rises from 0.038 to 0.045, an increase of approximately 18%. This confirms that the rudder becomes progressively less effective as the sail provides more thrust.

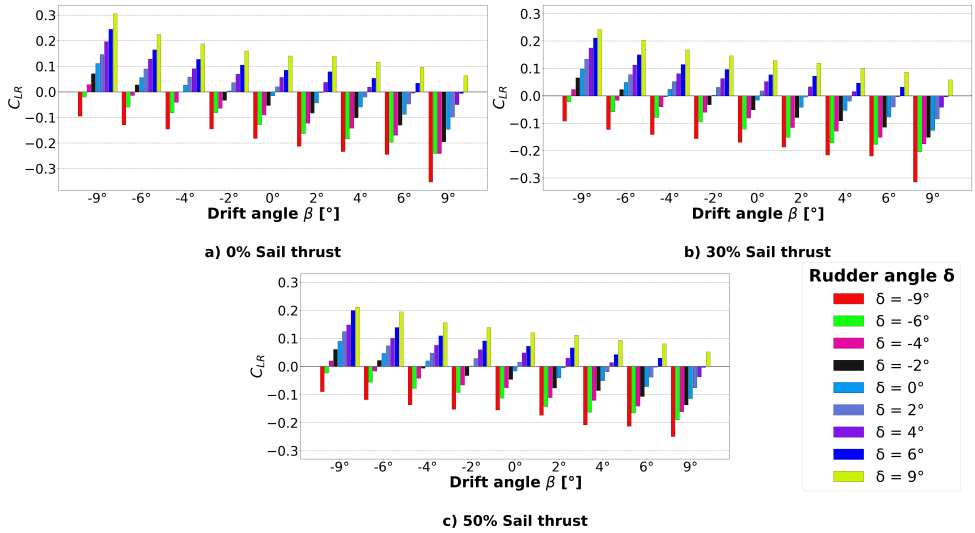


Fig. 5: Rudder lift force coefficient C_{LR} as a function of drift angle β, for each rudder angle δ and sail-thrust condition.

As shown in Figure 7, the trend of the hull side force is similar across all sail-thrust conditions, while its magnitude increases significantly with increasing drift angle. This shows that, within the conditions studied, the hull side force is mainly affected by the leeway (drift) angle, while the sail-thrust condition has a relatively small or negligible effect.

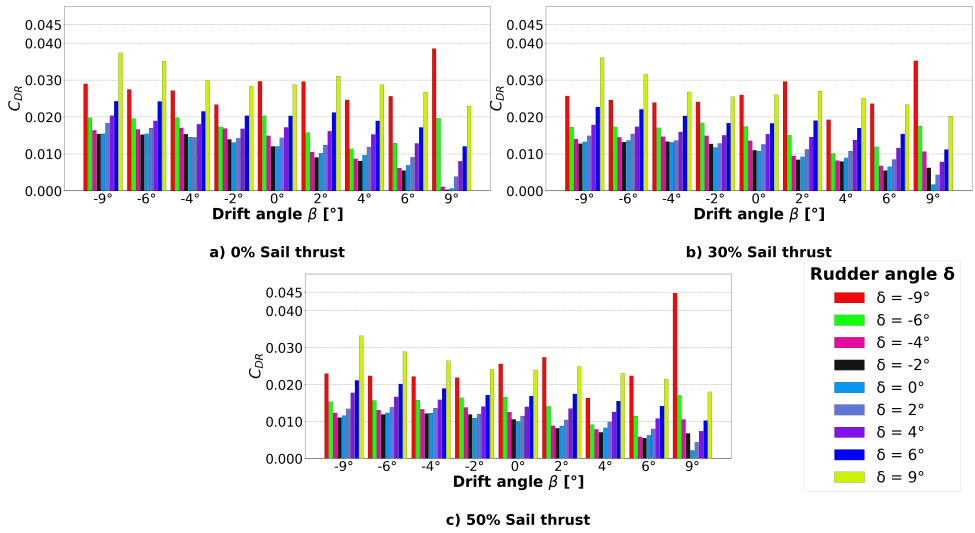


Fig. 6: Rudder Drag force coefficient C_{DR} as a function of drift angle β, for each rudder angle δ and sail-thrust condition.

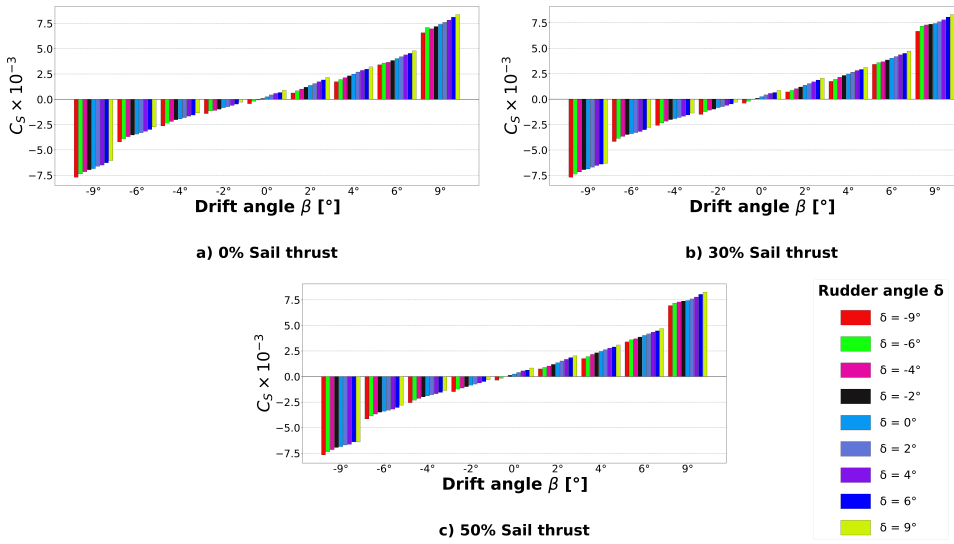


Fig. 7: Side force coefficient C_S as a function of drift angle, for each rudder angle δ and sail-thrust condition.

4 Conclusion and Future Work

This study investigated the hydrodynamic behaviour of a wind-assisted ship under different drift angles and sail-thrust conditions, with particular emphasis on rudder and side forces. The results show that the rudder force is sensitive to both drift angle and sail thrust. In most cases, increasing the sail contribution from 0% to 50% reduced the rudder lift coefficient by approximately 30% while increasing the drag coefficient by approximately 18%, indicating a loss of rudder effectiveness as the propeller is unloaded. In contrast, the overall side-force trend was governed mainly by drift angle, with only a comparatively small influence from sail-thrust condition.

Future work should incorporate free-surface effects and apply the sail forces directly as thrust, rather than through the propeller-unloading approach used in the present study.

References

Ammar, N.R., and Seddiek, I.S. (2022). Wind assisted propulsion system onboard ships: case study Flettner rotors. *Ships and Offshore Structures*, 17, 1616–1627.

Branlard, E. (2017). The blade element momentum method. In *Wind Turbine Aerodynamics and Vorticity-Based Methods: Fundamentals and Recent Applications* (pp. 181–211). Springer.

JoRes Project (2023). Joint Research Project. Available at: `https://jores.net/`

Eça, L., and Hoekstra, M. (2014). A procedure for the estimation of the numerical uncertainty of CFD calculations based on grid refinement studies. *Journal of Computational Physics*, 262, 104–130.

Gaggero, S., Villa, D., and Viviani, M. (2017). An extensive analysis of numerical ship self-propulsion prediction via a coupled BEM/RANS approach. *Applied Ocean Research*, 66, 55–78.

ITTC (2014). Practical guidelines for ship CFD applications. *ITTC Recommended Procedures and Guidelines*, 7.5-03-02-01.

Kramer, J.V., Steen, S., and Myrhaug, D. (2022). Sail-induced resistance on a wind-powered cargo ship. *Ocean Engineering*, 257, 111683.

Chou, T., Kosmas, V., Acciaro, M., and Renken, K. (2021). A comeback of wind power in shipping: An economic and operational review on the wind-assisted ship propulsion technology. *Sustainability*, 13(4), 1880.

Ouchi, K., Uzawa, K., Kanai, A., and Katori, M. (2013). ‘‘Wind Challenger’’ the Next Generation Hybrid Sailing Vessel. In *Proceedings of the Third International Symposium on Marine Propulsors (SMP’13)*, Launceston, Tasmania, Australia, 5–8 May 2013, pp. 562–567.

Shang, Y., and Horrillo, J.J. (2021). Numerical simulation and hydrodynamic performance predicting of two-dimensional hydrofoils in tandem configuration. *Journal of Marine Science and Engineering*, 9(5), 462.

Van der Kolk, N.J., Keuning, J.A., and Huijsmans, R.H.M. (2019). Part 1: Experimental validation of a RANS-CFD methodology for the hydrodynamics of wind-assisted ships operating at leeway angles. *Ocean Engineering*, 178, 375–387.

Experimental and numerical analysis of the wave-making resistance of a self-propelled KCS at drift

Saeed Hosseinzadeh, Muhammed Talha Ozdenoglu[1], Tahsin Tezdogan, Joseph Banks, Dominic Taunton, and Stephen Turnock

Maritime Engineering Group, School of Engineering, University of Southampton, Boldrewood Innovation Campus, Building 176, SO16 7QF, U.K.

1. Introduction

Wave-making resistance is an important component of a ship's calm-water resistance and a key target for hull-form optimisation. Predicting it accurately under realistic operating conditions, particularly when the ship advances at a drift angle, remains challenging. Classical potential-flow approaches, such as thin-ship theory (Michell, 1898) and Rankine-source panel methods (Ikehata & Tahara, 1987) were developed to estimate wave-making resistance and its contribution to total resistance. More recently, Bašić et al. (2020) extended Michell's thin-ship theory to non-slender hulls by incorporating boundary-layer and nonlinear effects, producing more accurate wave-resistance curves than the original theory and the Holtrop-Mennen method. Nevertheless, such reduced-order approaches cannot fully resolve viscous effects, propeller-hull interaction, or the asymmetric separated cross-flow that develops when the hull operates at leeway. These limitations motivate the use of computational fluid dynamics (CFD) validated against experiments.

Viscous-flow simulations resolve features of the wave field that potential-flow methods cannot fully represent, since the boundary layer, nonlinear and breaking near-field waves, and propeller action are computed directly rather than simplified or neglected. However, they introduce uncertainties associated with turbulence modelling and discretisation, making verification and validation against experimental data essential. In this context, Olivieri et al. (2007) provided detailed measurements using geometrically similar ship models at two scales, including mean and fluctuating wave elevations and the velocity field beneath the breaking bow and shoulder waves. Their results linked steep wave slopes to large fluctuations in wave elevation and showed that breaking generates free-surface scars and vortices. These observations indicate that part of the energy transferred to the free surface is dissipated locally through wave breaking rather than radiated into the far field. Later, Zhang (2010) simulated the free-surface flow around the KCS hull using three grid sets and verified and validated the predicted resistance and wave profile in accordance with International Towing Tank Conference (ITTC) procedures. The calculations were then repeated with an operating propeller represented first by a body-force model and subsequently by a sliding mesh. Both approaches reproduced the measured hull-propeller interaction with reasonable accuracy, indicating that a simplified propeller model can be suitable when the wave field, rather than detailed propeller performance, is the primary focus.

Beyond characterising the near-field flow, the computed wave field can be analysed to estimate wave-pattern resistance directly. The longitudinal cut method (LCM) was originally developed for towing tank measurements, where the available record length is constrained by the tank dimensions and wall reflections (Newman, 1963; Sharma, 1966; Eggers, 1967). To overcome these limitations, Wang et al. (2025) applied the LCM within CFD simulations and validated the approach for a Wigley hull, a Series 60 model, and a Wigley catamaran. For full hull forms, the method underestimated wave-making resistance (R_W) and was sensitive to both the transverse location of the cut and the treatment of the transverse-wave contribution. Kim et al. (2025) further assessed the method for the KCS by comparing towing tank measurements with panel-method and CFD predictions. When extrapolated to the ship centreline, the wave-pattern resistance (R_{WP}) recovered about 55% of the wave-making resistance in the experiment and about 40% in the CFD. They also showed that the transverse cut position should be scaled by the fundamental wave number rather than ship length because the wavelength varies with

[1] Corresponding author.
E-mail address: M.T.Ozdenoglu@soton.ac.uk

Froude number. Extending this analysis to scale effects, Chen (2026) used viscous-flow simulations at four geometrically similar scales under Froude similarity. As the scale increased, the thinner boundary layer strengthened the stern-wave crest and increased the wave-pattern resistance, producing a 17.5% difference between the smallest model and full scale.

While these studies demonstrate the value of analysing computed wave fields, the influence of leeway on wave-pattern development has received less attention. Göksu et al. (2025) investigated a ship at several leeway and rudder angles using CFD and quantified the resulting changes in wave-making and total resistance coefficients. However, wave-making resistance was obtained through force decomposition, without directly examining the wave field. Consequently, comparisons between computed wave patterns and measured wave elevations for a self-propelled ship operating at a drift angle remain limited. To address this gap, the present study develops and validates a numerical model of a single-screw, self-propelled ship against dedicated towing tank measurements at a Froude number of 0.195. The investigation considers two leeway angles and two propeller rotational speeds, together with a non-propelled reference condition. Wave elevations recorded by an array of fixed probes are compared with numerical wave cuts extracted at the corresponding transverse positions, while wave-making resistance is determined from paired free-surface and double-body simulations. This combined analysis quantifies the effects of drift and propeller loading on the wave pattern and assesses how much of the associated change in resistance can be inferred from the wave field.

2. Methodology

2.1 Experimental model

The experiments were conducted in the University of Southampton's Boldrewood towing tank, which is 138 m long, 6 m wide, and 3.5 m deep. A 1:60.96-scale model of the KCS was tested in calm water, with a length between perpendiculars of 3.773 m and a total wetted surface area of 2.567 m², including the rudder, which was fitted throughout the tests. The water temperature was 16.3 °C. Tests were performed at a Froude number of 0.195, corresponding to a model speed of 1.186 m/s, under both non-propelled and self-propelled conditions. Two leeway angles, $\beta = 0°$ and $\beta = -5°$, were considered, with the negative leeway angle denoting drift towards starboard relative to the direction of travel, and the self-propelled cases were conducted at propeller speeds of 448 and 566 rpm. The model was allowed to heave and pitch freely. Four resistance-type wave probes were installed at a single longitudinal station near the middle of the tank and on the same side of the model track. The probes were positioned at transverse distances of 1.605, 1.855, 2.105, and 2.355 m from the track centreline, and the wave elevation was sampled at 100 Hz as the model passed. The four cuts lie at y/L_{PP} between 0.43 and 0.62, which satisfies the minimum transverse distance recommended by the ITTC (2021b). Further details of the experimental arrangement are provided by Hosseinzadeh et al. (2025a, b), and the propulsive performance of the same model at leeway is reported in Hosseinzadeh et al. (2026).

2.2 Numerical setup

A numerical model was developed in Simcenter STAR-CCM+ 2406.0001 (Build 19.04.009) to predict the wave-making resistance and compare the computed wave elevations with the experimental measurements. The unsteady Reynolds-averaged Navier–Stokes (URANS) equations were solved, with the free surface captured using the volume-of-fluid (VOF) method and the HRIC scheme. Turbulence was represented by the Realizable K-Epsilon Two-Layer model with Two-Layer All y+ Wall Treatment, and second-order discretisation schemes were employed in both space and time. The water density and dynamic viscosity were specified as 998.9 kg/m³ and 1.100×10^{-3} Pa·s, respectively, corresponding to fresh water at the temperature of 16.3 °C.

The domain reproduced the towing tank cross-section. Its longitudinal coordinate has its origin at the rudder stock and is positive downstream, with boundaries at x = -8.5 m (-2.25 L_{PP}) and 12 m (3.18 L_{PP}). Wave-cut coordinates in Section 2.3 onwards instead originate at midship and are positive towards the bow. The domain was 6 m wide, extending from z = -3.5 to 3.5 m. A velocity inlet and pressure outlet were imposed upstream and downstream, with a 1.4 m (0.371 L_{PP}) damping zone before the outlet. Side walls and the bottom were no-slip boundaries. Dynamic fluid body interaction (DFBI) allowed free heave and pitch. At leeway, the hull was rotated while inflow remained parallel to the tank walls. A

virtual disk represented propeller loading using KP505 open-water data from the Tokyo 2015 CFD workshop (Hino et al., 2020).

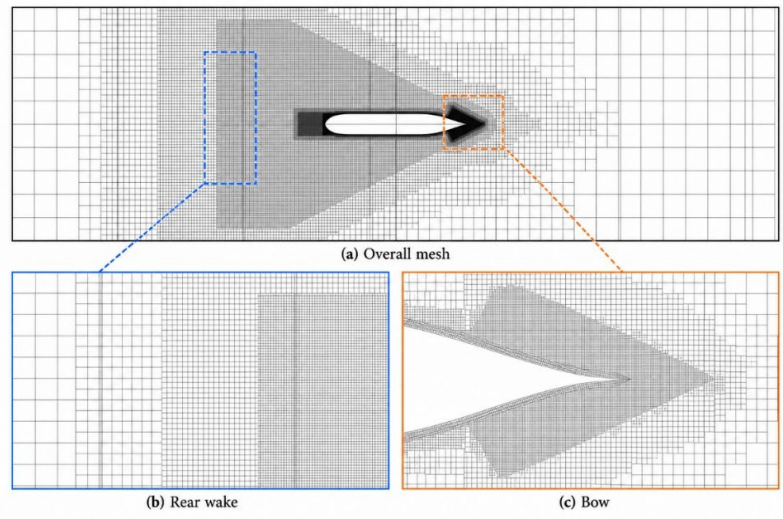


Fig. 1: Computational mesh for the zero-leeway case, with detailed views of the bow and wake refinement regions.

The computational mesh is shown in Fig. 1 shows the trimmed hexahedral mesh, with six prism layers on the hull. Their total thickness was 6.25% of the 0.07546 m (0.02 L_{PP}) base size, or approximately 0.00472 m (0.00125 L_{PP}), with a stretching factor of 1.5 and $y+ > 30$. The mesh contained approximately 3.01 million cells, with refinements around the hull, free surface and Kelvin wake; downstream refinement followed the flow direction. The time step was 0.016 s (approximately 0.005 L_{PP}/U), with five inner iterations, satisfying the ITTC (2024) guideline of $\Delta t < 0.01\ L_{PP}/U$ for two-equation turbulence models. Separate double-body simulations used the same numerical configuration and propeller representation with free-surface effects removed. Wave-making resistance (R_w) as calculated as the difference between free-surface and double-body resistance.

2.3 Analysis

Wave-pattern resistance (R_{wp}) is determined from wave cuts using the longitudinal cut method (Insel, 1990; Molland et al., 2004). Each cut records the wave elevation along a line parallel to the ship track at a fixed transverse distance. Decomposing this record into the free-wave components of the ship-generated system allows the resistance to be calculated from the energy carried away from the hull. The analysis also accounts for the finite width and depth of the tank by considering the discrete propagation angles imposed by the side walls. The analysis is scaled by the fundamental free-surface wavenumber, $k_0 = g/U^2$, where g is gravitational acceleration and U is ship speed, with the corresponding transverse wavelength $\lambda_0 = 2\pi/k_0$. Wave elevation and transverse cut position are expressed as $k_0\eta$ and k_0y, respectively, enabling direct comparison across different Froude numbers. The wave-pattern resistance coefficient is defined as $C_{WP} = R_{WP}/(1/2\rho U^2 S)$, where S is the wetted surface area. Wave-making resistance R_w and wave-pattern resistance R_{wp} differ in how they are obtained: in the present study, R_w is determined from the difference between the free-surface and double-body resistance, whereas R_{wp} is derived from the wave-elevation field using the longitudinal cut method. In viscous flow, R_{wp} may be lower than R_w because of local wave-breaking losses, the linear wave approximation used in the longitudinal cut analysis, and limitations in representing the transverse-wave contribution (Baba, 1969; Kim et al., 2025). The C_{WP} values reported in this study were extrapolated to the ship centreline from the measured transverse cut positions.

As an initial validation, the computed wave field was compared with the towing tank measurements of Kim et al. (2025) at Fr = 0.26. Fig. 2 presents the profiles at k_0y = 1.5, 2.5, 3.5, and 4.5, with the longitudinal coordinate measured from midship, x/L_{PP}=0, and positive towards the bow. The numerical and measured profiles agree closely and reproduce the same transverse wavelength, confirming the

adopted scaling and speed. The Pearson correlation coefficient, calculated between the computed wave elevations and the digitised experimental profiles after linear interpolation onto a common grid over $-2.5 \leq x/L_{PP} \leq 1$, with a spacing of $\Delta(x/L_{PP}) = 0.005$, decreases from 0.975 at the innermost cut to 0.882 at the outermost cut, where the wave field is weaker. The computed amplitudes are 14-18% higher than the measurements, particularly in the troughs. At the two outer cuts, the aft oscillations are slightly underpredicted, likely because the mesh becomes coarser away from the hull. The same scaling and analysis were then applied to the measured and computed wave cuts at Fr = 0.195. Fig. 3 shows the computed wave-elevation fields at leeway angles of 0° and -5°, with a symmetric wave pattern about the ship's track at 0° becoming asymmetric at -5°.

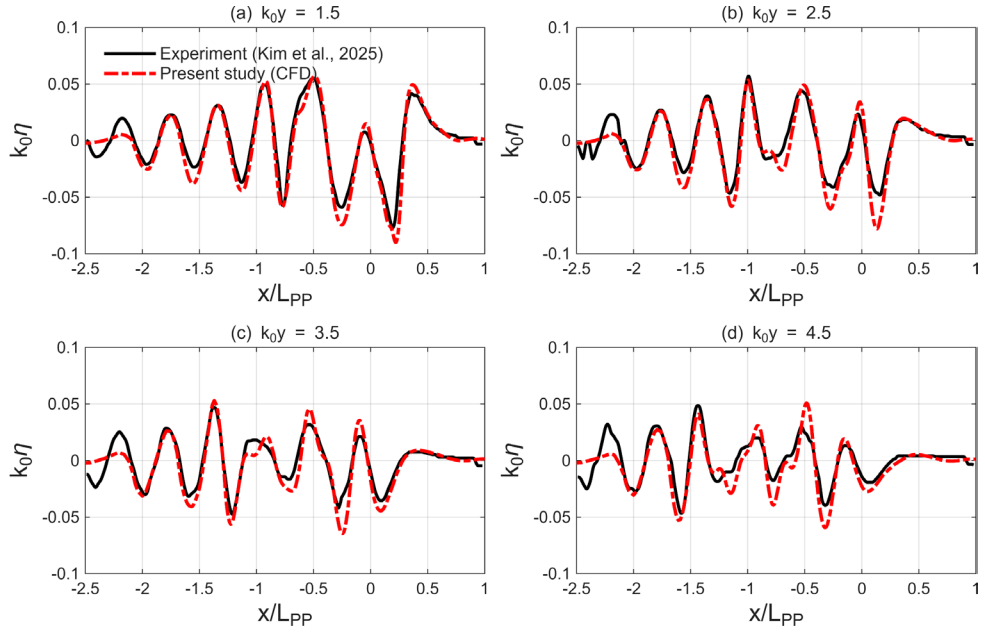


Fig. 2: Non-dimensional wave elevation at Fr = 0.260 compared with the measurements of Kim et al. (2025) at four transverse positions.

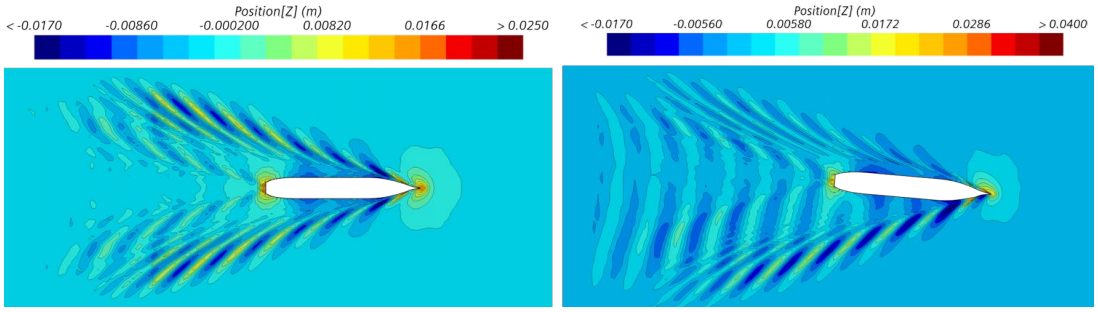


Fig. 3: Computed wave elevation field at Fr = 0.195. Left, β = 0 degrees. Right, β = -5 degrees.

3. Results and discussion

The effects of leeway and propeller loading on wave-making and wave-pattern resistance are assessed using the measured and computed longitudinal wave cuts. Fig. 4 compares the four probe records for the non-propelled case at a leeway angle of -5°. Both datasets remain flat ahead of the Kelvin wedge, which reaches the innermost probe at $x/L_{PP} = -0.70$ and the outermost at $x/L_{PP} = -1.27$. From the wedge boundary to approximately $x/L_{PP} = -1.5$, the numerical predictions agree closely with the measurements in both phase and amplitude. Farther downstream, the computed amplitudes are increasingly underpredicted, particularly at the outer probes. This discrepancy is mainly attributed to numerical damping as the free-surface mesh becomes coarser away from the hull. Sidewall reflections also affect the measured signal, reaching WP4 at $x/L_{PP} = -2.23$ and WP1 at $x/L_{PP} = -2.80$; however, the numerical amplitudes begin to decay before these reflections arrive, indicating that mesh-induced damping is the dominant cause.

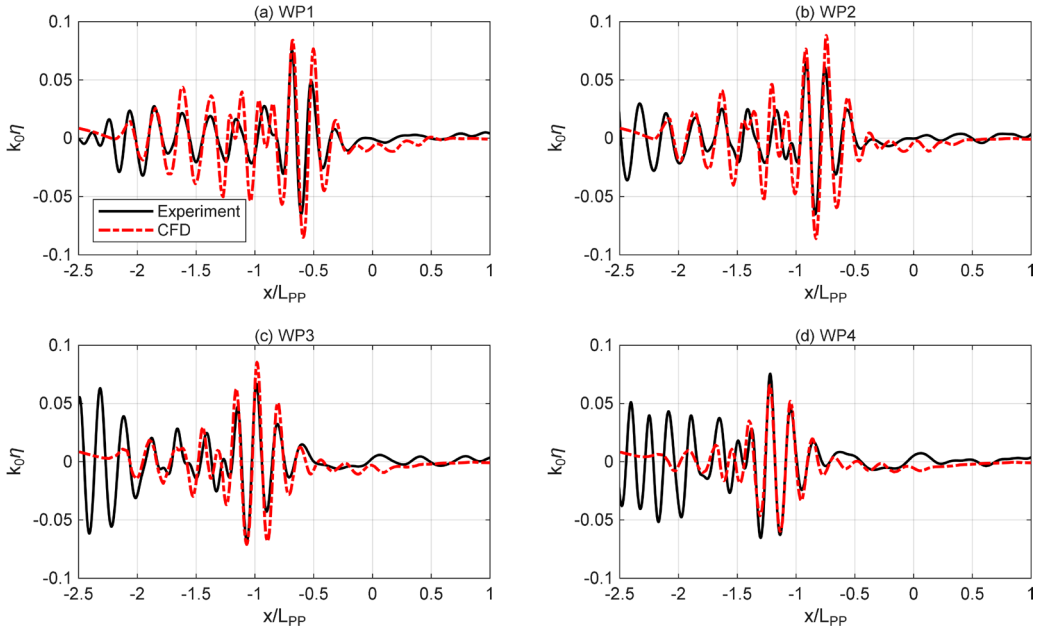


Fig. 4: Measured and computed wave cuts at the four probe positions for the non-propelled condition at β = -5 degrees, Fr = 0.195.

Fig. 5 illustrates the influence of leeway and propeller loading at the innermost probe. For the non-propelled condition, the wave amplitude at -5° remains higher than at zero leeway throughout the record (Fig. 5a). The measured C_{WP} increases from 0.105×10^{-3} to 0.216×10^{-3}, while the computed value rises from 0.121×10^{-3} to 0.225×10^{-3}. Hence, both show that leeway approximately doubles the wave-pattern resistance. A similar trend is obtained from the double-body decomposition, for which the C_W increases from 0.247×10^{-3} to 0.491×10^{-3}.

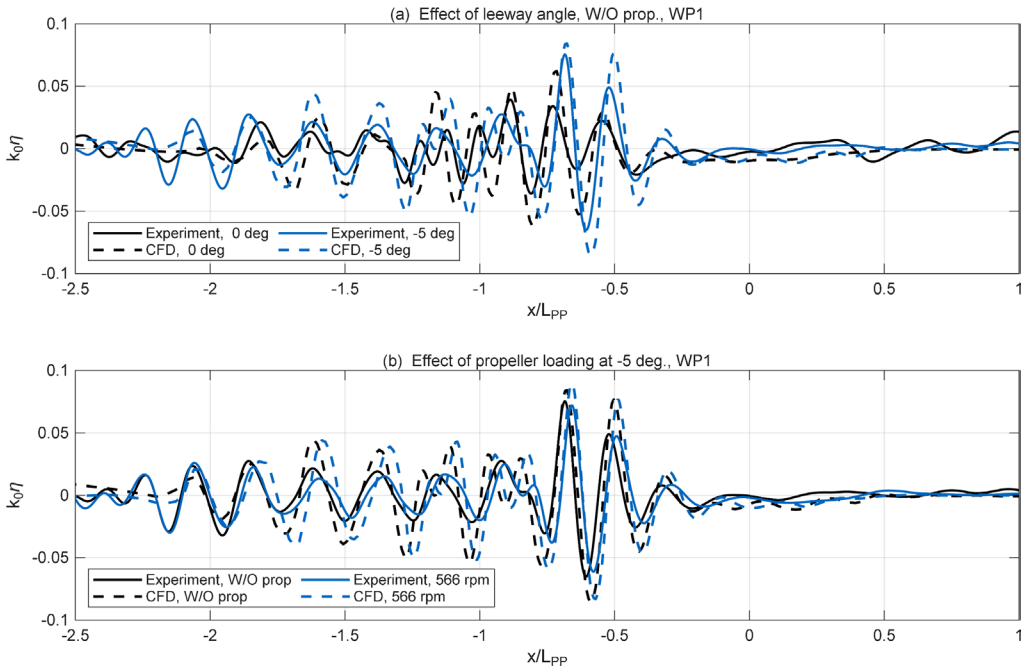


Fig. 5: Wave cuts at WP1, k_0y = 11.2, Fr = 0.195. (a) Effect of leeway angle in the non-propelled condition. (b) Effect of propeller loading at β = -5°; the overlapping 448 rpm trace is omitted.

The effect of propeller loading is shown in Fig. 5b. At WP1, the RMS wave elevation decreases from 2.263 mm in the non-propelled condition to 2.107 and 2.116 mm at 448 and 566 rpm, respectively, corresponding to reductions of 6.9% and 6.5%. The two propelled cases differ by 0.4%, indicating that propeller loading has a limited effect on the individual wave cut. This observation is consistent with the

limited differences between non-propelled, propeller-driven, and waterjet-driven models reported by Molland et al. (2004) between non-propelled, propeller-driven, and waterjet-driven models based on individual wave cuts. Wave-pattern resistance is more sensitive because it varies with the square of wave elevation and is derived from all four cuts, allowing small systematic variations that are not apparent in one trace to influence the result. The root-mean-square elevation, averaged over the four probes between the arrival of the Kelvin wedge at the first probe and the first wall reflection at the fourth, decreases by 7%, from 3.36 mm without the propeller to 3.11 mm at 566 rpm. Between the same two conditions the measured C_{WP} decreases by 13%, from 0.216×10^{-3} to 0.188×10^{-3}, consistent with the change in wave elevation. Each record was analysed over four windows of different length and position, and the reduction is comparable to the 11% spread between them for both cases, while the computed values show no corresponding decrease. Moreover, at zero leeway the measured effect is more pronounced. The wave-pattern resistance falls from 0.105×10^{-3} without the propeller to 0.047×10^{-3} at 448 rpm and 0.044×10^{-3} at 566 rpm. The computed values for the same three conditions are 0.121, 0.137 and 0.134×10^{-3}, respectively (Table 1).

At Fr = 0.260, the computed total resistance coefficient is 4.369×10^{-3}, compared with the measured value of 4.364×10^{-3}, corresponding to a difference of only 0.1%. The C_W obtained from the difference between the free-surface and double-body total resistance coefficients, is 0.580×10^{-3} and differs by 1.6% from the value reported by Kim et al. (2025) for the same condition. Table 1 summarises the coefficients for all six cases at Fr = 0.195. At this speed, the ITTC-1957 correlation line gives a frictional resistance coefficient (C_F) of 3.530×10^{-3}, while the form factor derived from the non-propelled double-body calculation using $C_{T\text{-}DB}/C_F$ is 1.1205, and a single value is used for all conditions. For the non-propelled cases, decomposition of the measured total resistance using this form factor yields experimental wave-making resistance coefficients of 0.169×10^{-3} at zero leeway and 0.929×10^{-3} at -5°. The latter exceeds the computed C_W of 0.491×10^{-3} because the friction line does not remove the induced drag generated at a leeway angle, which the double-body calculation gives as 0.269×10^{-3}. This procedure cannot be applied to the self-propelled cases because the measured total resistance includes the thrust-deduction effect, which is not removed by the friction line. At zero leeway, the measured thrust-deduction fraction is 0.22 at both propeller loadings.

For Cases 1, 2, and 4, the computed total resistance agrees with the experimental measurements within 4%, whereas, for the remaining three cases, the CFD results underpredict the measurements by 6-12%. The pressure force generated by the virtual disk represents 59-71% of the measured thrust deduction, and the unrecovered portion explains most of the discrepancy in total resistance for the self-propelled conditions. At 448 rpm the expected increase in total resistance is only about 0.2×10^{-3}, so the residual lies within the numerical uncertainty, whereas at 566 rpm it is three times larger and a clear rise is obtained. In five of the six cases, the computed wave-pattern resistance (C_{WP}) accounts for 46–58% of the computed wave-making resistance (C_W), consistent with the range reported by Kim et al. (2025) for analyses that include the complete downstream record.

Table 1: Total, wave-making and wave pattern resistance coefficients at Fr = 0.195. All coefficients $\times 10^3$. $C_F = 3.530 \times 10^{-3}$ from the ITTC-1957 correlation line and 1+k = 1.1205 from the non-propelled double-body computation. $\Delta C_T = (C_{T,CFD} - C_{T,exp})/C_{T,exp}$. C_W CFD is the difference between the free-surface and double-body total resistance coefficients, while C_W exp follows the ITTC-1978 form factor method, so the two are not directly comparable. C_W exp. is not given for the self-propelled cases, where the measured total resistance includes the thrust deduction.

Test Cases	Propulsion	β [deg]	C_T exp.	C_T CFD	ΔC_T %	C_W CFD	C_W exp.	C_{WP} CFD	C_{WP} exp.
1	W/O prop.	0	4.124	4.202	1.9	0.247	0.169	0.121	0.105
2	448 rpm	0	4.325	4.158	-3.8	0.236	–	0.137	0.047
3	566 rpm	0	4.705	4.399	-6.5	0.245	–	0.134	0.044
4	W/O prop.	-5	4.884	4.715	-3.5	0.491	0.929	0.225	0.216
5	448 rpm	-5	5.351	4.699	-12.2	0.381	–	0.269	0.156
6	566 rpm	-5	5.674	4.975	-12.3	0.524	–	0.261	0.188

4. Conclusions

The wave-making and wave-pattern resistance of a self-propelled KCS model have been investigated at two leeway angles using measured and computed longitudinal wave cuts. The numerical model was first validated at a higher Froude number, where the predicted wave-making resistance coefficient agreed with published towing tank data within 2%. For the non-propelled conditions, the computed total resistance agreed with the experimental measurements within 4%, whereas, under propelled conditions, the CFD predictions underestimated the measured values by up to 12%. This difference is mainly because the virtual-disk model represents only part of the thrust deduction measured in the towing tank. The computed wave system agrees well with the measurements near the Kelvin wedge, although the wave elevation is underestimated farther downstream. At zero leeway the same thrust-deduction fraction was measured at both propeller loadings, indicating that the self-propulsion measurements are consistent. The wave-making resistance obtained as the difference between the free-surface and the double-body computations is not affected by the thrust deduction, because the same propeller setting appears in both cases and the effect cancels.

A leeway angle of -5° approximately doubles both wave-making and wave-pattern resistance. This increase is shown independently by the force decomposition and the wave-cut analysis. Propeller loading causes little visible change in the individual wave profiles; however, small differences become evident when wave-pattern resistance is calculated from all four cuts. Wave-pattern resistance is therefore a more sensitive measure of changes in the wave system, and individual wave cuts alone are insufficient to determine the effect of propeller loading. In the numerical results, wave-pattern resistance accounts for approximately half of the wave-making resistance.

Several aspects should be considered in future work. The free-surface mesh should be refined further from the hull, so that the far wake and the wave reflected from the tank wall are resolved with the same accuracy as the near field. The propeller model could be improved for the cases at a leeway angle, where the virtual disk recovers only part of the measured thrust deduction, and a resolved propeller would remove this limitation. Future measurement campaigns would benefit from wave probes placed closer to the ship's track, because the record available between the Kelvin wedge and the first wall reflection becomes longer as the transverse distance is reduced. Repeat runs at each condition would allow the repeatability of the wave records to be quantified, which would in turn allow the small differences between the propelled and non-propelled conditions to be resolved. Finally, extending the test matrix to include additional leeway angles and speeds would provide a clearer understanding of the overall trends.

Acknowledgments

This work was supported by the European Union's Horizon Europe research and innovation programme through the Marie Skłodowska-Curie Actions under grant agreement No. 101209334 (NuWAS project). The authors gratefully acknowledge the dedicated staff of the Boldrewood Towing Tank at the University of Southampton and the 2025/26 cohort of students enrolled in SESS6077 Zero Carbon Ship Resistance and Propulsion for their assistance with the experiments. The second author gratefully acknowledges the University of Southampton for funding his PhD studies. The authors further acknowledge the use of the University of Southampton's high-performance computing facilities, including the IRIDIS 6 cluster.

References

Michell, J. H. (1898). XI. The wave-resistance of a ship. *The London, Edinburgh, and Dublin Philosophical Magazine and Journal of Science*, *45*(272), 106-123.

Ikehata, M., & Tahara, Y. (1987). Influence of Boundary Layer and Wake on Free Surface Flow around a Ship Model. *Journal of the Society of Naval Architects of Japan*, *1987*(161), 49-57.

Bašić, J., Blagojević, B., & Andrun, M. (2020). Improved estimation of ship wave-making resistance. *Ocean engineering*, *200*, 107079.

Olivieri, A., Pistani, F., Wilson, R., Campana, E. F., and Stern, F. (2007). Scars and Vortices Induced by Ship Bow and Shoulder Wave Breaking. ASME. *J. Fluids Eng*. November 2007; 129(11): 1445–1459. https://doi.org/10.1115/1.2786490

Zhang, Z. R. (2010). Verification and validation for RANS simulation of KCS container ship without/with propeller. Journal of Hydrodynamics, Series B, 22(5, Supplement 1), 932–939. https://doi.org/10.1016/S1001-6058(10)60055-8

Newman, J.N., 1963. The determination of wave resistance from wave measurements along a parallel cut. In: *International Seminar on Theoretical Wave Resistance*. University of Michigan, Ann Arbor, Michigan.

Sharma, S. (1966). An attempted application of wave analysis techniques to achieve bow-wave reduction. In: *Proceedings of 6th Symposium on Naval Hydrodynamics*, Washington, D.C.

Eggers, K. W. H. (1967). An assessment of some experimental methods for determining the wavemaking characteristics of a ship form. *Sname Transactions*, *75*, 112-157.

Wang, X., Zhu, R., Xu, D., Wang, H., & Gu, Y. (2025). Mechanism analysis and prediction of longitudinal cut wave pattern resistance based on CFD simulation. *Journal of Ocean Engineering and Science*, *10*(2), 258-273.

Kim, M., Seo, J., Kim, M. A., Kim, M. S., Kim, D. H., Park, J., & Seok, W. (2025). Examination of wave pattern resistance estimation method by experiments and numerical analyses. *International Journal of Naval Architecture and Ocean Engineering*, 100679.

Chen, Y. H. (2026). Study on scale effect of ship on flow field and near-field wave generation. *Frontiers in Physics*, *14*, 1670851.

Göksu, B., Garad, S., Pandini, S., Sirolla, E., Palin, R., Townsend, N., & Tezdogan, T. (2025). Impact of leeway and rudder angles on ship resistance: A numerical planar motion mechanism approach. *Ocean Engineering*, *338*, 121952.

International Towing Tank Conference (2021a). Resistance tests. ITTC Recommended Procedures and Guidelines, Procedure 7.5-02-02-01, Revision 05. International Towing Tank Conference.

International Towing Tank Conference (2021b). Wave profile measurement and wave pattern resistance analysis. ITTC Recommended Procedures and Guidelines, Procedure 7.5-02-02-04, Revision 00. International Towing Tank Conference.

Hosseinzadeh, S., Turnock, S. R., Lee, H., and Olvera, R. (2025a). Experimental dataset of a model-scale ship in calm water and waves. Data in Brief, 58, 111257.

Hosseinzadeh, S., Hudson, D., Turnock, S. R., Prince, M., and Banks, J. (2025b). Influence of hull–propeller–rudder interaction on the self-propulsion of wind-assisted ships. Physics of Fluids, 37(8), 087216.

Hosseinzadeh, S., Turnock, S. R., Banks, J., Hudson, D., & Prince, M. (2026). Impact of leeway and rudder angles on propulsive performance of a single screw wind-powered ship. *Ocean Engineering*, *365*, 127431.

International Towing Tank Conference (2024). Practical Guidelines for Ship CFD Applications. ITTC Recommended Procedures and Guidelines, No. 7.5-03-02-03, Revision 02, International Towing Tank Conference.

Hino, T., Stern, F., Larsson, L., Visonneau, M., Hirata, N., & Kim, J. (Eds.). (2020). Numerical ship hydrodynamics: An assessment of the Tokyo 2015 workshop. Springer Nature.

Insel, M. (1990). An investigation into the resistance components of high-speed displacement catamarans (Doctoral dissertation, University of Southampton).

Molland, A. F., Wilson, P. A., Taunton, D. J., Chandraprabha, S., & Ghani, P. A. (2004). Resistance and wash measurements on a series of high speed displacement monohull and catamaran forms in shallow water. *Transactions of The Royal Institution of Naval Architects Part A: International Journal of Maritime Engineering*, *146*(2), 19-38.

Baba, E. (1969). A new component of viscous resistance of ships. *Journal of the Society of Naval Architects of Japan*, *1969*(125), 23-34.

Proceedings of the Numerical Towing Tank Symposium
NUTTS 2026
September 19–21, 2026, Duisburg, Germany

Numerical Investigation of Rudder and Propeller Loads during Steady Turning Maneuver of the ONR Tumblehome

A. Nath[1], H. Peng[1], A. Akinturk[2], and W. Qiu*[1]

[1]Department of Ocean and Naval Architectural Engineering, Memorial University of Newfoundland, St John's, Canada
[2]Ocean, Coastal, and River Engineering, National Research Council, St. John's, Canada
anath@mun.ca, hpeng@mun.ca, ayhan.akinturk@nrc-cnrc.gc.ca, qiuw@mun.ca

Aug 17, 2026

I. Introduction

With increasing interest in reducing emissions and the recent adoption of net-zero regulations by the International Maritime Organization, there has been a surge in research on the performance of propellers under off-design conditions, focusing on improving safety and efficiency and avoiding propeller-induced vibrations and noise. The assessment of propeller performance under off-design conditions, such as maneuvers, is crucial, as propellers operate in conditions markedly different from their designed straight-ahead motion due to oblique, vortex-dominated inflow. In addition, ships with twin screw propulsion exhibit different performance for the windward and leeward propellers. This study uses Unsteady-Reynolds-Averaged-Navier-Stokes simulations of the free-running steady turning maneuvers of the Office of the National Research Tumblehome (ONRT) surface combatant appended with two propellers and rudders, moving at an approach velocity corresponding to FN=0.2, three different rudder angles: 35°, 25°, and 15°, using the StarCCM+ CFD software. A Proportional-Integral (PI) controller is used during the approach phase of the maneuver to estimate the propeller RPM at the self-propulsion point. The Overset approach is used to ensure mesh quality during large ship motions resulting from the execution of the maneuver and to enable the relative motion of the rudders with respect to the ship. A fully discretized rotating propeller mesh using the sliding interface approach has been used to capture propeller-induced forces and the hull-propeller-rudder interactions during the maneuver. The turning circle simulations validated against experiments by Aram and Mucha [1]. International Towing Tank Conference (IITC) variables are used for quantitative analysis of the maneuvers, and a detailed study of the effect of rudder angle on in-plane loads on the hull, propeller, and rudder is presented.

II. Numerical Modelling

The Star-CCM+ CFD software is used to solve the viscous, incompressible, two-phase RANS equations. The equation of continuity solved by StarCCM is given as:

$$\begin{aligned} \frac{\partial \rho}{\partial t} + \nabla \cdot (\rho \overline{\mathbf{v}}) &= 0 \\ \frac{\partial \rho \overline{\mathbf{v}}}{\partial t} + \nabla \cdot (\rho \overline{\mathbf{v}} \otimes \overline{\mathbf{v}}) &= -\nabla \cdot \overline{P}\mathbf{I} + \nabla \cdot \mathbf{T} + \mathbf{f_b} \end{aligned} \tag{1}$$

where $\overline{\mathbf{u}}$ is the mean velocity vector, ρ is the density, $\overline{P}$ is the mean pressure, $\mathbf{I}$ is the Identity Matrix, $\mathbf{T}$ is the Reynolds stress tensor and $\mathbf{f_b}$ is the resultant of the body forces.

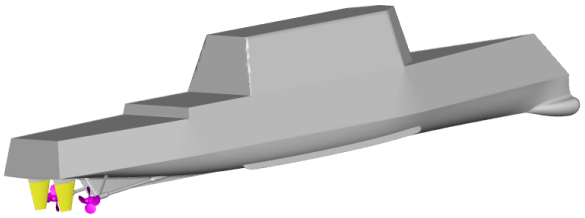
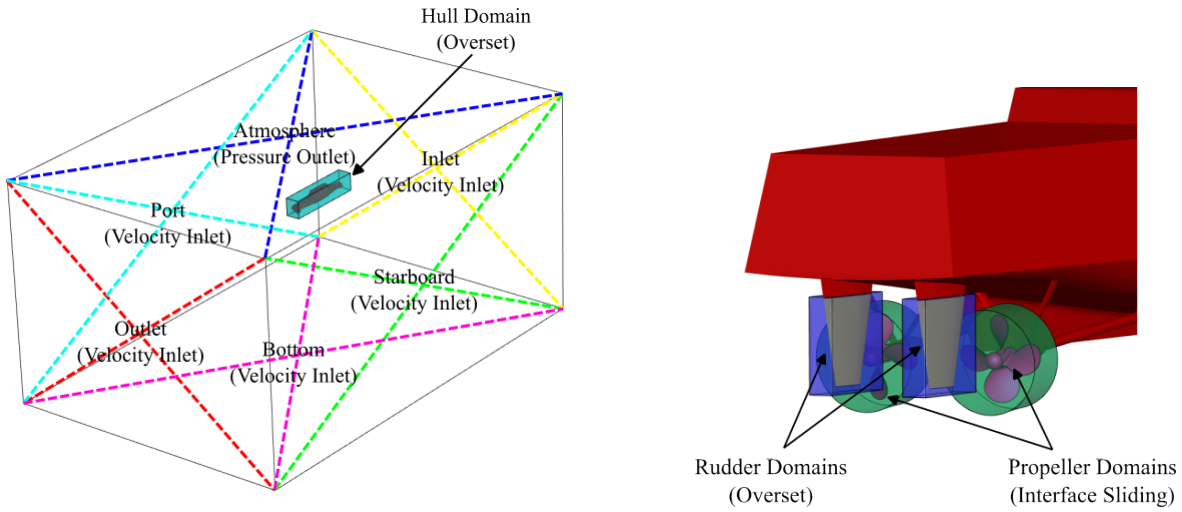


Figure. 1: ONR Tumblehome Geometry

The $k-\omega$ SST model based on the Boussinesq Hypothesis proposed by [2] is used as the turbulence closure model as per the best practice settings recommended by [3] for the closure of the RANS equations. The Volume-of-Fluid (VoF) model, along with the High-Resolution-Interface-Capturing Method, is used for two-phase simulations and to capture sharp



(a) Background and Hull Domains

(b) Propeller and Rudder Domains

Figure. 2: Computational Domain and Boundary Conditions

interfaces between the two fluids. A 1^{st} order implicit scheme is used for temporal derivatives, and 2^{nd} order schemes are used for convective and diffusive fluxes.

Due to the relative motions between the rudder, hull, & propeller and the large motions associated with the turning circle maneuver, the computational domain is comprised of several subdomains. The transfer of flux between the sub-domains occurs in two different ways. The *Interface Sliding method* is used between Hull-propeller domains, while the overset technique is used for rudder-hull and hull-background domains. The Interface Sliding method is more computationally efficient and uses a geometry-based one-to-one matching of faces at the shared internal boundary surface for the transfer of flux. The Overset technique requires more computational effort as it requires cells to be marked as "active", "inactive," or "interpolated" and the flux transfer between the domains occurs at the cells marked as "interpolated" using a 2^{nd} order scheme using shape functions.

III. Geometry, Computational Domain and Mesh Details

The ONR Tumblehome (ONRT) is an open-access modern surface combatant vessel widely used for benchmark studies. The fully appended ONRT features a centerline skeg, dual bilge keels, twin spade rudders, and inward rotating twin propellers as shown in Figure 1. The main particulars of the ONRT vessel are presented in Table I.

A right-handed Cartesian coordinate system is used, with the X direction toward the bow, the Y direction toward the port side of the model, and the origin at the intersection of the forward tip of the water plane and the ship's symmetry plane.

As mentioned previously, the computational domain comprises sub-domains w, with a cuboidal hull domain embedded as an overset in the background domain. and the two cuboidal rudder & two cylindrical propeller domains embedded within the hull domain as oversets and sliding interfaces respectively, as shown in Figure 2

TABLE. I: Main Particular

Hull		
	Full Scale	**Model Scale**
Scale	1	48.935
Lwl [m]	154	3.147
Bwl [m]	18.78	0.38
T [m]	5.494	0.11
Δ [kg]	8596 $\times 10^3$	73.36
GM [m]	2.065	0.042
kxx/B	0.377	
kyy/Lwl	0.251	
kzz/Lwl	0.251	
Propeller		
Diameter [m]	5.216	0.107
Blades	4	
Rotation	Inwards	

The cuboidal background domain extends $3L_{wl}$ downstream from the stern, $2L_{wl}$ upstream from the bow, $1L_{wl}$ above the waterline, $2L_{wl}$ below the waterline, and $2L_{wl}$ to either side of the centreline. The boundary conditions applied at the extents of the background domain are detailed in Figure 2a.

The computational mesh comprises hexahedral cells generated using the StarCCM+ meshing utility. The meshing strategy employed follows the recommendation by [3]. Accordingly, cells of size $L_{wl}/\Delta x = 518$ are distributed along the surface of the hull and the rudder, and a cell size of $\Delta x/D = 7.30 \times 10^{-3}$ is maintained along the surface of the propeller as shown in Figure 4. Additional local refinements are introduced at the bow and aft regions (Figure 3) of the model to capture flow separations and complex interactions with the hull, propeller, and rudder. To ensure a good resolution of the free surface, 25 cells are inserted along the z-

direction in the expected wave height. In addition, to capture the Kelvin wake created by the ship, the free surface in the vicinity of the model is isotropically refined. The free surface mesh refinements are shown in Figure 5. Special care is taken to guarantee overset interpolation accuracy by maintaining at least 4 cells of similar size in gaps (Rudder-Hull Gap) and close to boundaries (Hull-Background) in overset and corresponding overlap regions in the background domains. Prism layers are inserted along the hull and propeller to achieve a target $Y^+ = 50$.

The final mesh consists of approximately 12 million cells with 6 million in the background domain, 4 million in the hull domain, and 1 million in each propeller domain.

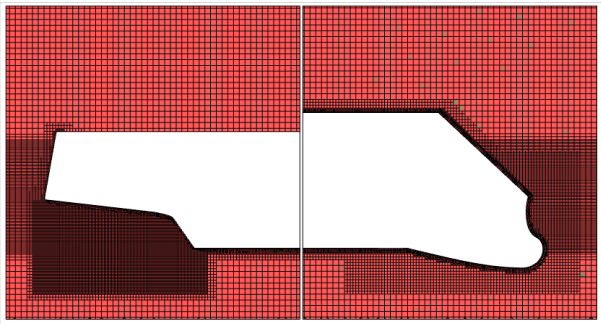


Figure. 3: Hull Grid - Stern and Bow

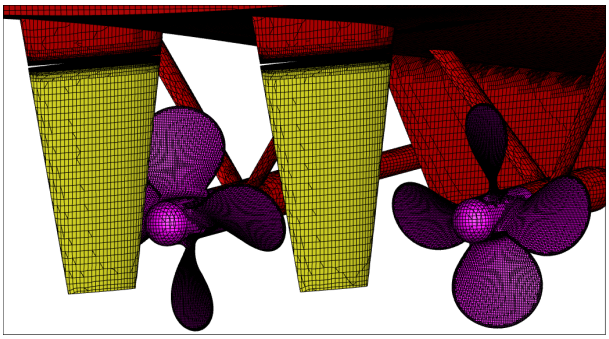


Figure. 4: Rudder and Propeller Meshes

IV. Simulation Methodology

Prior to the execution of the maneuver, to meet the approach-phase requirements, a three-DoF simulation is used, in which the ship is free to surge, heave, and pitch, and a Proportional-Integral (PI) Controller controls the propeller RPM. The approach phase of the maneuver is achieved when the ship moves at the target velocity corresponding to $F_N = 0.200$ and the propeller RPM and ship attitude have converged to steady values.

The free-running (six-DoF) steady turning maneuvering simulations are conducted for three different rudder angles: 35°, 25°, and 15°. During the maneuver, the propeller RPM is set to the self-propulsion point corresponding to the approach-phase value. The maneuver is conducted until the ship heading is greater than 540° as per the ITTC guidelines [4].

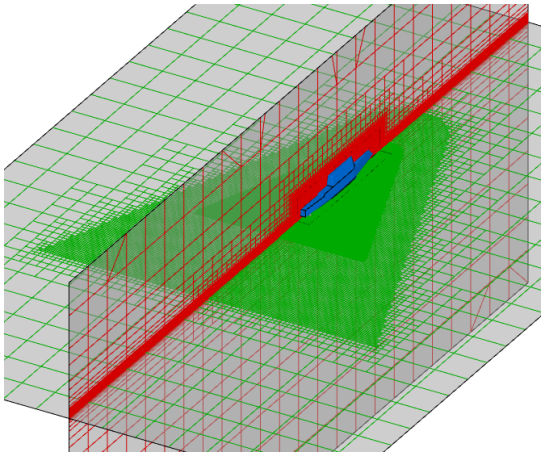


Figure. 5: Free Surface Refinement

V. Results and Discussion

The turning circle simulation results are presented and validated against experimental data from Aram and Mucha [1]. A parametric comparison using the ITTC variables for turning circle tests is presented in Table II and shows a good comparison against experiments, with deviations below 15%. Better agreement is observed for the 35° results, with deviations below 7%, whereas for the 25° maneuver, comparisons show slightly higher variations of up to 10%. The transient evolution of trajectory and time histories of ship attitude parameters presented in Figure **??** show similar results compared to the experiments. The EFD results show a tighter maneuver compared to CFD owing to lower surge velocity predictions as in the case of 25° maneuver or higher yaw rate as observed in both 25° and 35° maneuver. The deviations from experimental results could be due to inaccurate flow separation predictions and consequent inaccuracies in force and moments during stall conditions, which the starboard rudder is operating in due to the high angle of attack for both the 35° (complete stall) and 25° (partial stall), which is a known limitation of RANS. Other sources could also be due to the slight difference in the moment of inertia between the EFD and CFD models.

The parametric effect of the rudder angle on steady turning maneuver can be summarized as the execution of a tighter maneuver in a lesser time with an increase in the rudder angle, as is presented in Table II, as a consequence of an increase in yaw rate and sway velocity, and a decrease in surge velocity, consequently leading to a higher drift angle.

To further understand the transient and steady-state effects on the hull, propellers, and rudders, the terms of the body motion equation are studied. The 3 DoF body motion force balance equation for maneuvering is given by:

$$\begin{aligned} m\left(\dot{u} - vr + wq\right) &= X_H + X_{PP} + X_{PS} + X_{RP} + X_{RS} \\ m\left(\dot{v} - wp + ur\right) &= Y_H + Y_{PP} + Y_{PS} + Y_{RP} + Y_{RS} \\ I_Z\dot{r} + \left(I_Y - I_X\right)pq &= N_H + N_{PP} + N_{PS} + N_{RP} + N_{RS} \end{aligned} \tag{2}$$

where

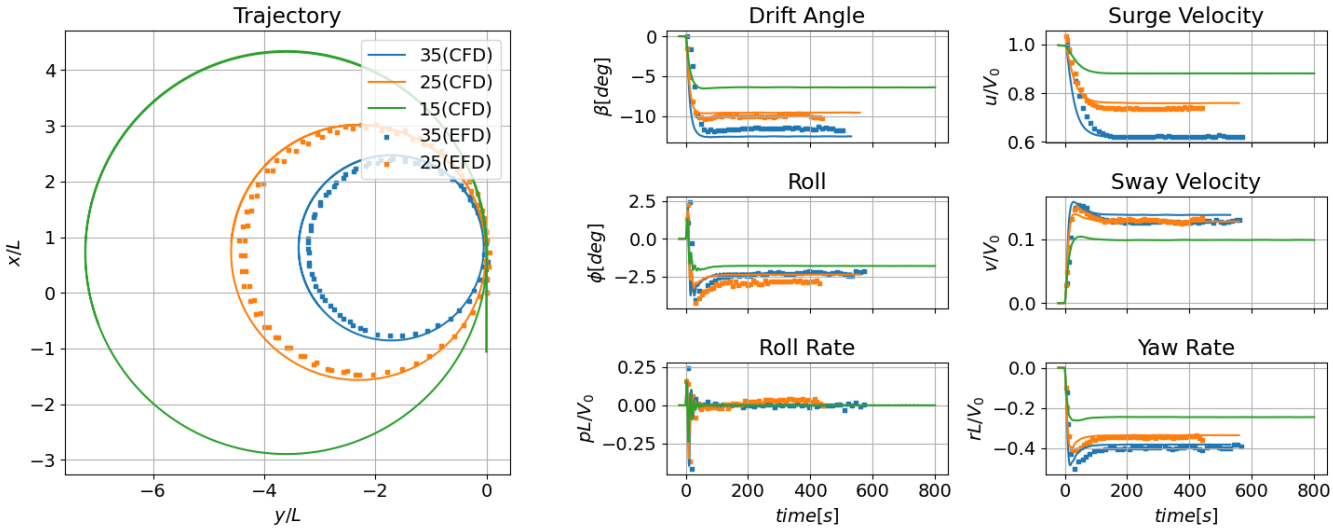


Figure. 6: Turning Circle Results - Position, Orientation, and Velocities

TABLE. II: Steady Turning - ITTC parametric result validation and comparison

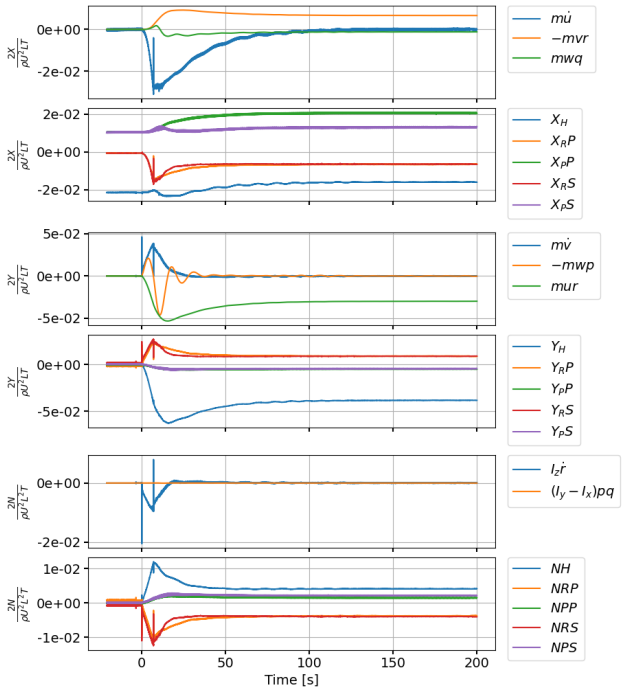
Case	35			25			15
	CFD	EFD	EFD%CFD	CFD	EFD	EFD%CFD	CFD
Advance, AD/L	2.429	2.320	4.72	2.986	2.890	3.34	4.322
Transfer, TR/L	1.348	1.310	2.90	1.921	1.750	9.74	3.197
Tactical diameter, TD/L	3.339	3.190	4.67	4.562	4.320	5.61	7.197
Time for 90 ° heading, $T_{90}V_0/L$	3.963	3.900	1.62	4.643	4.410	5.29	6.511
Time for 180 ° heading, $T_{180}V_0/L$	8.043	7.920	1.55	9.298	8.900	4.47	12.920
Steady diameter, SD/L	3.336	3.190	4.58	4.592	4.390	4.61	7.238
Sway velocity (Steady State), v_{ss}/V_0	0.138	0.130	5.97	0.128	0.132	-3.28	0.099
Yaw velocity (Steady state), $r_{ss}L/V_0$	-0.381	-0.390	-2.27	-0.335	-0.341	-1.70	-0.245
Drift angle (Steady state), β_{ss}	12.515	11.800	6.06	9.547	10.190	-6.31	6.388

- m is the mass
- I_X, I_Y, and I_Z are the moment inertia about the X, Y, and Z axes, respectively
- u, v and w are the surge, sway and heave velocities respectively
- p, q and r are the roll, pitch and yaw rates respectively
- $\dot{u}$, $\dot{v}$ and $\dot{r}$ are the surge, sway and yaw accelerations respectively
- X, Y, and N are the surge force, sway force, and yaw moment, respectively
- Subscripts H, PS, PP, RS, and RP are the surge force on the hull, starboard propeller, port propeller, starboard rudder, and port rudder, respectively

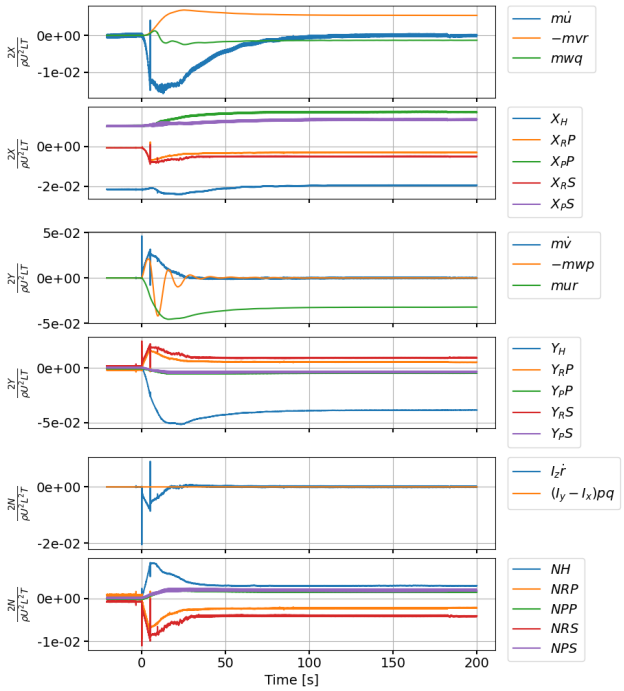
The evolution and steady-state values of the terms in the force balance equation are presented in Figure 7.

In the surge equation, as the maneuver is executed, the rudder resistance increases, leading to a higher deceleration rate with a higher rudder angle. Due to the higher deceleration, the propellers operate at a lower velocity as the rudder angle increases, resulting in higher thrust. Also, due to the ship's drift angle, the propeller and rudder forces are asymmetric, with higher thrust from the port propeller (windward propeller) owing to its direct exposure to the cross-flow and its inward rotation. The lower surge velocity also leads to a lower hull resistance in the Surge direction with an increase in the rudder Angle.

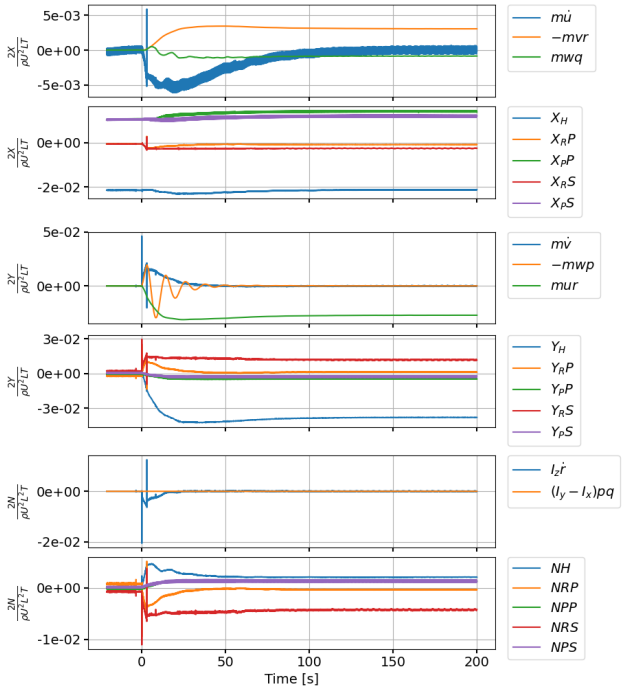
For the sway equation, as the ship drift angle increases, the acceleration-related inertial terms initially increase due to the rudder force and moment, and later due to the ship acting as a hydrodynamic foil. As the ship reaches steady state, they converge to zero. The mpw plays a role in the transient behavior due to the ship's roll and pitch motion, which also converge to zero. The main inertial component during the maneuver for sway force is the centrifugal term mur. The centrifugal term is mainly countered by the hull sway force, which shows a higher peak during the transient phase but shows similar results at steady state for 35° and 25° cases and a slightly lower value for 15°, mainly due to the trends of yaw rate and surge & sway velocity with the rudder angle. The rudder sway force plays a significant role in the maneuver, with a magnitude of an individual rudder around $1/3^{rd}$ of the hull force. The rudder opposes the hull force and exhibits pronounced asymmetry as the rudder angle decreases. At 15°, the windward port rudder force is negligible



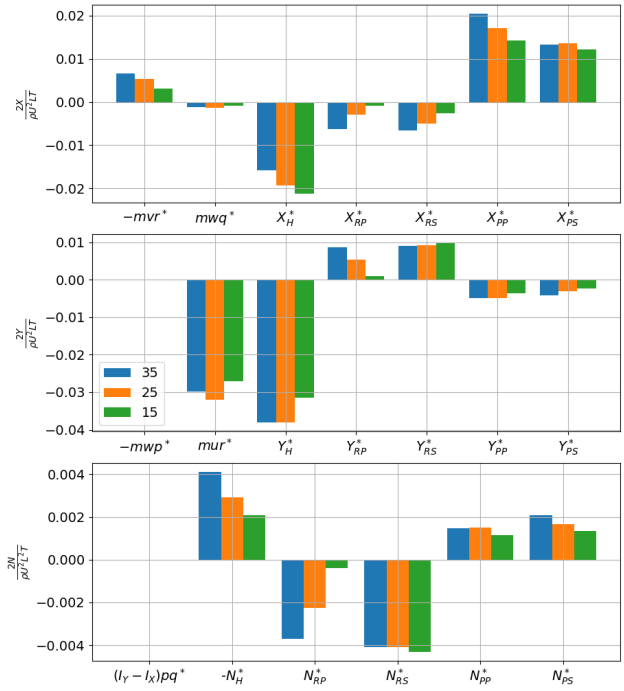
(a) TC 35° starboard



(b) TC 25° starboard

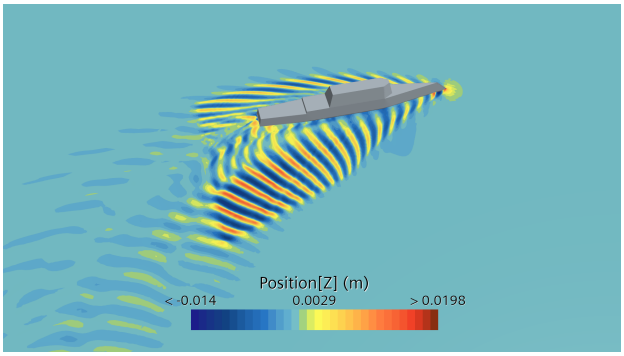


(c) TC 15° starboard

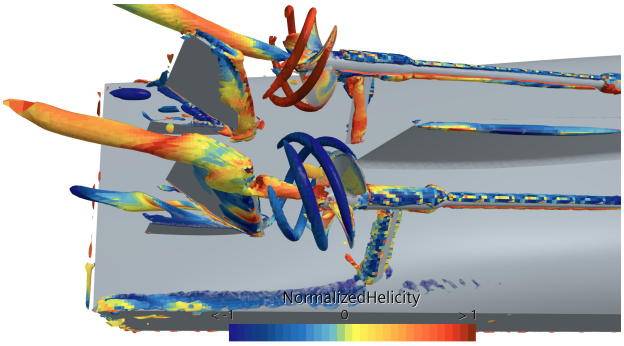


(d) Steady-state results

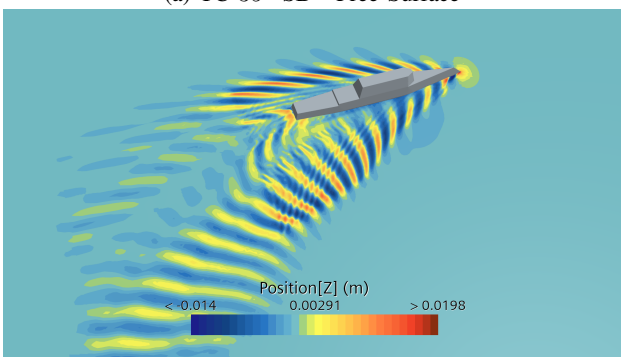
Figure. 7: Force Balance during turning circle maneuver



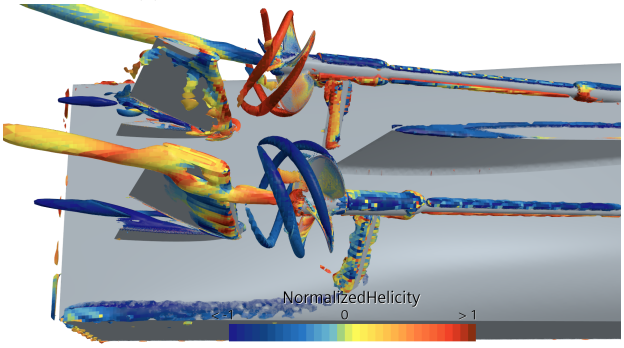
(a) TC 35° SB - Free Surface



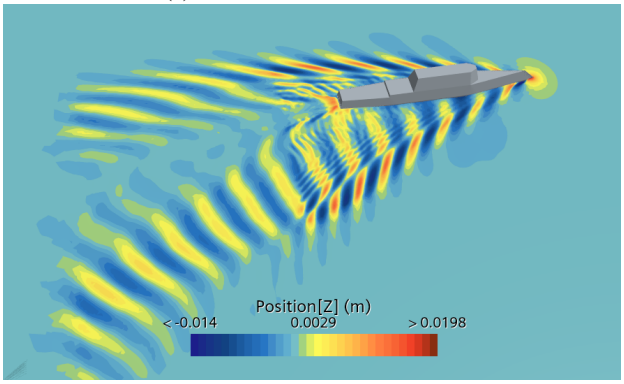
(b) TC 35° SB - Vortical Structures



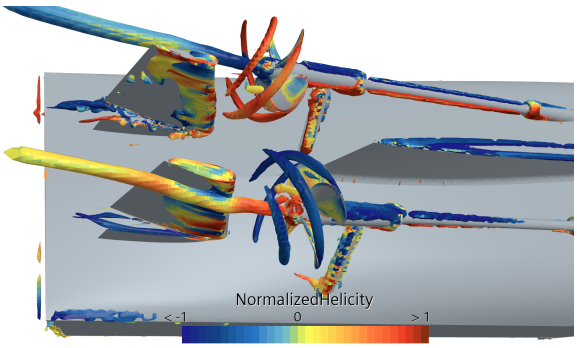
(c) TC 25° SB - Free Surface



(d) TC 25° SB - Vortical Structures



(e) TC 15° SB - Free Surface



(f) TC 15° SB - Vortical Structures

Figure. 8: Steady state vortical structures and free-surface

at steady state. The propeller sway forces, which act against the centrifugal force, play a minimal role in the sway equation and show limited sensitivity to rudder angle.

The hydrodynamic external-moment terms dominate the yaw-moment equation. During the transient phase, the yaw acceleration term increases and later converges to zero in the steady-state phase. The rudder moment is countered by the hull and propeller moments. As with the sway equation, the windward rudder force is negligible at steady state. The propeller moments are not negligible, mainly due to the ship's drift angle, the moment lever from the propellers' position, and the rudder's slow, limited sensitivity to the rudder angle.

Finally, the free-surface and vortical structures at steady state for the three maneuvers are shown in Figure 8. The vortical structures at different angles, presented using the Q-criterion plot and colored by the normalized helicity, show the interaction of the hub vortex with the rudder during the stalling of the port rudder at 35° and 25°.

VI. Conclusion

The steady turning maneuver for the ONRT hull, with a twin-rudder, twin-bilge-keels, and twin propellers, is studied at three different rudder angles for an approach velocity corresponding to $F_N = 0.200$ using the StarCCM+ CFD software.

Validation of the numerical results against the experiments from Aram and Mucha [1] using ITTC turning circle parameters shows good agreement, with deviations below 10%. The transient result comparisons also show that both CFD and EFD follow similar trends, with a slightly tighter maneuver

execution in experiments owing to lower surge and sway velocities and a higher yaw rate compared to CFD. The variations are mainly attributed to port rudder stalling at 35° and 25° in the starboard-turning-circle cases, and to the inability of RANS solvers to predict flow separation accurately under such conditions.

Comparisons between the cases show that an increase in rudder angle results in a tighter maneuver executed in a shorter time, owing to an increase in yaw rate and sway velocity, a decrease in surge velocity, and a consequent higher drift angle. A detailed investigation of the terms of the 3-DoF body motion equation is presented to quantify the contributions of the hull, propellers, and rudders. The evolution of the forces and moments for each term, as well as the impact of the rudder angle, is presented. The effect of rudder angle on forces and moment from the rudder is significant, while the effect on the propellers is minimal. The rudder angles cause pronounced asymmetric behavior between the windward and leeward rudders from equal contribution at 35° to negligible contribution from the windward rudder for sway force and yaw moment at 15°.

Future work includes providing a comprehensive overview of the accuracy of other propeller models in the literature against fully discretized rotating propellers and experiments in steady turning maneuvers at different rudder angles.

ACKNOWLEDGEMENT

This research was undertaken thanks in part to funding from the Canada First Research Excellence Fund (CFREF-2022-00062).

REFERENCES

[1] Aram, Shawn and Mucha, Philipp. "Computational fluid dynamics analysis of different propeller models for a ship maneuvering in calm water." *Ocean Engineering* Vol. 276 (2023): p. 114226.

[2] Menter, Florian R, Kuntz, Martin, Langtry, Robin et al. "Ten years of industrial experience with the SST turbulence model." *Turbulence, heat and mass transfer* Vol. 4 No. 1 (2003): pp. 625–632.

[3] Jin, Shanqin, Peng, Heather, Qiu, Wei, Oldfield, Chad and Stockdill, Barton. "Best modeling practice for self-propulsion simulation of ship model in calm water." *Physics of Fluids* Vol. 35 No. 10 (2023).

[4] Procedures, ITTC Recommended. "Guideline on Use of RANS Tools for Manoeuvring Prediction." *Proceedings of 26rd ITTC* (2011).

[5] Abkowitz, Martin A. "Measurement of hydrodynamic characteristics from ship maneuvering trials by system identification." Technical report no. 1980.

[6] Yasukawa, Hironori and Yoshimura, Yasuo. "Introduction of MMG standard method for ship maneuvering predictions." *Journal of marine science and technology* Vol. 20 No. 1 (2015): pp. 37–52.

[7] Carrica, Pablo M, Ismail, Farzad, Hyman, Mark, Bhushan, Shanti and Stern, Frederick. "Turn and zigzag maneuvers of a surface combatant using a URANS approach with dynamic overset grids." *Journal of Marine Science and technology* Vol. 18 No. 2 (2013): pp. 166–181.

[8] Carrica, Pablo M, Mofidi, Alireza, Eloot, Katrien and Delefortrie, Guillaume. "Direct simulation and experimental study of zigzag maneuver of KCS in shallow water." *Ocean engineering* Vol. 112 (2016): pp. 117–133.

[9] Christian Milano, Yugo Sanada Zhaoyuan Wang Hironori Ya-sukawa, Deniz Ozturk and Stern1, Frederick. "Free-Running CFD for KRISO Container Ship Transient Maneuvers." *Proceedings of the 13th International Workshop on Ship and Marine Hydrodynamics*. Fukuoka, Japan, August 25–28, 2025.

[10] Nath, Adwaith, Peng, Heather and Qiu, Wei. "Numerical analysis and validation of turning circle and zig-zag maneuvers of KRISO container ship in calm sea using body force method." (2025).

[11] Stern, F, Kim, HT, Patel, VC and Chen, HC. "A viscous-flow approach to the computation of propeller-hull interaction." *Journal of Ship Research* Vol. 32 No. 04 (1988): pp. 246–262.

Numerical Analysis of a Hydrofoil Performance in Waves Compared to Calm Water

Nils Lundqvist[1], Alex Shiri[1], Arash Eslamdoost[1]

[1]Department of Mechanical Engineering, Chalmers University of Technology, Gothenburg, Sweden

nils.lundqvist@chalmers.se

Keywords: hydrofoil hydrodynamics, RANS-VOF, free-surface effects, towing tank

1 Introduction

Hydrofoil development dates back to the early 20th century, with peak activity from the 1950s to the 1980s. Originating in military applications, the technology later transferred to fast ferries, providing a means to achieve higher speeds and improved ride comfort. Despite the enthusiasm and innovation surrounding foiling vessels in its golden age, safety concerns and maintenance challenges, coupled with technological limitations, particularly regarding control strategies, progressively led the foiling crafts to lose ground. It is mostly at the beginning of the 2000s that high-performance sailing revived interest in hydrofoils. New manufacturing advances, including lighter composite materials and increased computational power, enabled a new leap forward and renewed momentum.

Nomenclature

Symbol	Definition	Description
U	–	Foil velocity
c	–	Reference chord
h	–	Submergence
α	–	Angle of attack
H, a	$a = H/2$	Wave height/amplitude
λ	–	Wavelength
T	–	Wave period
k_w	$2\pi/\lambda$	Wave number
ω	$2\pi/T$	Wave frequency
T_e	–	Encounter period
ω_e	$2\pi/T_e$	Encounter frequency
c_g	–	Group velocity
Re	$\rho U c/\mu$	Reynolds number
k_r	$\omega_e c/(2U)$	Reduced frequency
ka	$k_w H/2$	Wave steepness
u_w, w_w	–	Orbital velocities
α_{eff}	$\alpha + \tan^{-1}\frac{w_w}{U+u_w}$	Effective AoA

Early foiling vessel development identified collisions with floating objects, hydrofoil structural failure, and, most importantly, loss of stability in flight and the risk of subsequent crashes. Various solutions were invented to provide sufficient stability in the operating envelope, relying on foil shapes designed for self-stabilized flight control.

Advances in computational power have enabled onboard control systems that require multiple sensors, actuators, and near real-time adaptation to external disturbances. However, controller tuning is necessary and can be improved by understanding the correlation between waves and hydrodynamic load behavior under various conditions, enabling the vessel to be stabilized through actuator control. Studies led by (Lau et al. 2024) and Sun et al. 2023 have investigated implementing a hydrofoil to stabilize vessels through active control. Researchers have also addressed hydrofoils in the context of free-surface interactions by developing flapping hydrofoils that imitate whale propulsion, such as presented by Abgrall et al. 2026. Further work coupling data-driven tools to the modeling and control of hydrofoils operating in waves was initiated in the research projects by Tavakoli, Roohi, and Namaghi 2024 and Godø et al. 2024. However, despite numerous works on free-surface interactions in calm water (Perali et al. 2024; Pernod et al. 2023), few have addressed wave interactions.

2 Methods and setup

The flow physics is simulated using the commercial CFD RANS solver STAR-CCM+ 25.06, implementing k-ω - SST (Menter 1994) coupled with γ-transition model, keeping $y+ < 1$. A second-order implicit unsteady time discretization is imposed. The free surface is modeled using the HRIC Volume of Fluid (VOF) method (Hirt and Nichols 1981), generating regular fifth-order Stokes head waves in wave conditions, and the Flat VOF Wave model is implemented for calm-water cases. The motion of the hydrofoil is obtained through a Moving Reference Frame where the whole domain is translated at the carriage velocity. A time step $\Delta t = 0.0015s$ is used to ensure a fine enough time discretization per wave period as well as keeping $CFL < 1$ in the free surface refinement region. The space discretization is set up so the mesh comprises 100 cells per wavelength in the longitudinal direction and 20 cells in the vertical direction for the smallest simulated wavelength. Submergence (h=400mm; h/c =2.09) and angle of attack ($\alpha = 4°$) are kept constant, and wave parameters are varied as reported in Table 1. Velocity is kept constant to U=4m/s throughout the test matrix, corresponding to a Reynold's number $Rn = 7.61e5$

Table 1: Test conditions for the head-wave cases. Angle of attack $\alpha = 4°$, submergence depth $h = 0.400$ m.

Run	U	T	H	λ	k_w	c_g	T_e	k_r	α
–	$(\mathrm{m\,s^{-1}})$	(s)	(m)	(m)	$(\mathrm{rad\,m^{-1}})$	$(\mathrm{m\,s^{-1}})$	(s)	–	(deg)
1	4.00	1.012	0.06	1.6	3.927	0.791	0.287	0.523	4
2	4.00	1.132	0.06	2.0	3.142	0.707	0.296	0.507	4
3	4.00	1.386	0.06	3.0	2.094	0.577	0.310	0.484	4
4	4.00	1.601	0.06	4.0	1.571	0.500	0.320	0.469	4

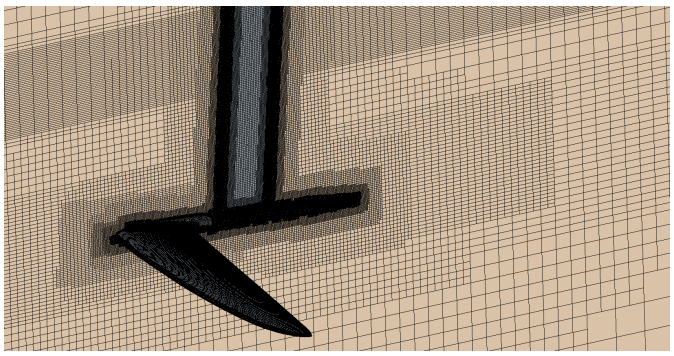
The computational mesh is generated using the surface remesher, trimmed-cell mesher, and prism-layer mesher. The near-wall region consists of 30 prism layers that fully resolve the boundary layer, with prism-layer thickness following a geometric progression with an expansion factor of 1.2. Volumetric refinements are applied in the near-free-surface region, near the hydrofoil and its wake, and around the tip vortices, resulting in a mesh comprised of around 19M cells. Table 2 summarizes the boundary conditions, and Figure 1a shows the mesh.

Table 2: Boundary conditions of the computational domain.

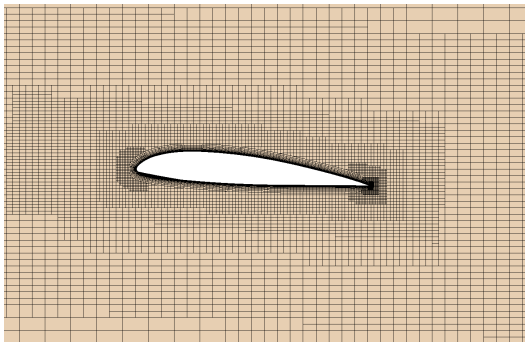
Boundary	**Condition**
Hydrofoil surface	No-slip wall
Centre plane	Symmetry
Lateral boundary	Symmetry
Bottom boundary	Symmetry
Top boundary	Pressure outlet
Upstream boundary	Velocity inlet
Downstream boundary	Velocity inlet

Table 3: Computational domain and operating conditions.

Parameter	**Symbol**	**Value**
Upstream extent	L_{up}	6 m (31.4c)
Downstream extent	L_{down}	16 m (83.8c)
Lateral extent	L_y	7 m (36.6c)
Water depth	d	2.5 m
Air-region height	H_{air}	1.5 m
Reference chord	c	0.191 m
Hydrofoil span	b	1.256 m



(a) Computational mesh - perspective view



(b) Cross-section of the wing

3 Results and discussion

Airy's linear wave theory provides a framework for describing regular-wave disturbances under the assumptions of incompressible, irrotational flow and small wave steepness ($ka \ll 1$). Wave-induced orbital velocities modify the local flow encountered by the hydrofoil, producing variations in effective angle of attack α_{eff} and hydrodynamic loads at the encounter frequency ω_e. The following analysis compares these load variations with calm-water conditions across different wavelengths and examines their phase relationships with the wave kinematics, before investigating the contributions of pressure and friction drag.

3.1 Comparison between Calm water and Wave cases

Table 4 gathers results from CFD simulations carried out in calm water and in regular head waves. Effects of the wave-induced disturbances translate in the oscillations of the hydrodynamic loads around mean values that are close to the calm water ones. Numerical results from simulated cases (Fig.2) show that the variation in mean dynamic loads compared to calm water remains under 1%. This result suggests that the induced signals are periodic and that the minor discrepancies are due to numerical error or moderate unsteady effects.

As mentioned, orbital velocity from the wave-induced motion causes the perceived angle of attack by the wing to vary and contributes to load oscillations. Figure 4 shows the signals amplitude as a function of wavelength. The theoretical effective angle of attack is estimated from the local wave-induced velocity as:

$$\alpha_{\text{eff}} = \alpha + \tan^{-1}\left(\frac{w_w}{U + u_w}\right), \tag{1}$$

$$u_w = a\omega e^{-kh}\cos\theta, \tag{2}$$

$$w_w = a\omega e^{-kh}\sin\theta. \tag{3}$$

where u_w (Eq.2) and w_w (Eq.3) are respectively the horizontal and vertical orbital velocity components, θ the wave phase angle, ω wave angular frequency, h the submergence, and k the wave number. The effective angle of attack α_{eff} values shown in the following study were computed considering the wave elevation at the origin placed at the mid-chord. This choice is motivated by the tapered geometry of the wing, making the leading position vary.

Figure 3, presents wave elevation, load, and α_{eff} time series over three different wave periods T. The wave elevation curves show the free-surface elevation relative to the undisturbed free surface, extracted at the hydrofoil mid-chord. A phase shift between the instantaneous lift, drag, and effective angle of attack is observed relative to the wave elevation across the studied wave

periods. However, the loads and the wave elevation present a phase difference. Table 4 summarizes the hydrodynamic load results as well as amplitudes of oscillating variations compared to the loads' time-averaged values.

It can be observed that the load oscillation amplitudes $A_F/\overline{F}$ increase as the wavelength λ increases. This observation is consistent with Airy's wave theory, which states that wave disturbances decay less for longer wavelengths; consequently, the effects of waves are felt with higher intensity at constant submergence.

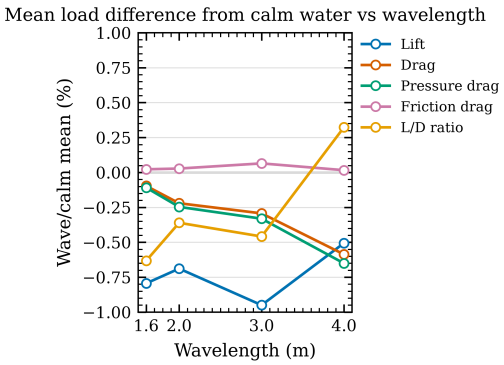


Figure 2: Wave time-averaged load variation compared to calm water

Analysis of Figure 4 shows a strong correlation between hydrodynamic load variations and effective angle of attack oscillation amplitude. With the exception of friction drag, which undergoes the smallest deviation from the mean value, the amplitude of the other loads double from the short- to the long-wavelength case. The proximity of the pressure and total drag curves indicates that pressure-drag variations contribute more than friction-drag variations. Additionally, the shared trend between lift and drag suggests that most drag variations arise from induced drag due to oscillating lift forces.

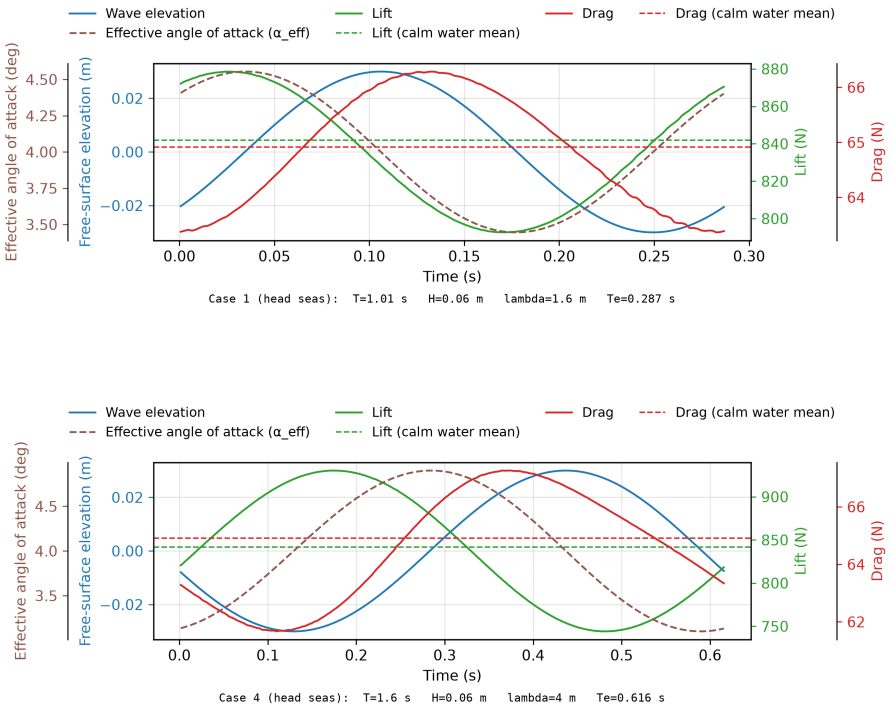


Figure 3: Time histories of lift, drag, and wave elevation for head-wave cases 1-4.

Table 4: Mean hydrodynamic loads and oscillation amplitudes for the head-wave cases. Changes in mean values are relative to the corresponding calm-water reference.

Case	Wave condition		Lift		Drag		Pressure drag		Friction drag		L/D
	λ (m)	f_e (Hz)	$\overline{L}$ (N)	$A_L/\overline{L}$ (%)	$\overline{D}$ (N)	$A_D/\overline{D}$ (%)	$\overline{D_p}$ (N)	$A_{D_p}/\overline{D_p}$ (%)	$\overline{D_f}$ (N)	$A_{D_f}/\overline{D_f}$ (%)	$A_{L/D}/\overline{L/D}$ (%)
1	1.60	3.484	835.22	5.15	64.85	2.25	–	2.39	–	1.77	6.98
2	2.00	3.378	833.28	6.99	64.87	2.91	–	3.10	–	2.08	9.25
3	3.00	3.226	834.65	9.88	64.70	3.91	–	4.17	–	2.56	12.76
4	4.00	3.125	837.58	11.13	64.54	4.34	–	4.65	–	2.73	14.30
			$\overline{L}$		$\overline{D}$		$\overline{D_p}$		$\overline{D_f}$		L/D
Calm	–	–	841.88	–	64.91	–	58.68	–	6.23	–	12.97

Although Figure 4 shows common trends in varying oscillation amplitudes between loads and α_{eff}, Figure 3 and Figure 5 has evidenced varying lag differences between loads and effective angle of attack α_{eff}, suggesting lad variations to be dependent on wave characteristics or encounter frequency. From Figure 5, it can be seen that variation in angle of attack is 90° ahead wave propagation. Furthermore, hydrodynamic loads show fixed lags across all wavelengths tested: lift responds first to wave perturbations, followed by friction drag (≈70° after lift) and finally total and pressure drag (≈130° after lift).

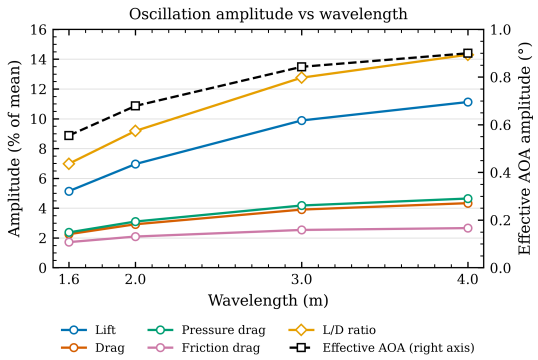


Figure 4: Load oscillation amplitude as a function of wavelength λ

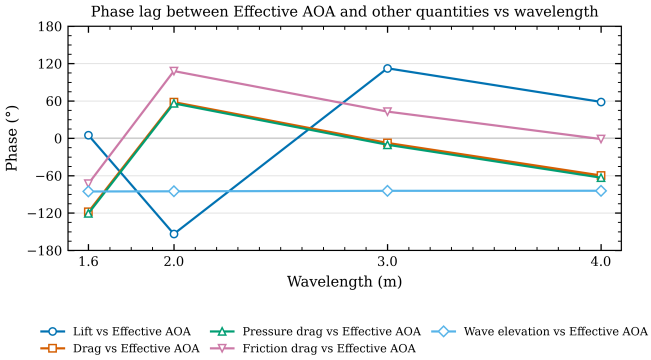


Figure 5: Phase difference evolution as a function of wavelength λ.

Drag components in Table 5 further confirm the large contribution of pressure drag to total drag suggested by Figure 4. 90% ($\overline{D_p}/\overline{D}$) of the total drag is due to pressure drag, with variations $A_{D_p}/\overline{D_p}$ around the mean value ranging from 2.39% (Case 1) to 5.64% (Case 4) compared to the more modest oscillations of friction drag $A_{D_f}/\overline{D_f}$ evolving between 1.77% (Case 1) and 2.73% (Case 4). Consequently, pressure drag contributes to a large extent to total drag variations as further illustrated in Figure 6. Furthermore, friction drag exhibits a moderate phase shift of $\Delta\phi_{D_f \to D} = 7°$ from Case 1 to Case 4, increasing with wavelength as shown in Table 5.

Table 5: Pressure and friction drag: share of total drag, oscillation amplitude, and phase difference relative to total drag, by wavelength.

Case	λ (m)	Pressure drag $\overline{D_p}$ (N)	$\overline{D_p}/\overline{D}$ (%)	$A_{D_p}/\overline{D_p}$ (%)	$\phi_{D_p \to D}$ (°)	Friction drag $\overline{D_f}$ (N)	$\overline{D_f}/\overline{D}$ (%)	$A_{D_f}/\overline{D_f}$ (%)	$\phi_{D_f \to D}$ (°)
1	1.60	58.62	90.39	2.39	0.0	6.23	9.61	1.77	45.2
2	2.00	58.63	90.38	3.10	−2.1	6.24	9.62	2.08	49.8
3	3.00	58.46	90.36	4.17	0.0	6.24	9.64	2.56	53.3
4	4.00	58.30	90.34	4.65	−2.3	6.23	9.66	2.73	52.6

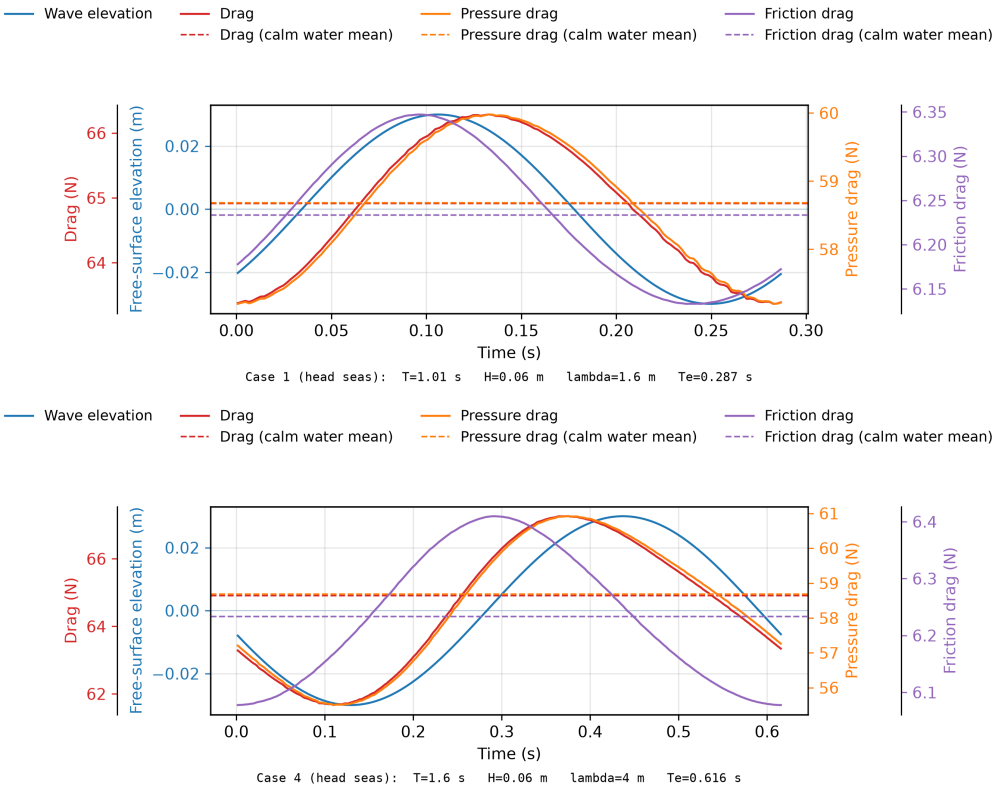


Figure 6: Time histories of friction drag, pressure drag, total drag and wave elevation for head-wave cases 1-4.

4 Conclusion and future work

This study shows that wave-induced hydrodynamic loads oscillate periodically at the encounter frequency around a mean value near the calm-water time-averaged load. Investigating phase differences and load oscillation amplitudes shows that perceived angle of attack is a main driver of load oscillation and that oscillation amplitudes correlate with the amplitudes of angle-of-attack variations. However, lag differences between load evolution and velocity-field variations highlight other potential mechanisms that influence load responses to wave disturbances.

Furthermore, the close coherence between lift and drag is attributed to induced pressure drag contributing more to total drag, with friction drag having only a minor effect on the overall oscillation amplitudes. A varying phase lag between pressure and friction drag has been observed and is attributed to viscous effects from perturbations in boundary-layer development.

This study is the preamble to a larger study where experimental data will be compared to RANS numerical solutions. Future work will extend the study to cases in the following wave conditions over a broader range of test conditions. A comparison will be made between fully turbulent modeling and results obtained with γ-transition model with the aim of understanding potential contribution from laminar separation to the hydrodynamic load variations.

References

Abgrall, M., P. Perali, M. Sacher, B. Clément, J.-B. Leroux, K. Gokpi, and R. Lécuyer-Le-Bris (2026). "Experimental and Numerical Study of an Oscillating Foil Near the Free Surface". In: DOI: https://doi.org/10.5957/jst/2025.10.1.407.

Godø, J. M. K., S. Steen, D. Barrett, and M. S. Triantafyllou (2024). "Active wave energy extraction by hydrofoil vessels through deep reinforcement learning-based flight control". In: *Ocean Engineering* 312, p. 119236. DOI: 10.1016/j.oceaneng.2024.119236.

Hirt, C. and B. Nichols (1981). "Volume of fluid (VOF) method for the dynamics of free boundaries". In: *Journal of Computational Physics* 39.1, pp. 201–225. DOI: 10.1016/0021-9991(81)90145-5.

Lau, C.-Y., J. Ali-Lavroff, A. Dashtimanesh, D. S. Holloway, and J. A. Mehr (Apr. 2024). "High-speed catamaran response with ride control system in regular waves by Forcing Function Method in CFD". In: *Ocean Engineering* 297, p. 117111. DOI: 10.1016/j.oceaneng.2024.117111.

Menter, F. R. (Aug. 1994). "Two-equation eddy-viscosity turbulence models for engineering applications". In: *AIAA Journal* 32.8, pp. 1598–1605. DOI: 10.2514/3.12149.

Perali, P., M. Sacher, J.-B. Leroux, J. Wackers, B. Augier, F. Hauville, and P. Bot (Oct. 2024). "Performance prediction of a hydrofoil near the free surface using low (BEM) and high (RANS) fidelity methods". In: *Applied Ocean Research* 151, p. 104157. DOI: 10.1016/j.apor.2024.104157.

Pernod, L., M. Sacher, J. Wackers, and B. Augier (2023). "Free-Surface Effects on Two-Dimensional Hydrofoils by RANS-VOF Simulations". In.

Sun, Y., D. Zhang, Y. Wang, Z. Zong, and Z. Wu (Aug. 4, 2023). "Model Experimental Study on a T-Foil Control Method with Anti-Vertical Motion Optimization of the Mono Hull". In: *JMSE* 11.8, p. 1551. DOI: 10.3390/jmse11081551.

Tavakoli, A., E. Roohi, and M. S. Namaghi (Feb. 1, 2024). "Numerical Simulation of Free Surface Water Waves Around Wavy Hydrofoils: Prediction of Hydrodynamic Coefficients Using Machine Learning". In: *Journal of Fluids Engineering* 146.2, p. 021501. DOI: 10.1115/1.4063078.

28TH NUMERICAL TOWING TANK SYMPOSIUM (NUTTS)
MÜLHEIM, GERMANY, OCTOBER 19-21, 2026

CFD MODELING OF SURF-RIDING AND BROACHING DYNAMIC INSTABILITIES FOR THE ONRT VESSEL SUBJECT TO STERN-QUARTERING WAVE CONDITIONS

Etienne Fichers (Cadence Design Systems, Belgium)
Benoit Mallol (Cadence Design Systems, France)
efichers@cadence.com

1. INTRODUCTION

Surf-riding and broaching are among the most complex dynamic failure modes to model, as they lie at the intersection of several strongly nonlinear, coupled, and threshold-driven phenomena. As a result, the accurate prediction of these dynamic instabilities relies on models that allow for strong coupling between multiple physics, such as stability, resistance, propulsion, maneuverability, and seakeeping. Within this framework, numerical simulations emerge as one of the few tools suitable for detailed assessment of course stability loss.

This paper presents the seakeeping simulations performed on the model-scale ONRT vessel in the framework of the NuTTS 2026 conference, with the objective of assessing a CFD-based approach using an actuator-disk propulsion model for the prediction of surf-riding and broaching instabilities. The simulation parameters are defined to reproduce the experimental campaign conducted by *Chu et al.* on the ONRT vessel in stern-quartering waves and reported in reference [3]. The predictive capability of the methodology is evaluated through direct comparison with the published experimental data. Validation metrics include the vessel motions (roll, pitch, yaw), rudder angle, and surge speed.

The simulations are carried out with the Fine Marine flow solver, from the Cadence Fidelity suite, using an Unsteady Reynolds-Averaged Navier–Stokes (URANS) approach. The methodology leverages an overset-grid approach to accommodate large body motions, while wave generation is based on a Fourier Series Decomposition (FSD) technique allowing for an accurate representation of waves over a wide range of steepness values.

Recognizing the sensitivity of surf-riding and broaching predictions to the vessel characteristics and operating conditions, a step-by-step calibration procedure was adopted prior to the free-running simulations. The approach consists of: (1) calibrating the metacentric height through a Virtual Incline Test (VIT); (2) validating the roll inertia through roll-decay simulations; (3) determining the propulsion settings from calm-water resistance computations; and finally, (4) performing free-running seakeeping simulations for the assessment of surf-riding and broaching dynamic instabilities.

The paper is organized as follows. Section 2 provides the case description. Section 3 introduces the experimental campaign. Sections 4, 5 and 6 document the preliminary analyses performed to characterize the vessel's static and dynamic stability, as well as its propulsion conditions. Sections 7 and 8 detail the mesh setup and numerical setup, respectively. Section 9 discusses the simulation results. Finally, section 10 summarizes the main conclusions.

2. CASE DESCRIPTION

The dynamic stability of the ONRT vessel with respect to surf-riding and broaching is assessed through a set of four free-running seakeeping simulations in stern-quartering waves. The simulations are performed at a constant propeller revolution rate, which is progressively increased up to the onset of the instabilities. Considering the very large computational cost of a sliding-grid propeller model for such applications, the present work evaluates the applicability of an actuator-disk approach as a computationally efficient alternative.

As illustrated in Figure 1, the ONR Tumblehome (ONRT) is a preliminary design of a modern surface combatant, which is publicly accessible for fundamental research. The model has a wave-piercing hull design with 10 degrees tumblehome sides and a transom stern. The ship is appended with skeg and bilge keels, spade rudders, shafts and propeller shaft brackets.

The CAD model used in the present analysis corresponds to the scaled ONRT geometry provided for the Wageningen 2025 workshop [5]. The origin of the coordinate system is located at the aft perpendicular, and has its longitudinal axis aligned with the still waterline.

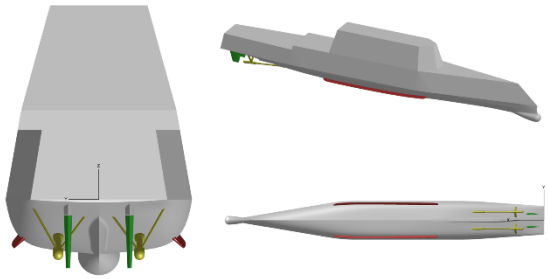


Figure 1 - ONRT geometry and axis system.

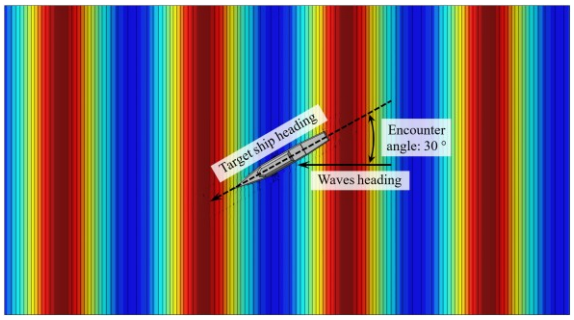


Figure 2 - Wave conditions.

3. EXPERIMENTS

The validation data used in the present work are taken from the experimental campaign conducted by *Chu et al.* and reported in reference [3]. The experiments consist of free-running model tests of the ONRT vessel in stern-quartering waves, with the ship propelled at a prescribed revolution rate and the rudders controlled by an autopilot to maintain the target heading. The test campaign was carried out in the large seakeeping and maneuvering basin of the China Ship Scientific Research Center (CSSRC).

The generated waves have an intermediate steepness of H_w/λ_w=0.05, a wavelength-to-ship-length ratio of λ_w/LWL=1.25 and a wave encounter angle of 30° relative to the target ship heading, as illustrated in Figure 2.

The principal particulars of the model are summarized in Table 1. The inertia, stability, and dynamic parameters reported by *Chu et al.* [3] are reproduced in Table 2 for reference.

Parameter	Value
Length of waterline, LWL [m]	3.8
Breadth, B [m]	0.464
Draft, T [m]	0.136
Displacement, Δ [kg]	128.0
Propeller Diameter, D_P [m]	0.129
Scale factor [-]	1/ 40.526

Table 1 - Geometry particulars.

Parameter	Value
Roll radius of gyration, k_{xx} [m]	0.44 B
Pitch radius of gyration, k_{yy} [m]	0.25 LWL
Yaw radius of gyration, k_{zz} [m]	*not reported*
Metacentric height, GM [m]	0.051
Natural roll period, T_n [s]	1.75

Table 2 – Inertia, stability and dynamic parameters.

The experimental acquisition system recorded multiple quantities including roll, pitch, and yaw motions, rudder angle, propeller revolution rate, wave elevation, and vessel speed. Only a subset of these measurements is reported in the reference paper.

4. METACENTRIC HEIGHT CALIBRATION

Metacentric height is a critical parameter when modeling the dynamic behavior of a vessel in waves. Through its influence on the roll restoring moment, it strongly affects the natural roll period and the roll response, which plays a key role in the onset and development of the surf-riding and broaching instabilities. For this reason, accurate calibration of the metacentric height appears essential for obtaining reliable simulation results.

The realized GM in a CFD simulation is grid dependent [4]. Consequently, defining the vertical center of gravity through the relationship GM = KM – KG does not automatically guarantee that the target metacentric height is achieved on every computational grid.

In the present work, the metacentric height is calibrated using the Virtual Incline Test (VIT) procedure proposed by *Sanada et al.* [6] and adopted during the Wageningen 2025 workshop [5]. The procedure consists of imposing a prescribed transverse shift to the center of gravity $(Y_{CG}/LWL) = 0.000344036$ and performing a calm-water

hydrostatic computation to determine the equilibrium heel angle φ. The corresponding metacentric height is then computed from $GM = Y_{CG}/\tan(\varphi)$.

By repeating the procedure for several values of the vertical center of gravity, the relationship between GM and Z_{CG} is established. Finally, this relationship is used to compute the Z_{CG} position that allows the target metacentric height to be achieved on the computational grid.

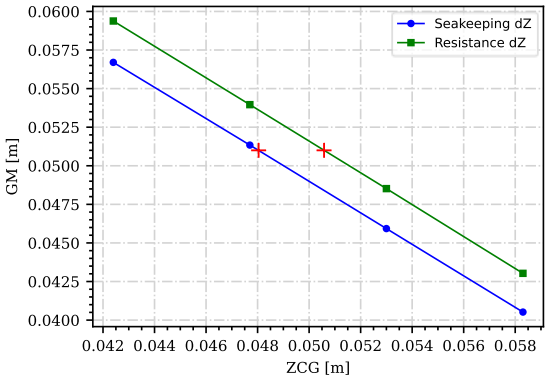


Figure 3 - Virtual incline test results.

Figure 3 shows the results of the VIT procedure for two different free-surface discretizations. The blue curve corresponds to the discretization adopted for the seakeeping and roll-decay simulations. For the target value of GM = 0.051 m, a value of Z_{CG} = 0.04804 m is required, corresponding to a deviation of -9.4% from the design value. This difference is attributed to the coarser free-surface refinement used in the seakeeping setup. The green curve corresponds to the discretization used for the resistance simulations. In this case, the target metacentric height is achieved for Z_{CG} = 0.05058 m, corresponding to a smaller deviation of -4.6%. These results demonstrate the strong sensitivity of the realized metacentric height to the free-surface discretization and justify the need for a grid-specific calibration of Z_{CG}.

5. ROLL DECAY CHARACTERIZATION

As an additional preliminary investigation, a roll-decay simulation is performed to validate the roll behavior of the vessel. The validation is, however, limited to a comparison of the CFD natural roll period with the experimental value T_n = 1.75 s, as no information regarding the roll damping characteristics is provided in reference [3].

The roll-decay simulation is performed in calm-water conditions, at zero forward speed, and for two initial heel angles: φ_0 = 5° and 10°. The numerical setup implements an unsteady time configuration, together with a 6-DoF body-motion resolution based on an overset grid approach. The mesh size equals 10.1 M cells. The geometrical model corresponds to the configuration without propellers shown in Figure 1.

Following a sensitivity analysis, a wall-function approach is retained, as a full resolution of the boundary layer was found to have a negligible influence on the predicted natural roll period (less than 0.5%) for the present case. The k - ω SST (Menter, 2003) turbulence model is used, and the time step is set to dT = T_n /200 s. Unless otherwise specified, all hydrostatic and inertia parameters are prescribed according to the experimental conditions reported in reference [3].

The free surface is discretized using the adaptive grid refinement procedure, resulting in an actual cell size of dZ = 0.012 m at the free surface, matching the seakeeping setup. Based on the conclusions of the VIT, the Z_{CG} = 0.04804 m value is used. Two values of the roll radius of gyration are used: k_{xx} = 0.44 B and k_{xx} = 0.387 B.

As illustrated in Figure 4 and Figure 5, the same natural roll period is obtained regardless of the initial heel angle. However, when setting the roll radius of gyration to k_{xx} = 0.44 B, as reported in the experimental campaign [3], the predicted natural roll period is T_{roll} = 1.98 s, resulting in a +13.4% deviation from the experimental value. Consequently, this inertia parameter does not allow the experimental roll response to be accurately reproduced. Since yaw and roll motions are strongly coupled for the present application, the accuracy of the surf-riding and broaching predictions is expected to be affected.

By contrast, when the roll radius of gyration is adjusted to k_{xx} = 0.387 B, the predicted natural roll period becomes T_{roll} = 1.78 s, corresponding to a deviation of only +1.8% from the experimental value. Therefore, this value is adopted for all computations presented in this paper.

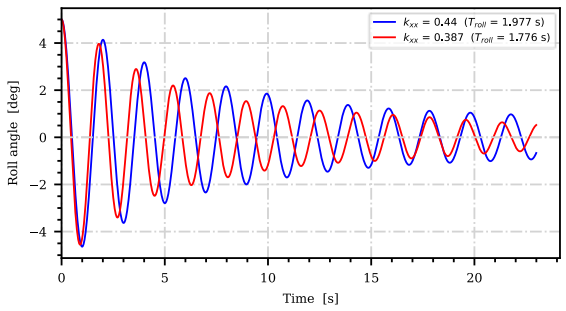


Figure 4 - Roll decay curve for $\varphi_0 = 5°$.

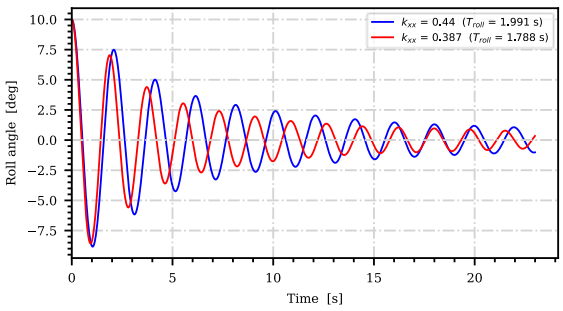


Figure 5 - Roll decay curve for $\varphi_0 = 10°$.

The incorrect specification of the ONRT roll radius of gyration to $k_{xx} = 0.44$ B in the Tokyo 2015 workshop instructions has been reported by several authors. Successive NATO research groups (AVT-280 and AVT-348) investigated the inconsistent ONRT behavior in waves and confirmed the discrepancy between the value specified in the Tokyo 2015 instructions and the actual value measured during the IIHR experiments [4]. This incorrect specification might have been reproduced in [3]. It should be noted that the roll radius of gyration depends on the ballast configuration adopted during model preparation and may therefore vary from one model to another.

6. POWERING CONDITIONS CHARACTERIZATION

The powering conditions of the seakeeping simulations are defined in terms of a nominal Froude number, corresponding to the calm-water speed achieved for a prescribed propeller rotational speed. During the seakeeping simulations, the propeller rotational speed is kept constant, while the vessel speed is allowed to vary in response to the wave-induced forces and motions. Consequently, the nominal Froude number defines the propulsion setting rather than the instantaneous vessel speed.

The resistance simulations are performed in calm-water conditions using a half-body configuration and a mesh size of 7.1 M cells including a Kelvin wake refinement. The numerical setup implements a steady time configuration with trim and sinkage resolution. Propulsion is modeled using an actuator-disk approach coupled with the open-water characteristics of the propeller obtained from reference [5]. The geometrical model corresponds to the configuration shown in Figure 1.

In addition to the four powering conditions required for the seakeeping simulations (F_n= 0.25, 0.30, 0.35 and 0.40), the simulation matrix is extended to cover additional operating conditions allowing for an extended comparison with the experimental data reported in reference [7].

Following a sensitivity analysis, a wall-function approach is retained, as a full resolution of the boundary layer was found to have a minor influence on the predicted propeller rotational speed (mean difference of -0.4%). The k - ω SST (Menter, 2003) turbulence model is used, and the time step is set to dT = LWL/(200 V_{REF}) s. Unless otherwise specified, all the parameters are prescribed according to the experimental conditions reported in reference [3].

Figure 6 displays the comparison of the computed propeller revolution rate with the experimental data obtained by the CSSRC, for the range of nominal Froude numbers. An average difference of +2.6% is observed with respect to the experiments, as detailed in Table 3.

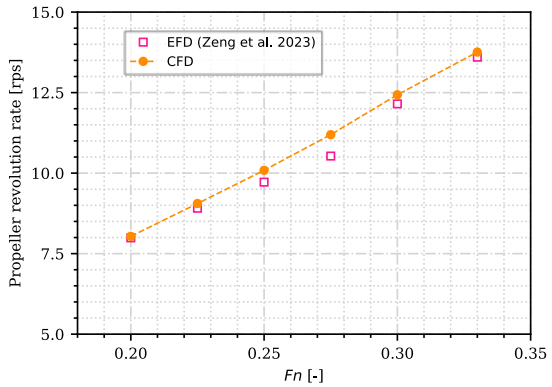


Figure 6 - Propulsion curve.

Froude [-]	EDF [rps]	CFD [rps]	Difference
0.200	7.99	8.04	0.6 %
0.225	8.91	9.06	1.6 %
0.250	9.72	10.09	3.8 %
0.275	10.53	11.19	6.3 %
0.300	12.15	12.43	2.3 %
0.330	13.6	13.76	1.2 %
0.350	-	14.65	-
0.400	-	17.56	-

Table 3 - Propeller revolution rate and comparison to experiments.

7. SEAKEEPING MESH SETUP

The seakeeping mesh setup used for the prediction of surf-riding and broaching instabilities follows a recently developed methodology applicable to all wave encounter angles and is particularly well suited to simulations in following- and quartering-wave conditions. It is composed of four domains: a vessel domain, two rudder domains, and a background domain, assembled in an overset-grid configuration, as illustrated in Figure 7. The mesh is generated with version 2025.2 of Cadence Fidelity Hexpress software, relying on the Volume-to-Surface (V2S) approach and a fully hexahedral meshing technique.

The vessel domain accounts for 8.8 M cells, while the rudders and the background domains are 0.59 M cells each, leading to a total cell count of 10.6 M cells.

7.1. Background domain meshing

The background domain is sized to ensure an appropriate propagation of the wave field and an adequate resolution of the vessel's wake. The domain has a square shape, and its dimensions are defined as ($4\lambda_w$ + LWL; $4\lambda_w$ + LWL; $6\lambda_w$) in the (x; y; z) directions respectively, with the vessel located at the domain center.

The refinement strategy adopted for the background domain is straightforward to implement and relies on a single refinement box covering the entire domain in the x/y plane and extending a distance ($H_w/2$) above and below the mean free surface. The initial cell size is set to 0.76 m, while the wave field is refined to $\lambda_w/80$ in the wave-propagation and vertical directions. In the direction perpendicular to wave propagation, the resolution is relaxed to $\lambda_w/20$. It should be noted that the adaptive grid refinement procedure will further refine this initial mesh, especially in the vertical direction at the free-surface and underneath.

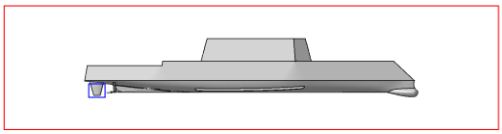


Figure 7 – Illustration of the multi-domain configuration (blue: rudder domains, red: vessel domain).

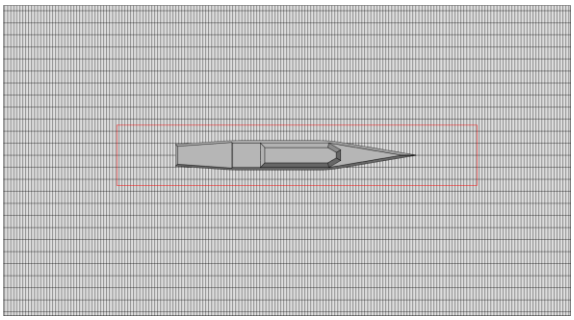


Figure 8 – Detail of the free-surface discretization in the background mesh.

7.2. Vessel and rudder domain meshing

For the vessel and the rudder domains, the initial cell size is set to 0.0475 m and 0.00297 m respectively. When setting the initial cell size for those domains, a specific focus is placed on obtaining a power-of-two ratio in cell size across the overset grid interface to optimize the interpolation of the flow solution between the different overset domains.

As an order of magnitude of the mesh refinements used, the surface mesh along the hull is set to 0.012 m and is further reduced to 0.00037 m on the bilge keels. The largest cells covering the rudder have a size of 0.0015 m. An illustration of the resulting surface mesh is provided in Figure 9.

Additional volume refinement boxes are used to ensure an adequate resolution of the actuator disk region and accurate capture of the propeller wake and its downstream interaction with the rudder.

The viscous layer mesh, illustrated in Figure 10, is generated using an inflation technique with up to 11 layers inserted along the hull surface. The first layer cell size is selected to achieve an average realized y+ around 30 at the lowest operating condition (Fn = 0.25) and an average realized y+ around 52 at the highest operating condition (Fn = 0.40). For the present wave conditions, characterized by an intermediate wave steepness, the flow physics is expected to be predominantly governed by pressure forces, making the simulation results only weakly sensitive to the near-wall viscous resolution.

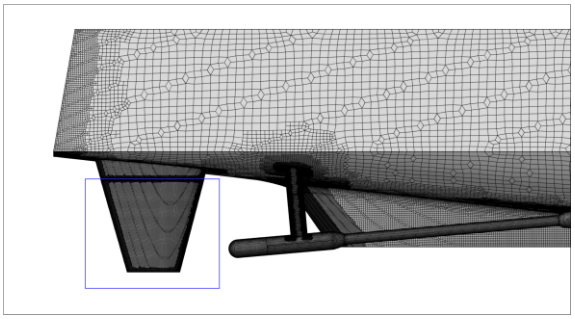


Figure 9 – Surface mesh on the vessel and rudders.

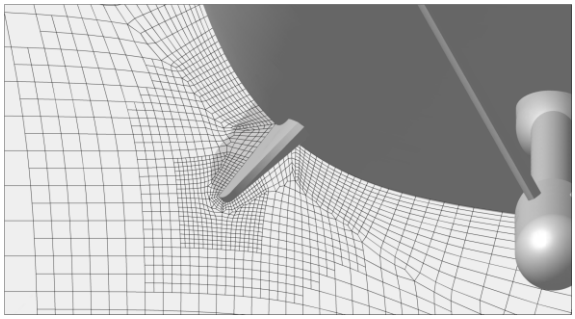


Figure 10 - Viscous layer mesh on the bilge keel and hull.

8. NUMERICAL SETUP

In Fine Marine, the numerical setup used for the prediction of surf-riding and broaching instabilities consists of two successive computations: an initialization computation during which the vessel motions are imposed to reproduce the experimental initial conditions, followed by a restart computation in which the unsteady behavior of the vessel is fully resolved. All computations are run with version 2025.3 of Fine Marine.

The following sections provide further details on the simulation setup.

8.1. Initialization computations

The objective of the initialization simulations is to reproduce the conditions prevailing in experiments [3] at the instant the vessel was released by the operator. This includes both the vessel state and the incident wave conditions.

During the initialization simulations, the wave field is established while the vessel is maintained at fixed values of surge velocity, roll, pitch and yaw angle, as well as fixed propeller rotational speed. Only the heave motion is resolved. The parameters used for the initialization simulations are summarized in Table 4.

The relative position of the vessel within the wave field at the release instant is also expected to influence the subsequent broaching behavior. However, no information regarding this parameter is provided in the reference paper. A sensitivity study was therefore conducted, and the best agreement with the experimental results was obtained when the vessel is released in the vicinity of a wave crest, as illustrated in Figure 11.

Froude	**0.25**	**0.30**	**0.35**	**0.40**
Roll [°]	2.3	0.0	0.0	0.0
Pitch [°]	3.7	5.9	6.3	6.5
Yaw [°]	209.7	207.9	218.2	210.0
Rudder angle [°]	1.7	3.4	16.4	7.8
Surge velocity [m/s]	0.358	0.358	0.358	0.358
Propeller rate [rps]	Same as for the restart phase			
Free-surface Z_{FS} [m]	-0.001 m			

Table 4 - Initialization conditions.

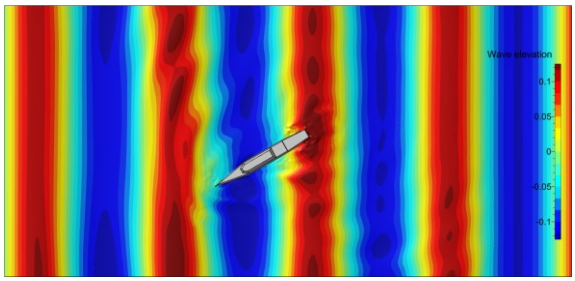


Figure 11 – Vessel release location near a wave crest.

Except for the specific settings described above, the numerical setup of the initialization simulations is identical to that of the restart simulations. The common settings are described in the following sections.

8.2. Physical conditions

The seakeeping simulations are performed using the propeller rotational speeds reported in Table 3. These rotational speeds correspond to the propulsion settings required to achieve the target nominal Froude numbers in calm-water conditions and are kept constant throughout the seakeeping simulations. Four nominal Froude numbers are investigated: Fn = 0.25, 0.30, 0.35, and 0.40.

The displacement and longitudinal center of gravity are obtained using Domhydro, the hydrostatic solver of Fine Marine, considering a draft of T = 0.135 m (i.e. Z_{FS} = -0.001 m) and the appended hull geometry without propellers, illustrated in Figure 1. The vertical position of the center of gravity is determined using the Virtual Incline Test procedure in Figure 3. The roll moment of inertia, I_{xx}, is prescribed according to the value identified from the roll-decay simulations described in section 5. The hydrostatic parameters are detailed in Table 5.

The wave conditions reproduced from the experimental campaign are reported in Table 6.

Parameter	Value
Water density [kg/m³]	999.1026
Air density [kg/m³]	1.2
Gravity intensity [m/s²]	9.81
Center of gravity [m]	(1.831; 0.0; 0.04804)
Mass [kg]	128.38
k_{xx} [m]	0.387 B
$k_{yy} = k_{zz}$ [m]	0.25 LWL

Table 5 - Hydrostatic parameters.

Parameter	Value
Wave height, H_w [m]	0.2375
Wavelength, λ_w [m]	4.75
Wave period, T_w [s]	1.72
Phase speed, c [m/s]	2.757
Wave heading, μ [°]	180 *(towards -x axis)*

Table 6 - Wave parameters.

The propulsion system is modelled using an actuator-disk approach coupled with the open-water characteristics of the model-scale propeller reported in reference [5]. This approach improves the physical fidelity of the propulsion model while retaining the computational efficiency of the actuator-disk method. The effect of propeller emergence is represented by a reduction in the actuator-disk thrust and torque. The propeller thrust centers are located at the coordinates (0.2785; ±0.1011; -0.1355) m.

8.3. Numerical parameters

Regarding the body dynamics, all six degrees of freedom of the vessel are resolved during the restart phase. The rudders are connected to the vessel through pin connections, and their rotational motions are imposed by means of a dynamic library implementing the autopilot model described later. In the reference frame of the geometrical model, the two pin connections are vertically aligned and located at the coordinates (0.1698; ±0.0761; -0.0379) m.

The solver is set to an unsteady time configuration, the maximum number of non-linear iterations is set to 20 and the time step is set to 0.008275 s. For seakeeping simulations, the time step is typically defined as a function of the encounter period, according to $dT = (T_{ENC}/r)$ with r generally ranging from 400 to 600. However, in following- and quartering-wave conditions, the encounter period T_{ENC} may become significantly larger than the wave period T_w. Consequently, relying solely on T_{ENC} may lead to an insufficient temporal resolution of the incident wave. Therefore, it is additionally recommended to ensure that $(T_w/dT) \geq 200$.

The k - ω SST (Menter, 2003) turbulence model is used.

8.4. Boundary conditions

The boundary conditions imposed on the outer limits of the far-field domain are the following: prescribed pressure boundaries with updated hydrostatic pressure are applied at the top and bottom boundaries; symmetry (mirror) conditions are imposed on the lateral boundaries in the y-direction; and wave-generator boundary conditions are prescribed at the upstream and downstream boundaries in the x-direction, as illustrated in Figure 12. Overset interfaces are defined at the boundaries of the vessel and rudder domains. Finally, all solid walls are modelled using wall-function boundary conditions.

8.5. Wave generation

The wave generation is achieved through a combination of wave-generator boundary conditions and wave-forcing regions where the theoretical wave field is enforced. These forcing regions prevent disturbances generated by the

vessel, including the wake system, from reaching the far-field boundaries and affecting the prescribed boundary conditions. The wave generation setup is illustrated in Figure 12.

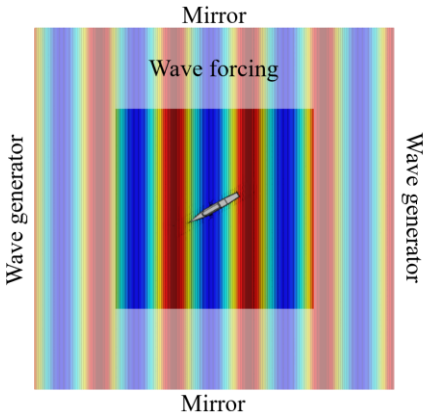


Figure 12 - Wave generation.

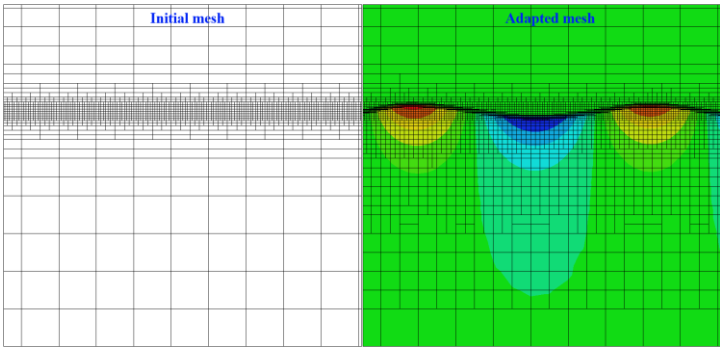


Figure 13 - Initial mesh and adapted mesh with AGR.

8.6. Adaptive grid refinement

The numerical setup leverages the Adaptive Grid Refinement (AGR) procedure to automatically and efficiently capture the relevant flow features throughout the simulation. A combined refinement criterion targets both the free-surface region, and the underwater flow features identified through the second spatial derivatives (Hessian) of the pressure field. The dynamic adaptation of the mesh to the instantaneous flow conditions enables a significant reduction in the total cell count while optimizing the resolution of the relevant flow features.

Figure 13 illustrates the adapted mesh, showing both free-surface refinement reaching an actual size of $H_w/20$, as well as the effect of the Hessian criterion refining the wave-induced pressure field underneath the free-surface.

8.7. Autopilot

To maintain the target course, the two rudders are controlled by an autopilot implementing a PD controller coupled with a steering-gear dynamics model, formulated as follows:

$$\dot{\delta} = 1/T_E * (-\delta - K_P * (\chi - \chi_c) - K_D * r)$$

where δ and $\dot{\delta}$ are the rudder angle and actuation velocity respectively, χ and χ_c are the instantaneous and target heading angles respectively, T_E is the steering-gear time constant, r is the yaw rate, finally K_P and K_D are the proportional and derivative gain coefficients, respectively.

As the control-law parameters are not reported in reference [3], a multivariate linear regression procedure was used to identify the controller parameters K_P, K_D and T_E from the experimental autopilot signals. The regression was performed using the experimental yaw angle as input and the rudder angle as output, based on the time signals reported in reference [3]. The parameter identification was carried out using the *scikit-learn* Python package.

Preliminary CFD simulations revealed a significant discrepancy between the predicted and the experimental yaw responses. Similar deviations were also reported by *Chu et al.* [3]. Subsequent analysis suggested that the effective target heading χ_c used during the experiments was different from the theoretical heading of 210°. For this reason, the target heading angle was treated as an additional unknown and identified simultaneously during the multivariate linear regression of the experimental signals.

The results of the identification process of the autopilot law is documented in Table 7.

Froude	**0.25**	**0.30**	**0.35**	**0.40**
R^2 coeff.	0.973	0.959	0.577	0.818
χ_c [deg]	206.5	206.2	208.9	204.7
K_P [-]	-2.9312			
K_D [s]	-0.1974			
T_E [s]	0.0105			

Table 7 – Result of the identification of the autopilot law parameters.

9. RESULTS

This section focuses on assessing the capability of the CFD approach to predict surf-riding and broaching instabilities. For completeness, detailed CFD and experimental time histories are provided in the Appendix.

Surf-riding is a dynamic instability that occurs in following or quartering seas when a ship is accelerated by a wave and becomes trapped on its forward slope, traveling at a speed greater than or equal to the wave phase velocity. Surf-riding is generally considered a precursor to broaching, which may endanger the ship by causing a sudden change in heading accompanied by large heel angles. While surf-riding primarily involves the ship's surge motion, broaching is a non-oscillatory yaw-roll dynamic instability characterized by a rapid and uncontrolled change of heading that cannot be corrected by the steering system and may, under severe conditions, result in capsize [1].

The signature of a surf-riding event requires the evaluation of the vessel velocity component in the wave-propagation direction. Since the sway velocity is not available in the experimental dataset [3], a first-order surf-riding signature is adopted using the surge-speed magnitude u and the vessel heading χ, leading to: $u/c \geq |1/\cos(\chi)|$. For the highest vessel speed investigated ($F_n = 0.40$), the corresponding threshold value is 1.14, using the target heading reported in Table 7. A broaching event is identified as a sustained yawing motion characterized by a yaw rate $\dot{\psi}$ and a yaw acceleration $\ddot{\psi}$ of the same sign, despite maximum counter-rudder action [2]. Additionally, a heading-deviation criterion of 20° is sometimes introduced. For the highest vessel speed investigated, the heading-deviation is quantified as $\chi_{threshold} \geq \chi_c + 20° = 224.7°$ with χ_c from Table 7.

Table 8 provides an assessment of the consistency between the CFD predictions and the experimental results reported in reference [3]. For this purpose, a set of global indicators is extracted from the time histories of the main variables involved in the signatures of surf-riding and broaching events. These indicators include the absolute maxima and minima of the roll angle, yaw angle, and non-dimensional surge speed, together with the average signal period for periodic cases. The signal analysis excludes the initial transient phase.

To facilitate the assessment of the CFD accuracy, the deviation from the EFD data is highlighted using a color-coded scheme. Green indicates good agreement, corresponding to deviations smaller than 3° for angular quantities, 0.3 s for periods, and 0.03 for the non-dimensional surge speed. Red indicates larger discrepancies, corresponding to deviations exceeding 5°, 0.5 s, and 0.05, respectively. Values falling between the green and red thresholds are highlighted in orange.

$F_n = 0.25$	Maximum		Minimum		Period [s]	
T_{min}=11s	EFD	CFD	EFD	CFD	EFD	CFD
Roll [°]	16.2	14.3	-11.4	-9.1	3.2	3.2
Yaw [°]	212.8	211.9	202.2	201.8	3.2	3.2
u/c [-]	0.65	0.62	0.35	0.36	3.2	3.2

$F_n = 0.30$	Maximum		Minimum		Period [s]	
T_{min}=11s	EFD	CFD	EFD	CFD	EFD	CFD
Roll [°]	23.3	19.1	-20.2	-17.0	4.1	4.1
Yaw [°]	216.3	213.8	202.1	198.5	4.0	4.1
u/c [-]	0.83	0.78	0.45	0.44	4.1	4.1

$F_n = 0.35$	Maximum		Minimum		Period [s]	
T_{min}=11s	EFD	CFD	EFD	CFD	EFD	CFD
Roll [°]	32.3	33.1	-22.1	-21.8	4.0	4.3
Yaw [°]	223.1	227.6	202.1	196.8	4.0	4.6
u/c [-]	0.94	0.94	0.48	0.48	4.8	4.8

$F_n = 0.40$	Maximum		Minimum		Period [s]	
T_{min}=5s	EFD	CFD	EFD	CFD	EFD	CFD
Roll [°]	43.7	36.4	-21.5	-26.2	-	-
Yaw [°]	236.6	236.2	199.2	185.8	-	-
u/c [-]	1.35	1.23	0.53	0.57	-	-

Table 8 – Global assessment of the consistency between CFD and EFD results.

The indicators reported in Table 8 show that the CFD approach, relying on the actuator-disk propulsion model, successfully reproduces the signal periods, as well as the increase in the non-dimensional surge speed and in the roll and yaw amplitudes as we approach the instability boundary.

For the highest nominal Froude number investigated ($F_n = 0.40$), both the CFD and EFD results predict a surf-riding event, with a maximum u/c ratio significantly exceeding the threshold value of 1.14. Both datasets also exhibit a large heading deviation, well above the broaching threshold value of 224.70°, together with a non-periodic response that is compatible with operation under a dynamic instability. For the three lowest Froude number conditions, both CFD and EFD exhibit periodic oscillatory responses. At $F_n = 0.25$, the oscillations remain highly regular and are readily controlled by the rudder system. In contrast, at $F_n = 0.35$, the responses become less periodic and more difficult to control, indicating that the vessel is operating close to the instability boundary. These trends are more readily observed in the time histories provided in the Appendix.

The color scheme in Table 8 highlights an increasing deviation between the CFD and experimental results as the operating condition approaches the instability region. This is an expected outcome as the behavior of the vessel close to the instability region is expected to be sensitive to the autopilot law as larger rudder corrections are required to maintain the course. However, the autopilot law was not documented in the reference paper [3] and had to be identified through a multivariate linear regression procedure, with an inherent level of uncertainty. The coefficients of determination R^2 reported in Table 7 are noticeably lower for the $F_n = 0.35$ and $F_n = 0.40$ conditions, which contributes to explaining the larger deviations from EFD results observed at those speeds. In addition, as the instability region is approached, the vessel response becomes less periodic and increasingly sensitive to the initial vessel-wave relative position, which was not documented in the reference paper [3].

Figure 14 illustrates the dynamic instability occurring at $F_n = 0.40$ by highlighting three characteristic stages of the vessel response. Between stages 1 and 2, the vessel is overtaken by a wave crest, resulting in a large heading deviation of 26° in the CFD signal, while the non-dimensional surge speed remains below the surf-riding threshold. Although the yaw angle exhibits a pronounced increase, the yaw acceleration $\ddot{\psi}$ is not sustained up to the maximum rudder deflection. Consequently, despite operating very close to the broaching boundary, the response does not fully satisfy the adopted broaching criteria. This conclusion is consistent for both the CFD and EFD results, indicating that both approaches capture the same physical behavior. This near-broaching event is then followed by a sustained surf-riding state in stage 3, developing on the next wave crest, and which matches the experiment well. Examination of the time histories in Figure 14 shows that CFD results closely reproduce the experimental surge-speed signal. Larger discrepancies are observed in the temporal evolution of the yaw and rudder angles, which is compatible with differences in the autopilot law controlling the rudder motion.

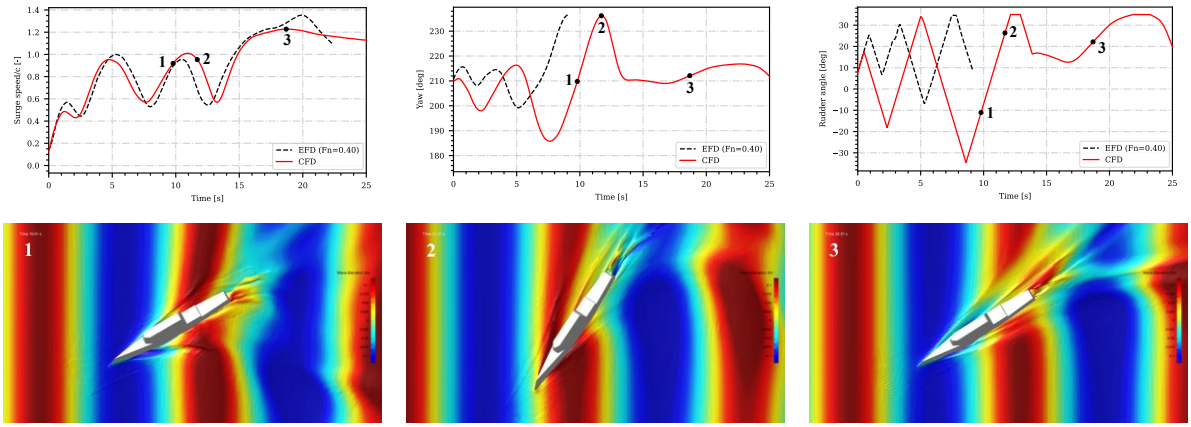


Figure 14 - Illustration of the dynamic instability at $F_n = 0.40$.

10. CONCLUSIONS

This paper investigates the applicability of a CFD-based approach using an actuator-disk propulsion model for the prediction of surf-riding and broaching instabilities. The investigated operating conditions reproduce the experimental campaign conducted by *Chu et al.* [3] on the ONRT vessel in stern-quartering waves. The predictive capability of the methodology is evaluated through direct comparison with the published experimental data. Validation metrics include the vessel motions (roll, pitch, yaw), rudder angle, and surge speed.

For the lowest Froude numbers investigated ($F_n = 0.25$, 0.30 and 0.35), the CFD approach reproduces the experimental motions, surge speed and signal periods. The consistency with the experimental results is particularly good for the $F_n = 0.25$ operating condition characterized by a strong periodic response.

As the operating conditions approach the instability boundary, the responses become less periodic and larger deviations are observed in the angular quantities (yaw, pitch, roll and rudder angle), while non-dimensional surge speed signal remains in good agreement with the experimental data. This good agreement in the surge-speed signal suggests that the larger discrepancies in the angular quantities are more likely related to differences in the autopilot law and in the initial vessel-wave relative position than to limitations of the actuator-disk propulsion model itself.

Despite these uncertainties, the overall agreement with the experimental observations supports the applicability of the CFD methodology and indicates that the dominant physical mechanisms governing the onset of the instabilities are well captured. Further work is nevertheless required to assess the origins of the deviations close to the instability boundary.

REFERENCES

[1] International Maritime Organization (IMO), “Revised Guidance to the Master for Avoiding Dangerous Situations in Adverse Weather and Sea Conditions”, MSC.1/Circ.1228, London, UK, 2007.

[2] Bonci, M., The Manoeuvrability of High-Speed Craft in the Following Sea, Ph.D. Thesis, Delft University of Technology (TU Delft), Delft, The Netherlands, 2019.

[3] Chu, J., Gu, M., Lu, J., Zhang, P., “A Prediction Method and Model Experiments on Surf-Riding and Broaching in Stern-Quartering Waves”, Journal of Marine Science and Engineering, Volume 12, 1538, 2024.

[4] Sanada, Y., Rosenblum, K., Kim, M., Stern, F., “W2025 CFD for ONRT Course Keeping in Regular Head and Oblique Waves, IIHR Internal Review of Data Submission Report”, conference proceedings, Wageningen workshop on CFD in ship hydrodynamics, 2025.

[5] Sanada, Y., Rosenblum, K., Kim, M., Stern, F., “ONR Tumblehome (ONRT) – Course Keeping in Waves”, test case instructions, Wageningen workshop on CFD in ship hydrodynamics, 2025.

[6] Sanada, Y., Rosenblum, K., Park, S., Milano, C., Starman, Z., Ozturk, D., Wang, Z., Stern, F., “Best Practices and Uncertainty Analysis for Mass Properties and Metacentric Height for Free Running Maneuvering Experiments and CFD,” in 13th International Workshop on Ship and Marine Hydrodynamics, Fukuoka, Japan, 2025.

[7] Zeng, K., Lu, J., Gu, M., Yang, C., “A Comparative Analysis of CFD and the Potential Flow Method for the Pure Loss of Stability in Following Waves”, Journal of Marine Science and Engineering, 11(11), 2135, 2023.

APPENDIX

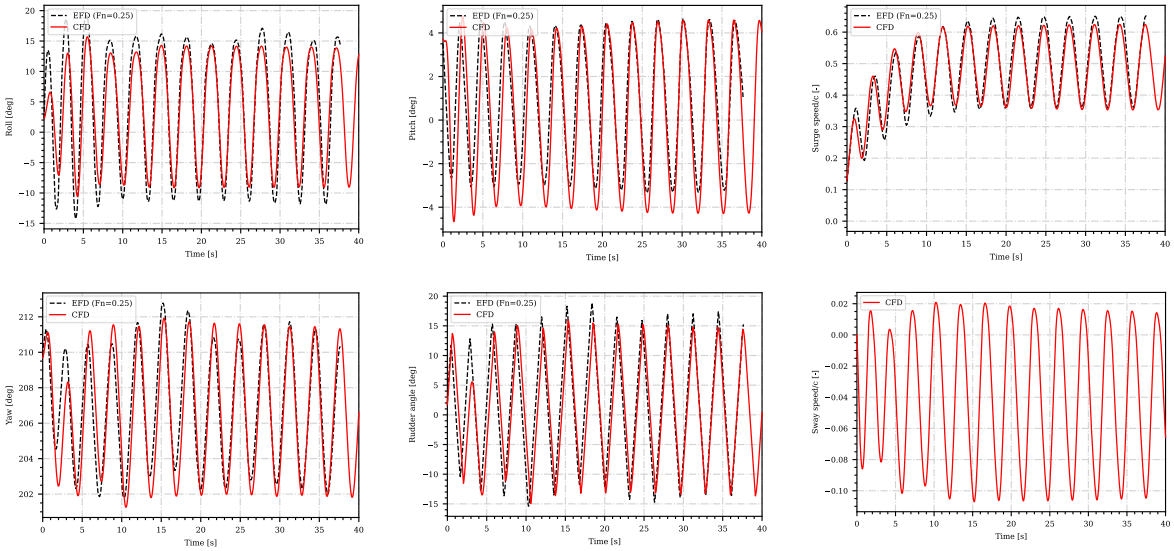
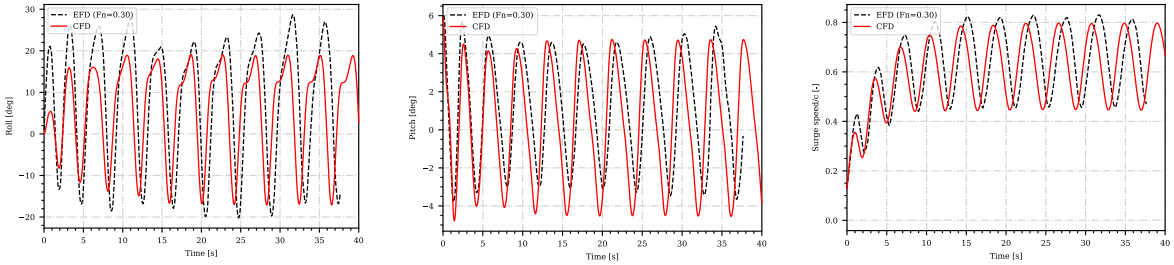


Figure 15 - Comparison of CFD and EFD time histories of the vessel response at $F_n = 0.25$.



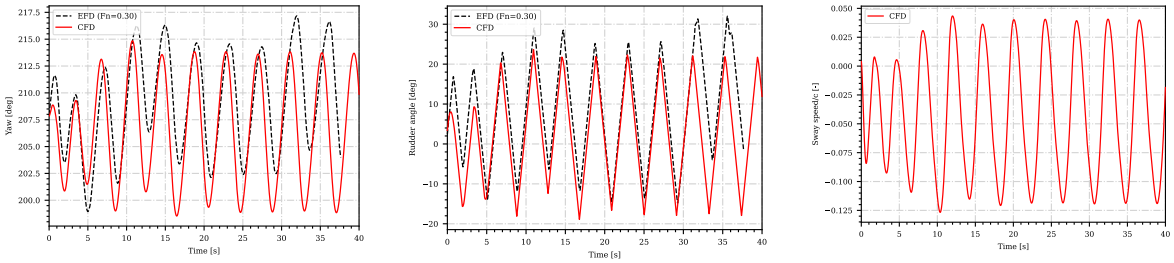


Figure 16 - Comparison of CFD and EFD time histories of the vessel response at $F_n = 0.30$.

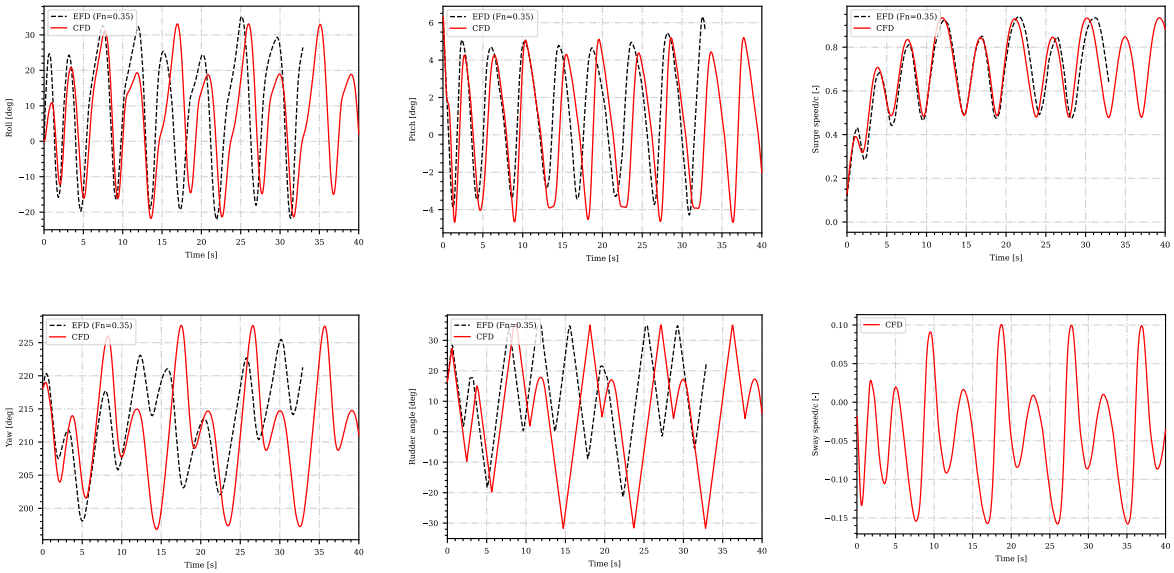


Figure 17 - Comparison of CFD and EFD time histories of the vessel response at $F_n = 0.35$.

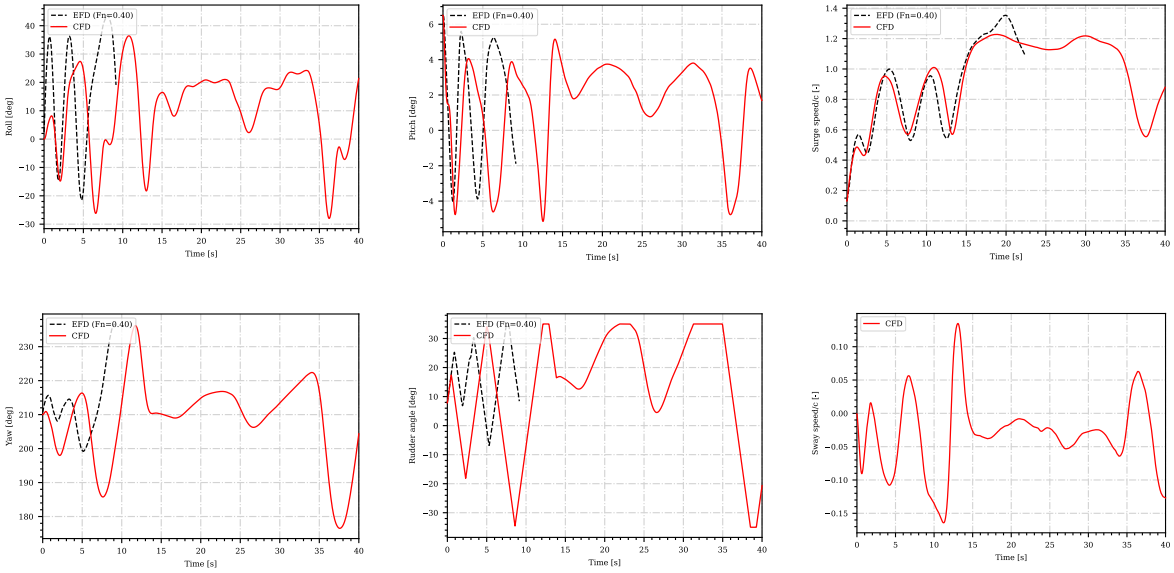


Figure 18 - Comparison of CFD and EFD time histories of the vessel response at $F_n = 0.40$.

Progressive development of a CFD framework for parametric rolling and the identification of green water as the dominant saturation mechanism

Zoran Čarija[1], Anton Turk[1], Jakov Čarija[2], Jasna Prpić-Oršić[1]
[1]Faculty of Engineering Rijeka, Croatia
[2]AITAC d.o.o., Kastav, Croatia
anton.turk@riteh.uniri.hr

1. Introduction

Parametric rolling is one of the most dangerous dynamic instabilities affecting modern container ships operating in longitudinal waves. When the encounter frequency approaches approximately twice the natural roll frequency, periodic variations of the restoring moment may trigger rapid growth of roll motion, leading to large roll amplitudes that threaten cargo safety and vessel operability. Although the onset of parametric rolling is well understood, accurate prediction of the saturated response remains challenging because it is governed by strongly nonlinear viscous and free-surface phenomena.
Conventional prediction methods are primarily based on potential-flow formulations combined with semi-empirical roll damping models. While computationally efficient, these approaches cannot directly resolve nonlinear flow separation, wave breaking and transient deck flooding. Building upon our previous coupled numerical, CFD and experimental investigation of parametric rolling [1], the present work continues the systematic development of a CFD framework for improving the prediction of the saturated response.
Recent advances in CFD have enabled direct simulation of nonlinear free-surface flows, viscous effects and ship motions. Numerous studies have investigated parametric rolling, viscous roll damping, scale effects, machine-learning-assisted prediction and the interaction between parametric rolling and internal sloshing [2–8]. Existing CFD investigations of green water, however, have focused primarily on deck impact loads and structural safety [9–11], while its influence on the nonlinear evolution and saturation of parametric rolling has received little attention.
The present paper summarizes the progressive development of four CFD configurations of increasing physical fidelity, ranging from a single-mesh approach to an overset-grid formulation including wave forcing and transient green-water overtopping. By systematically introducing additional physical mechanisms, the study demonstrates that green water represents one of the dominant nonlinear mechanisms governing roll saturation and provides the physical basis for future CFD-informed engineering prediction models.

2. Research development and numerical framework

The present work summarizes the progressive development of a numerical framework for investigating parametric rolling. The research began with a nonlinear potential-flow time-domain model, which enabled rapid identification of operating conditions susceptible to severe parametric rolling.

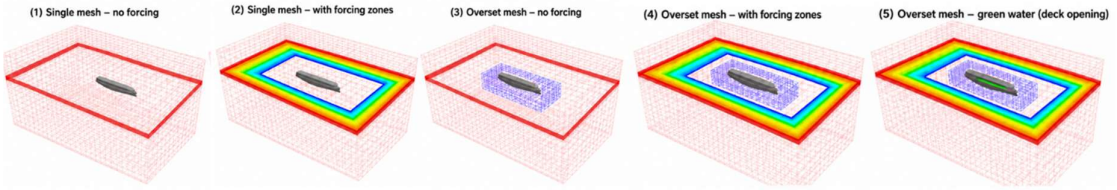
Based on these preliminary investigations, a dedicated experimental campaign was conducted at CEHIPAR within the HYDRALAB III programme. The experiments reproduced the numerically predicted wave conditions for a C11 containership (Table 1) and provided validation data for the numerical models. More importantly, video recordings revealed repeated green-water overtopping during the saturated stage of parametric rolling, indicating that this phenomenon could play an important role in limiting the roll response.

Table 1: Main particulars of a C11 container ship.

L_{PP}	262.0 m
B	40.0 m
T	12.34 m
V_S	20 knots

Besides providing validation data for the numerical simulations, the experiments revealed an important physical phenomenon that had received little attention during the initial modelling stage. Video recordings showed that, once large roll amplitudes had developed, significant green-water overtopping repeatedly occurred on the bow deck and appeared to coincide with the saturation of the roll response.

Motivated by these observations and by the rapid development of computational fluid dynamics (CFD), the numerical framework was extended to resolve the nonlinear viscous flow directly. A sequence of CFD models with progressively increasing physical fidelity was developed in order to isolate the influence of different modelling assumptions on the predicted ship motions. Figure 1 summarizes the investigated configurations.



	Case 1	Case 2	Case 3	Case 4	Case 5
Wave forcing	✗	✓	✗	✓	✓
Overset mesh	✗	✗	✓	✓	✓
Green water	✗	✗	✗	✗	✓

Figure 1: Progressive development of the numerical framework used to investigate parametric rolling.

All CFD configurations reproduced the onset of parametric rolling without artificial asymmetry, prescribed roll disturbances or external excitation. Consequently, differences in the predicted saturated response can be attributed solely to the additional physical and numerical modelling capabilities introduced at each stage.

The first configuration employed a single stationary mesh. Wave-relaxation zones were subsequently introduced to improve wave generation, followed by an overset-grid formulation enabling large-amplitude ship motions without mesh distortion. The final configuration incorporated an open bow deck, allowing transient green-water accumulation, drainage and the associated hydrodynamic loads to be resolved directly.

This progressive approach isolated the influence of wave generation, mesh motion and green-water dynamics within a consistent numerical framework. The final configuration demonstrated that transient green-water overtopping is one of the dominant nonlinear mechanisms governing parametric roll saturation.

3. Identification of the green-water damping mechanism

To illustrate the physical processes responsible for the additional damping identified in the previous section, representative CFD snapshots covering one characteristic roll cycle are presented in Figures 2–4. The selected instants follow the evolution of the overtopped water from its initial accumulation on the bow deck, through its transport and drainage, to the subsequent roll reversal. Together, these figures demonstrate that green water behaves as a transient fluid system whose dynamics are strongly coupled with the ship motions and play a key role in limiting the saturated roll amplitude.

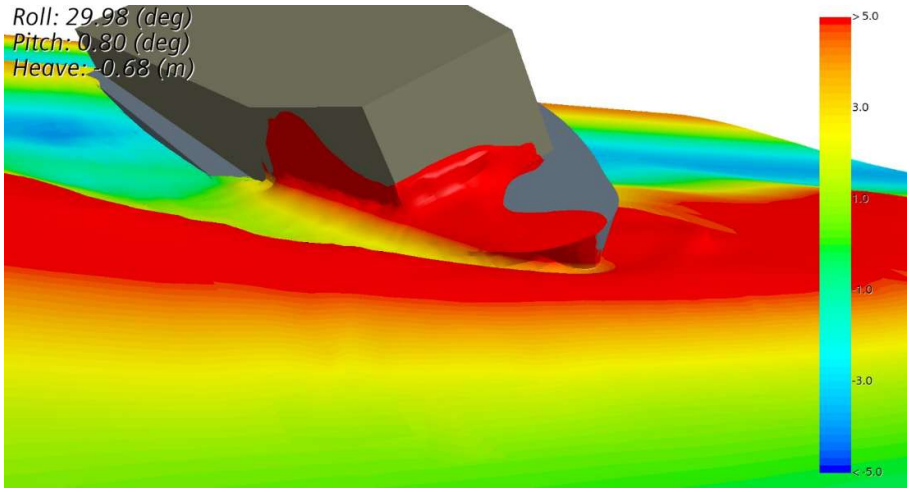


Figure 2: Initial green-water overtopping during the positive roll extreme.

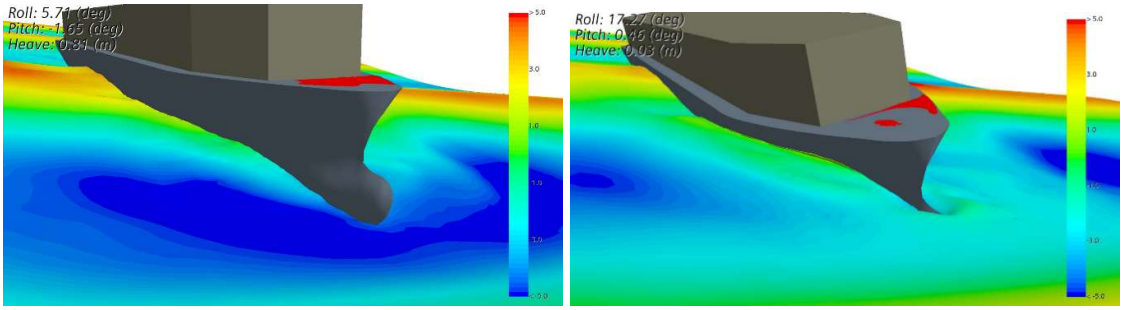


Figure 3: Evolution of the overtopped water during the return motion: (a) transport of the accumulated water across the bow deck as the vessel approaches the upright position (roll ≈ 5°); (b) progressive drainage of the deck water through the bow opening (roll ≈ 17°).

Figure 2 shows the onset of green-water overtopping during the positive roll extreme (approximately 30°), where the incident wave climbs onto the bow deck and a significant volume of water accumulates. As the vessel returns towards the upright position (Figure 3a), the overtopped water remains on deck and is transported longitudinally before progressively draining through the bow opening (Figure 3b). During this process, viscous shear, turbulent mixing and momentum exchange dissipate mechanical energy extracted from the ship motion.

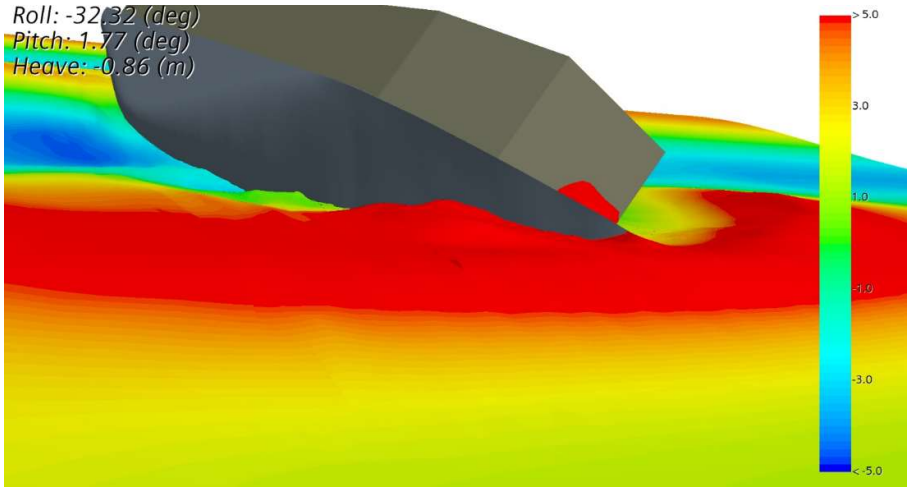


Figure 4: Completion of the green-water cycle at the opposite roll extreme..

Figure 4 shows the opposite roll extreme (approximately −32°), after most of the accumulated water has drained and the overtopping cycle is ready to repeat. This continuous sequence of accumulation, transport and drainage demonstrates that green water acts as a strongly nonlinear, phase-dependent damping mechanism, continuously removing energy from the roll motion and thereby reducing the saturated roll amplitude.

The preceding results demonstrate that green-water overtopping significantly improves the prediction of the saturated roll response. Figure 5 summarizes the physical mechanism inferred from the CFD simulations. Once the roll motion exceeds a critical amplitude, intermittent deck overtopping begins and the accumulated water undergoes continuous transport and drainage driven by the coupled ship motions. Rather than behaving as a static liquid mass, the moving water generates phase-shifted hydrodynamic forces and dissipates mechanical energy through viscous shear, turbulent mixing, wave breaking and momentum exchange with the ship.

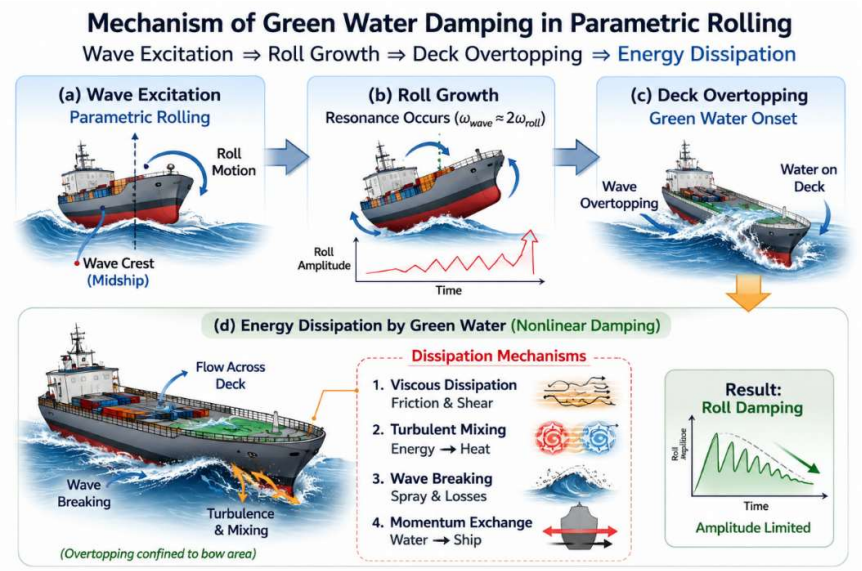


Figure 5: Conceptual illustration of the physical mechanism by which green water contributes to parametric roll damping.

The CFD simulations reveal that the moving water generates transient hydrodynamic forces and moments that are phase-shifted relative to the roll motion. Mechanical energy is dissipated through several coupled mechanisms, including viscous shear, turbulent mixing, wave breaking and momentum exchange between the moving water and the ship. Consequently, the overtopped water behaves as a transient nonlinear fluid system that extracts energy from the roll motion rather than simply modifying the hydrostatic restoring characteristics. This physical interpretation explains why green water acts as an effective nonlinear damping mechanism during the saturated stage of parametric rolling. It also provides the physical basis for representing the CFD-derived green-water contribution by an equivalent damping coefficient in the reduced-order nonlinear potential-flow model.

The comparison of the CFD configurations demonstrated that green-water overtopping substantially improves the prediction of the saturated roll response. Figure 6 summarizes the principal mechanisms identified during the present study. Two key observations emerge from the CFD simulations: (i) the onset of large-amplitude parametric rolling is accompanied by an upward translation of the mean heave level, indicating strong heave–roll coupling; and (ii) transient green-water overtopping introduces additional nonlinear energy dissipation, significantly reducing the saturated roll amplitude. Together, these findings provide the physical basis for the proposed equivalent green-water damping formulation.

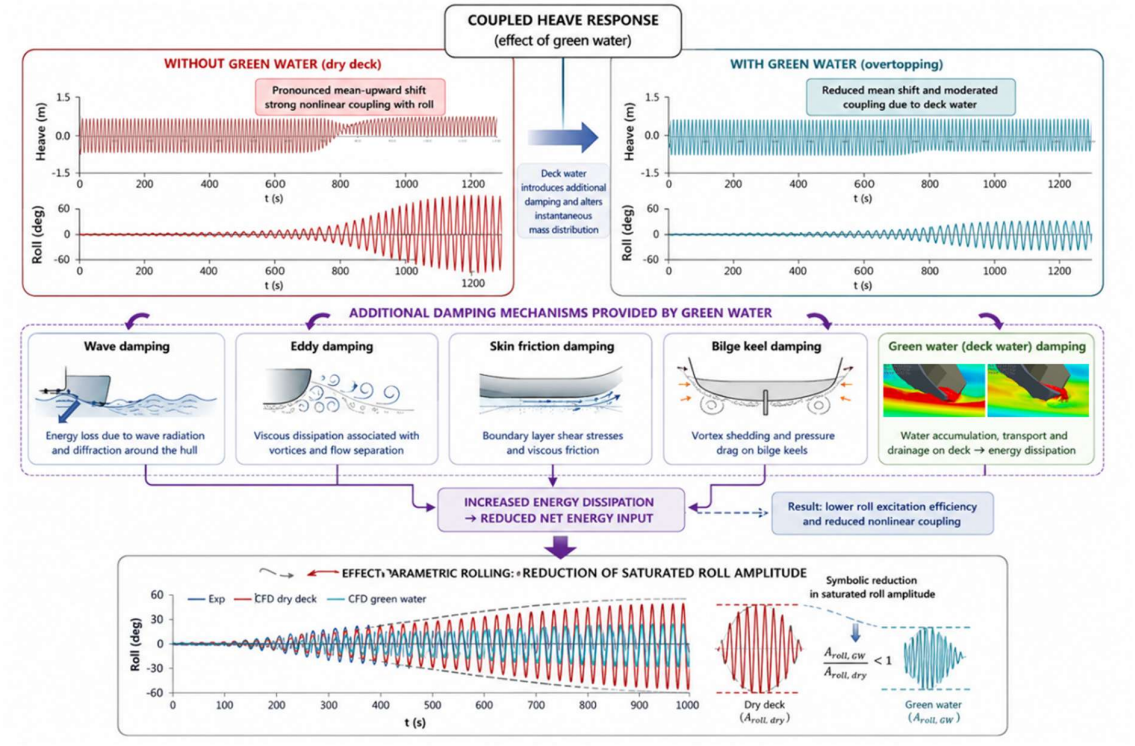


Figure 6: Progressive identification of green water as the dominant nonlinear damping mechanism governing saturated parametric rolling.

The upper part of Figure 6 compares the coupled heave and roll responses for the dry-deck and green-water simulations. While both configurations reproduce the onset of parametric rolling, the dry-deck model exhibits a pronounced upward shift of the mean heave position. In contrast, the green-water simulation shows a considerably smaller heave translation, indicating that transient deck flooding introduces additional energy dissipation into the coupled response.

The central part of the figure illustrates the physical origin of this behaviour. Rather than acting as a static mass, the overtopped water continuously accumulates, redistributes and drains from the bow deck, dissipating energy through viscous effects, turbulent mixing, wave breaking and momentum exchange with the ship. Consequently, the saturated roll amplitude is significantly reduced compared with the dry-deck solution. The reduced heave translation and attenuation of the saturated roll response provide strong evidence that transient green-water dynamics constitute one of the dominant nonlinear mechanisms governing parametric roll saturation and justify the introduction of a CFD-derived equivalent damping correction in the engineering model.

5. Conclusion and further work

This paper summarizes the progressive development of a CFD framework for investigating parametric rolling and identifies transient green-water overtopping as one of the dominant mechanisms governing roll saturation. Progressive improvements in the numerical model demonstrate that increasing physical fidelity leads to substantially improved prediction of the saturated response. The resulting physical insight provides the basis for incorporating CFD-derived green-water effects into computationally efficient engineering models. Future work will extend the methodology to additional ship types and operating conditions.

Acknowledgements
This work was supported by the Croatian Science Foundation under the project IP-IP-2022-10-2821 and by the two University of Rijeka projects, (PROJECTS no. PU-17 uniri-iz-25-10 - Funded by the European Union – NextGenerationEU) and (PROJECTS no. PU-17 uniri-iz-25-268 - Funded by the European Union – NextGenerationEU).

References

[1] Turk, A.; Čarija, Z.; Uzunoglu, E.; Prpić-Oršić, J. Assessment of parametric rolling using coupled numerical, CFD and experimental approaches. Brodogradnja 2026. 77(4): 77407. https://doi.org/10.21278/brod77407
[2] Liu, L.; Chen, M.; Wang, X.; Zhang, Z.; Yu, J.; Feng, D. CFD prediction of full-scale ship parametric roll in head wave. Ocean Engineering 2021. Volume 233, https://doi.org/10.1016/j.oceaneng.2021.109180
[3] Kianejad, S. S.; Enshaei, H.; Duffy, J.; Ansarifard, N.; Ranmuthugala, D. Ship roll damping coefficient prediction using CFD. Journal of Ship Research 2019. 63(02): 108-122. https://doi.org/10.5957/JOSR.07220021
[4] Liu L.; Zhang B.; Zhang H.; Gong J.; Tian Z.; Guo S.; Bao Y.; Zheng X. Study on numerical simulation and mitigation of parametric rolling in a container ship under head waves. Brodogradnja 2024. 75(3):1-19 https://hrcak.srce.hr/319375
[5] Wang, S.; Wei, J.; Chen, X.; Liu, L.; Zhang, Z. Numerical simulations of KCS parametric rolling in head waves. International Conference on Offshore Mechanics and Arctic Engineering, 2019. Wuhan, China.
[6] Zhou, X.; Li, H.; Huang, Y.; Liu, Y. Deep learning machine-based ship parametric rolling simulation and recognition algorithms, Ocean Engineering 2023. Volume 276, https://doi.org/10.1016/j.oceaneng.2023.114137
[7] Liu, L.; Feng, D.; Wang, X.; Zhang, Z.; Yu, J.; Chen, M. Numerical study on the effect of sloshing on ship parametric roll. Ocean Engineering 2022. Volume 247: 110612. https://doi.org/10.1016/j.oceaneng.2022.110612
[8] Phuong, N. T. H.; Taniguchi, T.; Katayama, T. Numerical study of scale effects of viscous roll damping for a container ship. Brodogradnja: An International Journal of Naval Architecture and Ocean Engineering for Research and Development 2025. 76(4), 1-23.
[9] Kangping, L.; Wenyang, D.; Qingwei, M.; Shan, M.; Jianming, Y. Numerical Simulation of Green Water on Deck with a Hybrid Eulerian-Lagrangian Method. Journal of Ship Research 2021. 66(01):1-18 https://doi.org/10.5957/JOSR.03190015
[10] Rosetti, G.F.; Pinto, M.; de Mello, P.; Sampaio, C.; Simos, A.; Silva, D. CFD and experimental assessment of green water events on an FPSO hull section in beam waves. Marine Structures 2019. Volume 65, 154-180 https://doi.org/10.1016/j.marstruc.2018.12.004
[11] Gatin, I.; Vukcevic, V.; Jasak, H.; Jeonghwa, S.; Shin H.R. CFD verification and validation of green sea loads. Ocean Engineering 2018. Volume 148 500-515.

Nonlinear potentialFreeSurfaceFoam

Josh Davidson[a], **Pál Schmitt**[b], **Christan Windt**[c], **Gabriel Barajas**[a], **Javier L. Lara**[a]
a IHCantabria, Spain,
b Queen's University Belfast,
c Technische Universität Braunschweig, Germany
p.schmitt@qub.ac.uk

1 Introduction

The OpenFOAM® solver `potentialFreeSurfaceFoam (PFSF)` occupies an unusual position in the single-phase numerical landscape. Like potential-flow methods, `PFSF` avoids the air phase, carrying the free surface as a single-valued elevation field on the upper boundary patch, such that there is no volume fraction to transport and none of the spurious air-phase velocities that can constrain the time step in a Volume-of-Fluid (VoF) computation (Deshpande et al. (2013); Larsen et al. (2019); Qwist and Christensen (2023)). It is not, however, a reduced model: it retains the full incompressible Navier–Stokes (NS) equations, and so admits viscous and rotational effects. Its niche is therefore the viscous, non-breaking end of free-surface modelling, in applications such as numerical towing tanks and flow around submerged or moving structures. Reported applications nonetheless remain few: calculating the power output and the lift and drag coefficients of a cross-flow tidal turbine, accounting for free-surface and blockage effects, by Feinberg et al. (2019); three-dimensional (3D) tsunami propagation by Oishi et al. (2020); a multi-code benchmark replicating a physical wave tank with a moving-wall wavemaker by Tran et al. (2024) and sloshing inside a cylindrical tank by Brown et al. (2026) and Davidson (2026).

The solver is based on the standard single-phase NS solver *pimpleFoam* with the governing equations as follows:

$$\partial_t \mathbf{U} + \nabla \cdot (\mathbf{U}\mathbf{U}) = -\nabla p_k + \rho^{-1} \nabla \cdot \mathbf{T} + \mathbf{F}_b, \qquad \nabla \cdot \mathbf{U} = 0. \tag{1}$$

In Eq. (1), $\mathbf{U}$ is velocity, $p_k = p/\rho$ the kinematic pressure, $\mathbf{T}$ the viscous stress tensor, and $\mathbf{F}_b$ are body forces such as gravity. What distinguishes `PFSF` is the *waveSurfacePressure* condition on the upper boundary, which carries a free-surface displacement $\boldsymbol{\zeta}$, stored per face as a surface-normal vector. Since $\boldsymbol{\zeta}$ is part of the solution rather than a prescribed boundary value, the surface requires two conditions. (i) The kinematic one advances $\boldsymbol{\zeta}$ using the signed volume flux ϕ_f through each face; (ii) the dynamic one sets the pressure:

$$\boldsymbol{\zeta}_f^{n+1} = \boldsymbol{\zeta}_f^{n} + \Delta t \, \mathbf{n}_f \, \phi_f / A_f, \qquad p_k = -\mathbf{g} \cdot \boldsymbol{\zeta} = g_n \, \zeta, \tag{2}$$

with A_f the face area and $\mathbf{n}_f$ the outward normal, which is vertical here, so the kinematic update is scalar in the elevation ζ, positive upward, and the dynamic condition is hydrostatic with $g_n = |\mathbf{g}|$ being the vertical component of the gravity vector. In practice the condition is applied to $p_{gh} = p_k - \mathbf{g} \cdot \mathbf{h}$, with $\mathbf{h}$ the position; this is the single-phase counterpart of p_{rgh} in `interFoam`, built from the kinematic rather than the static pressure.

Both conditions in Eq. (2) are imposed at the still-water plane rather than at the surface itself, and both are linear in ζ. The formulation is therefore based on infinitesimal amplitude free-surface theory, and two previous studies have mapped where its accuracy degrades. Davidson et al. (2026) replicate an experimental wave tank with a piston wavemaker and validate `PFSF` over amplitudes spanning Stokes second and third order, finding good agreement for the near-linear waves but significant deviations once nonlinearity became relevant. Similarly surface elevation was captured well by Schmitt et al. (2020) for linear waves before they transformed across the classic Dingemans bar, after which they did not match the experimental measurements.

Here we report on ongoing work to extend the solver's validity to such cases by restoring nonlinearity to the free-surface conditions, while retaining the single-phase formulation. The new solver is called `nonlinearPotentialFreeSurfaceFoam (NLPFSF)`. Progress is assessed based on the same, well-established Dingemans shoaling case.

2 Including nonlinearity

Two routes lead from the flat-top mesh of Fig. 1 (a) to finite-amplitude behaviour, and they differ in kind: the first changes only the boundary condition, the second the boundary-value problem.

2.1 Flat-top mesh: second-order transfer to still water

Written on the still-water plane, the stock kinematic condition is $\partial_t \zeta = w$, with w the vertical component of $\mathbf{U}$: the elevation follows the vertical velocity there. The exact statement is $\partial_t \zeta + \mathbf{u}_h \cdot \nabla_h \zeta = w$ evaluated on $z = \zeta$, with $\mathbf{u}_h$ and ∇_h the horizontal velocity and gradient and z the vertical coordinate. So two terms are missing: (1) the horizontal advection of a sloping surface, and (2) the difference between w at the surface and w at still water. Expanding w about $z = 0$ and eliminating $\partial_z w$ through continuity folds both into one divergence (Fig. 1 (b)),

$$\partial_t \zeta = w - \nabla_h \cdot (\zeta \, \mathbf{u}_h), \tag{3}$$

with $\mathbf{u}_h$ the horizontal velocity.

The dynamic condition is transferred the same way. On the true surface it is $p = 0$; at leading order on the still-water plane this is the stock hydrostatic condition $p_{gh} = -g\zeta$, and at next order it requires the vertical pressure gradient acting over the distance ζ. That gradient is taken from the vertical momentum balance, $p_{gh} = -g\zeta + \zeta \, \partial_t w$, rather than from unsteady Bernoulli: the quadratic term $\frac{1}{2}|\mathbf{U}|^2$ would double-count convective momentum already carried by Eq. (1), and reading the gradient from the pressure field would feed the top-patch value back into itself.

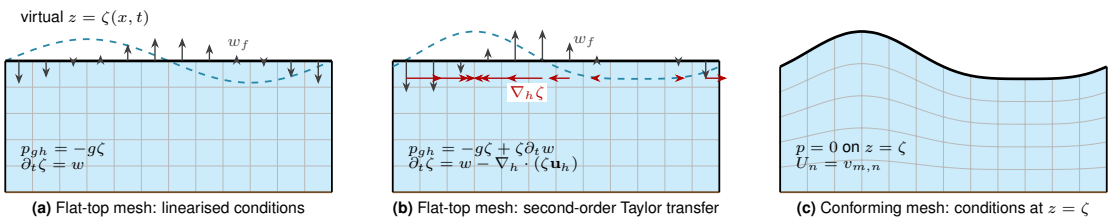
We implemented that pair in conservative surface-flux form, with a scale-selective filter and Picard iteration of the surface–pressure coupling, but did not obtain a stable scheme. Within a time step the coupling converges; the time evolution does not. Growth seeds at the station of maximum surface slope, the unstable mode is resolved-scale and zero-mean, and neither filtering nor tighter iteration shifted the threshold. Whether that is intrinsic to transferring finite-amplitude terms onto a fixed plane, or a discretisation we have not found, is not settled by these tests. Either way it motivated applying the conditions directly at the surface position.

2.2 Moving mesh: conditions on the true surface

The second route drops the transfer (Fig. 1 (c)) and identifies the top patch with $z = \zeta(x, t)$, putting its face centres $\mathbf{C}_f$ on the surface. The dynamic condition there is $p = 0$, which in the solved variable reads

$$p_{gh} = -(\mathbf{g} \cdot \mathbf{C}_f) = g_n \zeta. \tag{4}$$

That is the value `PFSF` already sets, but imposed at the correct surface position rather than at still water. The top-face normal speed then equals the fluid normal speed, and the elevation increment is the absolute volume flux through the face. Columns remain vertical, and the surface displacement is shared down each column, vanishing at the bed. The interior discretisation is unchanged (Eq. (1)); what changes is the mesh, the flux, and the free-surface conditions (Section 3).



(a) Flat-top mesh: linearised conditions **(b)** Flat-top mesh: second-order Taylor transfer **(c)** Conforming mesh: conditions at $z = \zeta$

Fig. 1: Single-phase free-surface treatments on the same tank. (a) Stock `PFSF`: linear kinematics and $p_{gh} = -g\zeta$ on the still-water plane; the surface exists only as the field ζ. (b) Second-order transfer onto that plane, adding horizontal advection and a transferred dynamic term. (c) Surface-conforming mesh: columns track ζ and both conditions are applied on $z = \zeta$.

3 ALE implementation

The mesh is now Arbitrary Lagrangian–Eulerian (ALE): identified with $z = \zeta$ at the top patch, it carries its own velocity $\mathbf{v}_m$, chosen independently of $\mathbf{U}$. Every face then carries three fluxes of the same kind: ϕ_{abs} from $\mathbf{U}$, ϕ_{mesh} from $\mathbf{v}_m$ (the rate at which the face sweeps volume) and their difference ϕ_{rel}, from $\mathbf{U} - \mathbf{v}_m$, in which conservation is written. Requiring each cell's volume change to equal what its faces sweep is the geometric conservation law: mesh motion alone can then neither create nor destroy fluid (Tuković and Jasak, 2012). The stock swept-volume field and flux correction are used unchanged. That freedom is used in a mixed Eulerian–Lagrangian way: columns stay vertical, so the surface is Lagrangian in the normal, $\mathbf{U} \cdot \mathbf{n} = \mathbf{v}_m \cdot \mathbf{n}$ at convergence, and Eulerian horizontally.

3.1 The σ-column mesh

Each time the surface moves, points are reset from the initial mesh at still water:

$$z_{\text{new}} = z_b + \sigma\,(z_s + \zeta_{\text{col}} - z_b), \qquad \sigma = (z_{\text{ref}} - z_b)/(z_s - z_b). \tag{5}$$

Only the vertical coordinate changes: z_{ref} is the point's height in that reference, z_b the bed and z_s the still-water surface in its column, so $\sigma \in [0, 1]$ is fractional height up the column. Since ζ lives on the top faces but points are what move, the column values ζ_{col} are interpolated from it with linear weights fixed once on the reference mesh. Subtracting the reference leaves a point displacement of $\sigma\,\zeta_{\text{col}}$: every point in the column moves, by a fraction of the surface displacement equal to its normalised height. Taking z_b beneath each column makes that fraction zero on the bed, so the bathymetry may vary along the tank and is never displaced by the stretch. Interface tracking normally solves an additional Laplace equation for the point motion (Tuković and Jasak, 2012); Eq. (5) is fully explicit, so each mesh update takes only one sweep over the points.

3.2 Conditions at $z = \zeta$

Because the top patch now *is* the surface, the dynamic condition needs no transfer: $p = 0$ holds, so p_{gh} follows from the face-centre position alone, Eq. (4). It carries no history and no reconstructed gradient, and returns the stock hydrostatic condition as $\zeta \to 0$. The kinematic update per top face uses the *absolute* flux,

$$\Delta\zeta_f = \phi_{\text{abs},f}\,\Delta t\,/\,(\mathbf{S}_f \cdot \hat{\mathbf{e}}_v), \qquad \phi_{\text{abs}} = \phi_{\text{rel}} + \phi_{\text{mesh}}. \tag{6}$$

Here $\mathbf{S}_f$ is the face area vector and $\hat{\mathbf{e}}_v$ the vertical unit vector, so $\mathbf{S}_f \cdot \hat{\mathbf{e}}_v$ is the column's horizontal footprint (rather than its area A_f which grows with slope). The surface is material, so the step must end with the mesh flux equal to the fluid flux, $\phi_{\text{mesh}} = \phi_{\text{abs}}$, leaving no relative flux through the face. Eq. (6) gets there by displacing from ζ^n by the absolute flux; displacing from the latest position by the residual instead ends in the same state (Tuković and Jasak, 2012; Cheraghi and Vakilipour, 2024).

The velocity condition on the top patch takes the tangential component, $\mathbf{U}_t$, from the interior and sets the normal part to the mesh-face speed, $\mathbf{U} \cdot \mathbf{n} = \mathbf{v}_m \cdot \mathbf{n}$, which reduces to slip on a static mesh. Stock conditions that infer the normal velocity from the face flux cannot be reused: that flux is ϕ_{rel}, so they come out short by $\mathbf{v}_m \cdot \mathbf{n}$.

3.3 Time loop

Surface, mesh and flux must stay consistent *inside* every outer iteration, not once per time step as in the stock `PFSF` solver (Fig. 2).

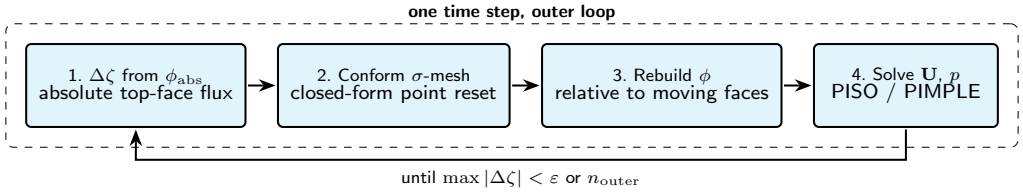


Fig. 2: Sequence within one outer iteration of the `NLPFSF` solver.

4 Test Case

As a first validation test case, we present an application to the wave propagation problem over the submerged bar of Dingemans (1994). The dimensions of the tank and the location of the five wave probes (WPs) are depicted in Fig. 3. The particular wave condition is the same as that used by Schmitt et al. (2020) to validate their VoF wave tank, comprising a regular wave of period 2.02 s and height 0.02 m. The case suits solver benchmarking since the nonlinearity is produced by the bathymetry rather than prescribed at the generator. The incident wave is of very small steepness, $H/\lambda \approx 0.005$, but over the crest of the shoal the depth falls to a quarter of its flat-section value, the wave shoals and steepens, so energy is transferred into bound higher harmonics; on the lee slope these are released as free waves travelling at their own celerity, leaving a strongly non-sinusoidal signal at WP4 and WP5 (see Fig. 3). WP1 therefore tests only propagation, while the probes above and behind the bar record strongly nonlinear conditions.

4.1 Performance Assessment

The test case is simulated using both the standard `PFSF` solver and the `NLPFSF` implementation, described in Section 3. To assess the performance, the wave time series measured by WP2-5 are compared against the experimental measurements by Dingemans (1994) [1], as well as the VoF results reported by Schmitt et al. (2019) using the `interFOAM` solver.

4.2 Wave Generation and Absorption

Waves are generated and absorbed with the impulse source method (Schmitt et al., 2020). Rather than hard-coding the wavemaker into a fork of the solver, it is here implemented entirely at runtime through OpenFOAM's `fvOptions`, so the same source is able to drive `PFSF` and `NLPFSF` solvers without modification[2]. The source region and the two absorbing beaches are marked in Fig. 3 and are defined as cell zones. A sinusoidal impulse of period 2.02 s is set as input, the amplitude is calibrated, from the measured wave amplitude at WP1, using the method described by Schmitt et al. (2019).

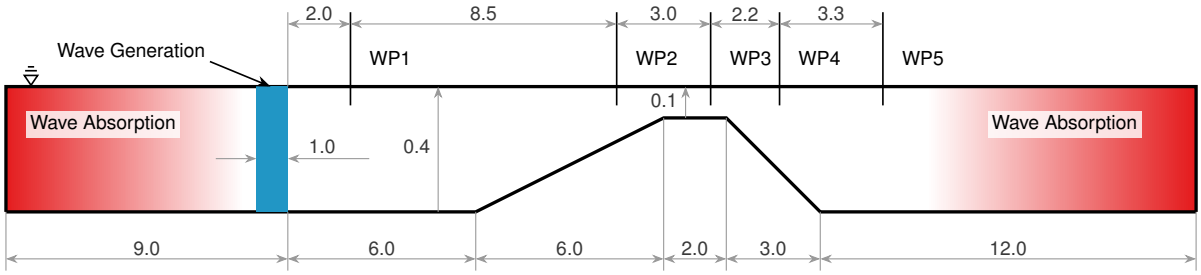


Fig. 3: Schematic of the NWT for the Dingemans test case (not to scale). All dimensions in [m]

5 Results

Fig. 4 (a-d) present surface elevation traces of the experiments by Dingemans (1994), the standard `interFoam` and `PFSF` solvers and the new `NLPFSF` solver for WP 2–5. On the upslope of the shoal, at WP 2, all solvers show overall good agreement with the experimental data, although `PFSF` fails to capture the slight skewness of the waves. When wave transformation occurs over and beyond the shoal `PFSF` fails to capture significant parts of the signal. At WP3, Fig. 4 (b), the wave crest is underestimated by 25 % and the secondary peak, located in normalised periods at 0.6 and 1.6, is not captured at all. At WP4, Fig. 4 (c), all solvers capture the wave crests, but `PFSF` shows only a secondary peak of 0.2 normalised amplitude compared to the 1.7 observed in all other signals. The two nonlinear free-surface solvers `interFoam` and `NLPFSF` deviate very little from each other and match the experimental data well. Only for WP 5, Fig. 4 (d), maximum deviations of up to 0.2 are found for the wave trough. Fig. 5 shows snapshots of the mesh and the p_gh field as a wave crest passes WP3.

[1] Data extracted from plot in pdf document using the WebPlotDigitizer tool: https://automeris.io/wpd/

[2] Tutorial case for the `PFSF` case available at: https://github.com/SeaFD/impulseSourceWavemaker

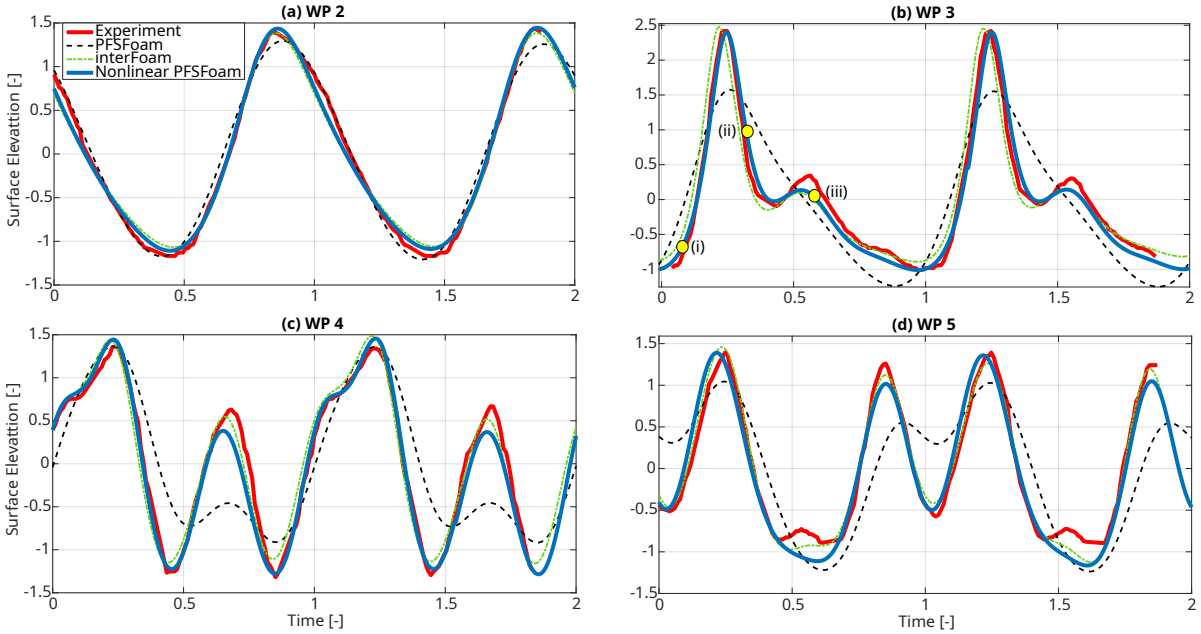


Fig. 4: Surface elevation time series, normalised by wave amplitude and period, for the Dingemans experiments (red line), `PFSF` (black dashed), `interFoam` (green dash-dot) and the proposed `NLPFSF` (blue line) at (a) WP2, (b) WP3, (c) WP4 and (d) WP5. The yellow markers (i), (ii) and (iii) on WP3 correspond to instances on the snapshots in Fig. 5.

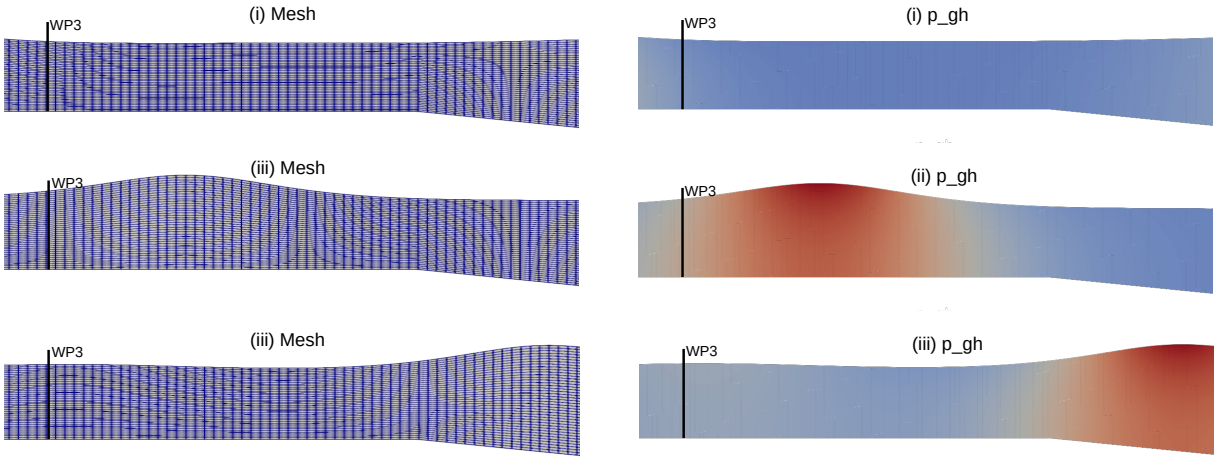


Fig. 5: Zoomed in snapshots around WP3 and the start of the downslope of the mesh (left) and the p_gh field (right) at instants (i), (ii) and (iii) as denoted on Fig. 4 (b).

6 Conclusion

This paper presented an extension of the `PFSF` solver to enable the simulation of non-linear wave conditions by enabling mesh motion and deformation of the free surface patch. A first application to the experiment described by Dingemans (1994) demonstrated the increased capabilities. Highly nonlinear wave transformations were captured with the same level of accuracy as the conventional `interFoam` solver. Further work is required to explore the computational efficiency and applicability to other use cases, such as wave loading of surface piercing structures.

References

Brown, S., Colville, S., Francis, V., Zhao, T., Lee, Y., Cao, D., Chen, H., Chen, J., Chen, S., Davidson, J., et al. (2026). A blind comparative study on isothermal sloshing in a circular tank (ccp-wsi blind test series 5). *Ocean Engineering*, 362:126290.

Cheraghi, B. and Vakilipour, S. (2024). Developing a coupled free-surface flow solver using interface tracking algorithm in foam-extend. *Amirkabir Journal of Mechanical Engineering*, 56(2):149–184.

Davidson, J. (2026). Efficient single-phase rans modelling of sloshing in cylindrical tanks: Applicability and limits. *Ocean Engineering*, 363:126626.

Davidson, J., Kramer, M., and Schmitt, P. (2026). Numerical wave tank implementation and validation using potentialfreesurfacefoam. *Preprint*.

Deshpande, S. S., Anumolu, L., and Trujillo, M. F. (2013). Evaluating the performance of the two-phase flow solver interfoam. *Computational science & discovery*, 5(1):014016.

Dingemans, M. W. (1994). Comparison of computations with boussinesq-like models and laboratory measurements. Technical report, Deltares (WL).

Feinberg, M., Schmitt, P., Donegan, J., and McEntee, J. (2019). An efficient numerical framework for the assessment of free surface effects on crossflow tidal turbines. In *Proceedings of the 13th European wave and tidal energy conference, Napoli*.

Larsen, B. E., Fuhrman, D. R., and Roenby, J. (2019). Performance of interfoam on the simulation of progressive waves. *Coastal Engineering Journal*, 61(3):380–400.

Oishi, Y., Shinde, T., Yamazaki, T., Makinoshima, F., Baba, T., T.Maeda, Chikasada, N., Tsushima, H., and Takagawa, T. (2020). Three-dimensional tsunami propagation simulation of nankai trough great earthquake tsunami. *Journal ofJapan Society Civil Engineers*.

Qwist, J. R. K. and Christensen, E. D. (2023). Development and implementation of a direct surface description method for free surface flows in openfoam. *Coastal Engineering*, 179:104227.

Schmitt, P., Windt, C., Davidson, J., Ringwood, J. V., and Whittaker, T. (2019). The efficient application of an impulse source wavemaker to CFD simulations. *Journal of Marine Science and Engineering*, 7(3):71.

Schmitt, P., Windt, C., Davidson, J., Ringwood, J. V., and Whittaker, T. (2020). Beyond VoF: alternative OpenFOAM solvers for numerical wave tanks. *Journal of ocean engineering and marine energy*, 6:277–292.

Tran, T. T., Meuris, B., Chartrand, C., Davidson, J., Andersen, J., Eskilsson, C., Kramer, M. B., Papadakis, G., and Nielsen, K. (2024). High-fidelity numerical wave tank verification & validation study: Wave generation through paddle motion. In *Developments in Renewable Energies Offshore: Proceedings the 6th International Conference on Renewable Energies Offshore, RENEW 2024*. CRC Press.

Tuković, Ž. and Jasak, H. (2012). A moving mesh finite volume interface tracking method for surface tension dominated interfacial fluid flow. *Computers & fluids*, 55:70–84.

Echo-Driven Modulation of Laser-Induced Cavitation Bubbles in Cylindrical Confinement

Mazyar Dawoodian[1], **Sasan Rezaee**[2], **Bettar Ould el Moctar**[1]

1 Technische Universität Berlin, Berlin, Germany

2 Universität Duisburg-Essen, Duisburg, Germany

Abstract. We combine high-speed imaging, acoustic modelling and molecular dynamics simulations to investigate laser-induced cavitation in cylindrical confinement. The experiments reveal changes in prolate deformation and collapse timing, while the simulations show that a returning pressure wave can deform a nanobubble. Early reflected pulses provide a plausible acoustic mechanism alongside the hydrodynamic effects of confinement [1].

1 Introduction

Laser-induced breakdown generates a cavitation bubble and a shock wave, as characterized by Vogel et al. [2]. Shock arrival relative to bubble oscillation affects collapse and jet formation [3], while pressure impulse governs collapse time and jet speed in the impulsive regime [4]. Confinement additionally modifies liquid inertia and bubble oscillation frequencies [5].

Here, wall reflections can return towards the originating bubble before collapse (Figure 1). We investigate how tube radius affects morphology and timing using experiments, acoustic modelling and molecular dynamics, considering both acoustic and hydrodynamic confinement effects.



Figure 1. Cavitation bubble inside a water-filled cylinder. Orange arcs represent the emitted pressure pulse; teal arcs and inward arrows show returning wall reflections. The dashed line indicates the cylinder axis. Conceptual illustration, not to scale.

2 Experimental method

Single bubbles were generated on the axis of acrylic cylinders with radii of 8–18 mm inside a 50 × 50 × 50 mm cuvette. Distilled water filled the cylinder and surrounding annulus at approximately 20 °C and 101 kPa. A Q-Smart 450 Nd:YAG laser supplied 1064 nm, 6 ns pulses with adjustable energy up to 450 mJ, focused at mid-depth. Water was initially quiescent, with sufficient time between shots for residual motion to decay.

A Phantom v2012 camera recorded LED-backlit shadowgraphs at 180,000 frames/s, 256 × 256 pixels and 0.86 µs exposure, synchronized by a TTL trigger. The frame interval was 5.56 µs. Repeat shots gave maximum equivalent radii reproducible within ±0.1 mm. Horizontal and vertical radii were extracted to characterize volume and deformation.

3 Bubble measures and echo model

Approximating the bubble as an axisymmetric ellipsoid, its equivalent-volume radius and aspect ratio are defined by

$$r_{eq} = (r_h{}^2 r_v)^{1/3}, \quad A = \frac{r_v}{r_h} \qquad (1)$$

Here, the vertical direction coincides with the tube axis. An aspect ratio above unity indicates a prolate bubble; the maximum equivalent radius characterizes bubble size. In the constant-wave-speed approximation, the arrival time of the k-th echo at the axis is [1]

$$t_k = \frac{2kR}{c}, \quad k = 1, 2, \ldots \qquad (2)$$

For a sound speed of 1500 m/s, the recurrence interval increases from approximately 10.7 µs at R = 8 mm to 24.0 µs at R = 18 mm. These are travel-time estimates, rather than direct measurements of individual shocks. Figure 2 illustrates outward propagation, partial wall reflection and radial refocusing. The reflected field contains both compressive and tensile components.

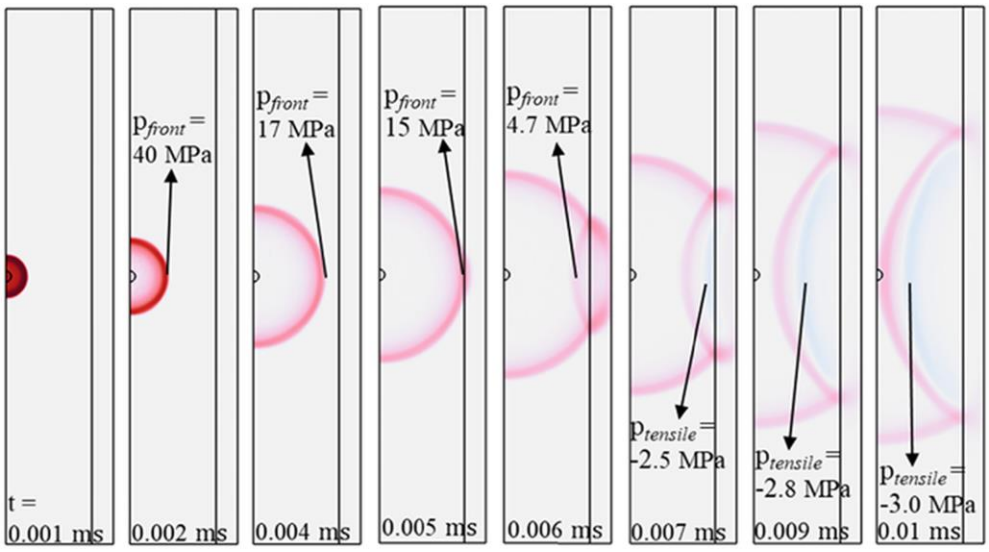


Figure 2. Simulated pressure-wave propagation in an acrylic cylinder of radius 8 mm and successive pressure-field snapshots. Reproduced from Fig. 2 of [1].

Reflection losses and imperfect three-dimensional refocusing reduce successive echo amplitudes. Consequently, late deformation need not imply strong late echoes: interface motion initiated by an early pressure impulse can persist after that pulse has passed. The finite bubble also scatters incoming waves, so a field calculated without the bubble does not give its exact interfacial pressure loading.

4 Experimental observations and interpretation

Figure 3 shows a representative sequence for a tube radius of 13 mm and a maximum equivalent bubble radius of 1.5 mm. The bubble is approximately spherical early in the sequence and becomes increasingly elongated along the cylinder axis during contraction. The most pronounced prolate shape occurs near the final collapse stage. This corresponds to lateral compression towards the axis, rather than compression along the axis.

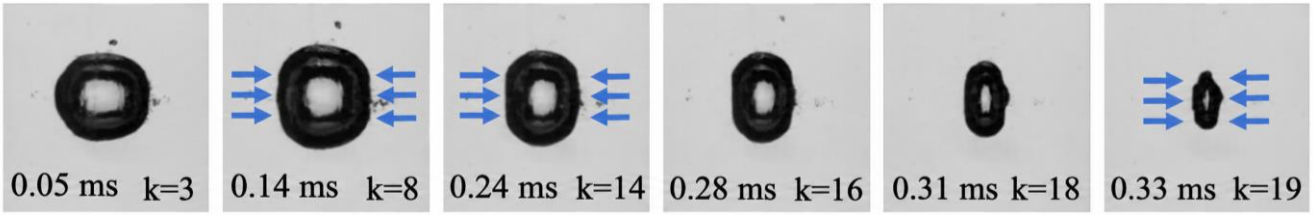


Figure 3. Bubble evolution for R = 13 mm and a maximum equivalent radius of 1.5 mm. Echo indices are acoustic-model estimates; arrows illustrate proposed forcing, not resolved pressure fronts. Reproduced from [1].

Across the tested conditions, changing the tube radius modifies both deformation and the reported collapse time. Narrower tubes generally exhibit longer collapse times for a given maximum bubble size. Larger bubbles show pronounced deformation over a wider range of confinement radii. Comparisons at equal absolute time should be interpreted with care because the oscillation period changes between cases: the same time can correspond to different stages of collapse.

The acoustic return-time relation establishes that smaller tubes produce earlier reflections. It does not, by itself, prove a larger reflected amplitude or explain the longer collapse time. The surrounding liquid inertia also changes with confinement. A consistent interpretation is that early reflected pulses can initiate a shape disturbance, which then develops through the coupled motion of the bubble and liquid. The observed morphology supports this mechanism, while its quantitative contribution remains to be separated from other confinement effects.

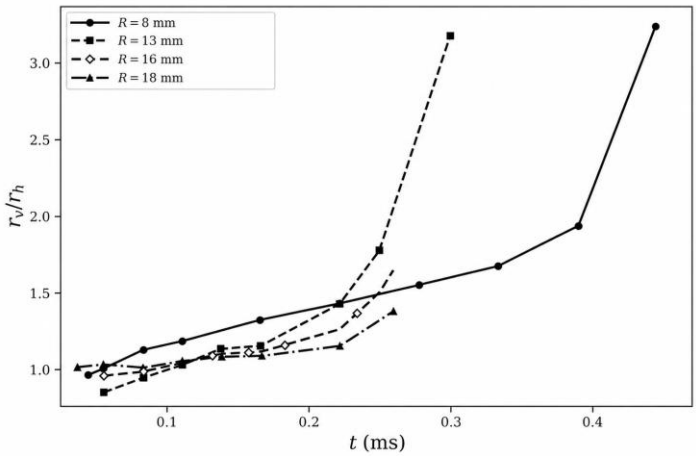


Fig. 4. Temporal evolution of the bubble aspect ratio for different tube radii at ($r_{eq,max}$ = 1.3) mm. Smaller tube radii resulted in more frequent echo interactions, causing stronger bubble elongation and delayed collapse.

5 Molecular dynamics comparison

To examine wave–bubble coupling at a smaller scale, coarse-grained molecular dynamics simulations were performed in LAMMPS for water confined within a rigid carbon nanotube bounded by aluminium end slabs. The system was equilibrated at 298 K before energy was deposited in a small central region. Two deposited energies, 1 and 10 fJ, were considered. This model represents the hydromechanical consequences of localized energy deposition; it does not resolve the electronic processes of optical breakdown.

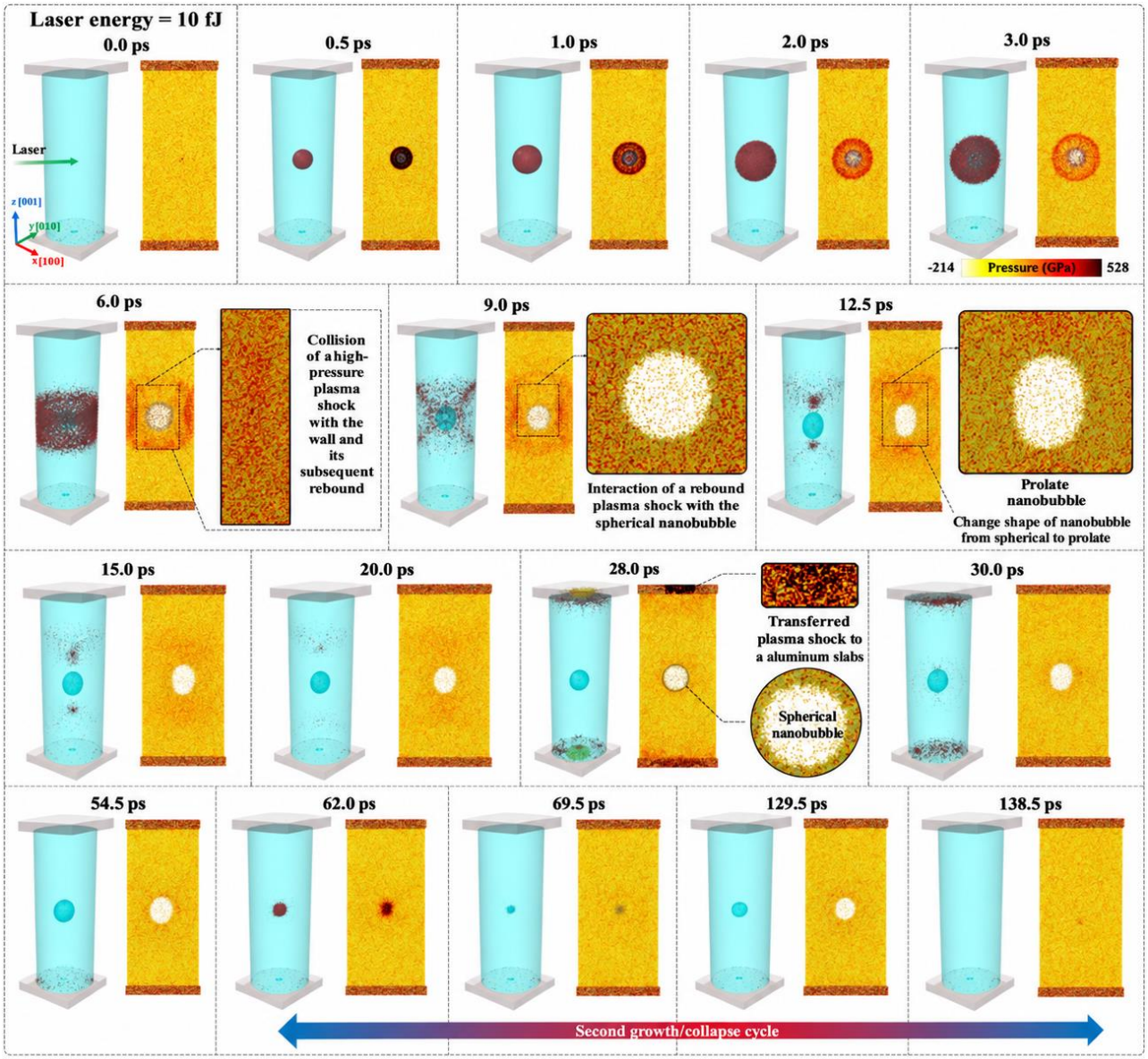


Figure 4. Surface mesh and pressure map under 10 fJ laser irradiation, showing plasma-shock propagation and subsequent nanobubble nucleation, growth, and collapse. The color bar indicates pressure in the 1 nm-thick z–x cross-section at 2.0 ps. Reproduced from [1].

At 1 fJ, a nanobubble forms, expands to a maximum radius of approximately 6.2 nm and subsequently collapses. The reflected disturbance weakens before appreciably affecting the interface. At 10 fJ, a stronger wave reaches the wall and returns to the bubble near 8 ps (figure 4). The ensuing interaction produces radial compression and a prolate shape visible around 12.5 ps. The bubble relaxes towards a nearly

spherical configuration by approximately 28 ps. Later dynamics also involve reflections from the end slabs and secondary growth–collapse cycles [1].

The higher-energy simulation therefore resolves a sequence of wave arrival, interface deformation and shape relaxation that is consistent with the proposed acoustic mechanism. However, the molecular and experimental systems differ in relative confinement, wall impedance, time scale and the balance between inertia and surface tension. Their comparison supports a qualitative physical interpretation, rather than a quantitative similarity law. In particular, the rapidly increasing capillary pressure at small bubble size favours fast restoration of sphericity at the nanoscale.

6 Conclusions and outlook

The experiments demonstrate that cylindrical confinement changes the morphology and collapse timing of laser-induced cavitation bubbles. Tube radius sets the approximate acoustic round-trip time, providing a geometric means of shifting reflected-wave arrival relative to bubble motion. The molecular dynamics results show that a sufficiently strong returning wave can induce radial compression and axial elongation, supporting early reflected pulses as a plausible source of the prolate deformation observed experimentally.

The present evidence does not isolate acoustic forcing from the change in liquid inertia caused by confinement. Direct pressure measurements or fully coupled wave–bubble calculations would help determine the relevant impulse and its dependence on bubble phase. Comparisons at matched oscillation phase, together with systematic changes in wall impedance and end-boundary conditions, would further distinguish the mechanisms. These steps would improve the use of confinement geometry to control cavitation while avoiding an interpretation based on the cumulative action of many strongly attenuated echoes.

References

[1] Dawoodian, M., et al. (2026). Interaction between reflected shock waves and laser-induced cavitation bubbles. Ultrasonics Sonochemistry, 129, 107842. doi:10.1016/j.ultsonch.2026.107842.

[2] Vogel, A., Busch, S., and Parlitz, U. (1996). Shock wave emission and cavitation bubble generation by picosecond and nanosecond optical breakdown in water. Journal of the Acoustical Society of America, 100, 148–165. doi:10.1121/1.415878.

[3] Sankin, G. N., Simmons, W. N., Zhu, S. L., and Zhong, P. (2005). Shock wave interaction with laser-generated single bubbles. Physical Review Letters, 95, 034501. doi:10.1103/PhysRevLett.95.034501.

[4] Bokman, G. T., Biasiori-Poulanges, L., Meyer, D. W., and Supponen, O. (2023). Scaling laws for bubble collapse driven by an impulsive shock wave. Journal of Fluid Mechanics, 967, A33. doi:10.1017/jfm.2023.514.

[5] Oguz, H. N., and Prosperetti, A. (1998). The natural frequency of oscillation of gas bubbles in tubes. Journal of the Acoustical Society of America, 103, 3301–3308. doi:10.1121/1.423043.

Interaction between reflected shock waves and laser-induced cavitation bubbles near a solid boundary

Gohar Moloudi[1], Mazyar Dawoodian[2], Sasan Rezaee[1], Ould el Moctar[2]

[1]*Institute for Sustainable and Autonomous Maritime Systems, University of Duisburg-Essen, 47057 Duisburg, Germany*

[2]*Autonomous and Energy-efficient Maritime Technologies, Technische Universität Berlin, 10623 Berlin, Germany*

Corresponding author: gohar.moloudi@stud.uni-due.de

1. Introduction

The dynamics of cavitation bubbles have been studied for many years because of their importance in engineering and medical applications (Brennen, 2015). A bubble in an unbounded liquid expands and collapses almost spherically, and its radius can be predicted with models of the Rayleigh–Plesset type (Lauterborn and Kurz, 2010). A nearby rigid wall breaks this symmetry. The liquid can flow freely towards the bubble only from the side away from the wall, so the bubble moves towards the wall and a liquid jet pierces it in the same direction (Blake et al., 1986; Lechner et al., 2020). Curved walls or a second wall change the direction and speed of this jet as well as the collapse time (Tomita et al., 2002; Brujan et al., 2018).

Pressure waves coming from outside also influence the collapse. A shock wave that hits a bubble compresses it unevenly and can drive a fast jet along the direction in which the wave travels (Sankin et al., 2005). When such a wave is reflected from a nearby rigid surface, the non-spherical collapse becomes stronger, the collapse time shorter and the jet faster (Calvisi et al., 2008; Zhao et al., 2026). Bubbles in narrow tubes, on the other hand, become elongated and live longer than in open water (Yuan et al., 1999; Li et al., 2024).

A laser-induced bubble produces its own shock wave at breakdown. At a water–solid boundary part of this wave is sent back, and the size of this part follows from the acoustic impedances of the two media (Kinsler et al., 2000). Inside a cylinder the reflected wave travels back to the axis, where the bubble sits, and the same happens again after every round trip. Dawoodian et al. (2026) found that these repeated echoes lead to a prolate (elongated) bubble shape and delay the collapse when they arrive early in the bubble lifetime, and that wider cylinders weaken the effect.

Although the effects of a rigid boundary and of cylindrical confinement on cavitation bubbles have each been investigated, little is known about their combined influence. In particular, it has not yet been examined how the asymmetry imposed by the wall interacts with the repeated loading by reflected shock waves during the collapse. The present study addresses this question experimentally. A laser-induced bubble is generated near a rigid wall inside a cylinder, the propagation and reflection of the breakdown shock wave are analysed, and the resulting bubble dynamics are compared with those near the same wall without confinement.

2. Experimental setup

Bubbles were produced by focusing single 6 ns pulses of a Q-switched Nd:YAG laser (Q-Smart 450, 1064 nm) into a water-filled acrylic cuvette of 50 mm inner edge length. An attenuator in the beam path set the pulse energy and thus the bubble size, and an aspheric lens placed the focus. Inside the cuvette stood an acrylic (PMMA) cylinder of radius R = 8 or 13 mm with 2 mm thick walls, open to the surrounding water. A 1 mm thick glass plate on an adjustable holder lay across the cylinder, perpendicular to its axis, and acted as the rigid wall (Fig. 1). The laser focus was placed on the cylinder axis at D = 1.645 mm above the plate. As a reference, the same plate was used in the cuvette without a cylinder.

A Phantom v2012 camera recorded shadowgraphs at 180 000 frames per second, i.e. one image every 5.6 µs, with 0.86 µs exposure and a diffused 60 W LED as back light; a TTL signal from the laser triggered the camera. Under identical settings the maximum equivalent bubble radius varied by about 1.3 % from shot to shot.

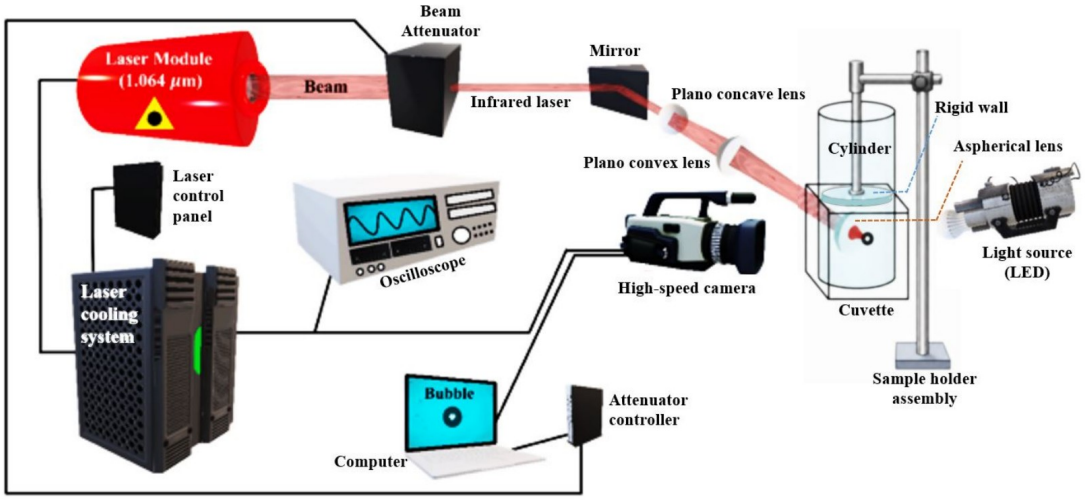


Fig. 1 Experimental setup for the generation of a laser-induced bubble near a rigid wall inside a cylinder and for shadowgraph imaging with a high-speed camera.

3. Results

3.1. Propagation and reflection of shock waves

Away from the small plasma volume, the peak pressure of the breakdown shock falls roughly inversely with distance; absorption in water reduces it further, but only slightly over the distances considered here (Dawoodian et al., 2026):

$$p(r) = p_0 \, (r_0 / r) \, \exp[-\alpha_{\mathrm{eff}} \, (r - r_0)]. \tag{1}$$

Here p_0 and r_0 stand for the pressure and the radius of the plasma region, taken as 1 GPa and 50 µm as in Dawoodian et al. (2026), and α_{eff} accounts for absorption. At a boundary between water (w) and a solid (s), only a fraction of the wave is sent back:

$$\Gamma = (Z_{\mathrm{s}} - Z_{\mathrm{w}}) / (Z_{\mathrm{s}} + Z_{\mathrm{w}}), \quad Z = \rho c. \tag{2}$$

Using 1.48 MRayl for water, 3.20 MRayl for PMMA and 13.75 MRayl for glass gives $\Gamma \approx 0.37$ for the cylinder and $\Gamma \approx 0.81$ for the glass plate. Because the cylinder wall surrounds the bubble, the wave reflected there travels back towards the axis and is concentrated on its way. Following Dawoodian et al. (2026), the peak pressure of the k-th echo on the axis is estimated as

$$p_{\mathrm{c}}^{(k)} = G \, p_0 \, (r_0 / R) \, \exp(-2\alpha_{\mathrm{eff}} R) \, \beta\Gamma \, [\beta\Gamma \exp(-2\alpha_{\mathrm{eff}} R)]^{k-1}, \quad k = 1, 2, \ldots \tag{3}$$

Here $\Gamma = \Gamma_{\mathrm{PMMA}}$, the gain $G = R/\Delta$ describes the concentration over a width Δ near the axis, and the factor $\beta \approx 0.135$ reduces it, because the wave still spreads along the axis. Since $\beta\Gamma$ is well below one, every further round trip leaves a much weaker echo, and the bubble is mainly affected by the first few. The reflection from the glass plate, in contrast, is a single, one-sided event and is not focused. The plate reflection and the cylinder echoes reach the bubble at

$$t_{\mathrm{w}} = 2D / c, \qquad t_{\mathrm{c}}^{(k)} = 2kR / c. \tag{4}$$

For $c = 1480$ m/s this gives 2.2 µs for the plate and an echo period of 10.8 µs for $R = 8$ mm and 17.6 µs for $R = 13$ mm. Since the bubble lives for roughly half a millisecond, it is hit by several tens of echoes.

To visualise these waves, the same geometry was modelled in COMSOL Multiphysics. A point source on the axis replaces the bubble, and the cylinder wall, the glass plate and its holder are included; the bubble itself is not modelled. Fig. 2 shows the computed pressure field.

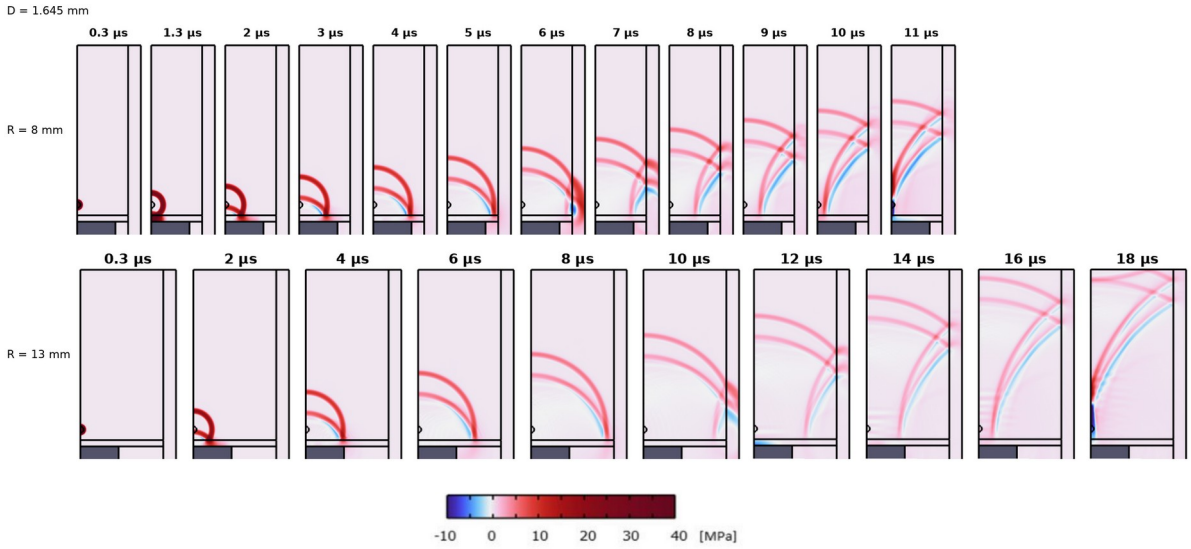


Fig. 2 Computed pressure field at successive times after breakdown for D = 1.645 mm; top: R = 8 mm, bottom: R = 13 mm. Each frame shows one half of the cylinder, with the axis on the left and the glass plate below the source.

The plate, being closest to the source, reflects the wave first, after about 2 µs, and this reflection moves upwards from one side only. The outgoing front meets the cylinder wall after about 5 µs (R = 8 mm) or 9 µs (R = 13 mm). The part reflected there moves back towards the axis, followed by a region of tension. The first cylinder echo arrives on the axis after about 11 µs in the small and 18 µs in the large cylinder, as predicted by Eq. (4).

3.2. Bubble dynamics near the rigid boundary

Fig. 3 compares a bubble with a maximum equivalent radius of $R_{eq,max} \approx 1.4$ mm inside the 8 mm cylinder with the same bubble in the cuvette. With D = 1.645 mm, the normalised stand-off distance $\gamma = D/R_{eq,max}$ is about 1.15, so the wall clearly influences the collapse in both cases. At their maximum size both bubbles are nearly spherical, apart from a slightly flattened lower interface on the wall side.

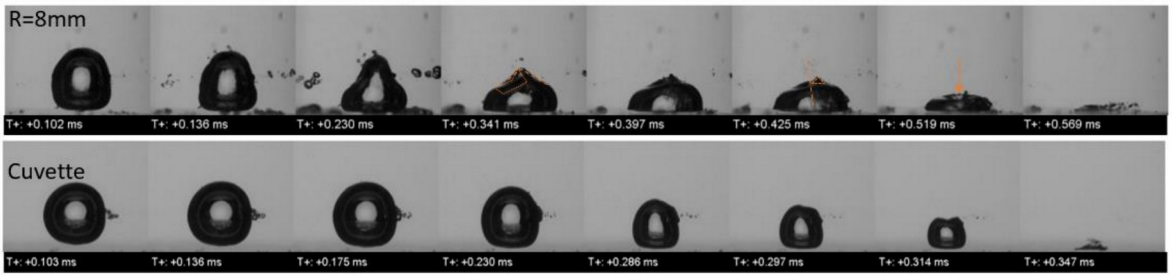


Fig. 3 Shadowgraphs of a bubble at D = 1.645 mm above the glass plate (bottom of each frame), inside the 8 mm cylinder (top row) and without a cylinder (bottom row); $R_{eq,max} \approx 1.4$ mm. Times are given after breakdown; the orange lines highlight the interface and the jet.

Without the cylinder, the lower interface flattens slightly further while the upper part remains nearly hemispherical, and the bubble contracts almost uniformly until the jet appears near the end of the collapse. The smallest volume is reached at about 0.35 ms.

Inside the cylinder, the lateral interfaces start to move inward soon after the maximum expansion, while the lower interface remains flat on the wall side. At 0.230 ms the bubble has a triangular profile with a broad base and a narrowing upper part. The lateral interfaces then curve inward and a sharp apex forms. Only then does the jet develop at the apex and penetrate the bubble towards the wall, and the remaining bubble collapses as a thin layer near the wall at about 0.57 ms.

The two sequences also differ in timing: the first collapse ends at about 0.57 ms inside the cylinder, compared with about 0.35 ms in the cuvette. When the triangular shape appears at 0.230 ms, about twenty cylinder echoes have already reached the bubble according to Eq. (4), so the deformation builds up gradually over many echoes rather than being caused by a single wave. In both cases the bubble

moves towards the wall during the collapse and the jet is directed at the wall. The cylinder therefore does not change the jet direction, but the jet forms later, only after the sharp apex has developed.

4. Conclusions

For a bubble 1.645 mm from a rigid wall inside a cylinder, the breakdown shock comes back in two ways: once from the wall, early and only from below, and many times from the cylinder, each time focused on the axis. The estimates and the simulation agree on when these waves arrive. In the experiment, the repeated waves compress the bubble laterally while the wall keeps its lower interface flat. The bubble develops a triangular profile and a sharp apex before the jet forms, and takes longer to collapse than without the cylinder. In a smaller cylinder the echoes return earlier and more often.

Next, further wall distances and bubble sizes will be examined, and numerical simulations of the bubble including phase change and heat transfer are planned.

References

Blake, J.R., Taib, B.B., Doherty, G., 1986. Transient cavities near boundaries. Part 1. Rigid boundary. J. Fluid Mech. 170, 479–497.

Brennen, C.E., 2015. Cavitation in medicine. Interface Focus 5, 20150022.

Brujan, E.A., Noda, T., Ishigami, A., Ogasawara, T., Takahira, H., 2018. Dynamics of laser-induced cavitation bubbles near two perpendicular rigid walls. J. Fluid Mech. 841, 28–49.

Calvisi, M.L., Iloreta, J.I., Szeri, A.J., 2008. Dynamics of bubbles near a rigid surface subjected to a lithotripter shock wave. Part 2. Reflected shock intensifies non-spherical cavitation collapse. J. Fluid Mech. 616, 63–97.

Dawoodian, M., Rezaee, S., Barman, D., el Moctar, O., Manso Sainz, R., Mettin, R., Lechner, C., 2026. Interaction between reflected shock waves and laser-induced cavitation bubbles. Ultrason. Sonochem. 129, 107842.

Kinsler, L.E., Frey, A.R., Coppens, A.B., Sanders, J.V., 2000. Fundamentals of Acoustics, 4th ed. John Wiley and Sons.

Lauterborn, W., Kurz, T., 2010. Physics of bubble oscillations. Rep. Prog. Phys. 73, 106501.

Lechner, C., Lauterborn, W., Koch, M., Mettin, R., 2020. Jet formation from bubbles near a solid boundary in a compressible liquid: Numerical study of distance dependence. Phys. Rev. Fluids 5, 093604.

Li, J., Zhou, M., Luo, J., Xu, W., Zhai, Y., Qu, T., Zou, L., 2024. Collapsing behavior of spark-induced cavitation bubble in rigid tube. Ultrason. Sonochem. 103, 106791.

Sankin, G.N., Simmons, W.N., Zhu, S.L., Zhong, P., 2005. Shock wave interaction with laser-generated single bubbles. Phys. Rev. Lett. 95, 034501.

Tomita, Y., Robinson, P.B., Tong, R.P., Blake, J.R., 2002. Growth and collapse of cavitation bubbles near a curved rigid boundary. J. Fluid Mech. 466, 259–283.

Yuan, H., Oguz, H.N., Prosperetti, A., 1999. Growth and collapse of a vapor bubble in a small tube. Int. J. Heat Mass Transf. 42, 3643–3657.

Zhao, J., Qi, M., Zhang, W., Pang, X., Cao, S., 2026. Shock-induced bubble collapse near a plate. Int. J. Mech. Sci., 111569.

Modelling Cavitation of Lifting Surfaces for use during Preliminary Design

Raul Bajimaya, Stephen Watson

QinetiQ, Gosport, United Kingdom, PO12 1GH
raul.bajimaya@qinetiq.com

Introduction

In hydrodynamics, cavitation can have significant impact on the performance, operability and structural integrity of devices. This is typically prominent for lifting surfaces where low-pressure regions localized around them can facilitate nucleation of vapour bubbles thus resulting in cavitation. Oscillations and violent collapse of these vapour bubbles lead to surface pitting and erosion along with an increase in cavitation induced noise. To minimize these detrimental effects of cavitation, it is essential that this phenomenon is taken into account during the preliminary design stages for such devices.

Current methods that predict the detailed cavitation characteristics of lifting surfaces generally require high fidelity numerical simulations. Although these simulations can provide accurate predictions, the computational costs associated with them make them unfeasible during preliminary design stages where rapid assessments are necessary. An in-house mathematical tool is being developed to resolve this and enable rapid predictions of cavitation at early stages of design cycles. This work aims to give some overview of the methodology and outline the capabilities of this mathematical model in predicting detailed cavitation behaviour of hydrodynamic devices.

The general objective is to develop a toolset which can take outputs from relatively low fidelity Computational Fluid Dynamics (CFD) simulations and return detailed predictions of cavitation performance for a bubble cloud system using bubble dynamics formulations. This is essentially a mixed-fidelity approach where fundamental bubble dynamics models are coupled with flow field predictions.

Preliminary results from such a tool are provided and compared against higher fidelity results – from CFD and/or experiments. The focus is mainly on the prediction capability of the process at the current stage. Comparisons will focus on not just absolute values but also on any performance trends in the design and operability space.

Standard Methods and Processes

It is worth nothing that the method includes several assumptions and idealisations at present. This includes assumptions such as bubbles are perfectly spherical, flow field is generally homogeneous etc.

Initially, flow fields of the relevant parameters are extract from converged results of steady Reynolds Averaged Navier-Stokes (RANS) based CFD simulations. Calculations are carried out on these flow fields to determine the behaviour and characteristics of bubbles. Bubble behaviour can then be used to extract useful parameters such as Sound Pressure Level (SPL).

Based on the flow field characteristics, the critical radius for nucleation of bubbles can be determined. The process uses classical nucleation theory with the assumption of homogeneous nucleation based on work from Gibbs (1878). This process compares the energy cost of creating an interface between vapour and liquid of a bubble and the energy state of the vapour and the liquid. This comparison leads to the equation for critical radius, r_{crit}:

$$r_{crit} = -\frac{2\gamma}{\Delta G_v} \tag{1}$$

In equation 1, γ is the surface tension and ΔG_v is the Gibbs free energy during phase change. For simplicity, the value of ΔG_v is set as the difference between the vapour pressure inside the bubble (from CFD extracted flow field) and the pressure of the surrounding liquid (freestream value). This critical size is necessary for later calculations.

Following the calculation for critical radius for nucleation, the growth and response to the ambient pressure field is determined for these bubbles. The standard method is to use the Rayleigh-Plesset (1949) equation which relates bubble response $\left(R, \dot{R}, \ddot{R}\right)$ to the pressure field $(p_B - p_\infty)$, surface tension (σ) and fluid viscosity (μ) (eq. 2).

$$R\ddot{R} + \frac{3}{2}\dot{R}^2 = p_B - p_\infty - \frac{2\sigma}{R} - \frac{4\mu\dot{R}}{R} \tag{2}$$

While the Rayleigh-Plesset equation can model bubble behaviour, it starts to break down during aggressive collapse conditions such as those found during cavitation. This is mainly because the pressure in the bubble does not remain constant during such complex conditions as explained by Brennan (1995). During such conditions, it is necessary to account for the effects of liquid compressibility. This enables more accurate modelling of the collapse and rebound phases during bubble oscillation.

There are a range of different methods to account for the liquid compressibility, however the well-established first order compressible Keller-Miksis equation has been elected for the purposes of this work. The primary appeal of the Keller-Miksis model is that it accounts for pressure, surface tension and viscosity – like the standard Rayleigh-Plesset equation – but also includes the effects of compressibility (related to speed of sound, c) and resulting acoustic radiation behaviour as shown by Keller et al. (1980). The Keller-Miksis formulation is given in eq. 3.

$$\left(1 - \frac{\dot{R}}{c}\right)R\ddot{R} + \frac{3}{2}\left(1 - \frac{\dot{R}}{3c}\right)\dot{R}^2 = \frac{1}{\rho}\left(1 + \frac{\dot{R}}{c} + \frac{R}{c}\frac{d}{dt}\right)\left(p_B - p_\infty - \frac{2\sigma}{R} - \frac{4\mu\dot{R}}{R}\right) \tag{3}$$

For a bubble in a prescribed pressure field with a defined surface tension and liquid viscosity, it is possible to solve the equation above and extract transient behaviour of bubble radius, wall velocity and wall acceleration. However, this assumes that the bubbles are uncoupled and act in isolation, but this is not always true. There are a range of ways in which bubbles affect one another. Two such mechanisms include acoustic coupling and coalescence.

Acoustic coupling in this case refers to the condition where the response of a given bubble does not only depend on the ambient pressure field but also on any radiated pressure waves from other cavitating bubbles. This process fundamentally requires the calculation of pressure wave propagation in bubbly liquids. This exact process is explained by Commander et. al. (1988) where they use vapour volume fraction (β) based continuity and momentum equations to arrive at a wave equation that relates the pressure field to the bubble sizes (equation 4).

$$\frac{1}{c^2}\frac{\partial^2 P}{\partial t^2} - \nabla^2 P = \rho\frac{\partial^2 \beta}{\partial t^2}, \qquad \beta = \frac{4}{3}\pi R^3 n, \qquad n = number\ density\ of\ bubbles \tag{4}$$

Simplifications to the above equation can be introduced by assuming a homogeneous field. The effect of pressure waves arriving from cavitating bubbles can be accounted for when calculating the dynamics of bubbles by coupling equations 3 and 4. The number of bubbles per unit volume (number density) can generally be estimated or tuned using a power law equation such as that proposed by Medwin et. al. (1989).

The second mechanism of interest is coalescence where two smaller bubbles combine to form one larger bubble. While the number of bubbles in the flow field has reduced the overall gas volume fraction is maintained as a constant. Coalescence is of interest as altering the size of a bubble results in a change in the response of the bubble in terms of the oscillation frequency and amplitude. The physics behind coalescence falls under the family of coagulation where two particles combine to form a single particle while ensuring volume is conserved. This process is described by Smoluchowski (1916). The general form of the Smoluchowski coagulation equation is given by equation 5.

$$\frac{dn_k}{dt} = \frac{1}{2}\sum_{i+j=k} K(i,j)n_i n_j - n_k\sum_{j=1}^{\infty} K(k,j)n_j \tag{5}$$

The above equation calculates the rate at which bubbles of size k are produced by combining bubbles of size i and j, and the rate at which bubbles of size k are destroyed. This is based on the number density (n) of bubbles of size i, j and k, and the coagulation kernel $K(x, y)$. This kernel describes the collision rate between bubbles of size x and y and is dependent on the type of system in which coagulation is taking place.

Combining and solving equations 3, 4 and 5 while using equation 1 to give the minimum bubble radius, the response of bubble clouds to the local flow field can be calculated while accounting for compressibility, acoustic radiation, acoustic coupling and coagulation. The Keller-Miksis equation is a second order ordinary differential equation and is solved using standard mathematical processes. This method has been developed in MATLAB R2025b and all CFD simulations have been run in STAR CCM+.

Sample Results

The purpose of this section is to mainly demonstrate the current capabilities of the current process.

It is initially necessary to ensure that the process and the code work as intended and is without any errors. To achieve this, a sample result from Brennen (1995) is compared against the equivalent predictions from the currently developing process. A comparison is made of the peak bubble oscillation frequency as a function of bubble radius at a range of ambient pressures (Figure 1).

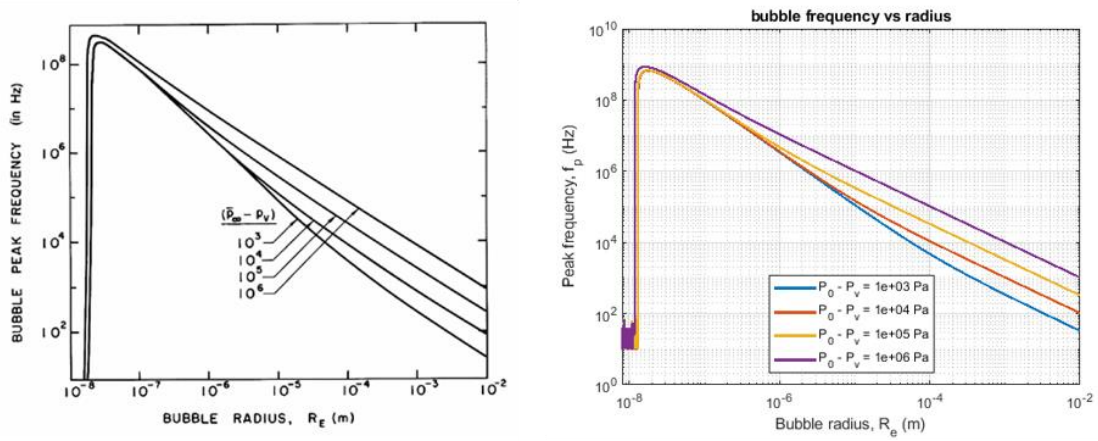


Figure 1 Comparison of relation between bubble radius and peak frequency predicted in literature (left) and predicted by the current model (right).

The model is able replicate results from literature. The overall trends within the explored space are similar. For example, at a given bubble radius (greater than 10^{-5}m), increasing the ambient pressures increases the peak oscillation frequency. It is also clear that as bubble radius decreases, the peak oscillation frequency increases but eventually collapses. This behaviour has been captured by the model. This indicates that overall physics has been captured without any errors.

The response behaviour in Figure 1 can be explained by analysing the bubble as a mass-spring-damper system. The mass is related to the bubble size, the damping contribution comes from viscosity, and the stiffness is related to the surface tension. As the size of the bubble decreases, the mass decreases which causes the peak frequency to increase. As the size further decreases the fluid viscosity, relative to the stiffness, becomes large resulting in a highly damped system without any oscillations leading to the abrupt frequency collapses.

From the Keller-Miksis equation (eq. 3), it is possible to extract the unsteady cavitation characteristics of a given bubble by applying a synthetic gaussian pressure pulse to that bubble. Detailed characteristics at the bubble wall can be extracted and the physical effects of viscous damping and the acoustic radiation damping can also be modelled. This behaviour can be seen in Figure 2.

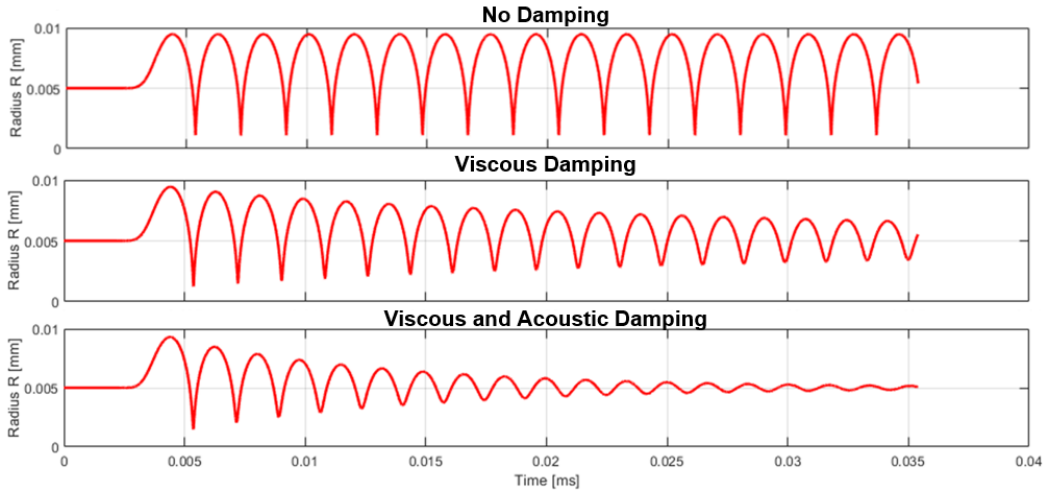


Figure 2 Bubble response to a synthetic pressure pulse calculated using the Keller-Miksis model without any damping (top), with viscous damping (middle), and with viscous and acoustic damping (bottom).

The displacement plots show an oscillatory response with a smooth bubble growth and a sharp bubble collapse pattern which is characteristic of cavitation. Without any damping, the amplitude remains constant with time. As viscous damping is introduced, there is a gradual reduction in amplitude and frequency. This amplitude and frequency decrease is further amplified when acoustic radiation damping is also introduced.

Depending on the strength (amplitude) and the duration of the synthetic gaussian pressure pulse, it is possible to explore the response of the bubble and characterise if a given bubble cavitates. By processing the bubble response behaviour, the difference between a cavitating bubble and a non-cavitating bubble becomes apparent. Bubbles that cavitate often have a large difference between their minimum and maximum radius. Bubbles that do not cavitate result in a sinusoidal wall displacement response (Figure 3).

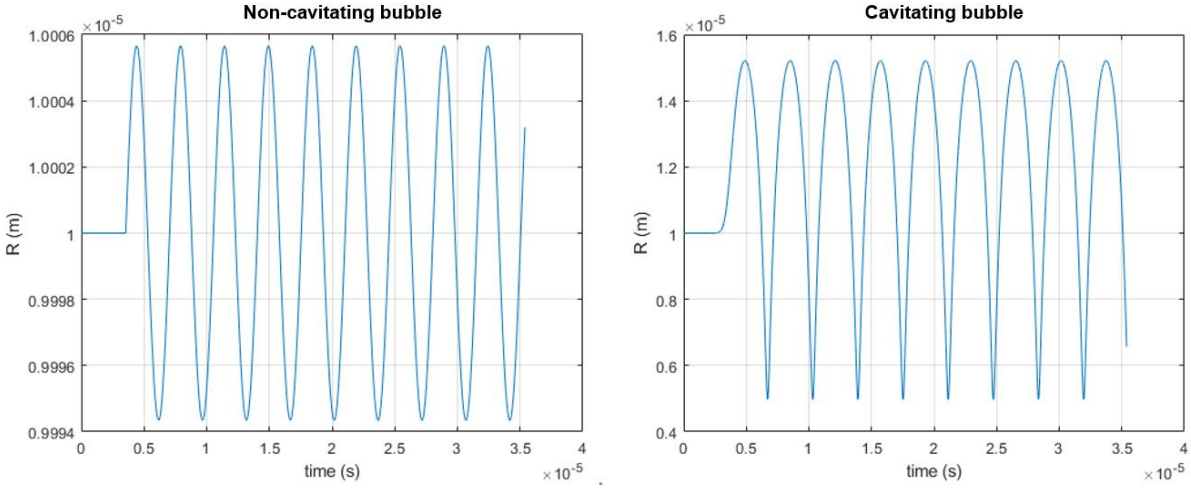


Figure 3 Response to a weak synthetic pulse resulting in a non-cavitating bubble (left) and a strong synthetic pulse resulting in a cavitating bubble (right).

One method to use the above signals to characterise if a bubble is cavitating is by finding the ratio of the amplitude of the second highest peak to the amplitude of the highest peak in the frequency domain. For sinusoidal (non-cavitating) signals, such a process gives an amplitude ratio of close to zero while for cavitating bubbles, that ratio is higher. Conducting a sweep of Gaussian pulse amplitude and duration across a sensitivity space allows identification of regions where cavitation occurs (Figure 4). The yellow region represents the area within which cavitation occurs – localised around the high amplitude magnitude and long pulse duration. At very high pulse amplitude magnitudes and very long pulse durations, the bubble grows continuously and does not oscillate resulting in no data in the upper-left region of the plot.

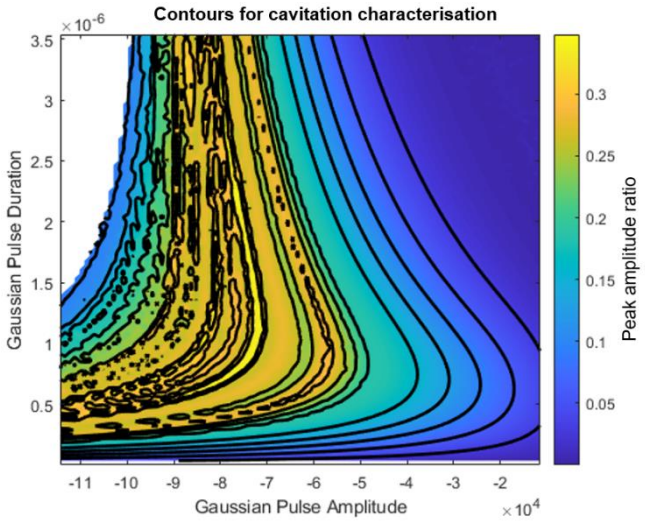


Figure 4 Contour of ratio of amplitudes of the first two peaks of bubble response signal in the frequency domain.

A realistic use of this cavitation modelling tool is to apply it to bubble clouds in conjunction with flow field outputs from CFD. Discrete bins of various bubble sizes can be selected, and the dynamics of these bubbles can be solved for pressure fields along flow paths extracted from CFD. This enables the calculation of bubble wall displacement response for all bubbles which can be converted to an unsteady pressure signal for all bubbles. This pressure signal can then be converted into an SPL signal to give cavitation noise predictions (Figure 5). The presented figure is for a Fruman hydrofoil case operating at an angle of attack of 5° and a freestream velocity of 20 m/s. The CFD simulation was run on STAR-CCM+ using steady RANS equations and the k-ω SST turbulence model. Both figures present results without any damping activated purely for demonstration purposes.

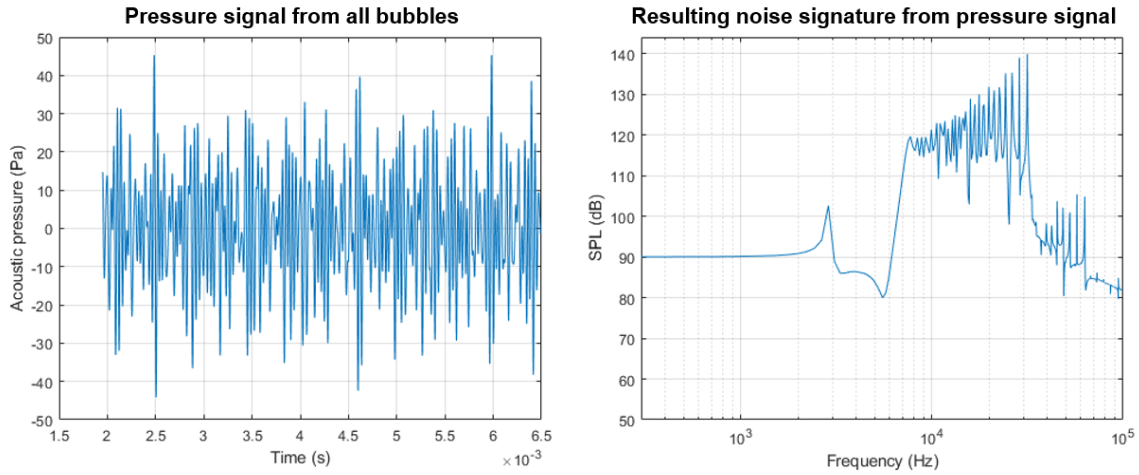


Figure 5 Pressure signal (left) and SPL plot (right) calculated by applying bubble dynamics model to CFD.

At the current stage, the model can also account for acoustic coupling and bubble coalescence to arrive at a prediction of SPL levels. CFD simulations were run for a simple unclassed 2-bladed propeller. The simulations were complemented by running experiments of the same propeller geometry at the same 1200 RPM in a cavitation tunnel simulated to operate in a wake. The experiments also measured the SPL properties of the propeller while cavitating. The experiment was run at a single tunnel speed of 4 m/s and 3 tunnel operating pressures of 0.4 bar, 0.6 bar and 0.8 bar. Having access to the noise data from experiments along with CFD simulations of the identical geometry at similar operating conditions means that the prediction capability of the full cavitation tool can be tested. The plot in Figure 6 shows SPL as a function of frequency at the three tunnel operating conditions. The solid lines are results from experiments while the dashed lines are predictions form the model. The resulting noise signal can generally be categorised into 3 sections: blade rate (low frequency), cavitation (intermediate frequency) and high frequency. The blade rate noise frequency only responds to blade rate. As such, a shift in the tunnel pressure only affects the noise amplitude. Both amplitude and frequency of cavitation induced noise are sensitive to variations in tunnel pressure. Fundamentally, by reducing the background pressure, the critical radius for nucleation increases while the number density of bubbles decreases. The reduction in the number density is offset by the increase in bubble oscillation amplitudes. This means that at lower ambient pressures, larger bubbles are present in the flow which have a lower frequency of oscillation leading to a lower frequency noise relative to higher ambient pressure conditions. The higher frequency noise signature is most likely associated with tunnel noise and other background sources. Generally, it was found that low operating pressures result in higher noise amplitudes. This is because at such low pressures, any pre-esisting bubbles become more acoustically active and sensitive to fluctuations in pressure leading to larger oscillation ampltidues, hence increased noise levels.

Comparing experiements to predictions from the cavitation model, the amplitude and the frequency trends are similar. At low tunnel pressures, cavitation noise amplitudes are high but the frequencies are low, while the opposite is true at higher tunnel pressures. There are discrepancies in the absolute values of frequency and SPL level however this can be attributed to numerous factors. One such factor is the geometry of the bubbles. The current process only assumes purely spherical bubbles while bubbles in vortices are deformed, elongated. Such bubbles have a shift in frequency and amplitude – which needs to be accounted for by the model.

Overall, it was found that the general trends between the model and experiments were similar. At low operating pressures, the dominant frequencies were lower, and the peak SPL was higher than at higher frequencies (Figure 6). However, the absolute values of frequencies and amplitudes are not predicted to a suitable degree of accuracy. There are various reasons for these discrepancies including turbulence induced noise, motor and electrical noise and general tunnel noise (reverberations).

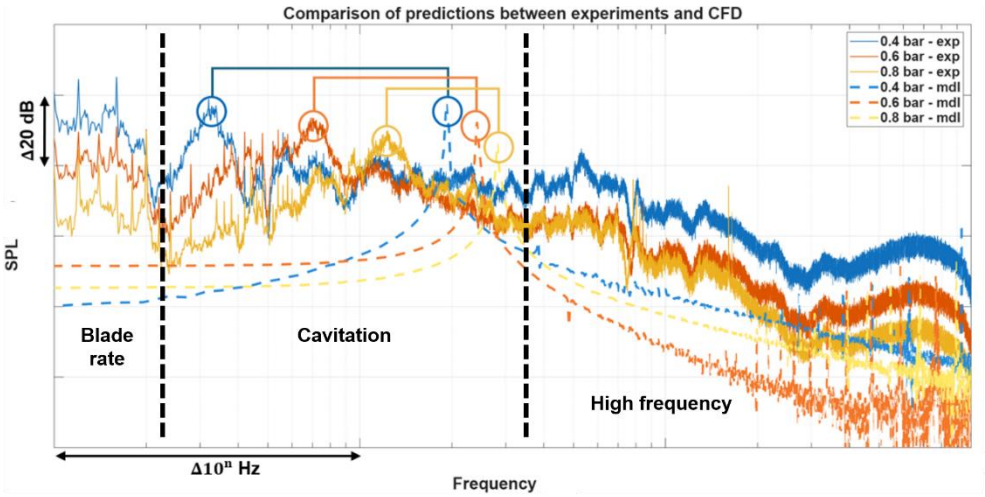


Figure 6 Comparison of SPL plot from experiments and model at three different operating pressures.

Conclusions, future steps and applications

This paper has demonstrated the capabilities of a cavitation modelling tool that is currently under development. The general process includes an initial estimation of the critical nucleation radius which is required for cavitation calculation using the Keller-Miksis model. This is a compressible formulation of the standard Rayleigh-Plesset equation. This is generally sufficient to get an initial assessment of the dynamics of a single bubble. However, the aim is to apply this tool to a bubble cloud where bubble-bubble interactions are prominent. Acoustic coupling of bubbles and coalescence models are also included in the tool.

Simple checks of the model have shown that it can replicate expected outputs such as the relation between bubble radius and peak oscillation frequency. Analysis of single bubble characteristic is possible, and processes are in place to characterize if a bubble is cavitating. For bubble clouds, it is possible to extract the acoustic pressure signal produced due to cavitation and the signal can be converted to SPL. Comparisons of measurements from CFD with outputs from the model have shown that there is a general agreement in terms of trends.

Acoustic measurements from experiments of a 2-bladed propeller have shown at low operating pressures, the frequencies associated with cavitation are low but peak SPL is high. At higher operating pressures, the cavitation-based frequencies are high but peak SPL is low. This trend was replicated by the model. However, the quantitative predictions of absolute values of frequencies are off by up to one order of magnitude.

Additional work needs to be done to improve the prediction capability of the tool. The current process does not account for any spread or uncertainties in coagulation properties. There are also sections where assumptions of a homogeneous or isotropic flow field are not strictly correct. Addressing these issues may result in better predictions of absolute values of properties such as noise signatures. It may also lead to more reasonable SPL profiles with broader peaks across wider frequency bands.

References

Gibbs, W. (1878). On the equilibrium of heterogeneous substances, Vol. 1. https://doi.org/10.5479/sil.421748.39088007099781

Plesset, M.S. (1949), The Dynamics of Cavitation Bubbles, J. of App. Mechanics, Vol. 16, Issue 3, pp:277-282

Brennan, C.E., (1995), Cavitation and Bubble Dynamics, https://doi.org/10.1017/CBO9781107338760

Keller, J.B, and Miksis, M., (1980), Bubble Oscillations of Large Amplitudes, Journal of the Acoustical Society of America. Vol.68, pp:628–633

Medwin, H., Breitz, N.D., (1989) Ambient and transient bubble spectral densities in quiescent seas and under spilling breakers, Journal of Geophysical Research: Oceans, Vol. 94, Issue C9, pp:12751-12759

Smoluchowski, M. V., (1916) Drei Vorträge über Diffusion, Brownsche Molekularbewegung und Koagulation von Kolloidteilchen, Physik. Zeit., vol. 17, pp:557-585

Investigation of Simplified Bulbous Bow Shapes for Small Cargo Ship

Yoshihisa Okada[*], Manaka Isobe[*], Mai Kishikawa[†] and Kenji Mokuo[†]
[*]Nakashima Propeller Co., Ltd., Okayama/Japan, [†]Fluid Techno Co., Ltd., Nagasaki/Japan
yoshihisa@nakashima.co.jp

1. Introduction

The bulbous bow was developed by Inui et al. with the aim of reducing wave resistance[1)2)3)]. BHP reducution by bulbous bow was confirmed 13% in actual ship test. However, the manufacturing process for bulbous bows involves increased working time due to processes such as pressing and line heating (Fig.2), leading manufacturers to prefer simpler, easier-to-manufacture bulbous bow shapes. Furthermore, with the increasing prevalence of low-speed ship operation in recent years, extreme bulbous bows are becoming less common. On the other hand, some ships still require bulbous bows. For example, small cargo ships of approximately 70m in length sailing along the Japanese coast at speeds of 11.5-12.5 knots. Their Froude number is around 0.24. In ships with such high Froude numbers, wave-making resistance accounts for a significant portion of the total hull resistance.

This study proposes a simplified spherical bow for small cargo ships operating in the coastal waters of Japan. The proposed bow features a simple geometry designed to improve manufacturability while maintaining favorable hydrodynamic characteristics. Its hydrodynamic performance was evaluated using computational fluid dynamics (CFD).

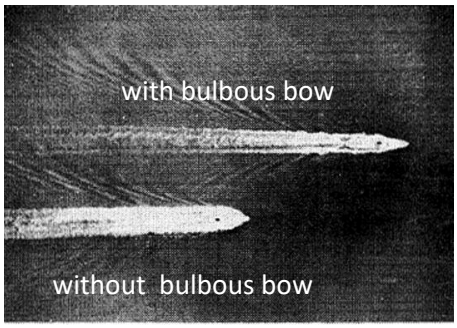


Fig.1 Comparison of wave pattern

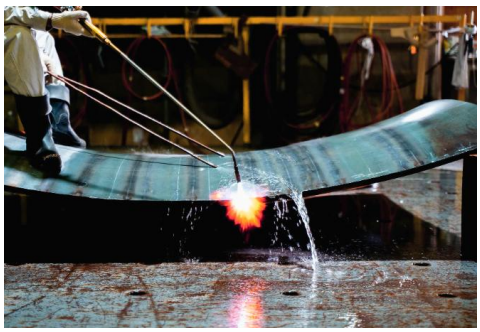


Fig. 2 Line heating for hull form[4)]

2. Target Ship for Development of Simplified Bulbous Bow

The hull form was based on that of a typical 499 GT cargo ship. The principal dimensions of the vessel are Lpp = 69.0 m, B = 12.0 m, and D = 7.12 m. As shown in Figure 3, the small cargo ship has a large cargo hold, which limits the design freedom of the bow geometry. Consequently, modifications were confined to the region forward of the Forward Perpendicular (F.P.). The shape of the original bulbous bow is shown in Figure 4.



Fig.3 General cargo for 499 GT [5)]

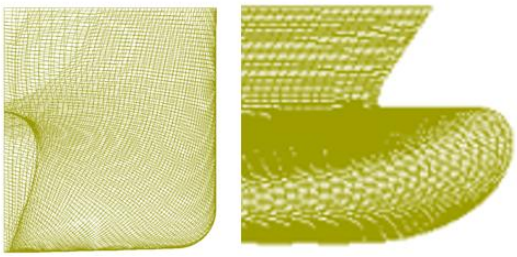


Fig.4 Bulbous bow for original ship

3. Calculation Method

CFD analysis of resistance conditions are conducted using NAGISA, a RaNS solver developed by National Maritime Research Institute (NMRI). The total number of cells is about 0.98 million. EASM is applied for the turbulence model. The calculations are carried out from 0.23 to 0.25 of froude number on a model scale (1/34.5). Figure 5 shows computational domain and hull surface.

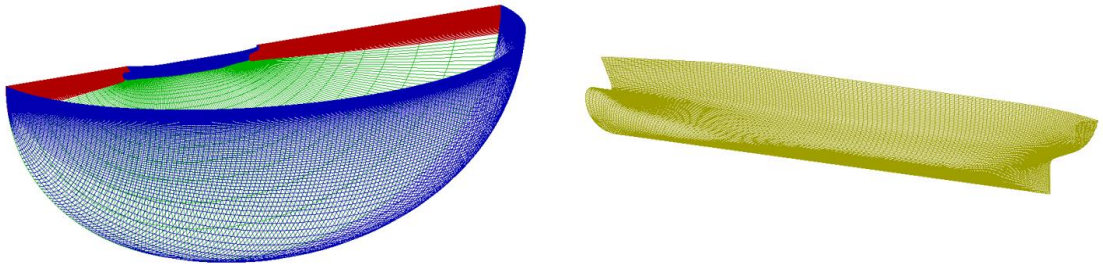


Fig. 5 Computational domain and hull surface

4. Design Variations of Simplified Bulbous Bows

4-1.Profile of Bulbous Bows

As a simplified bulbous bow, the basic N1 shape was designed. The long nose, which is easy to manufacture, was attached to the bow. Furthermore, a series of modified bow geometries was generated based on the N1 design. Based on the N1 design, the T-series was developed by systematically varying the horizontal thickness of the bulb, whereas the H-series was developed by systematically varying the bulb height. The geometries of the T series and H series are presented in Figures 6 and 7, respectively.

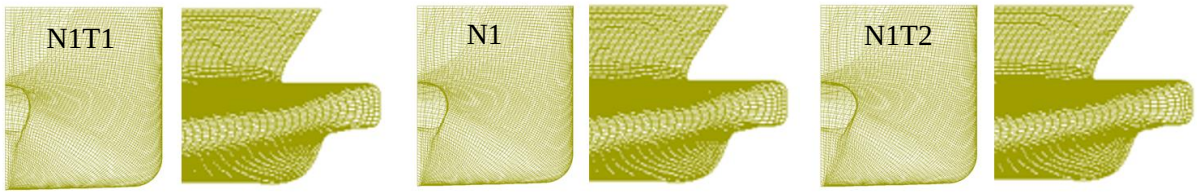


Fig.6 T-series shapes of simplified bulbous bow

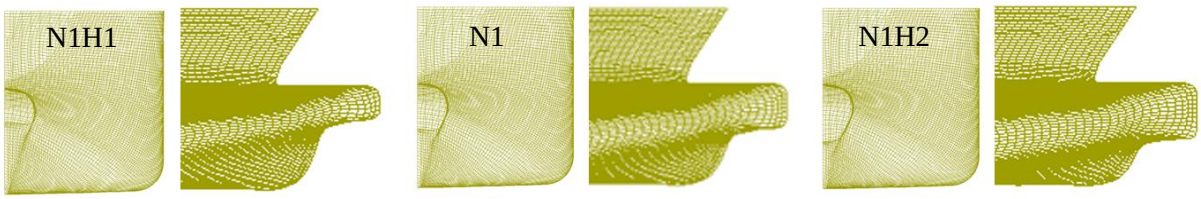


Fig.7 H-series shapes of simplified bulbous bow

4-2.Calculation Results

Figure 8 compares the wave-making resistance coefficient (Cw) of each bulbous bow under the full-load and ballast conditions. Under the full-load condition, all designs except N1T1, which has the thinnest bulb, exhibited lower wave-making resistance coefficients (Cw) than the original hull. In particular, N1T2, which has the thickest bulb, showed the largest reduction in Cw. These results indicate that a larger bulb is more effective in reducing the wave-making resistance under the full-load condition. Under the ballast condition, only N1T1, which has the thinnest bulb, and N1H1, which has the highest

bulb position, exhibited lower Cw values than the original hull. In contrast, N1T2, which has the thickest bulb, showed a marked increase in the wave-making resistance coefficient. These results indicate that a large bulb, although effective under the full-load condition, increases the wave-making resistance under the ballast condition. These results indicate that N1H1, which has the highest bulb position, is the only design that achieves a reduction in the wave-making resistance coefficient (Cw) under both the full-load and ballast conditions. This finding suggests that raising the bulb position is an effective approach for improving the wave-making performance over a wide range of loading conditions.

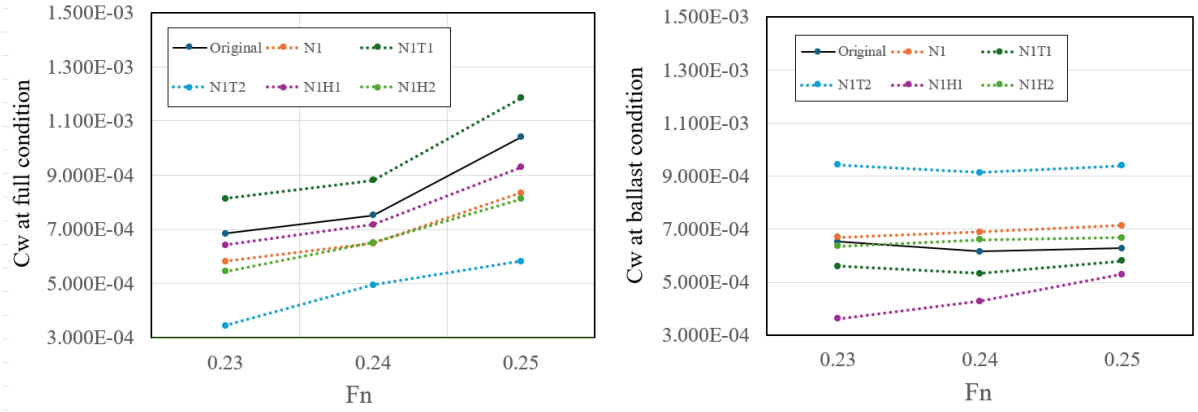


Fig.8 Comparison of Cw at full-load and ballast conditions

Figure 9 compares the effective horsepower (EHP) of each bulbous bow design under the full-load and ballast conditions. Under the full-load condition, N1T2, which has the thickest bulb, was the only design that exhibited lower EHP than the original hull over the entire range of Froude numbers investigated. In contrast, under the ballast condition, N1T2 and N1H2, which has the lowest bulb position, exhibited higher EHP than the original hull. Among all the designs, N1H1, which has the highest bulb position, achieved the greatest reduction in EHP under the ballast condition. Considering both the full-load and ballast conditions, N1H1, which has the highest bulb position, exhibited the best overall hydrodynamic performance among the simplified bulbous bow designs.

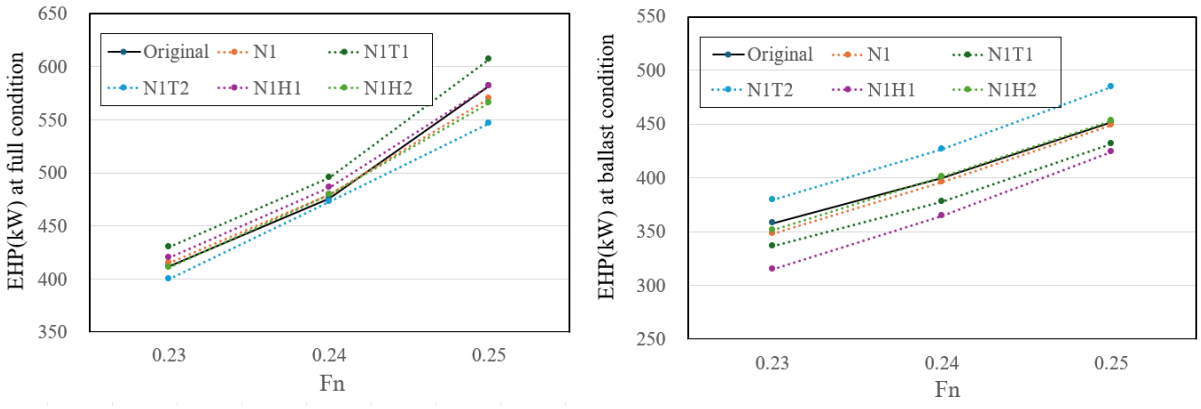


Fig.9 Comparison of EHP(kW) at full-load and ballast conditions

5. Hydrodynamic Performance of Simplified Bulbous Bows

In this section, the wave patterns of N1T2, which exhibited the lowest hull resistance under the full-load condition, and N1H1, which exhibited the lowest hull resistance under the ballast condition, are compared with those of the original hull at Fn = 0.24.

Figure 10 shows the bow wave profiles and pressure distributions of the original hull and the modified bulbous bow designs under the full-load condition. The original hull and N1H1 exhibit a distinct wave crest at the bow, whereas N1T2 produces a considerably smoother wave profile with a less pronounced wave crest.

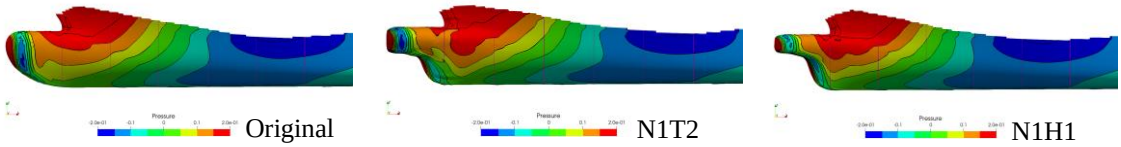


Fig.10 Wave height and pressure distribution at full-load (Fn=0.24)

Figure 11 compares the wave patterns of the original hull and the modified bulbous bow designs under the full-load condition. Compared with the original hull, N1T2, which achieved the lowest wave-making resistance coefficient (Cw), exhibits a noticeable reduction in the bow wave. This result indicates that the larger bulbous bow enhances the wave interference effect, thereby reducing wave-making resistance.

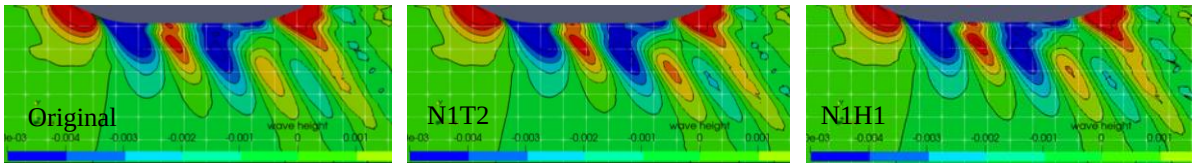


Fig.11 Wave pattern at full-load (Fn=0.24)

Figure 12 shows the bow wave profiles and pressure distributions of the original hull and the modified bulbous bow designs under the ballast condition. For the original hull and N1T2, the bow wave propagates over the upper surface of the bulbous bow, resulting in a pronounced wave crest and trough. In contrast, for N1H1, the bow wave is effectively suppressed by the extended nose of the bulbous bow, producing a flatter wave profile downstream.

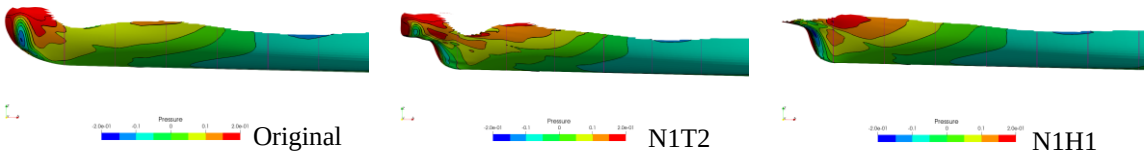


Fig.12 Wave height and pressure distribution at ballast condition (Fn=0.24)

Finally, Figure 13 compares the wave patterns under the ballast condition. Compared with the original hull and N1T2, N1H1 exhibits a noticeable reduction in wave height around the hull, indicating an overall decrease in wave generation.

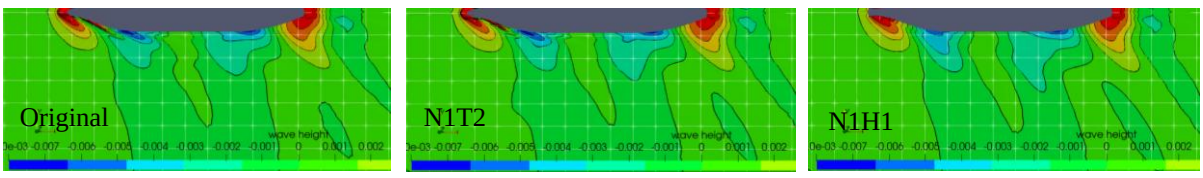


Fig.13 Wave pattern at ballast condition (Fn=0.24)

6. Conclusions

In this study, a simplified bulbous bow was designed based on a 499 GT cargo ship. In addition, the T-series, in which the horizontal thickness of the bulb was varied, and the H-series, in which the vertical position of the bulb was varied, were developed and evaluated using computational fluid dynamics (CFD). The principal findings are summarized as follows:

1) Under the full-load condition, N1T2, which has the greatest horizontal bulb thickness, achieved the largest reductions in both the wave-making resistance coefficient (Cw) and effective horsepower (EHP) compared with the original hull.

2) Under the ballast condition, N1H1, which has the highest bulb position, exhibited the lowest values of both Cw and EHP among the investigated designs.

3) Considering both the full-load and ballast conditions, N1H1 exhibited the best overall hydrodynamic performance among the simplified bulbous bow designs.

7. References

1) The Wave-Cancelling Effects of Waveless Bulb on the High Speed Passenger Coaster M/S “KURENAI MARU”(Part I-The Model Resistance and Propulsion Experiments), Takao Inui and Tetsuo Takahei, 1961Volume 1961Issue 110 Pages 75-89.

2) The Wave-Cancelling Effects of Waveless Bulb on the High Speed Passenger Coaster M/S “KURENAI MARU”((Part II-The Full-Scale Experiment), Michiya Shigemitsu and Keiji Kai, 1961Volume 1961Issue 110 Pages 91-104.

3) The Wave-Cancelling Effects of Waveless Bulb on the High Speed Passenger Coaster M/S “KURENAI MARU”(Part III-Photogrammetrical Observations of Ship Waves), Tetsuo Takahei, and Takao Inui, 1961Volume 1961Issue 110 Pages 105-118.

4) Yano Industry Co., Ltd., URL: https://www.yano-kk.jp/technology/bending/.

5) Yamanaka Shipbuilding Co.,Ltd., URL: http://yamanaka-zousen.co.jp/wordpress/?cat=7&paged=4.

Research of a Hybrid Bulbous Bow for Small Cargo Ships by CFD

Manaka Isobe[*], Yoshihisa Okada[*], Mai Kishikawa[†] and Kenji Mokuo[†]
[*]Nakashima Propeller Co., Ltd., Okayama/Japan, [†]Fluid Techno Co., Ltd., Nagasaki/Japan
isobe@nakashima.co.jp

1. INTRODUCTION

Japan is an island nation surrounded by the sea. Ships are an effective of transportation within Japan. In particular, small cargo ships classified as 499 GT in Japan are widely used because they can enter relatively small ports (Figure 1). However, there is a demand for cost reduction for 499 GT cargo ships. Therefore, improving the propulsion performance by installing energy-saving devices is often difficult.

The hybrid bulbous bow was developed based on a standard hull form for 499 GT cargo ships. In actual operation, these vessels typically operate under both full-load and ballast conditions while maintaining nearly the same operating speed, which is slightly lower than the design speed. Furthermore, the length between perpendiculars (Lpp) of a typical 499 GT cargo ship is approximately 70 m, and, as shown in Figure 2, wave-making resistance accounts for a relatively large proportion of the total hull resistance.

In this study, the authors developed a hybrid bulbous bow using computational fluid dynamics (CFD) to improve the hydrodynamic performance under both full-load and ballast conditions.



Fig.1: "Sanko Maru" of 499 G/T Cargo Ship[1)]

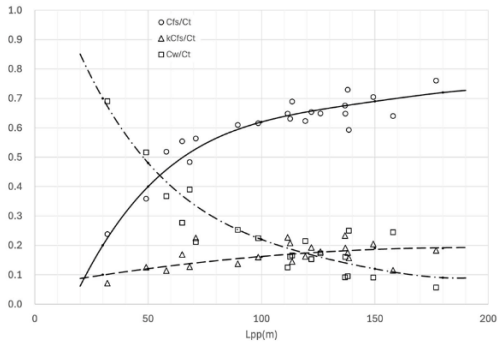


Fig. 2: Structure of hull resistance[2)]

2. DESIGN CONDITIONS FOR HYBRID BULBOUS BOW

The hull form was based on that of a typical 499 GT cargo ship. To isolate the effect of the bulbous bow, only the geometry forward of the Forward Perpendicular (F.P.) was modified, while all other hull dimensions were kept unchanged. The principal dimensions and design conditions of the original hull are summarized in Table 1. Because the vessel operates at nearly the same service speed under both the full-load and ballast conditions, the hybrid bulbous bow was designed to improve the hydrodynamic performance over the operating Froude number range of 0.22–0.24.

Table 1: Hull dimensions and design conditions

Kind of ship	499 GT Cargo Ship
L_{PP} x B x D	69.0 [m] x 12.0 [m] x 7.12 [m]
draft at full	4.159(aft) / 4.159(fore) [m]
draft at ballast	4.000(aft) / 2.470(fore) [m]
Design speed	12.5 [knot] / Fn=0.247

3. CALCULATION METHOD

The hull forms were designed using the Initial Lines Generator (I.L.G.), developed by Fluid Techno. I.L.G. is a hull-form design tool that enables the efficient generation and modification of hull lines through simple operations. Furthermore, because I.L.G. is integrated with NAGISA, both hull design and CFD analysis can be performed within a unified environment, significantly reducing the design cycle compared with conventional design tools. The resistance performance was evaluated using NAGISA, a Reynolds-averaged Navier–Stokes (RANS) solver developed by the National Maritime Research Institute (NMRI). The computational grid consisted of approximately 0.98 million cells, and the Explicit Algebraic Stress Model (EASM) was employed as the turbulence model. Simulations were carried out at model scale (1/11.2) over a Froude number range of 0.22–0.26. Figure 3 illustrates the computational domain and the hull surface mesh.

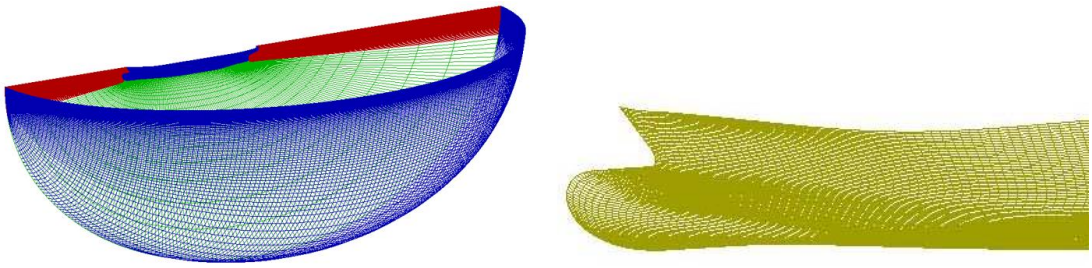
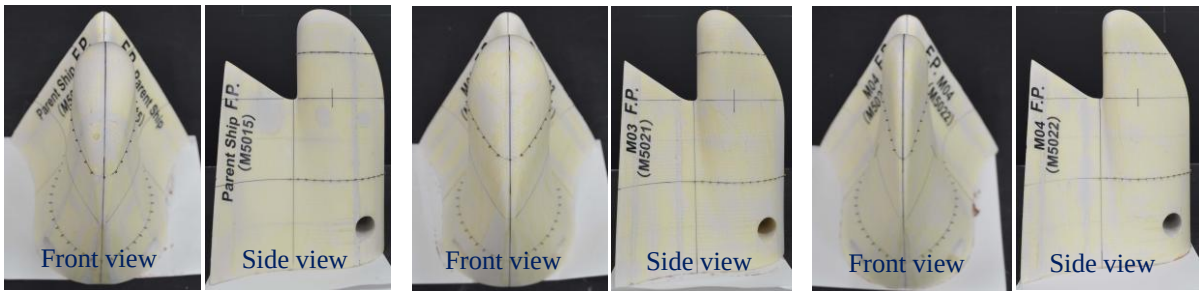


Fig. 3: Computational domain and hull surface

4. DESIGN FOR BULBOUS BOW FOR EACH DRAFTS

4-1.PROFILE OF BOULBOUS BOW

First, two bulbous bow designs were developed to reduce the wave-making resistance under the full-load and ballast conditions, respectively. M03 bulbous bow features a thicker bulb shape near the waterline and was designed to reduce the wave-making resistance under the full-load condition. In contrast, M04 bulbous bow has a slimmer bulb shape and was designed to reduce the wave-making resistance under the ballast condition. The bulbous bow geometries of the original hull, M03, and M04 are shown in Figure 4.



Original M03 M04

Fig.4 : Shape of bulbous bows

4-2. CALCILATION RESULTS

Figure 5, M03 hull exhibits a noticeable reduction in wave height under the full-load condition. This reduction is attributed to the larger bulbous bow located near the waterline, which effectively suppresses wave generation. In contrast, Figure 6 shows that M04 hull achieves a significant reduction in wave height under ballast condition. This improvement is attributed to the slimmer bulbous bow, which reduces the entrance angle of the bow and consequently decreases wave-making resistance.

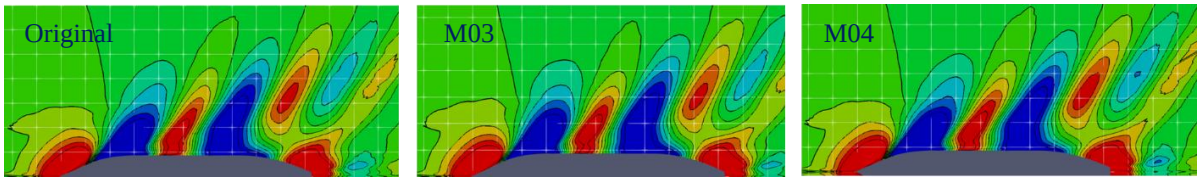


Fig.5 : Wave pattern at full condition (Fn=0.24)

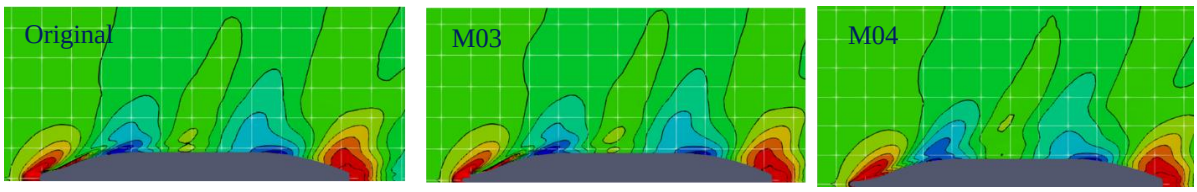


Fig.6 : Wave pattern at ballast condition (Fn=0.24)

Figure 7 shows the changes in the total resistance coefficient (ΔCt) of M03 and M04 relative to original hull. The definitions of the total resistance coefficient (Ct) and ΔCt are given below. Negative values of ΔCt indicate an improvement in resistance performance. Under full-load condition, the total resistance coefficient of M03 was reduced by up to 4.4% at Fn = 0.24 compared with original hull. In contrast, under ballast condition, M04 achieved a maximum reduction in the total resistance coefficient of 10.1% at Fn = 0.22.

$$Ct = \frac{R}{0.5\,\rho\,S\,V^2}$$

R : hull resistance
ρ : water density
S : wetted surface area
V : model velocity

$$\Delta Ct = \frac{Ct\ new - Ct\ original}{Ct\ original}\ 100$$

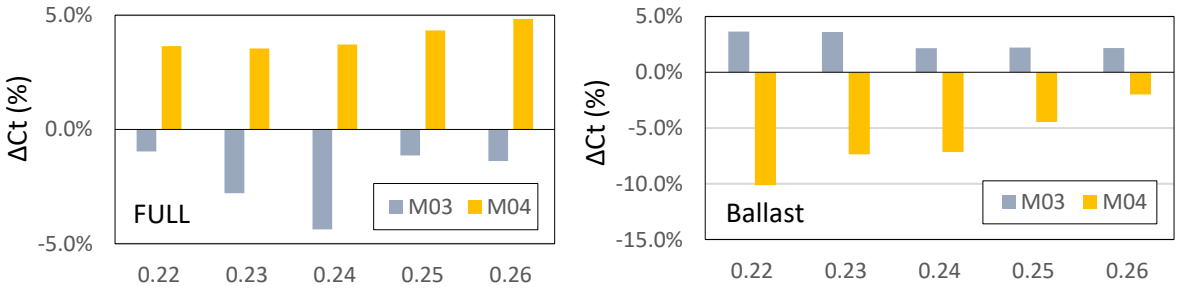


Fig.7 : Comparison of Δ Ct of M03and M04 with original

5. DESIGN FOR HYBRID BULBOUS BOW

5-1.PROFILE OF HYBRID BOULBOUS BOW

Figure 8 shows the shape of a hybrid boulbous bow for M06, designed to reduce the wave-making resistance at both full and ballast drafts. The hybrid bulbous bow features a hull design where the boulbous bow is larger near the waterline of the full condition, and the entrance angle is reduced below the waterline of ballast.

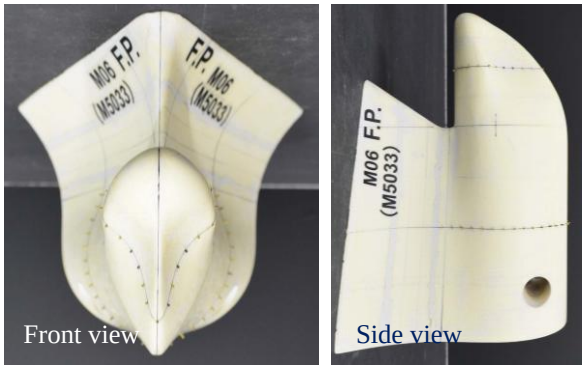


Fig.8 : Shape of hybrid bulbous bow (M06)

5-2. CALCILATION RESULTS

Figures 9 and 10 compare the wave patterns of the original hull and M06 under the full-load and ballast conditions, respectively. Under the full-load condition, M06 exhibited only a slight reduction in wave height compared with the original hull. In contrast, under the ballast condition, the wave height was significantly reduced. In addition to the bow region, the wave height along the parallel middle body was also reduced. This improvement is attributed to the slimmer bulbous bow geometry of M06, which effectively suppressed wave generation under the ballast condition.

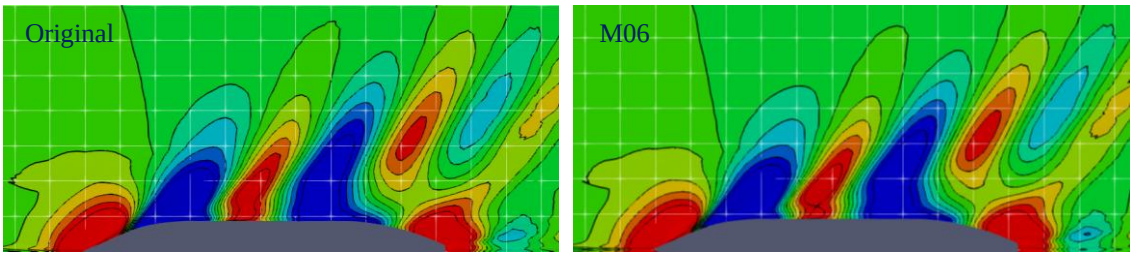


Fig.9 : Wave pattern at full condition (Fn=0.24)

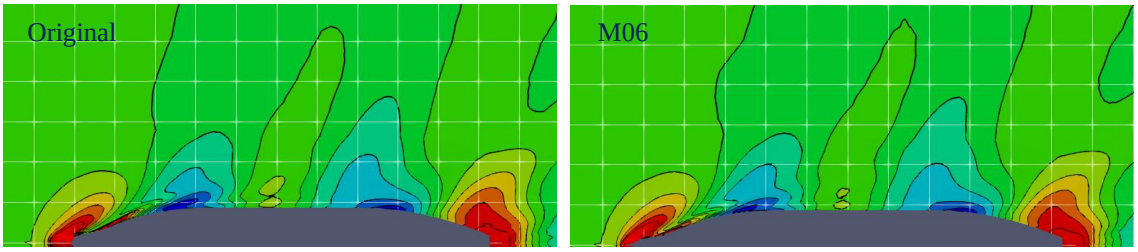


Fig.10 : Wave pattern at ballast condition (Fn=0.24)

Figure 11 compares the resistance reduction rates of M03, M04, and M06 relative to the original hull. Under the full condition, the ΔCt of M06 is generally more negative than that of M04, indicating a greater resistance reduction. However, M06 achieves a reduction in resistance relative to the original hull only in the higher Froude number range. Under the ballast condition, M06 exhibits negative ΔCt values over the entire Froude number range investigated, indicating lower resistance than the original hull. These results demonstrate that the hybrid bulbous bow developed in this study improves the resistance performance under the ballast condition, whereas further improvement is required under the full condition.

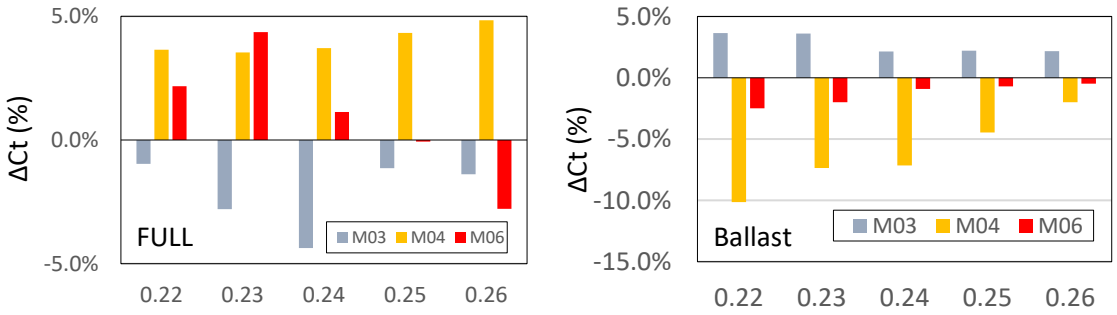


Fig.11 : Comparison of ΔCt of M03, M04 and M06 with original

6. CONCLUTION

The characteristics of the newly developed bulbous bow designs were investigated using computational fluid dynamics (CFD).

First, M03 and M04 were developed to reduce the wave-making resistance under the full-load and ballast conditions, respectively. M03 features a larger bulb near the full-load waterline, whereas M04 has a smaller bow entrance angle below the ballast waterline. The CFD results showed that M03 reduced wave generation under the full-load condition, while M04 reduced wave generation under the ballast condition. Correspondingly, the total resistance coefficient (Ct) was reduced under their respective design conditions.

Next, a hybrid bulbous bow (M06) was developed to improve the hydrodynamic performance under both the full-load and ballast conditions. At Fn = 0.24, M06 exhibited a reduced wave pattern compared with the original hull due to its hybrid geometry. However, under the full condition, the resistance of M06 increased relative to the original hull in the lower Froude number range. These results indicate that further optimization of the hybrid bulbous bow geometry is required to improve its resistance performance under the full condition.

7. REFFERENCE

1) “The Japan Shipping Exchange”, URL: https://www.jseinc.org/newship/detail.html?ID=659.

2) “Ship design considering current flow and estimation of actual ship performance”, M.Tamashima, 360th KFR Seminar, 2015.

A Zonal URANS-SLH Hybrid Approach for Accurate Prediction of Ship Resistance and Stern Wake

Morteza Feizbakhsh, Nikolai Kornev

Lehrstuhl für Modellierung und Simulation, Universität Rostock, Rostock, Germany

morteza.feizbakhsh@uni-rostock.de, nikolai.kornev@uni-rostock.de

Accurate numerical prediction of ship stern flow is vital for evaluating complex wake vortex structures. While conventional URANS models capture attached frictional shear stresses, they over-damp turbulent kinetic energy and fail to resolve separated flow. Conversely, scale-resolving models like the Shielded LEMOS Hybrid (SLH) [1, 2] accurately capture vortex dynamics but suffer from modeled stress depletion, underestimating frictional drag. To address this trade-off, this study develops a zonal URANS–SLH hybrid framework in OpenFOAM. Pure URANS is maintained along the bow and midbody to preserve skin friction, while the SLH model is activated exclusively in the stern region to resolve bilge vortices. Using two bulk carriers (JBC and SVA M1749S030), generalized geometric and flow-based criteria are established to determine the optimal interface location *a priori*, restricting skin-friction deviations to below 5% without sacrificing wake fidelity.

1. Introduction and Problem Statement

Accurate numerical prediction of the viscous flow around full-form ship hulls is essential for powering forecasts, hull optimization, and evaluating propulsive Energy Saving Devices (ESDs). Conventional Unsteady Reynolds-Averaged Navier–Stokes (URANS) closures, such as standard k–ω SST [3], accurately capture attached boundary-layer shear stresses along the parallel middle body. However, due to excessive isotropic turbulent viscosity, URANS models over-damp turbulent fluctuations, smear out longitudinal bilge vortices, and heavily underpredict turbulent kinetic energy (TKE) in the propeller disc [4]. Conversely, scale-resolving simulations using hybrid turbulence models demonstrate superior fidelity in capturing unsteady separation and wake vortex dynamics [1,2]. Nevertheless, when applied globally across the entire hull, hybrid models suffer from Modeled Stress Depletion (MSD) along unseparated boundary layers. On standard practical grids, this leads to an artificial underestimation of the skin-friction coefficient (C_f) by approximately 15% to 18% relative to the ITTC line, along with a corresponding overprediction of pressure resistance (C_p) [4].

To resolve this trade-off, this study employs a **zonal hybrid approach** decomposing the computational domain into:

1. An upstream **pure URANS zone** (k–ω SST) along the bow and midbody to accurately preserve wall shear stresses.
2. A downstream **SLH scale-resolving zone** [2] restricted to the aftbody to resolve bilge-vortex separation and wake turbulence.

The objective is to establish generalized empirical criteria for positioning the zonal interface such that skin-friction errors (ΔC_f) remain strictly below 5% relative to standard ITTC formulations, while simultaneously ensuring high-fidelity wake velocity and TKE predictions.

2. Zonal Domain Decomposition Implementation

All numerical simulations and model developments in this work are implemented within the open-source finite-volume CFD framework OpenFOAM [5]. The turbulence modeling strategy relies on the scale-resolving Shielded LEMOS Hybrid (SLH) model developed by Kornev et al. [1,2]. The zonal transition between the upstream URANS domain and the downstream scale-resolving SLH domain is realized via a spatial blending coefficient $\alpha_{\text{RANS}}(\mathbf{x})$:

$$\nu_t(\mathbf{x}) = \alpha_{\text{RANS}}(\mathbf{x})\, \nu_t^{\text{RANS}}(\mathbf{x}) + [1 - \alpha_{\text{RANS}}(\mathbf{x})]\, \nu_t^{\text{SLH}}(\mathbf{x}) \tag{1}$$

The spatial field $\alpha_{\text{RANS}}(\mathbf{x})$ is defined based on the chosen axial interface station $x_{\text{int}}/L_{\text{pp}}$:

$$\alpha_{\text{RANS}}(\mathbf{x}) = \begin{cases} 1.0, & \text{for } x < x_{\text{int}} \quad \text{(Pure URANS Region)} \\ 0.0, & \text{for } x \geq x_{\text{int}} \quad \text{(Active SLH Hybrid Region)} \end{cases} \tag{2}$$

Upstream of x_{int}, the model enforces pure URANS mode ($\alpha_{\text{RANS}} = 1$), eliminating modeled stress depletion along the flat bottom and sides. Downstream of x_{int}, α_{RANS} switches to 0, fully activating the SLH hybrid model to resolve unsteady vortex shedding in the stern region.

3. Interface Location Sensitivity and Resistance Predictions

The sensitivity of the integral resistance components was analyzed across two benchmark bulk carriers: the Japan Bulk Carrier (JBC, $Re = 7.43 \times 10^6$) and the SVA Bulker M1749S030 ($Re = 7.40 \times 10^6$). The axial interface position $x_{\text{int}}/L_{\text{pp}}$ was systematically varied between $75\%\, L_{\text{pp}}$ and $95\%\, L_{\text{pp}}$.

Table 1: Resistance coefficient variations across different zonal interface positions for JBC and M1749S030 hulls.

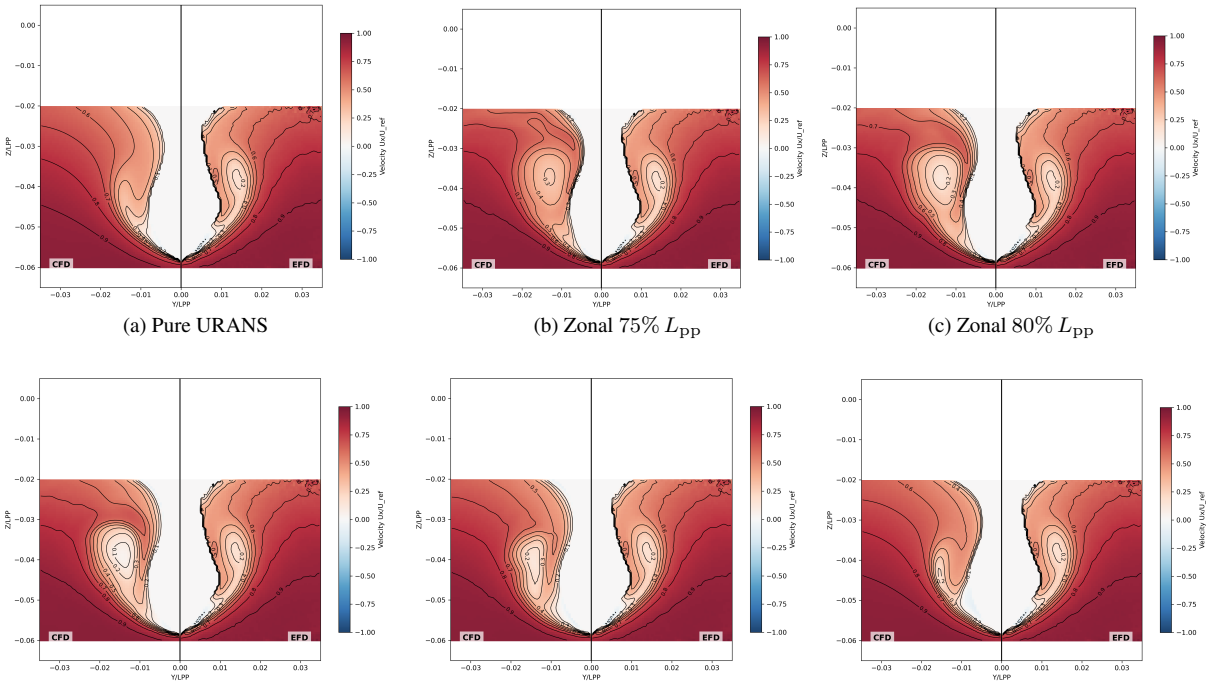
Case / Configuration	$x_{\text{int}}/L_{\text{pp}}$	$C_d \times 10^3$	$C_p \times 10^3$	$C_f \times 10^3$	ΔC_f **vs. ITTC**	ΔC_d **vs. EFD**
JBC Hull						
Pure URANS (Full)	—	4.158	1.048	3.110	-1.54%	-3.06%
Zonal SLH	0.75	4.168	1.328	2.840	-10.10%	-2.82%
Zonal SLH	0.80	4.316	1.408	2.908	-7.95%	$+0.63\%$
Zonal SLH	0.85	4.404	1.419	2.985	-5.51%	$+2.68\%$
Zonal SLH	0.90	4.416	1.358	3.058	-3.20%	$+2.97\%$
Zonal SLH	0.95	4.251	1.154	3.097	-1.98%	-0.89%
M1749S030 Hull						
Pure URANS (Full)	—	3.777	0.638	3.139	-0.78%	-3.65%
Zonal SLH	0.75	3.692	0.819	2.874	-9.15%	-5.82%
Zonal SLH	0.80	3.806	0.858	2.948	-6.82%	-2.90%
Zonal SLH	0.85	3.866	0.859	3.007	-4.93%	-1.38%
Zonal SLH	0.90	3.898	0.830	3.068	-3.02%	-0.56%
Zonal SLH	0.95	3.763	0.640	3.123	-1.29%	-4.01%

As documented in Table 1, the target skin-friction threshold ($|\Delta C_f| < 5\%$) is strictly satisfied at $x_{\text{int}}/L_{\text{pp}} = 0.90$ and 0.95 for the JBC hull. For the M1749S030 hull, this condition is met across $x_{\text{int}}/L_{\text{pp}} = 0.85$, 0.90, and 0.95. However, identifying the optimal interface location cannot rely solely on integrated force coefficients. It requires verifying that stern wake features, specifically the axial velocity distribution and resolved TKE levels in the wake region, are accurately preserved relative to benchmark data.

4. Stern Wake and Turbulence Field Verification

4.1. JBC Wake Flow and Turbulence Resolution

To verify wake resolution fidelity, Figure 1 presents direct side-by-side axial velocity contour comparisons (u/U_{ref}) at Plane S2 ($x/L_{\text{pp}} = 0.925$), contrasting the CFD predictions on the left against the EFD benchmark measurements on the right for all configurations.



(a) Pure URANS (b) Zonal $75\%\, L_{\text{pp}}$ (c) Zonal $80\%\, L_{\text{pp}}$

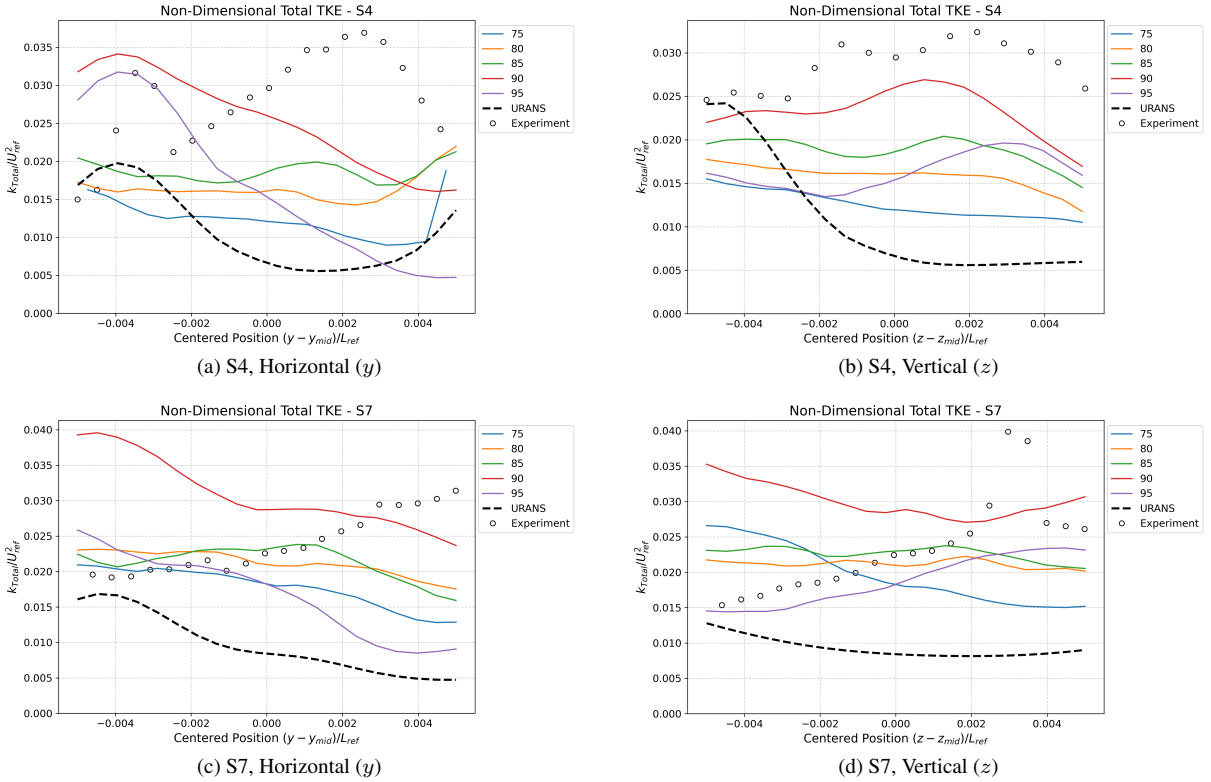
(d) Zonal $85\%\, L_{\text{pp}}$ (e) Zonal $90\%\, L_{\text{pp}}$ (f) Zonal $95\%\, L_{\text{pp}}$

Figure 1: JBC Hull: Direct comparison of axial velocity (u/U_{ref}) at Plane S2 ($x/L_{\text{pp}} = 0.925$) showing CFD on the left and EFD on the right.

The contour comparisons at Plane S2 (Figure 1) reveal that pure URANS and the delayed $95\%\, L_{\text{pp}}$ interface produce similarly over-diffused shear layers that fail to capture the detached bilge-vortex core observed in

the benchmark experiments. Although early and intermediate interface positions (75%, 80%, and 85% L_{pp}) successfully capture the vortical structures, they fail the preliminary skin-friction prerequisite ($|\Delta C_f| > 5\%$) due to modeled stress depletion over extended hull areas, eliminating them from practical consideration. Consequently, the 90% L_{pp} interface emerges as the only setup that resolves the detached core topology and matches local minimum velocity levels while strictly adhering to the integral friction constraint.

To quantitatively evaluate turbulence development across all investigated configurations, Figure 2 presents horizontal (y) and vertical (z) line distributions of total non-dimensional TKE ($k_{\mathrm{Total}}/U_{\mathrm{ref}}^2$) passing through the vortex core center. The core center was identified by peak axial vorticity ($\max|\omega_x|$) at Plane S4 ($x/L_{\mathrm{pp}} = 0.9625$, located between the propeller and duct) and Plane S7 ($x/L_{\mathrm{pp}} = 1.0$, the aft perpendicular).



(a) S4, Horizontal (y)

(b) S4, Vertical (z)

(c) S7, Horizontal (y)

(d) S7, Vertical (z)

Figure 2: JBC Hull: Total TKE line profiles extracted through the maximum $|\omega_x|$ core center at Planes S4 and S7 along the horizontal (y) and vertical (z) directions across all zonal interfaces (75%–95% L_{pp}), pure URANS, and experimental data.

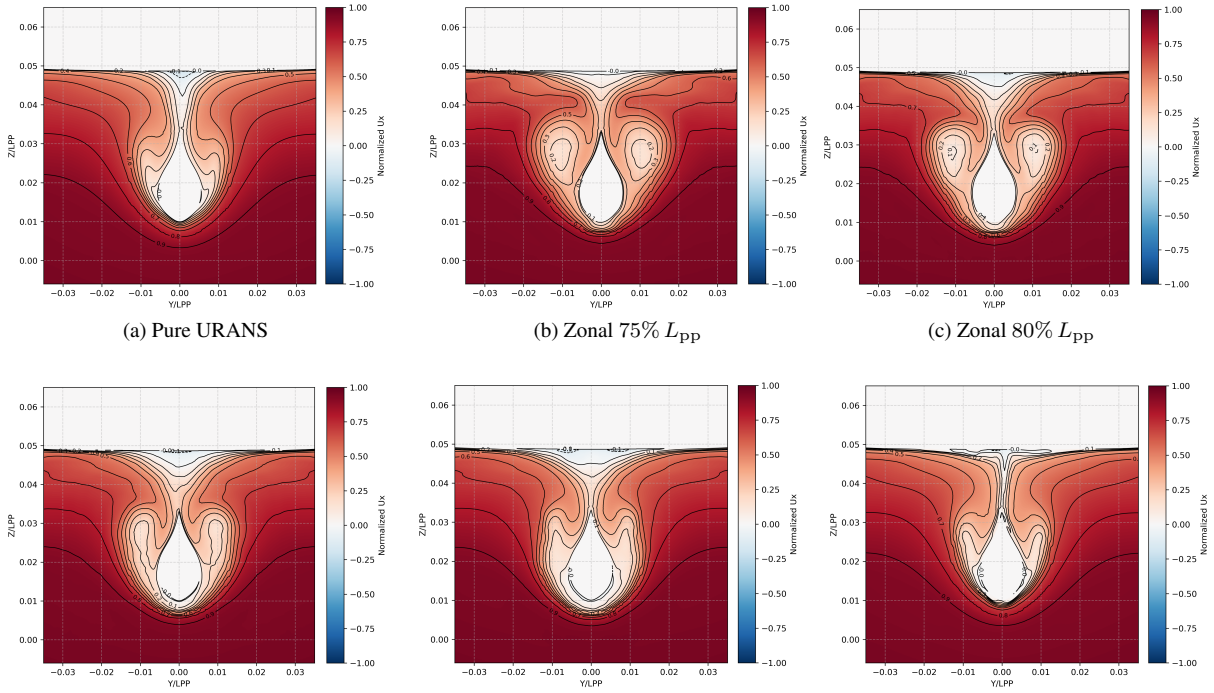
The quantitative line profiles in Figure 2 show that pure URANS heavily suppresses TKE across both stations due to excessive dissipation ($k_{\mathrm{Total}}/U_{\mathrm{ref}}^2 < 0.010$). While upstream interfaces placed at 75%–85% L_{pp} underestimate peak turbulence at Plane S4, the 90% L_{pp} interface recovers high turbulent kinetic energy ($k_{\mathrm{Total}}/U_{\mathrm{ref}}^2 \approx 0.03$), closely matching the experimental data. At the aft perpendicular (Plane S7), interfaces placed between 80% and 85% L_{pp} align with the central core plateau (0.020–0.025). Meanwhile, the 90% L_{pp} setup resolves comparable fluctuations across the propeller plane, bounds the upstream skin-friction error to $\Delta C_f = -3.20\%$, and maintains an accurate velocity profile at Plane S2. These combined characteristics confirm that 90% L_{pp} is the optimal interface location for the JBC hull.

4.2. M1749S030 Wake Flow and Turbulence Resolution

Because local experimental flow-field measurements are unavailable for the SVA Bulker M1749S030, wake resolution fidelity was assessed by examining the longitudinal vortex structures in the normalized axial velocity contours (u/U_{ref}) at Plane S2 ($x/L_{\mathrm{pp}} = 0.9625$), followed by the total non-dimensional TKE distributions ($k_{\mathrm{Total}}/U_{\mathrm{ref}}^2$) between the duct and propeller at Plane S4 ($x/L_{\mathrm{pp}} = 0.9843$).

Figure 3 presents the normalized axial velocity field at Plane S2. Although interface placements at 75% and 80% L_{pp} successfully reproduce the vortical structures, they introduce excessive skin-friction errors (-9.15% and -6.82%, respectively) that violate the target accuracy threshold, disqualifying them from practical implementation.

The axial velocity contours at Plane S2 (Figure 3) demonstrate that pure URANS diffuses the bilge vortex, yielding a shallow velocity deficit across the skeg with undeveloped counter-rotating vortex lobes. Delayed interfaces at 90% and 95% L_{pp} exhibit weak roll-up due to insufficient convective length upstream of Plane S2. Conversely, positioning the interface at 85% L_{pp} allows the crossflow to roll up fully into two symmetrical vortex cores, establishing a deep local velocity deficit surrounding the skeg.

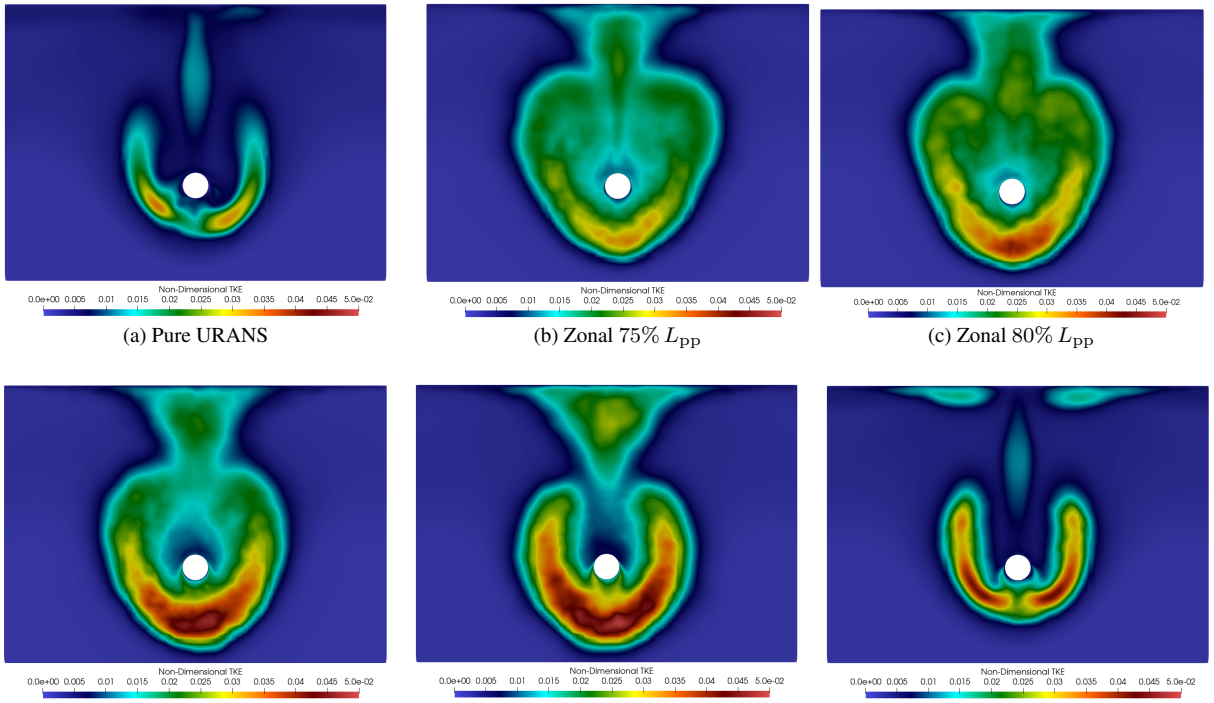


(a) Pure URANS (b) Zonal 75% L_{pp} (c) Zonal 80% L_{pp}

(d) Zonal 85% L_{pp} (e) Zonal 90% L_{pp} (f) Zonal 95% L_{pp}

Figure 3: M1749S030 Hull: Normalized axial velocity contours (u/U_{ref}) at Plane S2 ($x/L_{\mathrm{pp}} = 0.9625$) across all zonal interfaces (75%–95% L_{pp}) and pure URANS.

To evaluate how these vortex structures develop into the downstream wake, Figure 4 displays the non-dimensional total TKE contours ($k_{\mathrm{Total}}/U_{\mathrm{ref}}^2$) between the duct and propeller at Plane S4 ($x/L_{\mathrm{pp}} = 0.9843$).



(a) Pure URANS (b) Zonal 75% L_{pp} (c) Zonal 80% L_{pp}

(d) Zonal 85% L_{pp} (e) Zonal 90% L_{pp} (f) Zonal 95% L_{pp}

Figure 4: M1749S030 Hull: Non-dimensional TKE ($k_{\mathrm{Total}}/U_{\mathrm{ref}}^2$) contours between the duct and propeller at Plane S4 ($x/L_{\mathrm{pp}} = 0.9843$).

The TKE distributions at the propeller plane (Figure 4) indicate that pure URANS suppresses turbulence across the disc center, while the delayed 95% L_{pp} interface restricts high turbulence levels to a narrow shear band with limited lateral expansion. In contrast, both the 85% and 90% L_{pp} interfaces reconstruct the turbulence field effectively, producing a broad, circular turbulent core structure. Because the 85% L_{pp} interface captures the symmetrical

bilge-vortex core at Section S2 and satisfies the skin-friction criterion ($\Delta C_f = -4.93\%$), $x_{\text{int}}/L_{\text{pp}} = 0.85$ serves as the optimal interface location for the M1749S030 hull.

5. Generalized Empirical Criteria for Domain Decomposition

To identify the optimal interface location *a priori* without requiring exploratory sensitivity simulations, three predictive criteria were formulated based on geometric features and local flow characteristics.

5.1. Criterion 1: Sectional Block Coefficient ($C_B = 0.60$)

The sectional block coefficient $C_B(x)$ quantifies the longitudinal frame narrowing toward the stern:

$$C_B(x) = \frac{A_{\text{section}}(x)}{B \cdot T} \tag{3}$$

where $A_{\text{section}}(x)$ represents the underwater cross-sectional area, B is the beam, and T is the draft. The axial station where $C_B(x) = 0.60$ defines an effective transition point for activating the hybrid turbulence model. As shown in Figure 5, this criterion identifies $x_{\text{int}}/L_{\text{pp}} = 85.9\%$ for the M1749S030 hull and 89.6% for the JBC hull, predicting the observed optima within $1.0\%\, L_{\text{pp}}$.

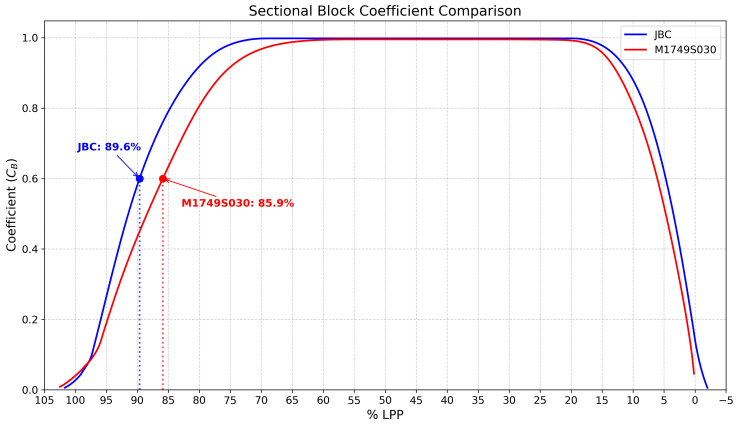


Figure 5: Sectional block coefficient (C_B) distribution along x/L_{pp} for M1749S030 (85.9%) and JBC (89.6%).

5.2. Criterion 2: Transverse Curvature Inflection Point

Evaluating the second spatial derivative of the transverse hull frames tracks the transition from the flat bottom and vertical side-shell to the curved bilge shoulder:

$$\frac{\partial^2 z(y)}{\partial y^2} < 0 \quad \text{along the bilge run-in} \tag{4}$$

Figure 6 illustrates the curvature analysis from $65\%\, L_{\text{pp}}$ to $100\%\, L_{\text{pp}}$, highlighting convex regions in green and concave regions in violet. Moving aft from midship, the first appearance of an inward (concave) inflection marks the onset of transverse crossflow convergence. This geometric inflection identifies the optimal scale-resolving transition station at $85\%\, L_{\text{pp}}$ for the M1749S030 hull and $90\%\, L_{\text{pp}}$ for the JBC hull.

5.3. Criterion 3: Skin-Friction Gradient and Lateral Component

In preliminary RANS calculations, the onset of three-dimensional crossflow separation can be identified by tracking the lateral shear ratio ($C_{f,\text{lat}}/C_f > 0.10$). As illustrated in Figure 7, applying a threshold of 0.10 yields 83.7% for the M1749S030 hull and $x/L_{\text{pp}} = 88.9\%$ for the JBC hull. Placing the zonal interface at or immediately ahead of this trigger station ensures that the entire detached bilge-vortex core remains within the scale-resolving SLH domain, while attached boundary layers remain under pure URANS control.

6. Conclusions

The proposed zonal URANS–SLH hybrid framework resolves the skin-friction underprediction typical of full-domain scale-resolving ship simulations. By maintaining pure URANS upstream and activating the SLH model exclusively in the stern region:

- The numerical error in the skin-friction coefficient (ΔC_f) remains strictly below 5% relative to ITTC benchmark values.

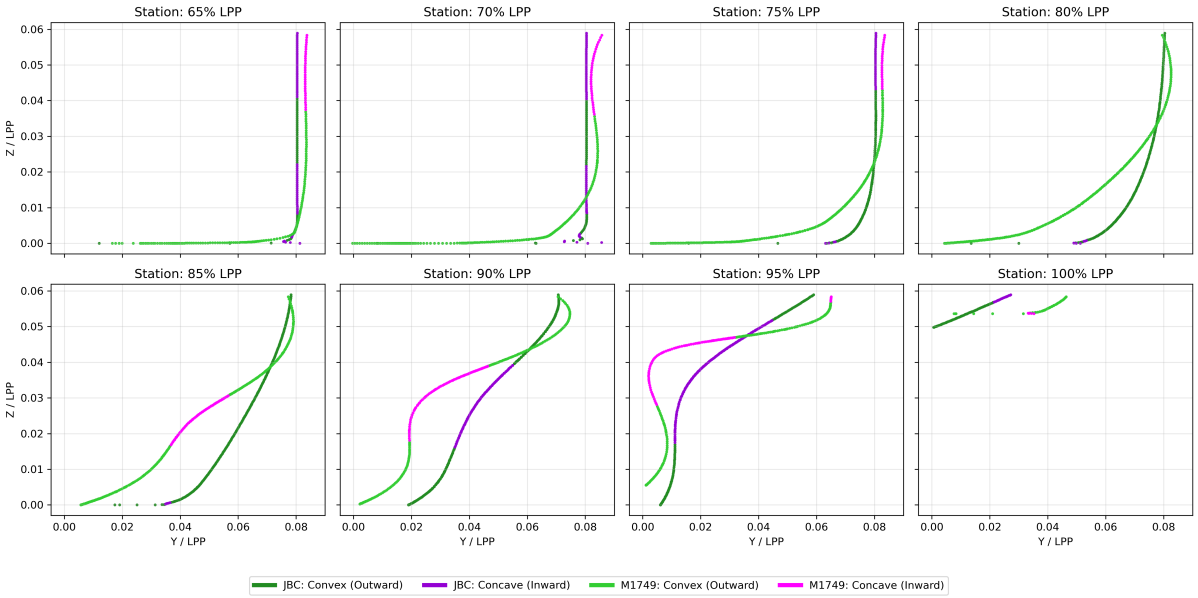
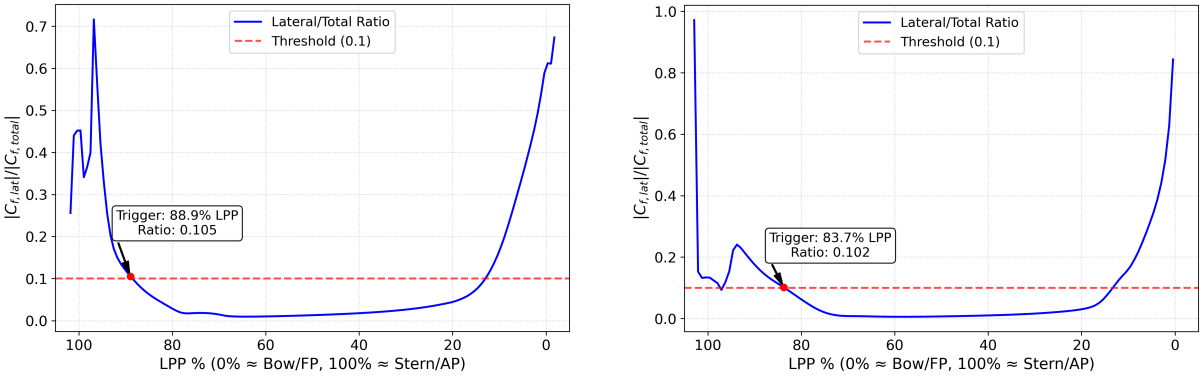


Figure 6: Transverse curvature analysis of M1749S030 and JBC hulls across stations 65%–100% L_{pp}, with convex regions in green and concave regions in violet.



(a) JBC Hull (Trigger: 88.9% L_{pp})

(b) M1749S030 Hull (Trigger: 83.7% L_{pp})

Figure 7: Identification of the zonal interface trigger location using the lateral shear ratio criterion ($C_{f,\mathrm{lat}}/C_f > 0.10$) for the JBC and M1749S030 hulls.

- Complex stern features, including the bilge-vortex core at Section S2, and peak TKE levels at Plane S4 and S7, are resolved with high fidelity relative to experimental data.
- Three generalized criteria ($C_B = 0.60$, transverse curvature inflection, and $C_{f,\mathrm{lat}}/C_f > 0.10$) provide practical rules for interface positioning on arbitrary full-form hulls without requiring preliminary trial simulations.
- It should be noted that all three proposed criteria can be considered robust, as they yield similar predictions for the URANS/SLH interface.

References

[1] Kornev, N., Taranov, A., Shchukin, E. and Kleinsorge, L. Development of hybrid URANS-LES methods for flow simulation in the ship stern area. *Ocean Engineering*, 38(16): 1831–1838, 2011.

[2] Shevchuk, I. and Kornev, N. Improved version of LeMoS Hybrid Model for Ambiguous Grid Densities. *International Journal of Naval Architecture and Ocean Engineering*, 10(3):270–281.

[3] F. R. Menter. Two-equation eddy-viscosity turbulence models for engineering applications. *AIAA J.*, 32(8):1598–1605, 1994.

[4] Kornev, N., Shevchuk, I., Abbas, N., Anschau, P. and Samarbakhsh, S. Potential and limitations of scale resolved simulations for ship hydromechanics applications. *Journal of Ship Technology Research*, 66(2): 83–96, 2019.

[5] H. G. Weller, G. Tabor, H. Jasak and C. Fureby. A tensorial approach to computational continuum mechanics using object orientated techniques. *Computers in Physics*, 12:620–631, 1998.

28th Numerical Towing Tank Symposium (NuTTS)
19–21 October 2026 | Mülheim an der Ruhr, Germany

Extension of Granville's Similarity Law for Heterogeneous Hull Roughness

Hasan Ozturk, Tahsin Tezdogan,
Kang Ren, Stephen Turnock

Department of Civil, Maritime and Environmental Engineering, School of Engineering,
University of Southampton, Boldrewood Innovation Campus, Building 176, SO16 7QF, UK
Email: hasan.ozturk@soton.ac.uk

1. Introduction

The research presented in this paper forms a specific part of a broader doctoral investigation that aims to develop a hybrid Machine Learning (ML) and Computational Fluid Dynamics (CFD) framework for predicting biofouling-induced hydrodynamic penalties and optimizing hull maintenance.

Biofouling and coating deterioration increase the frictional resistance of ship hulls and consequently raise the power required to maintain a prescribed operating speed. The magnitude of this penalty, commonly referred to as the roughness effect, depends not only on roughness height but also on the roughness function and the local hydrodynamic conditions of the flow (Schultz, 2007). A number of approaches have therefore been developed to quantify the resistance penalty associated with rough surfaces.

CFD can predict the roughness effect by incorporating a roughness function into the wall treatment. This provides a high-fidelity route because roughness can be represented directly on the body and the resulting flow field can include three-dimensional and form-related effects. However, CFD calculations remain comparatively expensive when a large number of hull conditions, full scale conditions or spatially varying biofouling distributions have to be evaluated. To enable rapid assessment and support efficient data generation within the overall framework, similarity-law approaches provide a computationally inexpensive yet physically sound alternative for estimating the frictional component of the roughness penalty.

One established engineering approach is the additional friction coefficient formulation of Townsin, while another is the similarity-law scaling proposed by Granville. Granville's formulation was developed from turbulent boundary-layer similarity laws and provides a rational means of extrapolating the frictional resistance of a uniformly rough surface between different scales and operating conditions (Granville, 1958, 1978). In practical ship-resistance applications, the method is attractive because its similarity-law formulation can be implemented in an efficient computational procedure. Previous studies have demonstrated the use of similarity-based approaches for assessing the effects of roughness and biofouling on ship resistance (Demirel et al., 2017).

The conventional application of the similarity-law approach, however, is based on a uniform roughness condition applied over a continuous surface. This idealisation is useful for controlled studies and for obtaining representative roughness penalties, but it does not directly represent the spatially non-uniform character of marine biofouling. Actual fouling develops unevenly over a hull: different longitudinal regions may experience different levels of slime, biofilm or calcareous growth, while relatively clean areas may remain between more heavily fouled regions. CFD studies have also demonstrated the importance of considering the spatial distribution of roughness and biofouling on ship hulls (Farkas et al., 2018; Song et al., 2019).

Song et al. (2021) investigated heterogeneous roughness on a Wigley hull experimentally and showed that roughness located in the forward part of the hull can produce a larger resistance penalty than roughness located in the aft part for the same roughened wetted area. That study highlighted the importance of zone-based assessment. Their study also proposed a prediction approach based on Granville's similarity-law scaling to account for heterogeneous roughness. Similarly, Ravenna et al. (2022) investigated zone-based heterogeneous roughness on the KCS using CFD and introduced the Roughness Impact Factor (RIF) to quantify the contribution of roughness applied to different hull regions. These studies demonstrate that the longitudinal distribution of roughness is an important parameter in ship resistance prediction.

Building upon existing studies that investigate heterogeneous roughness distribution and its emerging effect, he present study introduces a novel approach in which the similarity-law solution is propagated region by region through a virtual-length coordinate. The proposed method is intended to represent a continuous spatially varying roughness distribution while retaining the computational efficiency of the similarity-law framework.

An in-house computational code was first developed to implement Granville's similarity-law procedure for homogeneous roughness. The predicted friction coefficients were compared with results reported in the literature and good agreement was obtained, providing a baseline for the extension. The code was then extended to heterogeneous roughness by dividing the hull into consecutive longitudinal regions, each assigned an equivalent sand-grain roughness height, k_s. The central idea is to propagate the similarity-law solution from one region to the next using a

virtual-length formulation. This allows the accumulated boundary-layer development associated with an upstream roughness condition to be retained while the roughness condition is changed when the flow enters a new region.

The objective is not to replace CFD, but to provide a computationally inexpensive engineering method capable of representing spatially varying roughness within the limitations of a boundary-layer similarity framework. The approach is demonstrated using a full-scale KCS-type geometry and is intended as a first step towards linking spatially resolved fouling information with resistance prediction and, subsequently, data-driven hull-maintenance decision support.

2. Methodology

2.1. Granville similarity-law scaling framework

For a uniformly rough surface, the roughness effect can be expressed through the roughness function ΔU^+, representing the downward shift of the logarithmic velocity profile caused by surface roughness. The roughness Reynold number and roughness function is related to the equivalent sand-grain roughness through

$$k_s^+ = \frac{u_\tau k_s}{\nu}, \qquad U^+ = \frac{1}{\kappa}\ln y^+ + B - \Delta U^+ \tag{1}$$

where u_τ is the friction velocity, k_s is the equivalent sand-grain roughness height and ν is the kinematic viscosity of the flow. For a given k_s^+, the corresponding ΔU^+ is obtained from an empirical roughness-function correlation (Schultz, 2007), evaluated for the present study in Fig. 3 (Section 3.1). Granville's similarity formulation relates the rough-wall friction coefficient to a smooth-wall reference condition while maintaining turbulent boundary-layer similarity (Granville, 1958). The friction coefficient of smooth-plate follows the Kármán–Schoenherr line given in Eq. (2), which is solved iteratively by bisection method (Schoenherr, 1932).

$$\frac{0.242}{\sqrt{C_F}} = \log_{10}(Re_L \cdot C_F), \tag{2}$$

where ReL is the Reynolds number based on the length of the plate. It should be noted that the roughness effect on the residuary resistance is a function of the Froude number, Fn, and is assumed to be negligible on the residual coefficient. Therefore, this line is shifted by $\Delta U^+\kappa/\ln(10)$ in the $\log Re_L$ direction to obtain the rough friction line, $C_{F,rough}$. Then, the line of constant non-dimensional length L^+,

$$Re_L = \frac{L^+}{\sqrt{C_F/2}\left(1 - \frac{1}{\kappa}\sqrt{C_F/2}\right)}, \qquad L^+ = \frac{L\,u_\tau}{\nu}, \tag{3}$$

is plotted for the length scale of interest; and this constant-L^+ line is shifted by $\log(L_2/L_1)$ in the $\log Re_L$ direction when transferring the solution between two length scales L_1 and L_2 (for example, from the plate length used to define k_s^+ to the full-scale hull length). The intersection of the shifted $C_{F,rough}$ line with the shifted constant-L^+ line gives the rough friction coefficient and Reynolds number at the target scale.

For a homogeneous surface, the procedure is straightforward: the physical length L, operating speed U, and kinematic viscosity ν define the Reynolds number Re_L, the selected sand-grain roughness height k_s determines k_s^+ and the corresponding roughness function, and the resulting similarity solution gives the full-scale friction coefficient $C_{F,rough}$. Granville's similarity-law approach illustrated schematically in Fig 1.

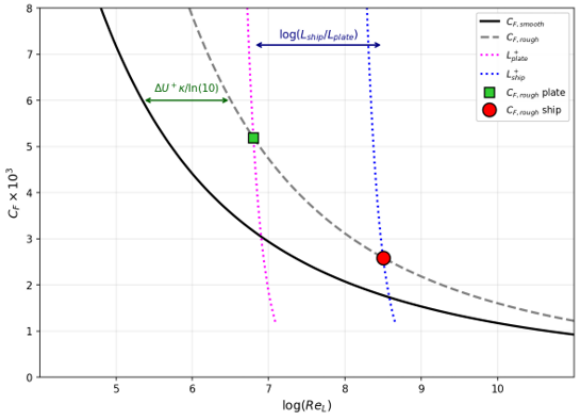


Figure 1: Graphical illustration of Granville's similarity-law scaling.

2.2. Extension to heterogeneous roughness

For a heterogeneous hull, the surface is divided into longitudinal regions which are treated sequentially so that the boundary-layer state developed over each upstream region is transferred to the downstream region, where $k_{s,i}$ denotes the local equivalent roughness height of region i. Hereafter, the subscript i denotes the region index used in the subsequent formulations. The cumulative boundary-layer state is represented by the momentum-thickness parameter

$$\theta_i = \frac{C_{F,i} L_{v,i}}{2}, \tag{4}$$

where $L_{v,i}$ denotes a virtual similarity length. At the entrance of a new roughness region, the virtual starting length $L_{v,i}^{start}$ is determined such that the similarity-law solution for the new roughness condition reproduces the θ inherited from the preceding region. This is obtained using a Newton–Raphson iteration. The physical length of the current region is then added according to

$$L_{v,i}^{end} = L_{v,i}^{start} + L_i. \tag{5}$$

The $C_{F,rough}$ at the end of each region is evaluated using the Granville formulation, and the resulting boundary-layer state is passed to the next region. The procedure therefore accounts for both the local roughness magnitude and its longitudinal position on the hull. The final heterogeneous friction coefficient is obtained from equation 6, where L is the total physical hull length.

$$C_{F,\text{hetero}} = \frac{2\theta_N}{L}, \tag{6}$$

2.3. Reference hull and roughness conditions

The methodology is demonstrated using a full-scale KCS-type hull with a characteristic length of approximately 232.5 m. The analysis is performed at full scale for a prescribed operating condition. The homogeneous cases provide a reference against which the heterogeneous formulation is assessed.

The selected roughness heights cover a broad engineering range ($k_s = 0, 30, 100, 300, 1000, 3000, 10000\ \mu$m).

The smooth case establishes the baseline friction coefficient, while the rough cases represent progressively more severe surface conditions. Equivalent sand-grain roughness is used because it provides a common engineering parameter for connecting surface roughness to the rough-wall similarity formulation. As an illustrative heterogeneous condition, the hull is first divided into four consecutive regions with

$$k_{s,i} = 600 - 100i\ \mu\text{m}, \qquad i = 1, 2, 3, 4. \tag{7}$$

This monotonically decreasing distribution represents a hull for which the forward region is more heavily fouled and the roughness gradually decreases towards the stern. This synthetic case is used purely to illustrate the sequential virtual-length mechanism before the method is confronted with full-scale CFD data (Section 3.3). For the CFD-validated case, the hull is instead segmented directly from the self-propulsion CFD geometry into eight and, separately, four longitudinal zones shown in Fig. 2, with equivalent sand-grain roughness. The four-zone case groups the same distribution into coarser regions to test the sensitivity of the method to spatial resolution.

$$k_{s,i} = 600 - 50i\ \mu\text{m}, \qquad i = 1, 2, 3, 4, 5, 6, 7, 8. \tag{8}$$

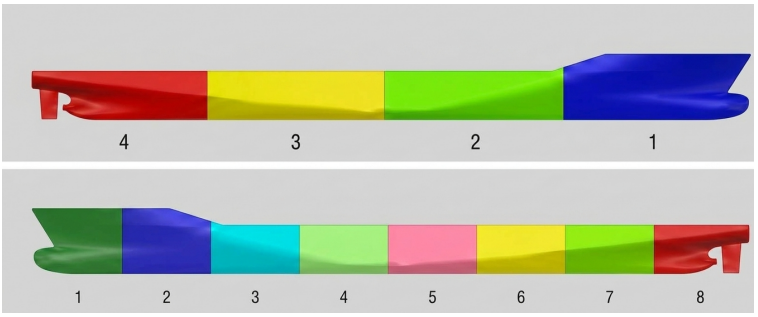


Figure 2: Longitudinal segmentation of the full-scale KCS hull used for the CFD-validated heterogeneous roughness cases: eight zones (bottom) and four zones (top).

3. Results and Discussion

3.1. Homogeneous roughness

The homogeneous calculations establish the expected increase in friction coefficient with increasing roughness. They were first validated against an independent full-scale self-propulsion KCS CFD study (own prior work (Ozturk et al, 2026), not the heterogeneous cases of Section 3.3) and against the homogeneous-roughness KCS results reported by Demirel et al. (2017). The principal particulars and conditions of the KCS simulations are given in Table 1, while the comparison of friction coefficients is summarised in Table 2. The roughness function model of Demirel et al. (2017), shown in Fig. 3, was applied in both the CFD wall treatment and the Granville code.

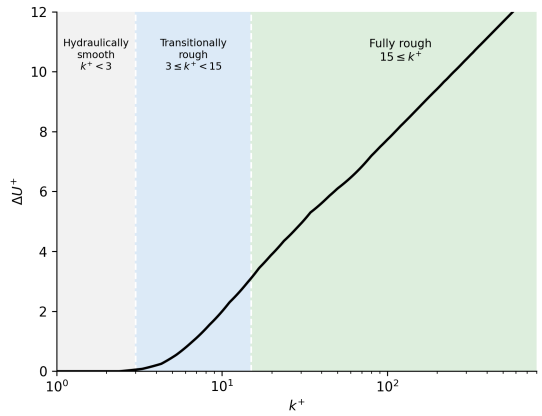


Figure 3: Roughness Function Model of Demirel et al. (2017).

Table 1: Principal particulars and conditions of the KCS simulations, adapted from Kim et al. (2001).

Main particulars	**Full-scale**	**Model-scale**
Scale factor, λ	1	31.6
Length between perpendiculars, L_{PP} (m)	230	7.278
Length of waterline, L_{WL} (m)	232.5	7.358
Beam at waterline, B_{WL} (m)	32.2	1.019
Depth, D (m)	19	0.601
Design draught, T (m)	10.8	0.342
Length–depth ratio, L_{PP}/T	21.30	21.30
Wetted surface area with rudder, S (m^2)	9539	9.553
Displacement, ∇ (m^3)	52 030	1.649
Block coefficient, C_B	0.6505	0.6505
Design speed, V (knot/(m/s))	24	2.196
Froude number at design speed, F_n	0.26	0.26

Table 2: Full-scale KCS friction coefficients for homogeneous roughness at 24 kn: own CFD, own multi-zone-code Granville implementation (homogeneous limit), and comparison with Demirel et al. (2017) (their Table 9).

k_s (μm)	**Own CFD** $C_F \times 10^3$	**Own Granville** $C_F \times 10^3$	**Error (%)**	**Demirel (2017) Granville–CFD (%)**	**Own CFD vs. Demirel CFD (%)**
0	1.443	1.331	7.75	7.117	1.538
30	1.615	1.478	8.47	9.926	2.398
100	1.885	1.757	6.80	5.566	2.455
300	2.180	2.043	6.27	6.529	2.810
1000	2.589	2.464	4.84	5.472	2.997
3000	3.053	2.968	2.80	3.824	1.309
10000	3.789	3.710	2.08	3.777	1.280

All full-scale simulations and the Granville code use fresh-water properties, $\rho = 997.561$ kg/m^3 and $\nu = 8.91 \times 10^{-7}$ m^2/s, applied consistently in both the CFD and the similarity-law code. This differs from the seawater properties ($\rho \approx 1025$ kg/m^3, $\nu \approx 1.1892 \times 10^{-6}$ m^2/s) typically used in full-scale KCS studies such as Demirel et al. (2017); the comparison in Table 2 should therefore be read as validating the present roughness-scaling methodology rather than as a strict like-for-like numerical match. The "Error" column is the deviation of the present Granville code from the present own CFD result; the "Demirel (2017)" column is the independently reported Granville–CFD deviation from Demirel et al. (2017) for the same roughness range on the KCS hull. Both error trends agree closely and fall from around 8% (transitionally rough) to 2–4% (fully rough) with increasing k_s, and the own CFD result stays within 1.3–3.0% of the CFD value reported by Demirel et al. (2017). This cross-validates the present homogeneous Granville implementation against an independent CFD study and an independent literature benchmark before it is extended to the heterogeneous cases of Section 3.3.

The trend confirms that the roughness penalty cannot be represented solely by a fixed increment in friction coefficient. The increase is nonlinear with respect to k_s, reflecting the dependence of the roughness function on the dimensionless roughness scale and the local wall-flow condition. Retaining the Granville similarity-law framework therefore provides a physically motivated treatment of the roughness effect.

The results also illustrate why scale effects must be considered carefully. A physical roughness height does not correspond to a unique resistance penalty independently of ship size and speed. The relevant quantity is the

roughness relative to the viscous scale, represented here through k_s^+. Consequently, a dimensional roughness measured on a model surface cannot be transferred directly to full scale without appropriate similarity scaling.

3.2. Heterogeneous KCS CFD and Extended Granville in comparison

Song et al. (2021) developed a heterogeneous roughness prediction method based on Granville's similarity law and demonstrated it against Wigley-hull towing tests. Their work provides important experimental evidence that roughness location matters. The present formulation is positioned as a complementary approach in which the upstream similarity state is explicitly propagated from one longitudinal region to the next through a virtual coordinate. To assess the capability of the proposed formulation against a realistic hull condition, full-scale self-propulsion CFD simulations of the KCS hull were carried out with a Virtual Disc (VD) model representing the KP505 propeller at a fixed rate of 103.7 rpm (Ozturk et al, 2026). Under the smooth-hull condition this rate corresponds to the vessel's design speed of 24.0 kn. Applying the non-uniform roughness distributions shown in Fig. 2 at the same propeller rate increases the shear resistance and reduces the achieved speed from the 24.0 kn design speed to approximately 22.8 kn. . The integrated hull shear force and the achieved speed from each CFD run were used to derive a reference rough friction coefficient, C_F^{CFD}, which is compared against the friction coefficient obtained from the multi-zone Granville code, $C_F^{\mathrm{Granville}}$, run with the same zone boundaries and roughness heights.

Table 3: Full-scale KCS self-propulsion CFD results and multi-zone Granville code predictions for the eight-zone and four-zone heterogeneous roughness distributions of Fig. 2.

Parameter	**8-zone**	**4-zone**	**Unit**
Propeller rate	103.7	103.7	rpm
Achieved speed, U	11.735 (22.81)	11.752 (22.85)	m/s (kn)
Total hull shear force	1 533 176	1 518 150	N
Wetted surface area, S	9 710	9 710	m^2
$C_F^{\mathrm{CFD}} \times 10^3$	2.300	2.270	–
$C_F^{\mathrm{Granville}} \times 10^3$	2.190	2.166	–
Relative error	4.78	4.58	%

The relative error is evaluated as

$$\text{Error} = \frac{C_F^{\mathrm{Granville}} - C_F^{\mathrm{CFD}}}{C_F^{\mathrm{CFD}}} \times 100, \tag{9}$$

giving 4.78% for the eight-zone segmentation and 4.57% for the four-zone segmentation. The multi-zone code consistently underestimates the CFD friction coefficient for rough case, as in the homogeneous case. By presenting this method, it is demonstrated that the Granville approach can be used to predict C_f even for non-uniform roughness.

Reported homogeneous Granville/Schultz-type formulations typically show deviations of 3–10% against experimental or high-fidelity numerical data (Schultz, 2007), and previous CFD studies confirm that roughness location and distribution influence ship resistance (Ravenna et al., 2022). The errors obtained here, below 5% for a non-uniform, multi-zone virtual-length treatment of a full-scale self-propelled hull, sit at the favourable end of that range, supporting the robustness of the proposed extension at a fraction of the computational cost of a self-propulsion CFD run.

3.3. Practical significance and limitations

The main practical attraction of the proposed method is computational cost: a spatially resolved fouling map can, in principle, be converted into a sequence of representative k_s values and propagated through the similarity-law calculation, bridging surface-condition inspection data and a full-scale friction estimate without a new three-dimensional CFD run for every fouling distribution.

Nevertheless, the method remains a boundary-layer approximation and is not expected to reproduce three-dimensional effects associated with hull geometry, pressure gradients, separation, appendages, or pressure-related resistance components. CFD therefore remains important where such effects are significant; the proposed approach is best regarded as a fast engineering model that complements, rather than replaces, high-fidelity CFD.

It should be noted that in CFD simulations using wall functions, the near-wall grid spacing (e.g., initial cell height in STAR-CCM+) must exceed the roughness height, establishing the strict requirement of $y^+ > k^+$. If the first cell center falls within or below the roughness layer ($y^+ \leq k^+$), standard log-law wall functions cannot mathematically resolve the flow within the sublayer. Consequently, maintaining this threshold is essential to prevent unphysical velocity shifts, severe numerical errors, or solver divergence near rough boundaries.

4. Conclusions and Recommendations

A region-by-region extension of Granville's similarity-law framework has been formulated for heterogeneous hull roughness. The principal conclusions are:

1. Granville's similarity-law framework provides a physically motivated and computationally inexpensive route for transferring a prescribed roughness condition to full-scale friction resistance.

2. A heterogeneous hull cannot in general be represented adequately only by a single roughness height or a roughened-area average because the longitudinal location of roughness can influence the resistance penalty. In real life applications, uniform roughness over submerged or ship bodies is also unrealistic, as surface roughness is typically spatially heterogeneous.

3. The proposed virtual-length formulation allows the similarity-law calculation to proceed sequentially from the bow towards the stern while retaining the accumulated effect of upstream roughness.

4. Once the virtual length is added, the effective length of the plate (or the ship treated as an equivalent plate) becomes greater than its original physical length.The virtual coordinate is an equivalent similarity-law quantity and should not be interpreted as a physical change in ship dimensions.

5. Full-scale self-propulsion CFD comparisons for the KCS hull under non-uniform roughness give relative errors of -4.78% (eight-zone segmentation) and -4.58% (four-zone segmentation) between the multi-zone Granville code and CFD, within the lower part of the 3–10% range typically reported for homogeneous similarity-law formulations, and essentially unchanged between the two zone resolutions.

The next stage should focus on systematic validation against CFD and experimental data for multiple heterogeneous distributions. Forward-rough, aft-rough, alternating, and smoothly varying roughness patterns should be investigated at comparable roughened areas. The sensitivity to region length, roughness-function choice, and the rate of change between neighbouring regions should also be quantified.

A further objective is to connect the method with spatially resolved biofouling observations. An inspection image or fouling map could be converted into a distribution of equivalent k_s values, which could then be evaluated using the proposed similarity-law procedure. This would provide a low-cost intermediate model between raw fouling observations and high-fidelity CFD and could ultimately support data-driven hull-maintenance and cleaning decisions.

References

Demirel, Y. K., Turan, O., & Incecik, A. (2017). Predicting the effect of biofouling on ship resistance using CFD. *Applied Ocean Research*, 62, 100–118.

Farkas, A., Degiuli, N., & Martic, I. (2018). Towards the prediction of the effect of biofilm on the ship resistance using CFD. *Ocean Engineering*, 167, 169–186.

Granville, P. S. (1958). The frictional resistance and turbulent boundary layer of rough surfaces. *Journal of Ship Research*, 2(4), 52–74.

Granville, P. S. (1978). Similarity-law characterization methods for arbitrary hydrodynamic roughnesses. *Naval Ship Research and Development Center Report*, 78/002.

Kim, W. J., Van, S. H., & Kim, D. H. (2001). Measurement of flows around modern commercial ship models. *Experiments in Fluids*, 31(5), 567–578.

Ozturk et al. (2026). The ongoing heterogeneous roughness CFD study in preperation for publication. -.

Ravenna, R., Song, S., Shi, W., Sant, T., De Marco Muscat-Fenech, C., Tezdogan, T., & Demirel, Y. K. (2022). CFD analysis of the effect of heterogeneous hull roughness on ship resistance. *Ocean Engineering*, 258, 111733.

Schultz, M. P. (2007). Effects of coating roughness and biofouling on ship resistance and powering. *Biofouling*, 23(5), 331–341.

Schoenherr, K. E. (1932). Resistance of flat surfaces moving through a fluid. *Trans. SNAME*, 40, 279–313.

Song, S., Demirel, Y. K., & Atlar, M. (2019). An investigation into the effect of biofouling on the ship hydrodynamic characteristics using CFD. *Ocean Engineering*, 175, 122–137.

Song, S., Ravenna, R., Dai, S., DeMarco Muscat-Fenech, C., Tani, G., Demirel, Y. K., Atlar, M., Day, S., & Incecik, A. (2021). Experimental investigation on the effect of heterogeneous hull roughness on ship resistance. *Ocean Engineering*, 223, 108590.

Improving hybrid RANS/LES simulation of ship flows through turbulence forcing

Antoine Monot*, Christophe Friess†, Emmanuel Guilmineau*,
Michel Visonneau* and **Jeroen Wackers***
*LHEEA Lab – Centrale Nantes / CNRS, † M2P2 – Aix-Marseille Univ, CNRS, Centrale Med
jeroen.wackers@ec-nantes.fr

1 Introduction

Ship flows are often characterised by strong separation zones and vortex creation on the aftship, appendages, and sharp corners. RANS models have difficulties representing the phsics of these flows exactly. Hybrid RANS/LES (HRL) turbulence models, which use a LES behaviour to represent these separated flows while limiting costs by representing the near-wall behaviour with RANS, appear like an ideal solution for high-fidelity ship simulation. And yet, even HRL simulations for ships are often plagued by incorrect velocity profiles and turbulent quantities.

The main cause of these issues is the grey area (GA), where the change from RANS to LES occurs. Here, models like Detached-Eddy Simulation (DES) and its subsequent iterations do not transfer modelled turbulent kinetic energy from the RANS part to resolved turbulence in the LES part. Instead, the modelled turbulence is artificially destroyed to make place for resolved turbulence. However, in doing so, the physical TKE balance is violated: the total TKE should be conserved over the paradigm change.

In Monot et al. (2024); Monot (2025) we proposed a mechanism for DES-type models, to transfer artificially destroyed modelled TKE to resolved eddies. The approach uses a volume forcing which amplifies already existing velocity fluctuations. The forcing amplitude is derived from the artificial dissipation of modelled TKE which DES-type methods use to transition to the LES mode; this unphysical dissipation is compensated by generating the equivalent amount of resolved kinetic energy. The turbulent scales in which the TKE is injected are extracted from the flow with a variable-coefficient temporal filter.

In this paper, the method is applied to DDES-SST (Gritskevich et al., 2012) and used to simulate two vortex-dominated ship flows: the the double-model Japan Bulk Carrier, and the DTMB 5415 destroyer in 10 degree sideslip conditions. For both cases, experimental data, standard DDES, and DDES with forcing are compared. Our in-house flow solver ISIS-CFD is used with the average-based adaptive mesh refinement approach of Mozaffari et al. (2022). We investigate to what extent the discrepancies in standard DDES simulations for these cases can be attributed to GA issues, and if the turbulence forcing improves the prediction of such complex, realistic flows.

2 Turbulence forcing method

In DES-type models based on $k-\omega$ SST (Menter, 1993), the additional dissipation of modelled energy required to switch from RANS to LES is obtained by artificially increasing the dissipation in the TKE equation. The original transport equation is defined as:

$$\frac{\partial \rho k}{\partial t} + \frac{\partial}{\partial x_j}\left(\underbrace{\rho u_j k}_{\text{Advection}} \underbrace{- (\mu + \sigma_k \mu_t)\frac{\partial k}{\partial x_j}}_{\text{Diffusion}} \right) = \underbrace{\tau_{ij}^u \frac{\partial u_i}{\partial x_j}}_{\text{Production}} - \underbrace{\rho \beta^* \omega k.}_{\text{Dissipation}(\rho\varepsilon_{k-\omega})} \tag{1}$$

For DDES-SST (Gritskevich et al., 2012), to obtain consistency with the original DES-SST formulation, we write the modified k-dissipation term as:

$$\varepsilon_{DDES} = \beta^* \omega k \, F_{DDES}, \tag{2}$$

where the DDES limiter F_{DDES} incorporates the delay function f_d (defined in the original paper):

$$F_{\text{DDES}} = \frac{l_{k-\omega}}{l_{k-\omega} - f_d \max\left(0, l_{k-\omega} - C_{\text{DES}}\Delta\right)}. \tag{3}$$

Transfer dissipation Our forcing method uses a decomposition of the dissipation term ε_{DDES} in two parts:

$$\varepsilon_{DDES} = \varepsilon_{SGS} + \varepsilon_{tr}, \tag{4}$$

where ε_{SGS} is the physical dissipation of the sub-grid scale model and ε_{tr} the transfer dissipation of modelled to resolved energy. While $\varepsilon_{SGS} = \varepsilon_{DDES}$ in fully developed RANS and LES zones, no expression for ε_{SGS} exists in the grey area. The simplest approximation is to represent ε_{SGS} by the RANS dissipation term $\beta^*\omega k$, which implies $\varepsilon_{\text{tr}} = \beta^*\omega k(F_{\text{DDES}} - 1)$. However, this estimation does not go to zero in fully developed LES flow (where $F_{\text{DDES}} > 1$), unless k becomes zero. Therefore, we evaluate the RANS dissipation with the total (modelled+resolved) TKE instead of the modelled TKE only, which yields:

$$\varepsilon_{\text{tr}} = \max(\beta^*\omega k F_{\text{DDES}} - \beta^*\omega k_{\text{tot}}, 0). \tag{5}$$

The resolved TKE k_{res} is estimated at the start of each time step. The total energy is then evaluated as $k_{\text{tot}} = k + k_{\text{res}}$. A time average is used to determine the value of k_{res} during the computation.

Targeted turbulent scales When creating turbulence through momentum forcing, the turbulent scales targeted by the forcing are crucial for achieving physically realistic resolved turbulence. We use a modification of the volume forcing by Lundgren (2003), which is based on the amplification of pre-existing turbulence. Thus, a body force $f_i = Au'_i$ is added as a source term to the Navier-Stokes equations, where u'_i are the pre-existing velocity fluctuations of the flow field defined using a low-pass filter: $u'_i = u_i - \widetilde{u}_i$ with $\widetilde{u}_i$ the filtered velocity, computed using an exponential averaging. This filter varies in time and space to make sure that turbulence is injected in the smallest scales that the mesh can represent.

Computation of the forcing For numerical robustness, the volume force f_i is computed with a splitting approach: in a time step, first f_i is computed as the force needed to transfer the energy $\varepsilon_{tr}\Delta t$ to the fluid, if all other forces are neglected. This f_i is then added to the momentum equations. Thus, the first step of the splitting requires:

$$\frac{1}{2}\rho\left(\|u'^{\dagger}\|^2 - \|u'^{n}\|^2\right) = \varepsilon_{tr}\Delta t, \tag{6}$$

with $\|u'^{n}\| = u'^{n}_i u'^{n}_i$ the amplitude of the estimated velocity fluctuation at time step n and $\|u'^{\dagger}\|$ the target fluctuation amplitude after the splitting step. Rewriting (6) yields:

$$\|u'^{\dagger}\| = \sqrt{\frac{2}{\rho}\varepsilon_{tr}\Delta t + \|u'^{n}\|^2}. \tag{7}$$

Thanks to the splitting, the velocity fluctuations and the forcing are aligned, so the body force is computed as follows:

$$f_i = \rho u'^{n}_i \left(\frac{\|u'^{\dagger}\|}{\|u'^{n}\|} - 1\right)/\Delta t. \tag{8}$$

3 Japen Bulk Carrier test case

The Japan Bulk Carrier (JBC) has a pronounced U-shape at the stern which creates flow separation and longitudinal vortices with intense turbulence. It is simulated in model scale and double-model configuration, with $L_{pp} = 3.513$ m, draught $T = 0.208$ m, inflow speed $U_\infty = 10$ m/s and Reynolds number $Re = 2.42 \cdot 10^6$. The experiments, and the full numerical setup, are described in Visonneau et al. (2026). The domain size corresponds to the bottom half of the TUHH wind tunnel test section where the experiments were performed. Boundary conditions are no-slip on the hull, wall law on the bottom, slip surfaces on the sides, and symmetry on top. Velocity and turbulence quantities are imposed at the inlet, and zero pressure at the outlet. The adaptively refined meshes have about 8M cells.

Figure 2 shows the flow in the S4D plane at the stern, and figure 3 the aftship flow structures. The attached boundary layer is modelled fully in RANS, until the flow separation on the aftship triggers a switch to LES (figure 1). This is a worst-case scenario for DDES-SST, which uses boundary layer

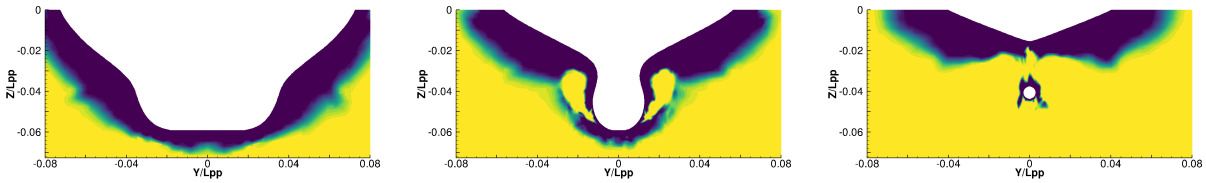


Fig. 1: JBC, DDES shielding function f_d (blue: shielded RANS, yellow: DES) in three locations on the aftship: $X/L_{pp} = [0.9, 0.95, 0.9811]$. The last two figures are the planes S1 and S4D.

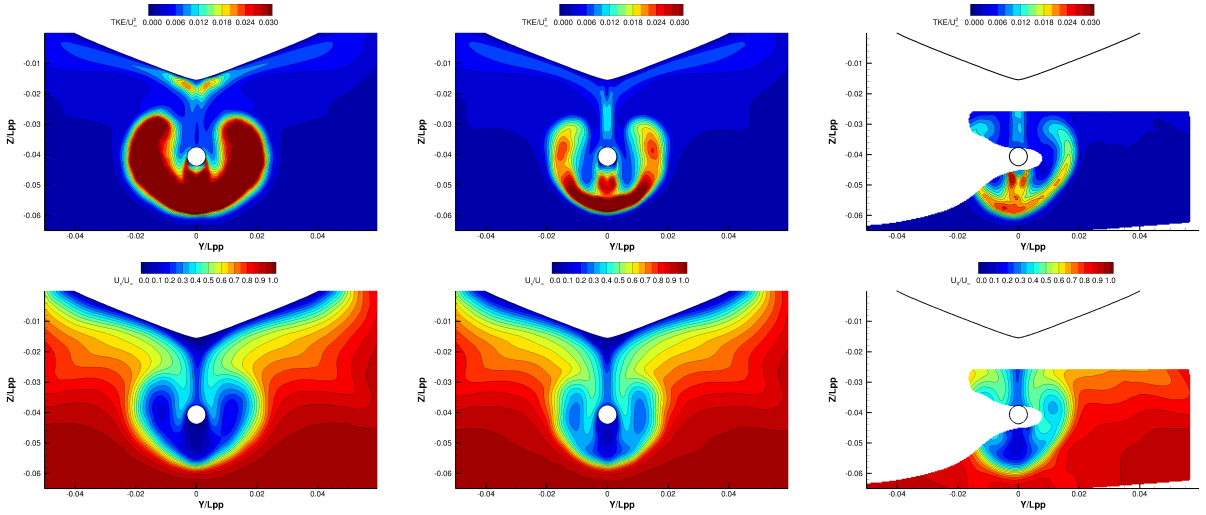


Fig. 2: Contour of $\langle k_{\text{tot}} \rangle$ (top), $\langle u \rangle$ (bottom) for the JBC, S4D plane ($x/L_{pp} = 0.9811$). Left to right: standard DDES-SST; DDES-SST with forcing; experimental data.

shielding through the function f_d to minimise the interaction between RANS and LES and prevent GA problems. For the JBC, the LES zone appears *inside* the RANS boundary layer (figure 1 centre), so no shielding can keep them apart; the case always has a significant GA. As a result, standard DDES-SST overestimates the total TKE behind the hull and the velocity wake is too thick (figure 2). This is explained by the turbulent structures, which show the (belated) development of large, persistent, and highly energetic eddies (figure 3 left). The flow behaves in fact like the destabilisation of a laminar separation, since the RANS attached boundary layer contains no resolved turbulence.

The turbulence forcing changes this. Figure 3 right shows that the TKE transfer ε_{tr} is active in a thin sheet at the start of the flow separation zone, injecting the destroyed modelled TKE as small-scale fluctuations. These trigger the destabilisation of the separated flow, so the turbulence that is physically generated in the aft-ship vortices also has smaller scales (figure 3 centre). This in turn leads to increased dissipation, which reduces the total TKE to a value close to the experiments (figure 2). Thus, in this case,

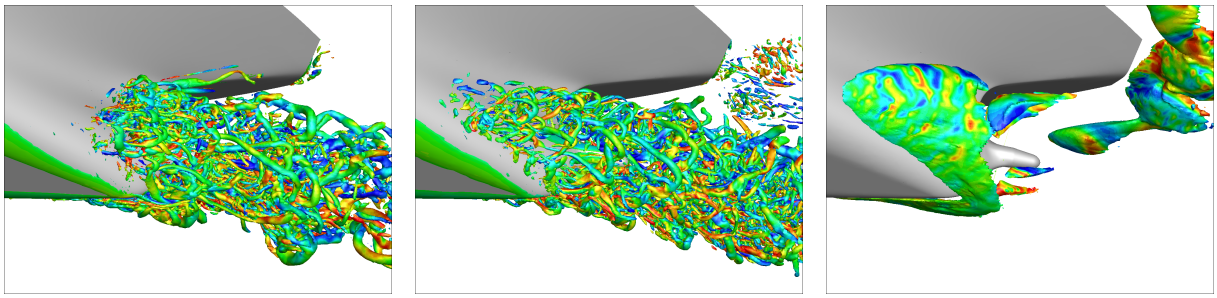


Fig. 3: JBC, instantaneous dimensionless Q-criterion $Q^* = 10^4$ coloured by helicity, for standard DDES-SST and DDES-SST with forcing; mean transfer dissipation $\langle \varepsilon_{\text{tr}} \rangle = 50\text{m}^2\,\text{s}^{-3}$ coloured by helicity.

the injection of transfer turbulence actually decreases the total amount of TKE. This shows that not only the conservation of the total turbulence, but also the creation of the right resolved scales is essential to correctly predict the flow in the grey area.

4 DTMB 5512 in sideslip

The second case concerns the DTMB 5512 in combined forward and sideways motion. This case features several separations, from the sonar dome, the bilge keels, and the aftship. Earlier studies like Visonneau et al. (2020) found that DDES-SST successfully reproduces all flow features but overestimates the TKE in the main vortex coming from the sonar dome.

The model-scale free surface case has a waterline length $L_{pp} = 3.048$ m, velocity $U_\infty = 1.53\ \mathrm{m\,s^{-1}}$, and viscosity $\nu = 1.004 \cdot 10^{-6}\mathrm{m^2\,s^{-1}}$, with Reynolds number $Re = 4.65 \cdot 10^6$ and Froude number $Fr = 0.28$. The model is in a fixed attitude, with a sideslip angle of 10° to port. Tomographic particle image velocimetry (TPIV) experiments were conducted by Iowa Institute of Hydraulics Research (IIHR) (Yoon et al., 2014). The simulation has no-slip conditions on the hull with $y^+ \approx 1$, imposed velocity on the vertical domain faces, and imposed pressure on the top and bottom. The adapted grid has 154M cells.

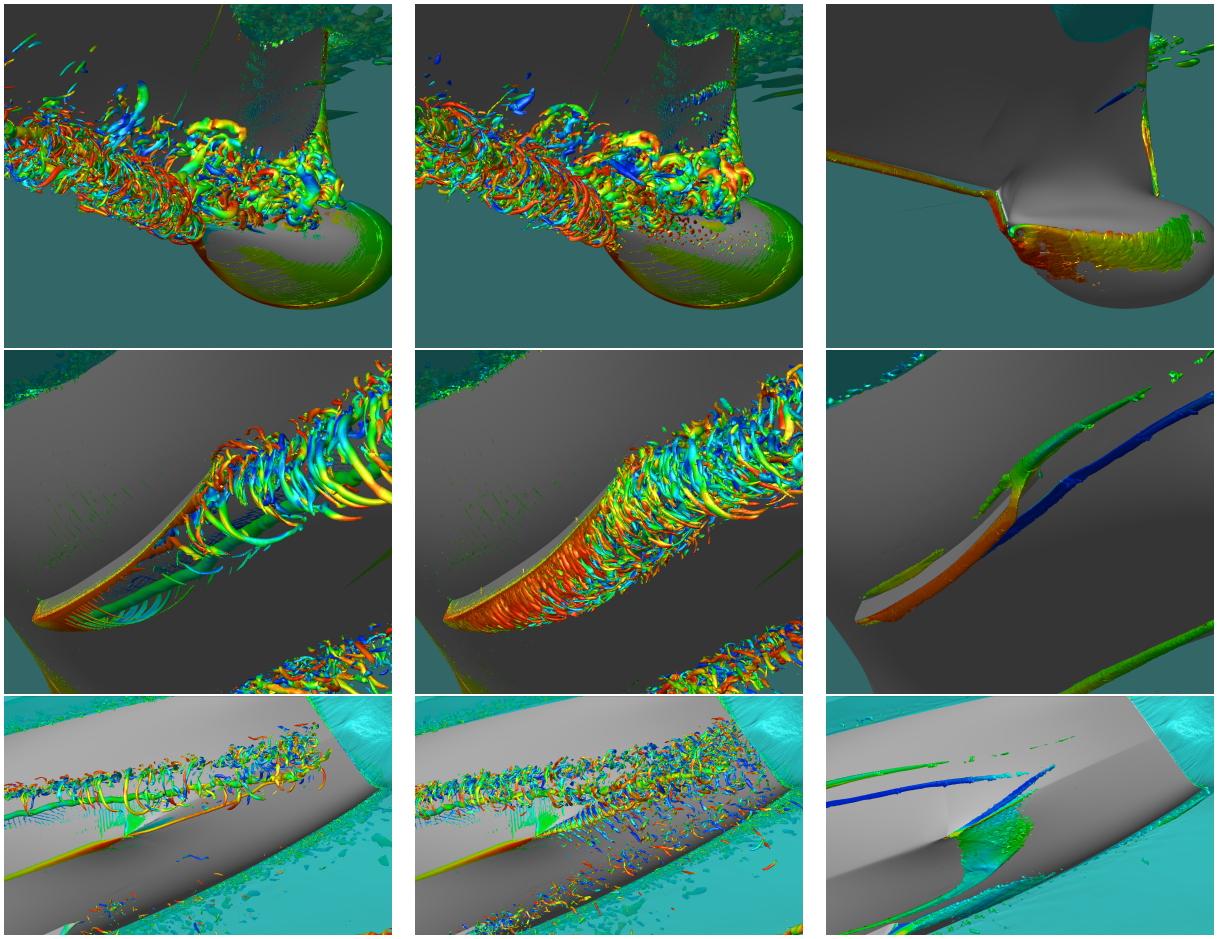


Fig. 4: DTMB 5512, closeup of vortex origins – Top to bottom: leeward side of the sonar dome; windward bilge keel; stern – Left to right: instantaneous Q-criterion $Q^* = 10^4$ coloured by helicity, for standard DDES-SST and DDES-SST with forcing; mean transfer dissipation $\langle \varepsilon_{\mathrm{tr}} \rangle = 50\mathrm{m^2\,s^{-3}}$ coloured by helicity.

While the turbulent structures with and without forcing (figure 4) are globally similar, the forcing adds small-scale eddies; its main effect is an earlier destabilisation of the flow in areas with boundary layer separation. This effect varies with the position on the hull, which determines the modelled turbulence in the boundary layer before separation. On the sonar dome, the attached boundary layer has had little chance to develop so the real separation is almost laminar; therefore, when this flow destabilises

on the leeward side, the two predictions are similar. The windward bilge keel, on the other hand, is immersed in the turbulent hull boundary layer, so the separating flow is turbulent. However, since the hull turbulence is modelled, without forcing it does not stimulate the flow in the GA near the keel, which causes unphysical quasi-laminar separation, like for the JBC. With the forcing, the flow is turbulent as expected. For the same reasons, the simulation without forcing predicts a vortex coming from the skeg (last row in figure 4), that appears laminar. Forcing creates a much more believable turbulent vortex.

The right column of figure 4 displays isosurfaces of $\langle \varepsilon_{\mathrm{tr}} \rangle$. The forcing is highly local and active in areas with strong separation (like the leeward side of the sonar dome and the edge of the bilge keel), and areas where a vortex is connected with the hull boundary layer through a shear layer. Both correspond to grey areas, due to the change from RANS to LES during separation, and the ambiguous grid in shear layers (which should be fine to capture the shear layer, but coarse for the RANS boundary layer).

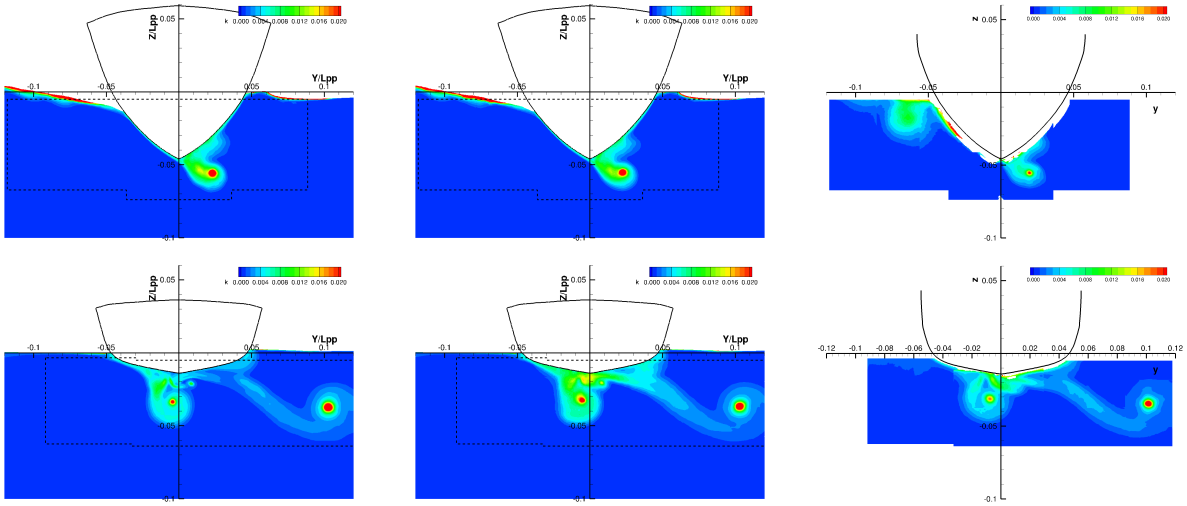


Fig. 5: Contour of $\langle k_{\mathrm{tot}} \rangle$ — Top to bottom: $X/L_{pp} = [0.2, 0.935]$ — Left to right: standard DDES-SST; DDES-SST with forcing; experimental data.

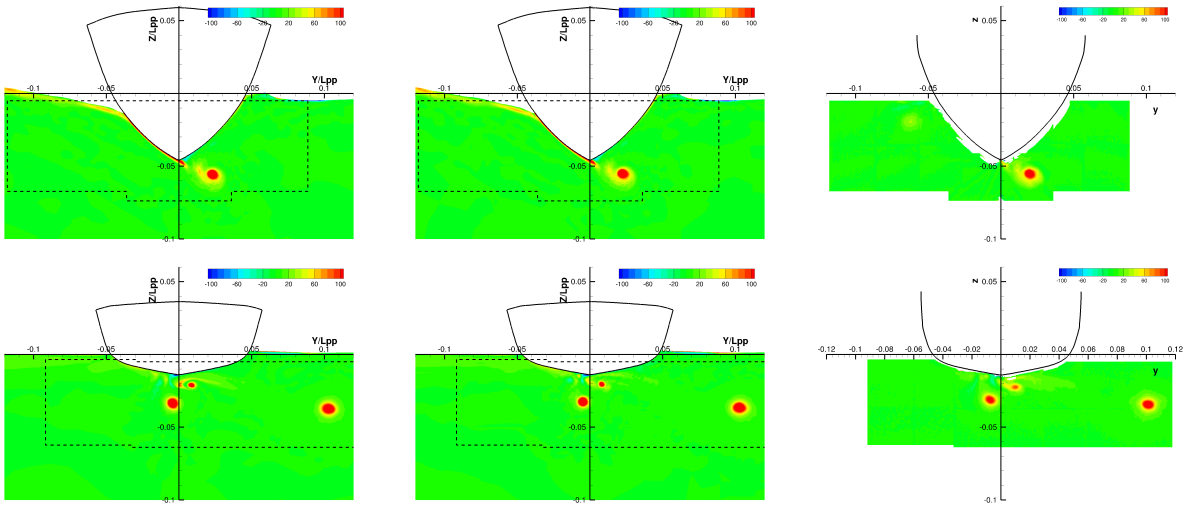


Fig. 6: Contour of axial vorticity — Top to bottom: $X/L_{pp} = [0.2, 0.935]$ — Left to right: standard DDES-SST; DDES-SST with forcing; experimental data.

Contours of the axial vorticity and TKE in two cross-sections along the hull are compared with experimental data in Figs. 5 and 6. The result with forcing remains close to the original DDES-SST, but several localized improvements can be identified. For the sonar dome tip vortex ($X/L_{pp} = 0.2$),

the forcing reduces the TKE in the periphery of the vortex core. The core turbulence is overestimated however, but since this error is identical with or without the forcing, this is probably not caused by the GA. The most significant improvement occurs in the small skeg vortex at $X/L_{pp} = 0.935$ (below the hull near the centreline), where the turbulent flow predicted with the forcing shows a more diffused vortex core that is in better agreement with the experimental data. However, the forcing increases the TKE throughout the wakes of the sonar dome and bilge keel tip vortices at $X/L_{pp} = 0.935$. This may be an issue with the estimation (5) of the transfer dissipation, since the JBC simulation also overestimates the TKE on the outside of the boundary layer (figure 2).

5 Conclusions

The tests in this paper show, first of all, that the transfer forcing is robust enough to be used for realistic flow simulations in ship hydrodynamics. The resulting conservation of the total TKE significantly improves HRL simulations with boundary layer separations; the DTMB case showed that the stronger the modelled turbulence before separation, the more significant the effect. The JBC results underline that the turbulent frequencies created by the forcing are as important for the flow physics as the total amount of turbulence; also, the forcing can counterintuitively lead to a reduction in the total TKE. Finally, the two different tests indicate that GA issues may be more prevalent in HRL simulations of ships than we think. Thus, reliable hybrid simulation requires a conservation strategy for the total turbulence.

Acknowledgements

The computations were performed using HPC resources from GENCI (Grand Equipement National de Calcul Intensif) (Grant-A0182A00129, Grant-A0192A15730) which is gratefully acknowledged.

References

Gritskevich, M. S., Garbaruk, A. V., Schütze, J., and Menter, F. R. (2012). Development of DDES and IDDES formulations for the k-omega Shear Stress Transport model. *Flow Turbulence Combust*, 88(3):431–449.

Lundgren, T. S. (2003). Linearly forced isotropic turbulence. *Annual Research Briefs of Center for Turbulence Research*, pages 461–473.

Menter, F. R. (1993). Zonal two equation k-omega turbulence models for aerodynamic flows. In *24th Fluid Dynamics Conference*, pages 1–22, Orlando, FL.

Monot, A. (2025). *Development of a stochastic forcing method to reduce modeled stress depletion for hybrid RANS-LES turbulence models*. PhD thesis, Ecole Centrale de Nantes, France.

Monot, A., Friess, C., and Wackers, J. (2024). Grey area mitigation for Detached-Eddy Simulations using volume forcing. *Int J Comput Fluid Dyn*, 38(2-3):246–264.

Mozaffari, S., Guilmineau, E., Visonneau, M., and Wackers, J. (2022). Average-based mesh adaptation for hybrid RANS/LES simulation of complex flows. *Comput Fluids*, 232:105202.

Visonneau, M., Guilmineau, E., and Rubino, G. (2020). Local flow around a surface combatant at various static drift conditions: The role played by turbulence closures. In *33rd Symposium on Naval Hydrodynamics*, pages 1–25, Osaka, Japan.

Visonneau, M., Shevchuk, I., Guilmineau, E., Rubino, G., Sahab, A., and Abdel-Maksoud, M. (2026). Prediction of the flow around the JBC in straight ahead condition. In *36th Symposium on Naval Hydrodynamics*, pages 1–20, Busan, South Korea.

Yoon, H., Gui, L., Bhushan, S., and Stern, F. (2014). Tomographic PIV measurements for a surface combatant at straight ahead and static drift conditions. In *30th Symposium on Naval Hydrodynamics*, pages 980–1000, Hobart, Tasmania, Australia.

28th Numerical Towing Tank Symposium (NuTTS)
19-21 October 2026 - Mülheim an der Ruhr, Germany

Numerical and Experimental Investigation of Inland Waterway Ship–Bank Interaction Using Scale-Resolving Simulation

Melissa Böhm[1,2], **Lahbib Zentari**[1], **Bettar Ould el Moctar**[2], and **Benjamin Friedhoff**[3]
[1]Bundesanstalt für Wasserbau (BAW), Karlsruhe/Germany,
[2]Department of Autonomous and Energy-Efficient Maritime Technologies, Technical University of Berlin, Berlin/Germany,
[3]Development Center for Ship Technology and Transport Systems, Duisburg/Germany
melissa.boehm@baw.de

1 Introduction

Climate change is expected to intensify low-water events, leading to increasingly restricted navigational conditions on inland waterways. This trend increases the difficulty of ship navigation, rendering it more challenging. To assess safety and ease of manoeuvring under these circumstances, accurate navigability analyses are necessary. These rely on mathematical manoeuvring models that take into account ship–waterway interactions, see Eloot and Vantorre (2011). Given the challenges posed by inland waterway vessels and the extreme confinement they are subjected to, Computational Fluid Dynamic (CFD) offers a powerful means of investigating in depth the complex hydrodynamic phenomena governing such ships when travelling near a bank with low under keel clearance. To this end, we analysed a representative case with lateral confinement in very shallow water, both experimentally and numerically. The focus is on comparing two numerical approaches using the following turbulence models: Unsteady Reynolds-Averaged Navier-Stokes (URANS) with the two-equation $k-\omega-$SST as formulated by Menter (1994), and the scale-resolving hybrid Improved Delayed Detached Eddy Simulation (IDDES) model by Gritskevich et al. (2012). We compared their computational costs and evaluated how well the simulated results agreed with the experimental data in terms of hydrodynamic forces and moments, as well as pressure distribution on the hull. The IDDES computations showed the best agreement with the experimental data, albeit at a higher computational cost.

2 Test case and Setup

The investigated test case was the inland waterway ship benchmark introduced by Mucha et al. (2017), at a scale of $\lambda = 16$. It represents a typical 135 m long cargo vessel routinely navigating the Rhine river. Main particulars are detailed in Table 1.

The experimental campaign for investigating bank effects was carried out at the Development Centre for Ship Technology and Transport Systems (DST) in Duisburg, Germany. The test basin has a length of 200 m and a breadth of 9.80 m. For this campaign, a vertical wall 55.35 m long was installed longitudinally to also capture unsteady effects in ship–bank interactions, forming a channel with a width of 6.385 m. The model ship was towed at a constant velocity U_0 of $0.556\,\mathrm{m\,s^{-1}}$ and gradually decelerated after passing the bank.

Figure 2 schematises the experimental setup. The ship, shown in yellow, started 65.00 m behind the wall and was gradually accelerated until reaching the constant speed U_0; it was then decelerated once its stern passed the far extremity of the bank, at 120.35 m from the starting position. The ship travelled with its starboard side close to the wall. Transducers mounted on the ship measured the hydrodynamic longitudinal force X, lateral force Y, and yaw moment N, as well as propeller and duct thrust, T_P and T_D respectively.

The experimental campaign covered various water depth-to-draft ratios h/T, wall distance-to-ship-length ratios d/L_{PP}, and ship speeds U_0, where d is the distance from the wall to midships, L_{PP} the ship length, h the water depth, and T the ship draft. In the present paper, we focused on the worst-case scenario, namely $h/T = 1.2$ and $d/L_{PP} = 0.1$, representing the highest confinement in the test matrix. To assess repeatability, selected tests were run at least twice.

A detailed description of the experimental setup, along with an in-depth uncertainty analysis, will be the subject of a future publication. Figure 2 shows a photograph of the experimental campaign during a test run.

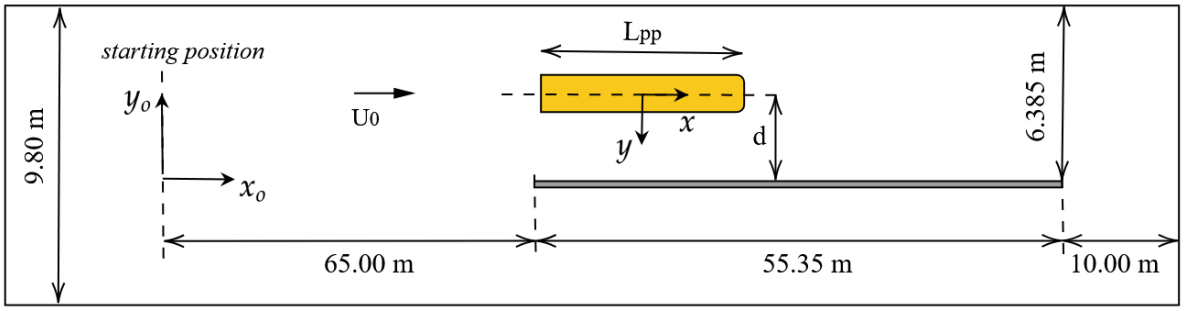


Fig. 1: Setup of the model experiments in the shallow water basin of the DST

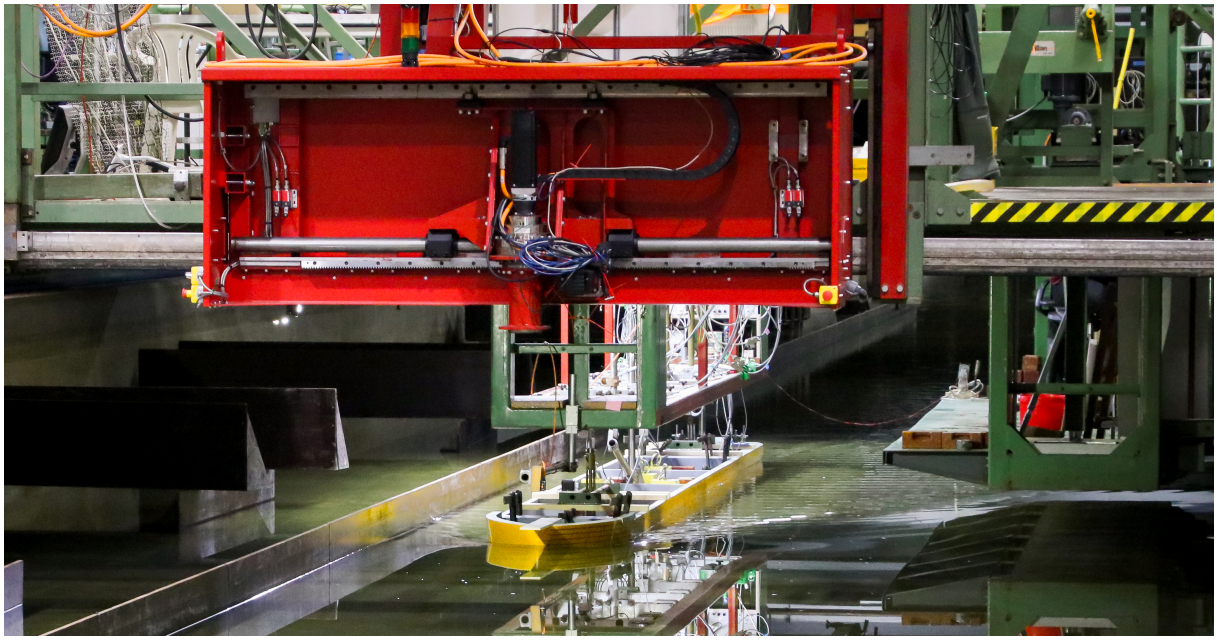


Fig. 2: Model ship and towing carriage during the model experiments in the shallow water basin of the DST

3 Numerical procedure

We performed our numerical flow simulations using the commercial solver Simcenter STAR-CCM+ Siemens (2023). The main objective of the present study was to assess different turbulence modelling approaches regarding accuracy and computational efficiency. For this purpose, we employed the k-ω SST turbulence model for closure, and the hybrid RANS/LES IDDES model. All simulations were conducted as unsteady simulations using the double-body method, motivated by the relatively low Froude number $F_r < 0.1$ and the correspondingly small free-surface disturbance. The trim and sinkage in the simulation are based on averaged model test values.

Figure 3 illustrates the computational domain and the boundary conditions. The domain inflow was specified as a velocity inlet, and the outflow as a pressure outlet. The top boundary was specified as a symmetry plane, and the sides and bottom as no-slip walls, with the relative velocity at the bottom and sides set to the ship speed. The ship hull was also specified as a

Table 1: Main dimensions of the testcase and its appendages under design loading conditions, in both full-scale and model-scale, based on Mucha (2017).

Description	**Symbol**	**Unit**	**Full scale**	**Model scale**
Scale factor	λ	–	1	16
Length of waterline	L_{WL}	m	134.42	8.4013
Length between perpendiculars	L_{PP}	m	135.00	8.4375
Breadth	B	m	11.44	0.7150
Draft	T	m	3.5	0.2188
Wetted surface	S_W	m^2	2376.1	9.2817
Volumetric displacement	∇	m^3	4992	1.2187
Block coefficient	C_B	–	0.92	0.92
Number of propeller blades	Z	–	4	4
Propeller diameter	D_P	m	1.6	0.1

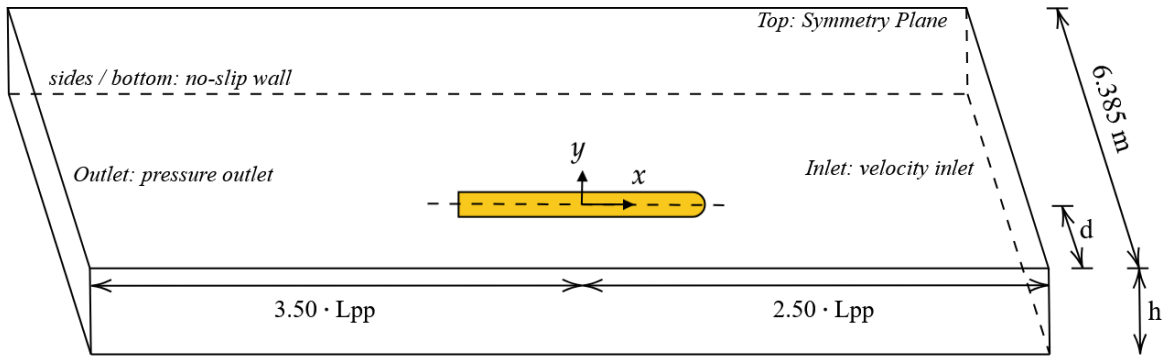


Fig. 3: Computational domain, that represents the period during which the ship travels alongside the wall in the 6.385-metre-wide canal during the experiments.

no-slip wall, with zero tangential velocity. The propeller was modelled using the reference frame method.

For all simulations, a time step of $\Delta t = 0.005\,\mathrm{s}$ and a base grid size of $\Delta x = 0.064\,\mathrm{m}$ were chosen, with second-order temporal discretization applied throughout. The hexahedral trimmed cell mesher was adopted to build an unstructured mesh. Areas of high pressure and velocity gradients were expected around the bow and stern of the model, near the propulsion and steering devices, and between the model and the bank. Accordingly, the grid was refined in these regions. The complete mesh comprised approximately 12.7 million cells, of which 2.3 million were located within the propeller subdomains. The boundary layer on the tank bottom and hull was fully resolved, with y^+ values below unity.

4 Results and Discussion

The main results of our investigations are presented in Figure 4. This figure shows a comparison between the numerical and experimental results for the integral lateral force Y, and yaw moment N acting on the ship as a system, i.e., including steering and propulsive forces. In this figure, the grey line represents the experimental time series, the orange line the results computed using the RANS model; the green line those obtained using the IDDES model. The results shown in this figure compare the time history of forces as the ship passed along the bank. Although the experimental time series was comparatively noisy, the agreement between numerical and experimental results was satisfactory for both models. Table 2 shows a quantitative comparison

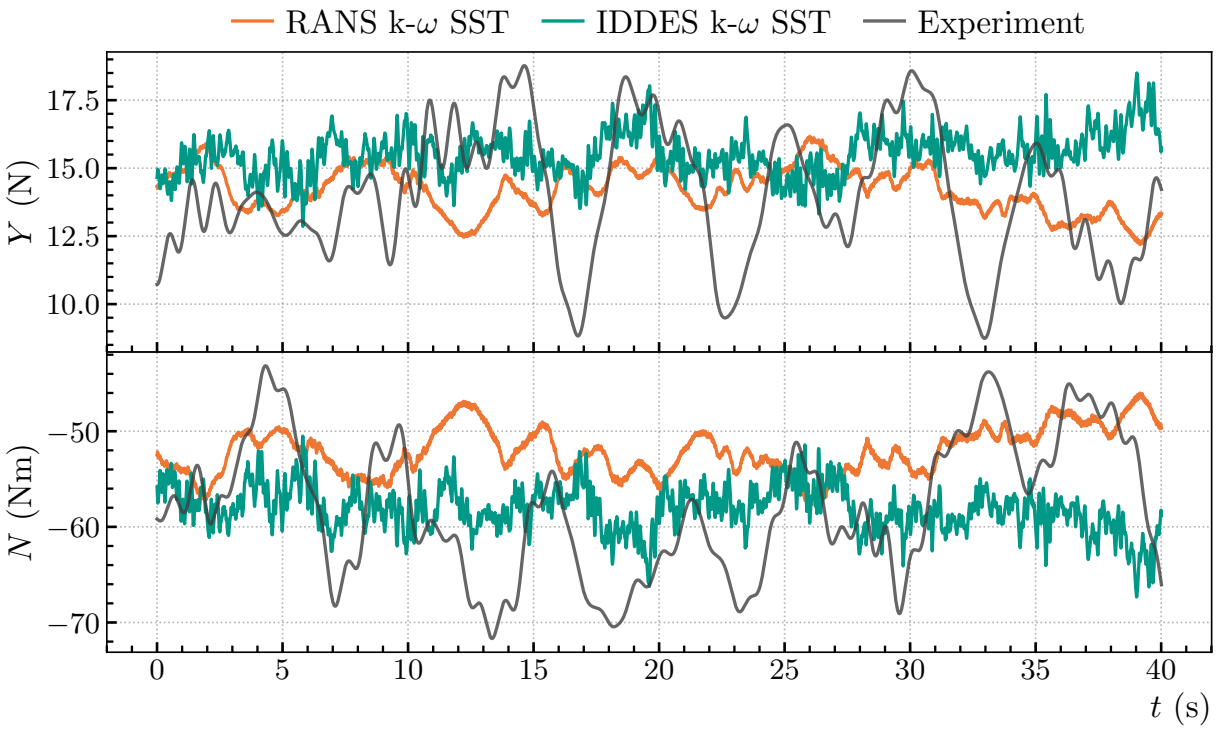


Fig. 4: Time series of hydrodynamic forces Y and N at $d/L_{PP} = 0.1$, $h/T = 1.2$ and $U_0 = 0.556\ \mathrm{m\,s^{-1}}$ comparing two numerical approaches with the experiment.

Table 2: Mean experimental and numerical results for Y and N, based on one experimental test run and two numerical approaches, with percentage differences relative to the experimental results (baseline).

	Y **(N)**	N **(Nm)**	ΔY **(%)**	ΔN **(%)**
Experiment	13.642	-56.085	–	–
RANS k-ω SST	14.268	-52.251	4.59	-6.84
IDDES k-ω SST	15.305	-57.592	12.19	2.69

between the mean force values, with the experimental results serving as the baseline. The best agreement was achieved using the IDDES method for the yaw moment N, while the RANS methodologies offered the best agreement for Y. However, the experimental methodology, which involved a sudden variation in the wall, may have introduced inherent unsteady effects that were not accounted for in the simulations. Indeed, our simulations only considered the quasi-steady case, i.e., a ship sailing straight at a fixed distance from the wall.

The differences between the computed forces obtained using each turbulence model may be explained by comparing the pressure distribution on the hull. Figure 5 and 6 shows the pressure coefficient distribution on the bow and stern region for both considered simulations. In the bow area, there was no clear difference between the approaches: the bank effect was equally visible in both, characterized by the shifted low-pressure zone on the starboard side, resulting from the pressure difference induced by the bank. In the aft region, however, where the flow was rather complex due to the rotating propeller and the complex ship–bank interactions, the pressure distribution revealed a clear difference between the methodologies. Given the scale-resolving nature of the IDDES simulation, its results showed a markedly different pressure field. Nonetheless, these instantaneous snapshots offer only a qualitative comparison.

For the same number of computational nodes on our high-performance computer the RANS

$k-\omega-$SST and IDDES simulations required approximately 3.2 and 3.5 hours of computational time, respectively, for a simulated time of 100 s.

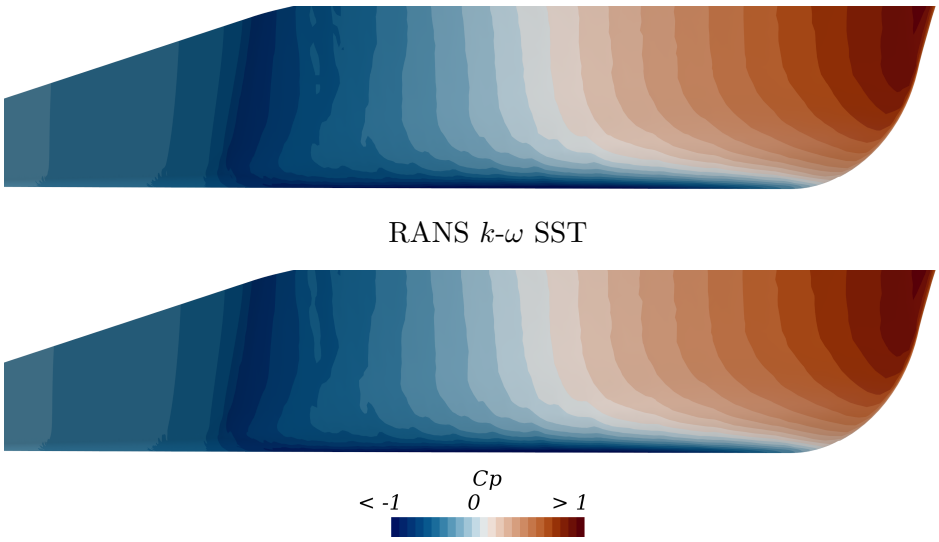


Fig. 5: Distribution of pressure coefficient on ship hull at $d/L_{PP} = 0.1$, $h/T = 1.2$ and $U_0 = 0.556\ \mathrm{m\,s^{-1}}$ for both numerical approaches.

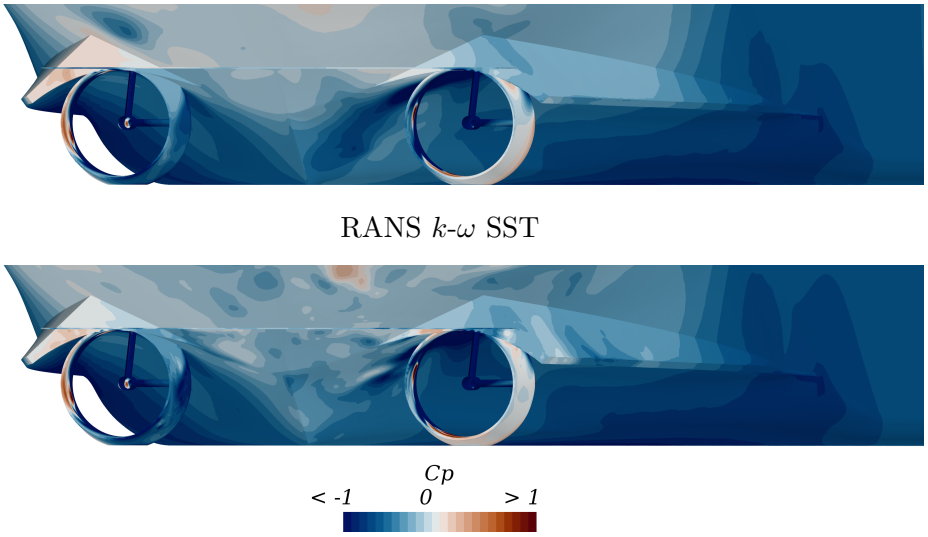


Fig. 6: Distribution of pressure coefficient on ship hull at $d/L_{PP} = 0.1$, $h/T = 1.2$ and $U_0 = 0.556\ \mathrm{m\,s^{-1}}$ for both numerical approaches.

5 Conclusion and Future Work

In this study, we investigated the influence of turbulence modelling on the prediction of ship–bank interaction effects for a representative inland waterway ship case, comparing a RANS approach and the hybrid IDDES method against experimental data. For this particular case, IDDES offered the most promising results for the prediction of the yaw moment N, which is of primary importance for navigability assessments. The RANS methodology, on the other hand, provided the best agreement for the lateral force Y. Nevertheless, the large variances observed in the

experimental time series indicate that a definitive assessment of whether RANS underpredicts the forces would require the study to span multiple bank distances and water depths. Future work will therefore focus on extending the present analysis to other bank distances and water depths, in order to assess the robustness of these findings across the confinement conditions relevant to inland waterway navigation. Additionally, the modelling of the complete unsteady manoeuvre, including the ship's approach to and departure from the bank, will be considered to capture the unsteady effects inherent to the experimental methodology, which were not accounted for in the present quasi-steady simulations.

Acknowledgements

This study originated from a joint research project between the Federal Waterways Engineering and Research Institute (Bundesanstalt für Wasserbau, BAW), the Department of Autonomous and Energy-Efficient Maritime Technologies of the University of Berlin and the Development Center for Ship Technology and Transport Systems (DST).

References

Eloot, K., Vantorre, M., 2011. Ship behaviour in shallow and confined water: an overview of hydrodynamic effects through efd, in: Assessment of stability and control prediction methods for NATO air and sea vehicles, NATO. Research and Technology Organisation (RTO). pp. 1–20.

Gritskevich, M.S., Garbaruk, A.V., Schütze, J., Menter, F.R., 2012. Development of ddes and iddes formulations for the k-ω shear stress transport model. Flow, Turbulence and Combustion 88, 431–449. doi:10.1007/s10494-011-9378-4.

Menter, F.R., 1994. Two-equation eddy-viscosity turbulence models for engineering applications. AIAA Journal 32, 1598–1605.

Mucha, P., 2017. On Simulation-based Ship Maneuvering Prediction in Deep and Shallow Water. Ph.D. thesis. Universität Duisburg-Essen. Duisburg.

Mucha, P., el Moctar, O., Dettmann, T., Tenzer, M., 2017. Inland waterway ship test case for resistance and propulsion prediction in shallow water. Ship Technology Research 64, 106–113. doi:10.1080/09377255.2017.1349723.

Siemens, 2023. Simcenter STAR-CCM+ 2310 User Guide.

Numerical and Experimental Investigation of Phase-Transition During Sloshing Impacts

Andreas Peters[1], Simon Tödter[1], Mohammad Zehab Ud Din[1], Ould el Moctar[2]
[1] Universität Duisburg-Essen, [2] Technische Universität Berlin

Following the global objective to lower carbon emissions, the demand for natural gas (NG) and the sea transport for liquefied natural gas (LNG) has been increasing. Furthermore, renewable and clean energy based on hydrogen represents a growing share in the global energy production and the transportation of liquefied hydrogen (LH2) will increase significantly in the future. Ships can transport these liquids in membrane tanks, which are vulnerable to local sloshing-induced high impact pressures.

Although numerical methods are used to investigate these impact pressures not all physical phenomena are always modelled. This includes phase changes of liquid to gas (vaporization) and vice versa (condensation), strong mixing of the phases, and the compressibility of this mixture. In general, existing numerical methods have not been able to simulate all these physical phenomena adequately.

Experimental investigations of these sloshing phenomena face other challenges. In the past, benchmark tests were mostly performed for sloshing impacts in tanks partially filled with water and air, which represent density ratios different from those of LNG and LH2 and neglecting phase transition processes. Within this work, we performed experimental sloshing tests of tanks partially filled with liquid and gaseous Novec 649, a fluid that boils already at slightly elevated temperatures and moderately reduced pressures controlled by a vacuum pump. Motions in three degrees-of-freedom were applied to generate single repeatable impact events. 25 pressure sensors measured impact pressures. Additionally, high-speed imaging and Background Oriented Schlieren (BOS) were used to record gas pockets and to observe the behavior of the gas phase, respectively.

We performed numerical and experimental investigations of the effects of phase transition between a gas and a liquid on sloshing-induced impact pressures acting on the walls of a partially filled tank. The numerical method solved the equations of conservation of mass, momentum, and energy as well as a transport equation for the volume fraction by considering phase transition, flow compressibility, and surface tension. We modelled phase transition by utilizing a mass transfer model, and validated our numerical method against our own experimental data.

We examined the effects of phase transition on sloshing-induced impact loads generated by a single-impact wave with gas pockets. Both simulations and experiments showed that phase transition during condensation considerably reduced the impact pressure peaks. The pressure oscillations after the first impact were strongly reduced by the vaporization process. The BOS measurement showed clear non-uniform distribution of the gas density within the gas phase, and a significant impact of the heat-intake by the pressure sensors on the behavior of the gas phase.

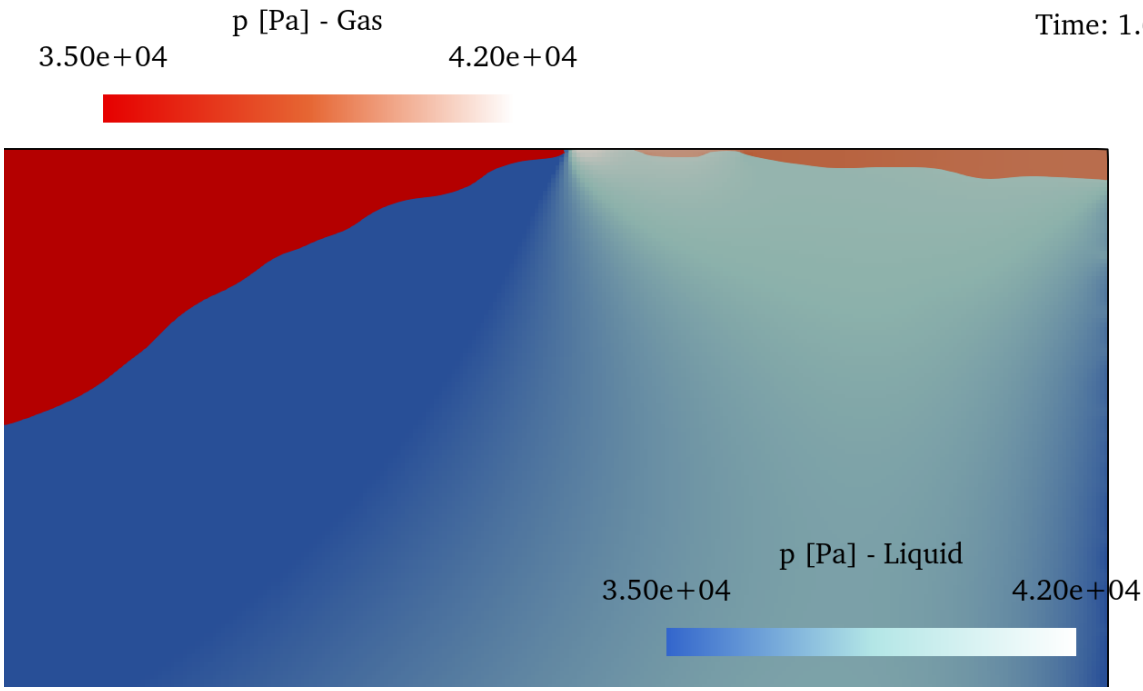


Figure 1: Pressure distribution in gas phase (red) and liquid phase (blue) for a C16 sloshing impact of Novec 649

Hydrodynamic Analysis of a Hybrid Wave Energy Converter–Floating Offshore Wind Turbine Farm Using a 3D Boundary Element Method: Workflow Development and Numerical Challenges

Ribeiro e Silva, Sergio; Fatano, Giacomo

MARETEC – Marine, Environment & Technology Center / LARSyS – Laboratory for Robotics and Engineering Systems, University of Lisbon, Instituto Superior Técnico, Lisbon, Portugal

ribeiro.e.silva@tecnico.ulisboa.pt; giacomo.fatano@tecnico.ulisboa.pt

1. Introduction

Combination of a Wave Energy Converter (WEC) with a Floating Offshore Wind Turbine (FOWT) are increasingly proposed as a route to reduce the Levelised Cost of Energy (LCoE) of deep-water renewable arrays, through shared mooring, shared seabed foundations and a common grid connection. This work considers a hybrid configuration formed by the UGen, a floater incorporating an internal U-shaped Oscillating Water Column (OWC) [1,2,3], installed upwave of the OC4-DeepCwind semi-submersible platform, referred here as DeepC [4]. Both devices have been extensively characterised in isolation: the UGen through 1:24-scale wave-tank testing [1] and frequency-domain modelling [2] and the DeepC through previous studies and tests [4]. Nevertheless, their combined behaviour when co-located has not previously been assessed.

Extending a validated single-body potential-flow model to two bodies is not routine: the scattered and radiated wave fields of each floater act as an incident disturbance on the other therefore the classical single-body added-mass, damping and excitation quantities must be re-analised with fully coupled 12×12 matrices. The objective is a systematic comparison between single-body and multi-body solutions at several separations in order to establish when the interaction is significant and when the single-body approximation remains adequate.

2. Numerical methodology

The analysis is carried out in the frequency domain with the three-dimensional panel method implemented in WaMIT [5]. Both hulls (Fig. 1-3) are generated by dedicated analytic Fortran subroutines rather than external meshes, and are discretised with a high-order panel representation within a single multi-body run, so that waves scattered or radiated by one floater are correctly re-diffracted by the other. The flow is assumed inviscid, incompressible and irrotational, and the free-surface and body boundary conditions are linearised.

Consider a floating body with six rigid-body Degrees of Freedom (DoF), $j = 1, 2 \ldots, 6$, plus the internal U-tank motion represented by generalized mode, $j = 7$. Fig. 2 shows a schematic of the UGen device described in [1,2,3], which will be used as a test case. The linear, potential flow, frequency-domain response, $x_j(t) = Re\{X_j(\omega)\, e^{i\omega t}\}$, to a time-harmomic incident wave at frequency ω is given by the solution to the equations of motion:

$$\sum_{k=1}^{7} Z_{jk} \cdot X_j = F_j^{wave} \qquad j = 1, 2 \ldots, 7 \tag{1}$$

$$Z_{jk} = R_{jk} + i\, I_{jk} \tag{1.a}$$

$$R_{jk} = -\omega^2 \boldsymbol{\mathcal{M}}_{jk} + \boldsymbol{C}_{jk} \tag{1.b}$$

$$I_{jk} = \omega \boldsymbol{B}_{jk} \tag{1.c}$$

where F_j^{wave} is the wave exciting force term, $\boldsymbol{\mathcal{M}}_{jk} = M_{jk} + A_{jk} + M_{jk}^0$, with M_{jk}, A_{jk} and M_{jk}^0 the inertia, added mass and possible external inertia matrices, $\boldsymbol{B}_{jk} = B_{jk} + B_{jk}^0$ the wave plus external damping matrices, and $\boldsymbol{C}_{jk} = C_{jk} + C_{jk}^0$ the hydrostatic plus possible external restoring matrices. Invoking both the *internal tanks* and the em *generalized modes* features of WaMIT, all of the frequency-dependent added-mass and damping hydrodynamic coefficients can be computed. The excitation force is obtained both by direct integration of the diffraction potential and from the Haskind relation, the two being compared as a consistency check.

In the two-body simulations the indices will be spanning from 1 to 12 DoF of the pair and Response Amplitude Operator (*RAO*) can be determined using the complex response amplitude X_j and A_w the incident wave amplitude as shown in Eqn. (2).

$$RAO_j = Re(X_j)/A_w \tag{2}$$

The global DoF indices, mapping each body's local 1 - 6 numbering onto the system's 1 - 12 range, are a recurring practical difficulty in multi-body runs.

Both floaters contain internal water with its own free-surface namely the UGen's U-tank and the ballast tanks in each of the DeepC's three columns. Before C_{jk} can be assembled, this Free-Surface Effect (FSE) must be separated from the solid mass and added as a correction to the vertical centre of gravity, given by Eqn (3).

$$FSE = (\rho_{\text{fluid}} / \rho_{\text{sw}}) \cdot i_{xx} / \nabla \tag{3}$$

where i_{xx} is the second moment of inertia of the internal free-surface area and ∇ is the displaced volume. The correction is substantial for both bodies (see Tables 1-2). The UGen's *KG* raises from 0.066 to 2.085 [m] and reduces the DeepC's transverse metacentric height, *GMt*, from 7.027 to 3.479 [m], lengthening its roll (traditionally designated pitch) natural period from 25.35 to 36.02 [s]. Since C_{ij} sets the position of every rigid-body resonance, this is a necessary and easily underestimated input upstream of the BEM analysis. The centres of gravity, inertias and mooring stiffness supplied to WaMIT reproduce the published OC4 data [4] exactly, and the hydrostatic values match an independent hand calculation.

The analysis is restricted to first-order potential flow. Mean drift loads are computed by both pressure integration and control-surface methods, but the full second-order problem including the quadratic transfer functions is not solved, and viscous effects such as flow separation at the U-tank duct or drag on the DeepC's bracing are outside the scope of the model.

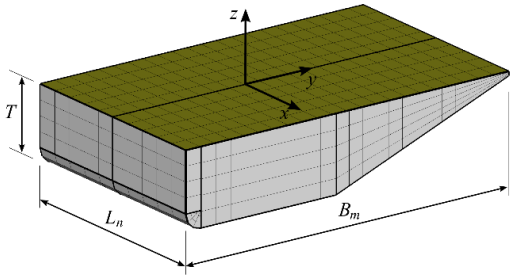
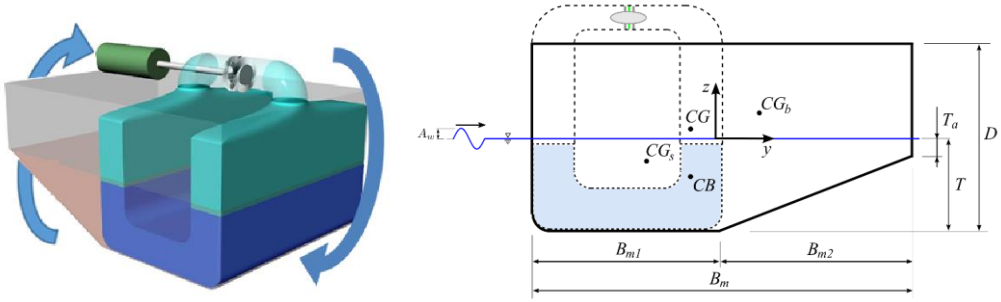


Fig. 1 — UGen's floater (WECV6), overall view with reference frame.



(a) UGen's 3D View (b) UGen's device dimensions

Fig. 2 — (a) WEC UGen's 3D view and (b) WEC UGen's cross-section, showing main dimensions, U-tank (OWC) with internal free-surface, solid CoG (CG), ballast CoG (CGb) and centre of buoyancy (CB) from [1].



Fig. 3 — FOWT DeepCwind semi-submersible (DeepC), three-column ballasted schematic.

Tab. 1 — Main particulars and free-surface correction, WEC UGen.

Parameter	Symbol	Value	Unit
Floater length	L_n	29.411	[m]
Floater beam	B_m	24.287	[m]
Draught	T	5.0	[m]
Displaced volume	∇	2540.62	[m³]
U-tank width (duct+lateral reservoirs)	w	7.8	[m]
Free-surface 2nd moment of inertia about x-axis	i_{xx}	5255.7	[m⁴]
FSE correction	FSE	2.018	[m]
KG, water as solid / free-surface	KG_s / KG_f	0.066 / 2.085	[m]

Tab. 2 — Main particulars and free-surface correction, FOWT DeepC platform.

Parameter	Symbol	Value	Unit
Equivalent length (column triangle)	L_n	43.301	[m]
Beam	B_m	50.0	[m]
Draught (mean)	T	20.0	[m]
Displaced volume	∇	13795.8	[m³]
Ballast tank radius per column	$R1$	6.0	[m]
Pitch/roll mass moment of inertia	I_{44}	$1.269 \cdot 10^{10}$	[kg·m²]
GM, water as solid / free-surface	GM_{ts} / GM_{tf}	7.027 / 3.479	[m]
Pitch period, solid / fluid	T_{44s} / T_{44f}	25.35 / 36.02	[s]

3. Results and discussion

Four relative arrangements were analysed in this study, varying only the transverse separation d between the two centres of gravity with no relative rotation: d = 50 [m] (identified as the safe minimum before the hulls would reciprocally encounter) 70, 90 and 110 [m] (Fig. 4). A single beam-sea heading $\beta = 90°$ is considered. Wave periods are sampled at 0.01 s between 2 and 15 [s] and coarsened to 0.1 [s] up to 40 [s], resolving both the short-period diffraction range and the longer-period rigid-body and internal-tank resonances. A prior convergence study showed the solution to be invariant when the panel size was refined to one half or one quarter of the characteristic length. WaMIT output is parsed by a dedicated Python routine and visualised in MatLab, a workflow designed to be reproducible and extensible. Only sway, heave and roll are reported here; at this heading the remaining modes are negligible in both the single-body and the multi-body runs.

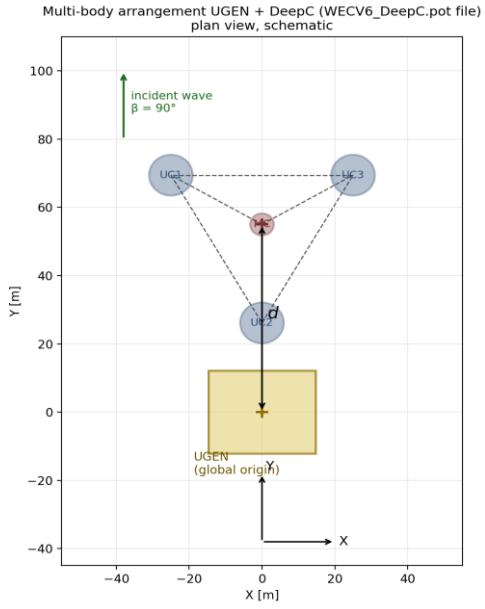


Fig. 4 — Array arrangement: DeepC offset a distance d from the UGEN, single heading β=90°.

The free-surface correction is first verified against runs in which the tank water is treated as a rigid mass (Fig. 5-6). For the DeepC the effect is clear: the sway and roll resonance moves from $T_{44s} \approx 25$ [s] in the solid-water case — matching the predicted solid roll period of 25.35 [s] to $T_{44f} \approx 34$ [s] once corrected, close to the predicted fluid period of 36.02 [s], while the peak sway RAO grows by a factor of about 2.5. The correction therefore shifts the platform's dominant resonance well clear of the energetic band; treating the ballast water as rigid would place it inside the range of periods actually encountered and would underestimate the response amplitude. This is a direct quantitative confirmation, independent of the cross-checks against the OC4 data, that the hydrostatic workflow propagates correctly into the coupled solution. The UGen comparison shows the same two resonant regimes, though the curves are less readily separated from the plot legend as generated; the check should be repeated with the full run metadata.

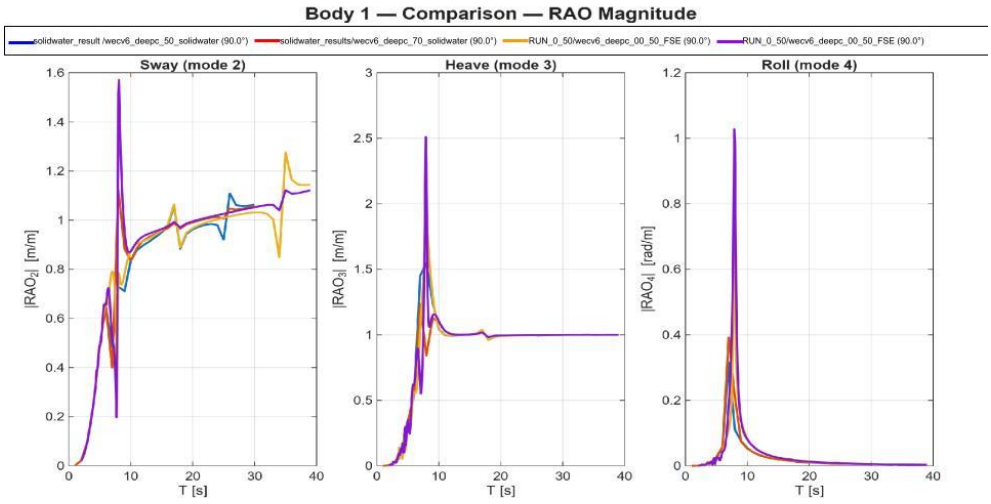


Fig. 5 — UGen's Sway, Heave and Roll RAOs: solid-water assumption vs free-surface-corrected runs.

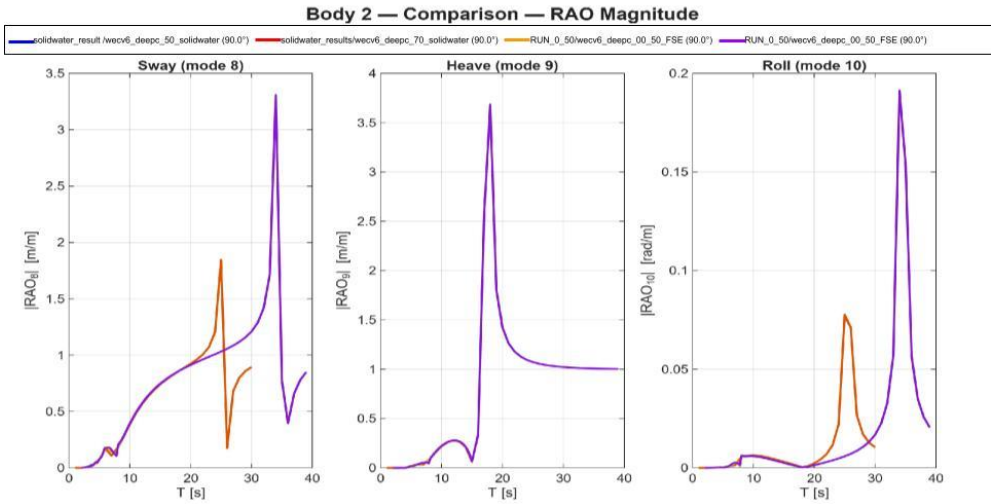


Fig. 6 — DeepC's Sway, Heave and Roll RAOs: solid-water assumption vs free-surface-corrected runs.

The coupled results reveal a pronounced asymmetry between the two floaters. The DeepC's RAOs do not show a monotonous trend with the separation, *d*. The UGen is measurably perturbed, and the perturbation depends strongly and non-monotonically on separation (see Fig. 7). At the closest spacing, d = 50 [m], two additional sharp resonances appear in heave and sway/roll near $T_{33} \approx 17.5$ [s] and $T_{44f} \approx 34$ [s], entirely absent from the single-body reference; these weaken rapidly with distance, leaving only a reduced feature at d = 70 [m] and essentially nothing at 90 and 110 [m]. Their appearance only in the coupled runs, only for the smaller body and only at close spacing is consistent with a trapped or gap-type resonance of the fluid confined between the two hulls, a phenomenon documented for closely spaced arrays. Confirming this requires relating their period to the physical gap width and running a second order simulation meshing also the tank inside UGen with its own free-surface inside.

More consequential for the device's operation is the amplitude of the primary resonance near $T \approx 8$ [s], which varies markedly with separation. In sway the ordering is clearly non-monotonic: $d = 70$ m gives the largest peak at 1.57 [m/m], followed by $d = 110$ [m] and $d = 90$ [m] at about 1.1 [m/m], with the closest spacing giving the smallest at 0.79 [m/m] — essentially the single-body value. The same ordering is reproduced in roll, the UGen's energy-capture mode, where the peak reaches 1.03 [rad/m] at $d = 70$ [m] against 0.92 [rad/m] at $d = 110$ [m]. Heave, by contrast, is almost insensitive to separation, all four cases peaking near 2.5 [m/m]. Since the interaction arises from the superposition of the incident, diffracted and radiated fields, whose relative phase at the UGen depends on the ratio of separation to wavelength, the response need not decrease monotonically with distance. At $T \approx 8$ [s] the deep-water wavelength is about 100 [m], so $d = 70$ [m] corresponds to roughly 0.7 wavelengths, at which the scattered field evidently arrives in a favourable phase relationship.

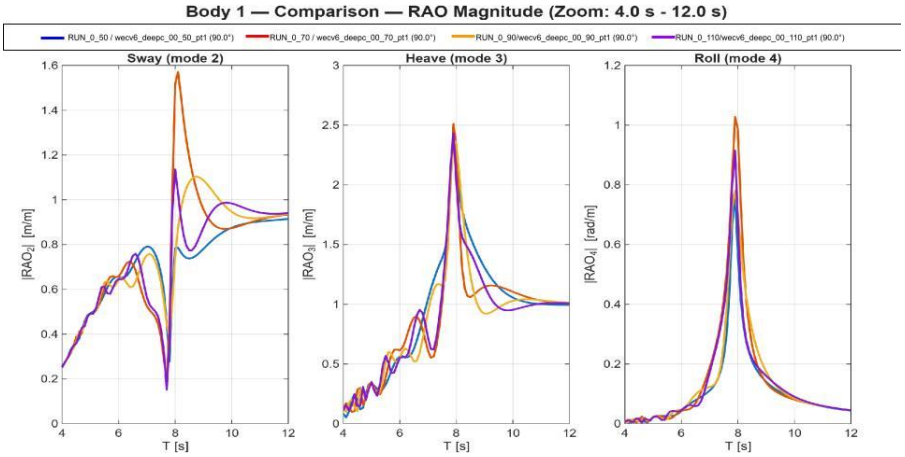


Fig. 7 — UGen multi-body RAOs for the four separations, zoom T= 4-12 [s].

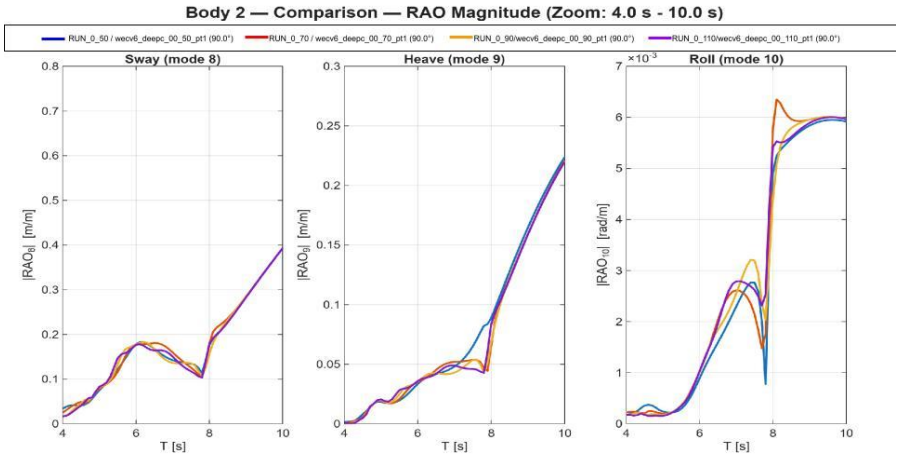


Fig. 8 — DeepC multi-body RAOs for the four separations, zoom T= 4-10 [s].

Two secondary features are worth noting. At short periods ($T < 5$ [s]) the UGen's heave RAO shows minor scatter and a small divergence between curves before they settle onto a common plateau, a plausible manifestation of the high-order panel method with irregular frequency removal applied. The DeepC's heave shows a distinct sharp resonance near $T \approx 18$ [s] with excellent single-/multi-body agreement, of the right order for an estimate based on its heave stiffness and infinite-frequency added mass; and the UGen's roll peaks near $T \approx$ 5-6 [s], comparable to the OWC/roll natural period reported for a related UGen configuration in [1].

These results have direct consequences for the envisaged wave-wind hybrid energy farm concept. For the FOWT, the relevant quantity is the platform's rotational motion in the operational wave band: the DeepC's roll RAO does not exceed about 6×10^{-3} [rad/m], roughly 0.35° per metre of wave amplitude, and is not degraded by the presence of the UGen at any separation tested. This matters because platform tilt changes the angle of attack seen by the blades over each revolution, introducing a cyclic variation in aerodynamic loading that both reduces mean

aerodynamic power and increases fatigue on blades and drivetrain. Keeping this response small and layout-independent is therefore a precondition for the hybrid concept to be viable at all, and the present results indicate that it is satisfied. A further benefit, not quantified here, is that the WEC UGen placed upwave absorbs part of the incident energy and therefore acts to some degree as a wave shield for the platform; verifying whether this produces a measurable load reduction requires the drift-force results rather than the RAOs alone.

For the wave energy converter the picture is the reverse, since roll is the motion the UGen converts into pneumatic power through the relative displacement of its internal OWC [1,2] and larger roll amplitudes in the energetic band are desirable. At $d = 70$ [m] the roll peak near $T \approx 8$ [s] is amplified by about 12% relative to the $d = 110$ [m] case and significantly above the single-body value, with the accompanying sway amplification close to a factor of two. As absorbed pneumatic power scales approximately with the square of the driving amplitude, this translates into an energy gain of the order of 25% at that period, before any weighting by the site's wave scatter diagram or account of the PTO damping. Notably, the separation that maximises capture is not the smallest one: the closest spacing, which one might expect to maximise interaction, in fact returns the UGen almost to its isolated behaviour in this band.

4. Conclusions

A multi-body WaMIT workflow for the envisaged WEC UGen - FOWT DeepC hybrid energy farm array concept has been developed and validated at several levels: the free-surface-corrected hydrostatic properties match both an independent hand calculation and, for the DeepC, the mooring stiffness and geometry published in the OC4 report; and the shift in the platform's dominant resonant period between a solid-water and a corrected representation of its ballast tanks, observed directly in the RAOs, matches the analytically predicted solid and fluid pitch periods.

The results point to three related conclusions. First, the interaction between the two floaters is markedly asymmetric: the DeepC is almost insensitive to the UGen's presence and to the separation distance, while the UGen is measurably perturbed, a consequence of the ratio in displaced volume. Second, that perturbation is not monotonic in distance — the closest spacing introduces resonances that no single-body model can reproduce, yet returns the response near $T \approx 8$ [s] almost to its isolated value, the largest amplification occurring instead at $d = 70$ [m]. Third, and consequently, the array separation is a design variable rather than a constraint: within the range examined, $d \approx 70$ [m] simultaneously amplifies the UGen's energy-capture mode and leaves the DeepC's roll unchanged at about 0.35 [°/m], the condition required for the turbine's aerodynamic performance and fatigue loading not to be degraded by co-location.

The last of these is the most relevant to the hybrid concept: a spacing can be chosen at which the hydrodynamic interaction is exploited to increase the WEC's capture at no cost to the platform's motions, a benefit that compounds with the shared mooring, foundation and grid infrastructure already motivating hybrid arrays and that would therefore act on both the energy yield and the shared capital cost in an LCoE assessment. Such an optimum is invisible to a single-body analysis, which contains no dependence on separation by construction. Quantifying the benefit requires the mean drift and mooring loads, a PTO model for the OWC and an annual energy assessment against a representative scatter diagram; extending the comparison to all 12 DoF, further headings, a generalised-mode treatment of the U-tank and a second-order analysis remains future work.

References

[1] S. Ribeiro e Silva, R.P.F. Gomes, B.S. Lopes, A.A.D. Carrelhas, L.M.C. Gato, J.C.C. Henriques, J.M. Gordo, A.F.O. Falcão (2021): "Model testing of a floating wave energy converter with an internal U-shaped oscillating water column", Energy Conversion and Management, Vol. 240, 114211.

[2] S. Ribeiro e Silva, R.P.F. Gomes, A.F.O. Falcão (2016): "Hydrodynamic optimization of the UGen: Wave energy converter with U-shaped interior oscillating water column," International Journal of Marine Energy, Vol. 15, pp. 112–126.

[3] S. Ribeiro e Silva, C. Guedes Soares, G. Vásquez Chillcce, and A. Marón (2012): "The stabilizing effects of U-tanks as passive and controlled anti-rolling devices", Proceedings of the ASME2012 31st International Conference on Ocean, Offshore & Arctic Engineering, OMAE2012-83501.

[4] A. Robertson, J. Jonkman, M. Masciola, H. Song, A. Goupee, A. Coulling, C. Luan (2014): "Definition of the Semisubmersible Floating System for Phase II of OC4," NREL/TP-5000-60601, National Renewable Energy Laboratory.

[5] C.H. Lee, J.N. Newman, (2006): "WaMIT® User Manual", WaMIT, Inc., Chestnut Hill, MA.

Partly implicit coupling of sub grids and across interfaces

Auke van der Ploeg
MARIN, Wageningen/Netherlands
a.v.d.ploeg@marin.nl

1 Introduction

Overset grids allow strong flexibility when computing flows around maritime constructions. Examples are a horn rudder in which the rudder flap oscillates, or ships passing each other in confined waters. If the motions between the bodies become too large, grid deformations may compromise the grid quality and therefore overset grids are the more reliable alternative.

Simulations for maritime applications frequently use interfaces. RANS-RANS simulations, for example, use sliding interfaces to compute the flow around a rotating propeller aft of a ship, and single propeller-blade computations use periodic boundaries, which are a special kind of interface, to include the effect of the full propeller in open water.

Previous studies, van der Ploeg (2025) showed that an implicit coupling approach can significantly speed-up the convergence of the non-linear loop or can even prevent stagnation or divergence. Especially in time-dependent applications, with a fixed maximum number of non-linear iterations per time step, an implicit coupling reduces the risk of spoiling the simulation with iterative errors.

Van der Ploeg (2025) focussed on verification cases with easy, regular meshes. Automated generated unstructured meshes around complicated geometries often contain cells with large eccentricity and deviations from orthogonality, especially near buffer layers between fine near-wall cells and the much coarser cells in the outer flow. To keep the discretization second-order accurate in space, cell-to-face interpolations in solvers that use a collocated, cell-centred variable arrangement and a face-based approach, require corrections. These corrections require gradients that can only be evaluated from previous non-linear iterations, making it more challenging to obtain fully converged solutions of the non-linear loop. In this paper, we show that in such cases a partly implicit coupling can improve the convergence.

2 Implementation

We use the CFD package ReFRESCO, *https://www.marin.nl/en/facilities-and-tools/software/refresco*, which is developed at the Maritime Research Institute Netherlands (MARIN) in collaboration with several universities and partners. It solves unsteady incompressible or compressible viscous flows based on the Navier-Stokes equations, complemented with turbulence models and volume-fraction transport equations for separate phases. ReFRESCO discretizes the equations using a finite-volume approach of the continuity and momentum equations written in conservative integral form, Ferziger et al. (2002), Moukalled et al. (2016) and Wesseling (2001). The discretization uses a collocated, cell-centred variable arrangement and a face-based approach that enables to use unstructured, body-fitted computational meshes with arbitrary polyhedral cells.

ReFRESCO solves the non-linear equations using Picard linearization. Both segregated and coupled approaches are available with mass conservation ensured using a SIMPLE-like algorithm, Patankar (1980), and a pressure-weighted interpolation technique to avoid spurious oscillations, Miller et al. (1988). For turbulence modelling different models are available depending on the application at hand. Mesh handling techniques such as moving, sliding, deforming and overset grids are available, as well

as adaptive grid refinement and coarsening. ReFRESCO uses Domain decomposition and MPI for parallelization.

At each time step it solves a system of non-linear equations with an iterative method called the outer loop. Each instance of this loop requires an inner loop to compute corrections for the velocity components, the pressure and other field quantities. The inner loop solves the discretized and linearized equations, by applying a conjugate-gradient like method to solve the system of linear equations denoted by $A(x^k-x^{k-1})=b(x^{k-1})-A(x^{k-1})$, in which k indicates the counter of the outer loop, A is a sparse square matrix with size equal to the number of cells and the vectors x and b denote, respectively, the field vector and the right-hand side vector.

An explicit coupling technique interpolates values from the previous outer loop, from x^{k-1}. Therefore, the interpolation between the sub grids and across interfaces does not affect the matrix, but only the right-hand side vector b. The corresponding rows in the matrix A contain 1 on the main diagonal and all off-diagonal entries are zero. An implicit coupling procedure, however, includes the interpolation coefficients as non-zero entries in the matrix A. As explained in Völkner et al, (2017), the entries in A that multiply field variables used in the interpolation scheme, contain minus the corresponding interpolation coefficient. As a result, the row sums become zero and the corresponding row is no longer strictly diagonally dominant.

A completely implicit coupling makes it more difficult to obtain a correction of the field variables at each non-linear iteration. Especially in combination with irregular meshes this can lead to insufficient convergence of the inner loop, which can, in its turn, spoil the convergence of the outer loop. Therefore, in this paper we assess a partly implicit coupling, which includes the interpolation coefficients multiplied by a fraction '*impFrac*,' between 0 and 1, in the matrix A as described above. Values of 0 and 1 indicate, respectively, a completely explicit and completely implicit coupling.

3 Results

3.1 Two inclined spheres

A partly implicit coupling procedure aims to speed up the outer loop, but because the inner loop deals with the linear part of the coupling, it is likely that it requires more iterations. In the first test case we study whether the overhead pays off. The motivation of this his test case comes from simulations of the flow around a ship with a horn rudder, in which a rudder flap can move independently from the rest of the rudder. The relative motions of the flap can become so large that deforming meshes would lead to highly distorted cells and the overset grid method is the more reliable alternative.

The test case concerns a 3D, time-dependent simulation of two spheres, in which one sphere is rotating and inclined in the other. The Reynolds number is five thousand. The left picture in Figure 1 shows a slice of the Hexpress-generated mesh. Each sub grid used in the overset grid methodology contains one of the spheres. The nearest-cell gradient method interpolates field values from one sub grid to the other. Adaptive grid refinement guarantees sufficient resolution in the gap between both spheres.

For this test case, overset grids are not strictly necessary. This enables us to study the effect of using overset grids, by comparing the computed forces and the computational effort with those obtained using only one mesh. Since the mesh between both spheres is extremely fine, the interpolation error is quite small, and therefore the force obtained with overset should be close to the force obtained without overset.

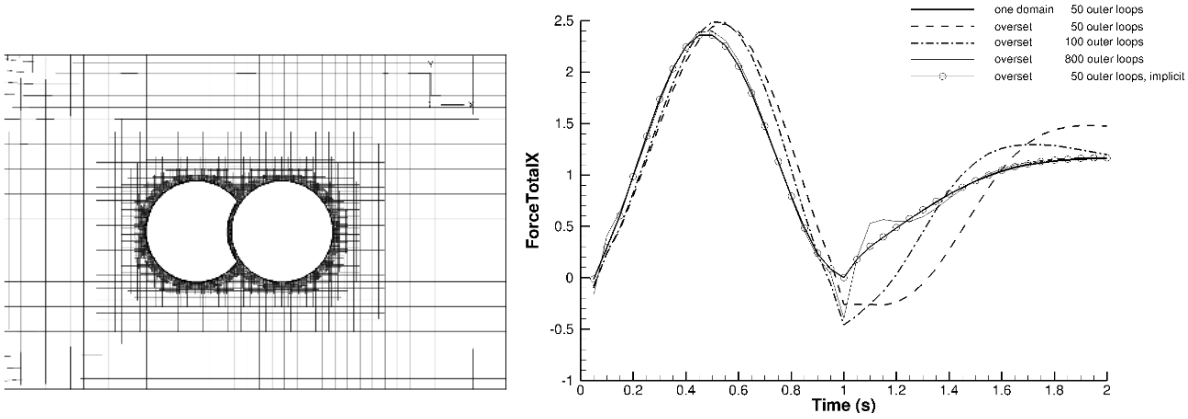


Figure 1 Left: slice of the geometry used for the two inclined spheres. Right: *x*-force obtained with varying number of outer loops per time step. Unless mentioned otherwise, overset uses completely explicit coupling between sub grids.

The right picture in Figure 1 compares the force in *x*-direction computed with and without overset, and for varying number of outer loops per time step. It shows that with the explicit coupling between sub grids; the force strongly depends on the number of outer loop iterations per time step. The outer loop requires more than eight hundred iterations to compute a force that is near the force obtained on one domain. However, with an implicit coupling, only fifty outer-loop iterations per time step are sufficient.

For this example, the implicit coupling increases the required computational effort per outer loop iteration with approximately 25%. Therefore, fifty outer-loop iterations with an implicit coupling cost approximately ten times less wall clock time that eight hundred iterations with an explicit coupling.

For this case, the time discretization helps to increase the diagonal dominance of the matrices in the correction equations. For this reason, the coupling between the sub grids can be completely implicit.

3.2 Propeller, all blades

In simulations with a rotating propeller aft of a ship, the propeller rotation is modelled by dividing the computational domain into two subdomains, one around the ship and one around the propeller, where the latter domain rotates, and the flow data is exchanged between the sub domains along sliding interfaces.

In recent practical design studies with automatically generated Fidelity meshes around the ship and propeller, it was difficult to obtain converged solutions. To focus on this problem, we compute the flow around the propeller in open water using a Fidelity mesh generated using the same settings as for the mesh around the ship-propeller combination. Of course, the resulting mesh is not an optimal mesh for a propeller in open water. The left picture of Figure 2 shows that the interfaces in front and aft of the propeller are not perpendicular to the mainstream direction, and the right picture shows that the mesh contains buffer layers near the cylindrical-shaped interface around the subdomain with the propeller.

The left picture in Figure 3 shows that for this test case it helps to treat the coupling across the interfaces not completely implicit. With *impfrac=1.0* the residuals stagnate, with 0.0 the computation converges slowly, and with 0.5 the convergence improves considerably. The right picture illustrates that the stagnation of convergence for *impfrac=1.0* is due to a region near the cylindrical-shaped interface. Figure 4 shows that the pressure computed with *impfrac=1.0* is completely wrong, whereas with *impfrac=0.5* it looks much better.

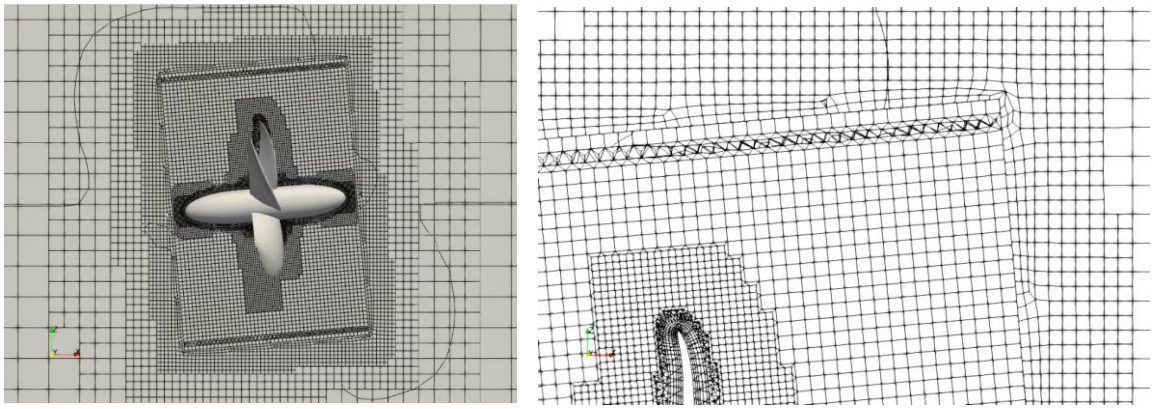


Figure 2 Left: slice of the mesh around the propeller. Right: zoom-in near the corner of the cylindrical-shaped interface around the propeller and the interface in front of the propeller.

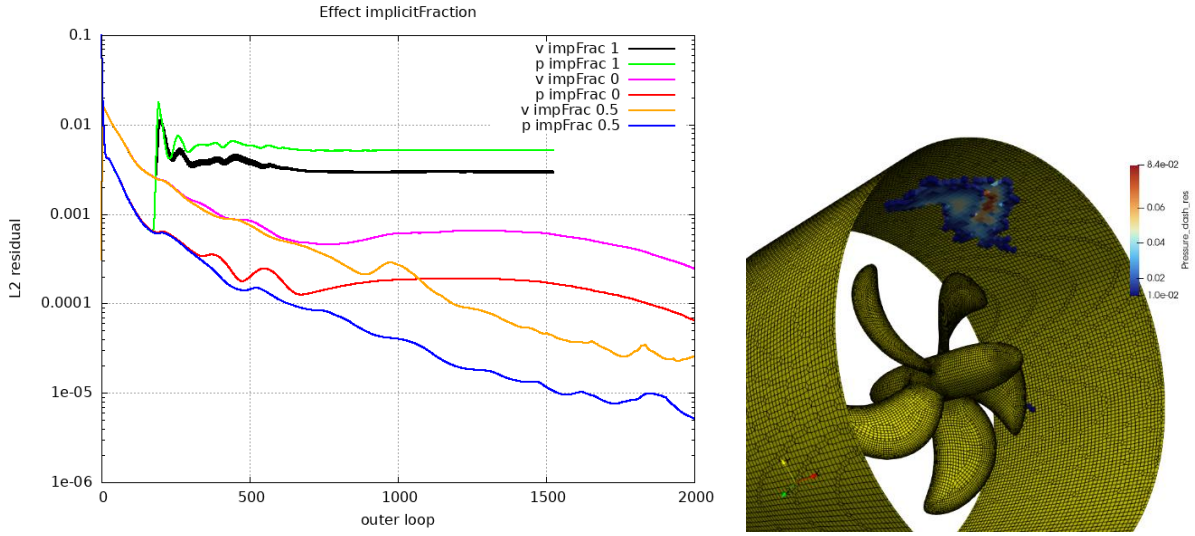


Figure 3 Left: convergence behaviour of the y-velocity and the pressure, for different values of *impFrac*. Right: Location of largest pressure residuals obtained for *impFrac*=1.

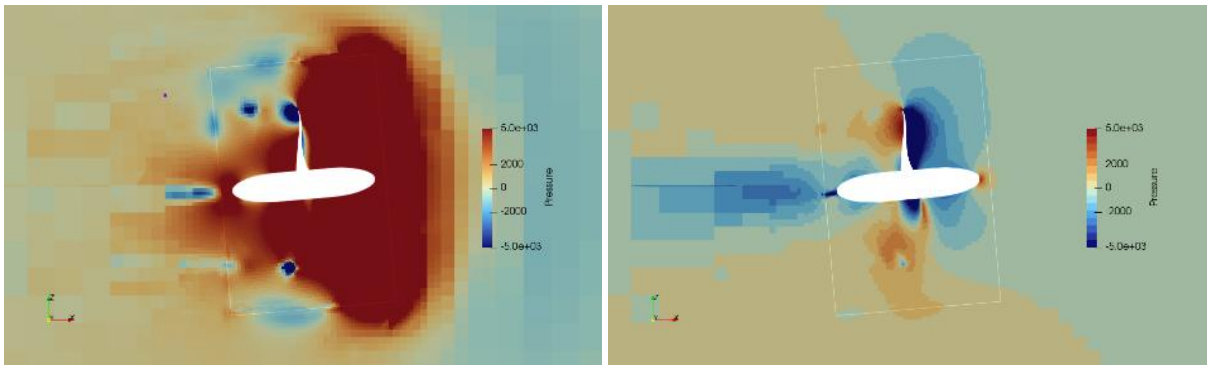


Figure 4 Computed pressure with *impFrac*=1 (left) and 0.5 (right) in the same slice as shown in Figure 2.

Each interface uses its own prescribed value for the parameter *impfrac*. For this case, especially the value corresponding to the cylindrical-shaped interface around the propeller appears to be critical. In order not to spoil the convergence, this interface requires a value of *impfrac* lower than 0.7, where the other interfaces can use a larger value of 0.9. However, after revising the mesh by increasing the number of layers between the buffer layer and the interface from 1 to 3, as shown in Figure 5, the cylindrical-shaped interface can use a value of 0.9 as well.

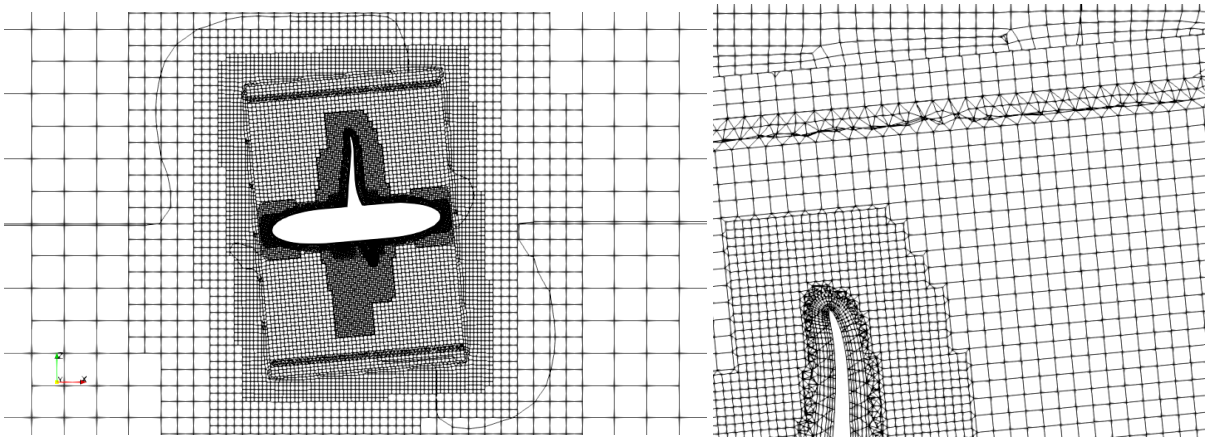


Figure 5 Left: slice of the revised mesh around the propeller with an increased number of layers between the buffer layer and the interface. Right: zoom-in near the corner of the cylindrical-shaped interface around the propeller and the interface in front of the propeller.

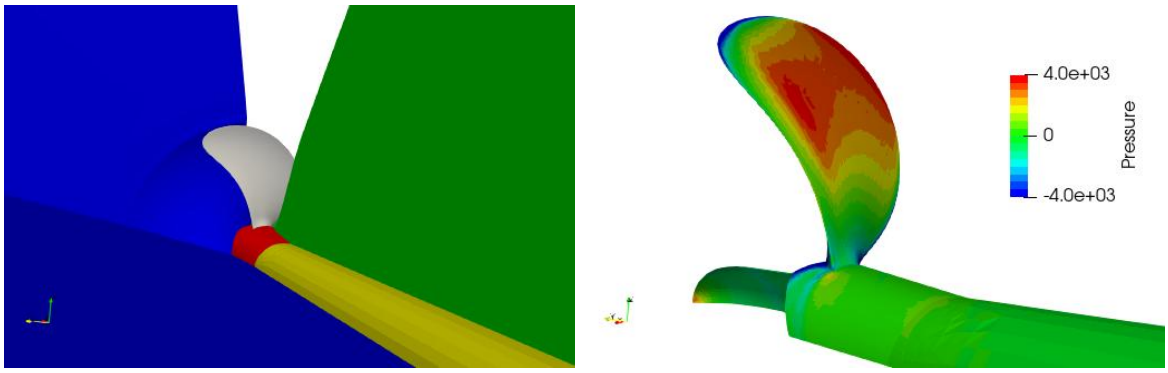


Figure 6 Left: periodic boundaries of the computational domain around one blade of a propeller. Right: computed pressure on the blade computed with *impFrac=0.5*.

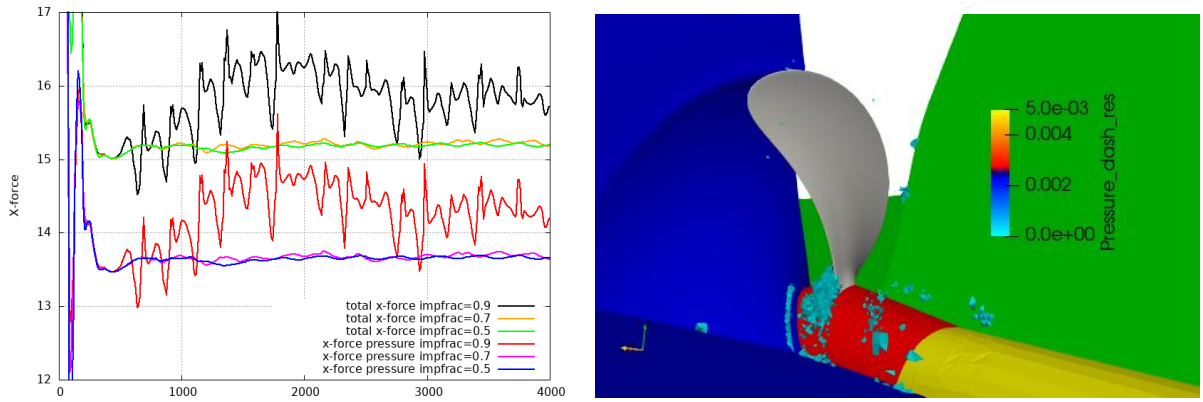


Figure 7 Propeller in open water using periodic boundary conditions. Left: variation in total and pressure forces in *x*-direction. Right: location of largest pressure residuals, which are away from the periodic interfaces.

3.3 Propeller, only one blade

The next test case concerns the computation of a model-scale propeller in open water, for advance coefficient *J=0.65*. This propeller is one in a series of propellers for a range of conditions. To reduce computational effort, the computational domains contained only single blades instead of full propellers. The simulations used Fidelity-generated meshes and periodic boundaries to simulate the presence of all

blades, as described in van der Ploeg (2025). With a completely explicit or completely implicit coupling of the flow across the periodic boundaries, not all computations converged. Figure 6 shows an example of such a propeller. The right picture shows the periodic boundaries of the computational domain around only one blade, and the right picture shows the computed pressure on this blade.

Making the coupling only partly implicit helps to prevent divergence of the simulation. The left picture in Figure 7 shows the effect of the parameter *impFrac*. This figure shows the convergence of the *x*-components of the total and pressure force. With *impFrac=0.9* the computation no longer diverges, although the forces do not converge. With values 0.5 and 0.7, the forces get more stable. The right picture in Figure 7 shows only the largest values of the residuals in the pressure equation. The corresponding residuals are not located near any of the periodic boundaries, which indicates that these boundaries are no longer the limiting factor that prevents convergence.

4. Conclusions

Simulation of flows around maritime constructions can use explicit, implicit, or partly implicit couplings across interfaces and between sub grids. Although an explicit coupling approach requires less computational effort per non-linear iteration, insufficient convergence of the non-linear loop can spoil the simulation with iterative errors, especially with a fixed maximum number of iterations.
If maritime applications of CFD contain complicated geometries, automated generated unstructured meshes can contain cells with large eccentricity and deviations from orthogonality, especially near buffer layers. This paper shows examples of such meshes in which both a completely explicit and completely implicit coupling fail, but a partly implicit coupling improves the convergence of the non-linear loop.

References

Van der Ploeg, A., “Coupling techniques between sub grids and across interfaces,” 27th Numerical Towing Tank Symposium (NuTTS'2025), Tomislavov Dom, Medvednica mountain (near Zagreb), Croatia, 14 – 16 September 2025.

Völkner, S., Brunswig, J., Rung, T., “Analysis of non-conservative interpolation techniques in overset grid finite-volume methods,” Computers and Fluids, 148, 39-55, 2017.

Ferziger, J.H., and Peric, M., "Computational Methods for Fluid Dynamics", 3rd Edition, Springer, ISBN: 978-3-540-42074-3, 2002.

Moukalled, F., Mangani, L., Darwish, M., "The Finite Volume Method in Computational Fluid Dynamics", Springer, ISBN: 978-3-319-16874-6, 2016.

Wesseling, P., "Principles of Computational Fluid Dynamics", Springer Series in Computational Mathematics, Springer, 2001.

Patankar, S., "Numerical Heat Transfer and Fluid Flow", https://doi.org/10.1201/9781482234213, Taylor & Francis Group, 1980.

Miller, T.F., Schmidt, F.W., "Use of a pressure-weighted interpolation method for the solution of the incompressible Navier-Stokes equations on a non-staggered grid system", Numerical Heat Transfer 14 (2), pp. 213-233, 1988.

Rapid Prediction of Marine Propeller Performance Using Artificial Neural Networks

Alper Yildirim[1], Robert Mutton[2], Batuhan Aktas[1], Mehmet Atlar[1]

[1] Department of Naval Architecture, Ocean and Marine Engineering, University of Strathclyde, Glasgow, UK

[2] Stone Marine Propulsion, Birkenhead, UK

alper.yildirim@strath.ac.uk

1. Introduction

Regulatory pressure on the efficiency of the existing fleet, expressed through the Energy Efficiency Existing Ship Index (EEXI) and the Carbon Intensity Indicator (CII), has renewed interest in propeller retrofits and in designs matched to the operating profile a vessel actually experiences rather than to a single contractual condition. Designing against a profile requires characterising every candidate geometry across a range of advance coefficients, and in a formal optimisation that characterisation is repeated for hundreds or thousands of candidates. Steady RANS is accurate enough for this but far too slow to sit inside the loop: a single open-water curve takes hours of computation, so evaluating even a few hundred candidates directly is not affordable within an industrial design cycle.

In recent years, machine learning has been applied to related problems in propeller performance prediction and design. Bakhtiari and Ghassemi (2020) trained a neural network on CFD data for a low-pitch cycloidal propeller; Doijode et al. (2022) coupled learning methods to a boundary-element solver inside a propeller design and optimisation loop; and Li et al. (2025) used a multitask network to predict the coefficients of polynomials fitted to the K_T and K_Q curves of 4-, 5- and 6-bladed propellers, which is the study closest in aim to the present one. The aim of this paper is to take the time-consuming CFD evaluation of candidate designs out of the propeller design process. A database for a specific propeller family is built once with full-scale steady RANS, and a neural network trained on that database then acts as a surrogate for the CFD calculation whenever a new propeller enquiry is received, becoming part of the design process itself. Because each candidate is evaluated almost instantly, the design cycle is shortened substantially, and far more alternatives can be examined before one is chosen, which brings the final design closer to the right propeller for the vessel.

The work reported here forms part of a Knowledge Transfer Partnership between the University of Strathclyde and Stone Marine Propulsion. The surrogate is intended for the partner's design office rather than as a general-purpose model. The training database is generated from a fully parametric propeller model built in CAESES and derived from the partner's design history. The model is sampled with a Sobol sequence within the bounds of current commercial practice, and the RANS setup was compared against in-house open-water measurements. Two aspects distinguish the surrogate: it returns the complete K_T and K_Q curves rather than performance at a single advance coefficient, together with the zero-thrust advance coefficient that indicates where each curve ends; and its accuracy is reported as absolute errors in the coefficients themselves, and against a polynomial regression fitted to the same data, rather than as a correlation coefficient. No systematic search over regression methods preceded the choice of a neural network; it was adopted because of the expected workflow direction, rather than for any measured advantage.

2. Database generation

2.1 Parametric model, design space and database generation

The parametric model is defined by a set of design variables standard in propeller design practice — radial distributions of pitch, chord, thickness, camber and skew, together with global quantities such as blade number, expanded area ratio and hub ratio. The functions mapping these variables onto the blade surface and the underlying section geometry were regressed from the industrial partner's historical design database and are proprietary; they are therefore not reproduced here. This paper characterises the model by the design variables and their sampling ranges given in Table 1a. The family is one the partner develops for container ships, which constrains several of those ranges.

The design of experiments does not sample the radial distributions directly. The quantities in Table 1a are sampled using a Sobol sequence in CAESES, a design environment that integrates parametric geometry, the design of experiments, and the optimisation driver, and that produces the corresponding blade. The pitch ratio is therefore derived rather than sampled, as are the other quantities that describe the blade. The dimensional inputs themselves do not appear among the network inputs. Two feasibility constraints are then applied, both taken from the partner's design practice: the pitch ratio at r/R = 0.7 must lie between 0.6 and 1.4, and the maximum skew angle must not exceed 35°. The sampled quantities are drawn independently, with no relation imposed at the sampling stage, so a substantial proportion of combinations falls outside these limits. Of 1200 samples, 199 satisfied both constraints

and were carried forward to CFD, in nearly equal proportions for the three blade numbers, so the sub-databases are comparable in sampling density. Two were later discarded as unusable, leaving 197 designs.

Sobol sampling Sobol, (1967) followed by rejection no longer yields a Sobol sequence, so the uniformity of the retained set was checked directly. Dividing each variable into ten equal intervals, no interval is empty, and fewer than one design in six would have to move to another interval to make the coverage exactly uniform. The ranges in Table 1a therefore describe the sampling bounds rather than the domain of validity: combinations of the tabulated extremes are not necessarily realisable.

The chain from a sampled design to a set of network labels then runs without manual intervention, as summarised in Fig. 1. Surviving geometries are passed to STAR-CCM+ and scanned in steps of 0.1 in advance coefficient, from J = 0.1 until the thrust becomes negative. The number of points is set by the design itself and ranges from 8 to 16, with a median of 12.

Post-processing fits third-order polynomials to the computed K_T and K_Q values as functions of J. The zero-thrust advance coefficient is not measured directly but is obtained from the fitted K_T polynomial: among its real roots, the one above the advance coefficient of the last positive K_T sample is selected to ensure it lies within the computed range. Each curve is then resampled onto the normalised grid described in Section 3.2, and the resulting values form the network labels. For each design, the largest residual between the fitted curve and the computed points is recorded. Across the database, the median is $\Delta K_T = 0.002$ and the worst case is 0.014; for the torque coefficient, the corresponding values are 0.00002 and 0.00023. These values limit the fidelity of the training labels.

The runs are executed on a workstation with an AMD Ryzen Threadripper PRO 9995WX processor, with four simulations running concurrently, each using 22 of its 96 cores; the database as a whole required approximately 23,000 core-hours.

Table 1a. Sampled design variables.

Sampled design variable	Lower	Upper
Blade number	4	6
Diameter [mm]	6000	9600
Shaft speed [rpm]	70	120
Delivered power [kW]	10,000	65,000
Expanded area ratio	0.40	0.70
Hub ratio	0.18	0.20
Rake angle [deg]	−5	0
Pitch shape coefficient	0.60	0.90
Skew coefficient	0.10	0.20

Table 1b. Network inputs and their range in the database.

Network input	Range in database
Blade number (one-hot)	4 / 5 / 6
(P/D) at r/R = 0.5 (derived)	0.653 – 1.55
Pitch shape coefficient	0.604 – 0.899
Expanded area ratio	0.402 – 0.699
Hub ratio	0.181 – 0.200
Rake angle [deg]	−4.97 – −0.10
Skew coefficient	0.101 – 0.163

Feasibility is assessed at r/R = 0.7, where $0.6 \leq (P/D) \leq 1.4$; the network is trained on the pitch ratio at r/R = 0.5, where the radial pitch distribution reaches its maximum. The two are not numerically interchangeable. The skew coefficient is sampled up to 0.20, but in the retained set it does not exceed 0.163, with the upper part of its sampled range removed by the 35° limit.

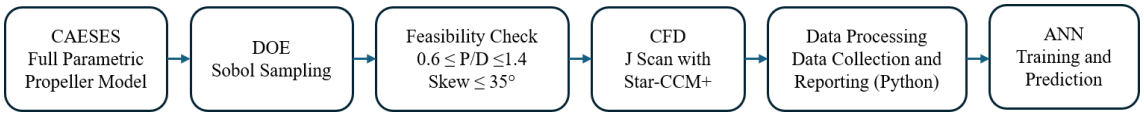


Fig. 1. Workflow from the sampled design variables to the network labels.

2.2 CFD setup, mesh independence and validation

The computations are carried out in STAR-CCM+ at full scale. The steady RANS equations are solved on a trimmed-cell mesh in a cylindrical domain with a uniform-velocity inlet, a pressure outlet and a symmetry outer boundary. Blade rotation is represented by a moving reference frame. Turbulence is closed with the k-ω SST model (Menter, 1994) and its curvature correction (Smirnov and Menter, 2009). The pressure-velocity coupling is segregated, and convection is discretised to second order for both the flow and the turbulence equations. Each design is scanned in steps of 0.1 in advance coefficient, from J = 0.1 upwards, until the thrust becomes negative.

Mesh independence was assessed on five propellers, chosen to differ from one another in both size and character rather than to repeat a single configuration, with each computed at five refinement levels. For the propeller shown in Fig. 2, these ranged from 1.0 to 33.5 million cells, and the other four cover a comparable span. The three finest levels yield results that are nearly indistinguishable, so we adopted the third for the database. In an industrial setting, time per design is a constraint, and the two finer levels cost several times as much for no change the surrogate could resolve.

The setup was then compared with experimental open-water data from the partner's earlier projects, using one of the partner's own propellers. Because the database is computed at full scale while the measurements were taken at

model scale, the computation was repeated at model scale for the comparison, as shown in Fig. 2. Over the working range of the curve, the computed thrust coefficient agrees with the measurement to within about 1% on average, the torque coefficient to about 3%, and the open-water efficiency to about 3%. The largest departures occur at the two ends of the range, where the curve is steepest.

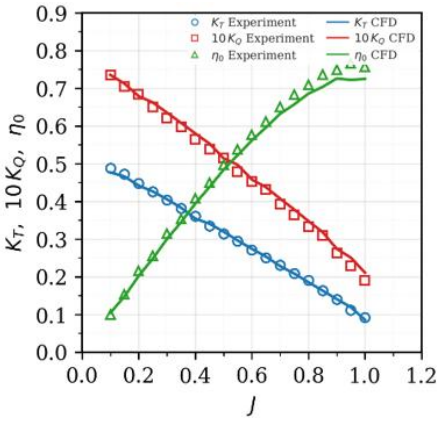


Fig. 2. Open-water validation at model scale: symbols are the measurements, lines the computation.

3. Surrogate formulation

3.1 Input reduction

The parametric model is driven by the sampled quantities listed in Table 1, but these are not the natural arguments of the open-water characteristics. Non-dimensionalising the steady open-water problem leaves the thrust and torque coefficients as functions of the advance coefficient and of the blade geometry expressed as ratios rather than absolute dimensions. Diameter, shaft speed and delivered power are dimensional quantities and do not survive that reduction. They enter only by setting the blade that the parametric model returns. Once the blade is described in ratio form, they carry no further information; therefore, they are not presented to the network.

Seven physical descriptors remain, listed in Table 1b. Blade number is categorical and represented by three one-hot encoded features, so the network receives nine numerical inputs. The pitch ratio is evaluated at r/R = 0.5, where the radial pitch distribution reaches its maximum, and encodes the pitch magnitude, while the pitch shape coefficient encodes its radial variation. Expanded area ratio, hub ratio, rake angle and skew coefficient are passed through unchanged.

A permutation test on the trained network, in which each input is shuffled in turn and the resulting increase in prediction error is recorded, ranks the pitch ratio first by a wide margin, followed by blade number and the pitch shape coefficient, then the expanded area ratio. Shuffling the hub ratio, the rake angle or the skew coefficient leaves the prediction almost unchanged. This aligns with the physics rather than contradicting it. The hub ratio spans only 0.18 to 0.20 here, too narrow for its influence to be distinguished from the rest, while rake and skew are sampled over their full ranges, yet their influence is not resolved within the present design space. In practice, they are chosen with unsteady behaviour behind a hull in mind, which an open-water model does not see, and they are retained here so that the same input set can serve when those conditions are added. All three are retained because the workflow is intended to be extended to exactly those conditions, where they become the parameters that matter.

3.2 Output representation

A surrogate that returns performance at a single advance coefficient is of limited use when the design is to be assessed over an operating profile, so the network is asked to return the whole curve. This requires a fixed-length output vector, which the computed data do not directly provide: the scans contain between 8 and 16 points and cover different ranges of J, with the zero-thrust advance coefficient varying from 0.71 to 1.56 across the database. Sampling every curve on a common physical grid would be incorrect in both directions, either falling beyond the zero-thrust point for a design with a low one or stopping short of the end of the curve for a design with a high one. In either case, the sampling points would sit at different relative positions on different curves, leaving the network to learn that displacement as well as the hydrodynamics.

The grid is therefore normalised by each propeller's zero-thrust advance coefficient. Each curve is sampled at twenty points along that normalised axis, so the points occupy the same relative positions on every curve, resolution is allocated where the curve actually lies, and no design is evaluated beyond its own zero-thrust condition. Fig. 3 illustrates the normalisation.

Normalising in this way removes the physical axis, which must be restored if the surrogate is to be used at a specified operating point. The zero-thrust advance coefficient is therefore predicted as an output in its own right,

allowing the physical axis to be reconstructed: given the predicted J_{zero}, the twenty normalised abscissae are converted back to physical advance coefficients, and the curve can then be interrogated at any J of interest. The network has forty-one outputs in total, comprising twenty values of K_T, twenty of K_Q, and J_{zero}.

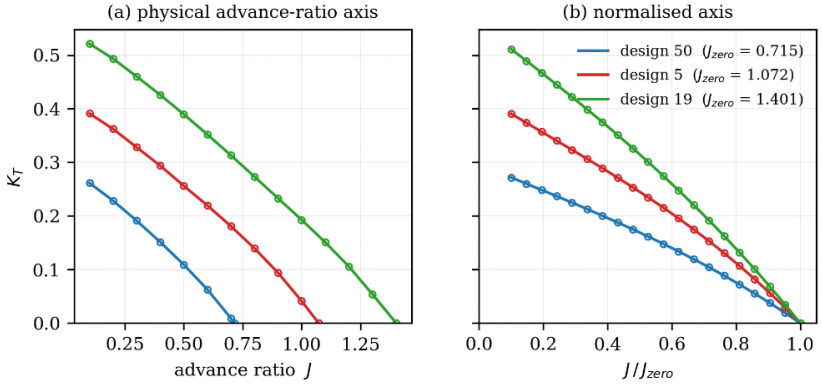


Fig. 3. Normalisation of the advance-coefficient grid.

3.3 Architecture and training

K_Q is about an order of magnitude smaller than K_T, so each output group, K_T, K_Q and Jzero, is standardised with a single mean and standard deviation, which prevents the K_T terms from dominating the loss while preserving the shape of each curve. A shared trunk feeds two linear heads, one returning the forty curve values of K_T and K_Q and the other Jzero. In the loss, the error of each group is averaged over its own outputs and carries its own weight, tuned during development.

The trunk depth and width were selected from nine candidates by five-fold cross-validation. Candidates were ranked by the mean of the three group R^2 values, with the points of each curve weighted by their spread across the database. The selected architecture, two layers of 64 SiLU neurons (about 7,500 parameters), was retrained on the development pool as a five-member ensemble differing only in initial weights, each early-stopped on the same 15% validation slice. A hold-out set stratified by blade number was set aside before the search and never used for training or model selection, and all scaling was fitted on the training designs alone.

As a reference point for the results that follow, a quadratic regression on the same nine numerical features was fitted to the same development pool and evaluated on the same locked designs using the same metrics.

4. Results

The surrogate was evaluated once on the twenty locked test designs, which did not participate in training or the architecture search. Errors are quoted per design as the mean absolute difference from the computed CFD points: the predicted twenty-point curve is placed on the physical axis using the predicted zero-thrust advance coefficient and interpolated linearly onto the advance coefficients at which the CFD was run. They therefore include both the shift introduced by that predicted coefficient and the residual of the intermediate curve fit. On that basis, the median absolute error in the thrust coefficient is 0.0020 and the worst design reaches 0.0033. For the torque coefficient, the corresponding figures are 0.00026 and 0.00045. The two contributions can be separated: measured against the fitted curves, the network's median thrust-coefficient error is 0.0017, while the fitted curves depart from the computed points by a median of 0.0011, so the intermediate fit is a real part of what the user sees. In terms of what a designer actually reads, the open-water efficiency curve is reproduced with a mean absolute error of 0.0049 in η_0 and a worst case of 0.0108, and the zero-thrust advance coefficient with a median of 0.0031. None of the twenty predicted curves is non-monotonic, although no smoothness or physics penalty appears in the loss.

Fig. 4 shows the best, median and worst of the twenty, ordered by thrust-coefficient error, with computed points plotted as symbols and predicted curves as lines. Even the worst design follows the computed points across their whole range and reaches its own zero-thrust root. The visible discrepancy is a small offset in level rather than a change of shape, which is less disruptive to a search over the curve than a change of shape would be. The efficiency curve is the more stringent of the three tests, since it combines the thrust- and torque-coefficient errors and divides by a quantity that becomes small.

Whether a network is needed at all for this database size can be checked against a simpler model. The quadratic regression defined in Section 3.3, fitted to the same nine numerical features using a full second-order basis with ridge regularisation, was scored on the same twenty locked designs in the same way. On the thrust and torque coefficients the two models are indistinguishable: the median thrust-coefficient error is 0.0020 for both, and the median torque-coefficient error is 0.00026 for the network and 0.00025 for the regression, a difference that twenty designs cannot resolve. The only clear difference is in the zero-thrust advance coefficient, where the median error is 0.0031 for the network and 0.0022 for the regression. At this database size, therefore, the capacity of the network

brings no measurable advantage, and that is itself the result. The open-water response of this low-dimensional parametric family is smooth enough for a quadratic basis to capture most of it, while the network has some seven thousand parameters to constrain from 177 designs.

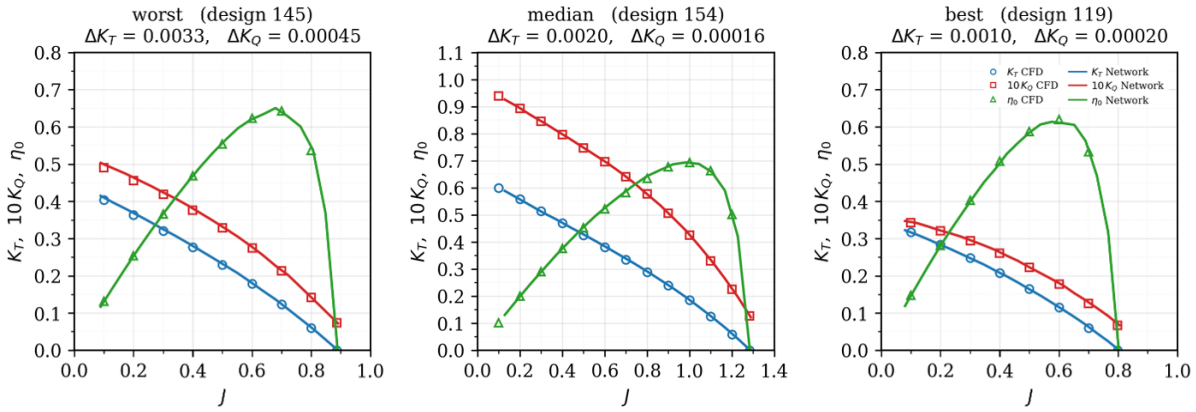


Fig. 4. Locked test designs, ordered by thrust-coefficient error. Symbols are the computed CFD points; lines are the network prediction. The torque coefficient is plotted as $10K_Q$ for legibility; the errors quoted are for K_Q itself.

Fig. 5(a) shows how the comparison between the network and the regression changes as the database grows: the network gains more from each additional design than the regression does, but neither model improves much beyond about 120 designs. Both models were retrained on nested subsets of the development pool, with ten random draws at each size, and scored each time on the same locked test set. The errors are measured against the fitted labels rather than the computed points, so that the two models are compared on a single target; their levels are therefore lower than the end-to-end errors quoted above. From sixty to a hundred and twenty designs, the thrust-coefficient error of the network falls by about forty per cent and that of the regression by about fifteen. Beyond about 120 designs both curves flatten, the network at 0.0012 and the regression at 0.0009. Within the present database, the network has not caught up with the regression, and whether it would with more designs is not settled by these data.

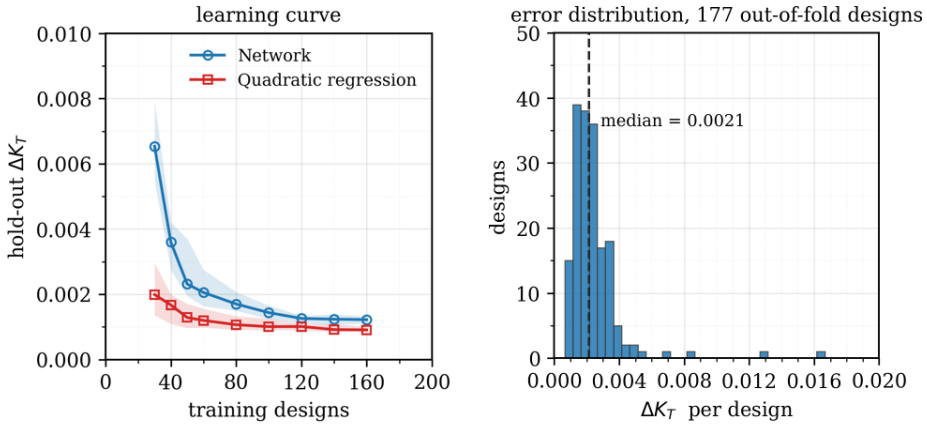


Fig. 5. (a) - (a, left) Thrust-coefficient error of both models on the locked test set as a function of database size, relative to the fitted labels. (b, right) Distribution of the end-to-end thrust-coefficient error over the 177 out-of-fold designs.

Fig. 5(b) shows the distribution of the thrust-coefficient error across the 177 out-of-fold designs. Measured on the same end-to-end basis, the distribution is single-peaked with a short tail: the median is 0.0021, three-quarters of the designs fall below 0.0027, and the largest error is 0.0167. This worst case exceeds that of the twenty locked designs, which is consistent with the larger sample and with the out-of-fold predictions coming from single-fold models rather than from the ensemble.

By comparison, the cost of the surrogate is negligible. A converged open-water curve costs of the order of 120 core-hours and five to six hours. The trained network produces the forty-one output values in well under a second, and the whole training procedure, including the architecture search over nine candidates and the final five-model ensemble, takes under two minutes on the same workstation.

These figures are lower than those reported for surrogates trained across propeller families, where relative errors of a few per cent are commonly reported. Taken as a relative measure over the part of the curve where the thrust coefficient is not close to zero, the present model reaches about 1.2%. The comparison is not like-for-like. Every design here comes from a single parametric family developed for container ships and computed using a single CFD setup, so the surrogate interpolates within that family rather than generalising across the design traditions of

different vessel types. The sampled ranges are correspondingly narrow. The hub ratio spans about a quarter, and the expanded area ratio about a third, of the ranges quoted for models trained on mixed propeller databases. The narrowness that makes the present accuracy attainable is the same narrowness noted as a limitation in Section 1.

5. Practical difficulties and further work

Several of the difficulties encountered in building the database are worth recording, together with what has been done about each.

The intermediate polynomial fit, described in Section 2.1, carries a residual of its own, which Section 4 separates from the error of the network. It is small compared with the uncertainties that dominate a full-scale powering prediction, and we do not regard it as the limiting factor for the intended use. If a later application requires more, the fit can be replaced by an interpolation passing through the computed points.

The feasibility constraints act on the pitch ratio, which the parametric model derives rather than samples, with two consequences. Most sampled combinations are rejected before any CFD is run, which is expected and inexpensive. Less obviously, a Sobol sequence uniform in the sampled variables is not uniform in the derived pitch ratio, and the upper end of its range is less densely populated. Errors are higher there, but they are also higher at the opposite, well-populated end, so most of the difference is an edge effect rather than a consequence of sparse sampling. The database is nevertheless being extended in that region. The upper end of the sampled skew range is a different matter: it is truncated by the 35° limit and will remain empty until the constraints are relaxed, which is expected as confidence in the model grows.

The most direct route to a measurable advantage for the network is more designs, although Fig. 5(a) leaves open whether it would catch up with the regression on a larger database. The gain available is, in any case, bounded by the residual of the intermediate fit, so the two are best pursued together. Beyond that, the workflow is intended to grow in the direction set out in Section 1, which may include wake-field information as further input, cavitation risk as an additional output, and further parametric families covering vessel types other than container ships.

6. Conclusions

An end-to-end ANN pipeline has been built that takes a sampled set of design variables through a parametric model, filters for feasibility and, using full-scale steady RANS, returns a complete open-water curve. Predicting the curve on a grid normalised by each propeller's zero-thrust advance coefficient, and predicting that coefficient alongside it, allows the full curve to be returned for designs with different operating ranges and restores the physical axis afterwards. Against the computed points, the surrogate reproduces the thrust coefficient with a median of 0.0020 and the open-water efficiency with 0.0049, and it does so in a fraction of a second, compared with the 120 core-hours required for a converged curve. At the current database size, the two methods are comparable, and the network is carried forward not because it is more accurate here, but because the problem it is being prepared for has more inputs and outputs than this one.

For Stone Marine Propulsion, the impact on the design process is substantial. A curve costing about 120 core-hours is returned in a fraction of a second, removing the computing budget as the limiting factor on how many candidates can be examined. The number of geometries a designer can assess within a tender or a retrofit study rises by orders of magnitude, and a candidate can now be judged while the design is still being discussed, rather than the following day. The surrogate does not replace computation — the geometry selected from a search is still confirmed by a full calculation — but it shifts where the effort goes, from computing a handful of variants to searching a design space that was previously out of reach. That is where the quality of the delivered propeller is decided, and it is the part of the workflow this Knowledge Transfer Partnership set out to change.

Acknowledgements

This work was carried out as part of Knowledge Transfer Partnership 10120912 between the University of Strathclyde and Stone Marine Propulsion, funded by UKRI through Innovate UK.

References

Bakhtiari, M., Ghassemi, H. (2020). CFD data based neural network functions for predicting hydrodynamic performance of a low-pitch marine cycloidal propeller. Applied Ocean Research 94, 101981.

Doijode, P.S., Hickel, S., van Terwisga, T., Visser, K. (2022). A machine learning approach for propeller design and optimization: Part I. Applied Ocean Research 124, 103178.

Li, L., Chen, Y., Huang, L., Hai, Q., Tang, D., Wang, C. (2025). Improvement of propeller hydrodynamic prediction model based on multitask ANN and its application in optimization design. Journal of Marine Science and Engineering 13(1), 183.

Menter, F.R. (1994). Two-equation eddy-viscosity turbulence models for engineering applications. AIAA Journal 32(8), 1598-1605.

Smirnov, P.E., Menter, F.R. (2009). Sensitization of the SST turbulence model to rotation and curvature by applying the Spalart-Shur correction term. Journal of Turbomachinery 131(4), 041010.

Sobol, I.M. (1967). On the distribution of points in a cube and the approximate evaluation of integrals. USSR Computational Mathematics and Mathematical Physics 7(4), 86-112.

A Representation Learning Framework for Efficient Exploration of Ship Hull Design Spaces

Daniel Akinmulewo[1,2], Florian Sprenger[2]

[1] *Schiffbau-Versuchsanstalt Potsdam GmbH*

[2] *University of Rostock Faculty of Mechanical Engineering and Marine Engineering, Rostock.*

Abstract

Efficient exploration of ship hull design spaces remains challenging due to the high dimensionality of geometric representations. In this work, we propose a geometry-conditioned 3D generative framework for learning a compact and interpretable latent space of ship hull forms. A beta-variational autoencoder is combined with parameter conditioning to jointly model hull geometry within a continuous latent representation. The resulting latent space provides a structured representation that enables controlled generation, interpolation, and reconstruction of hull forms while maintaining consistency with well-known ship design parameters.

1. Introduction

Simulation-based design and optimization (SBDO) has become a standard approach for ship hull form development. In general, this process comprises three main elements: hull form modification, performance evaluation, and optimization within an iterative design loop [1]. During each iteration, optimization algorithms explore the predefined design space to identify hull variants with improved hydrodynamic performance based on single- or multi-objective design criteria. This process is repeated until the optimization converges to a set of satisfactory design solutions.

Traditional parametric and deformation-based approaches [2,3,4,5] and [6,7,8] provide practical control but require manually defined variables and geometric constraints. Increasing geometric flexibility generally increases the dimensionality of the design space and the number of expensive evaluations required for exploration. Data-driven dimensionality reduction offers an alternative by learning compact representations directly from hull geometry. Linear methods such as Principal Component Analysis (PCA) also referred to as Proper Orthogonal Decomposition (POD) [9,10,11,12,13] and the Karhunen–Loève Expansion (KLE) [14,15]. are effective but may be limited in representing nonlinear geometric variation, while nonlinear generative models [16,17,18,19] do not necessarily provide controllable latent variables. Parameter-informed approaches such as the Shape Signature Vector [20] and Parametric Model Embedding frameworks [21,22] address this issue by introducing additional geometric or parametric information. Deep generative models, including Generative Adversarial Networks (GANs), diffusion models and autoencoder-based approaches, have also been investigated for ship hull generation and exploration [23,24,25,26,27,28] but controllability and physical interpretability of their latent representations remain important challenges.

This work therefore develops a geometry-conditioned beta-variational autoencoder (β-VAE) with a conditional prior and spatial latent representation to separate prescribed design characteristics from residual geometric variation and provide a compact design space for subsequent hull-form exploration.

The study focuses on: (1) a conditional prior-posterior β-VAE for sparse 3D hull representation; (2) a spatial latent grid with local cross-attention; (3) evaluation of reconstruction fidelity and geometric-relationship preservation; and (4) PCA-based reduction of the learned representation for latent-space exploration.

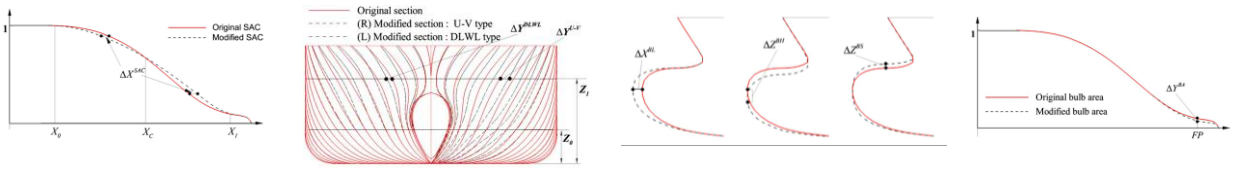
2. Ship Optimization and Design Space Reduction

2.1. Problem formulation

Consider a parametric shape-optimization problem defined on a parent hull geometry G_0 within a simulation-based design-optimization (SBDO) framework. The hull surface is described by the smooth mapping

$$\mathbf{g}: \Omega \times \mathcal{U} \to \mathbb{R}^3, \qquad (\boldsymbol{\xi}, \mathbf{c}) \mapsto \mathbf{g}(\boldsymbol{\xi}, \mathbf{c}) \tag{1}$$

where $\boldsymbol{\xi} \in \Omega$ denotes the parametric surface coordinates and $\mathbf{c}$ is the vector of design variables (geometric descriptors) that defines and controls the geometric characteristic of the hull. Each admissible design vector therefore generates a unique three-dimensional geometry while satisfying the geometric relationships and continuity requirements imposed by the parameterization.



(a) (b) (c)

Figure 1: Parametric modification functions based on [2] and used in this study: (a) SAC shape, (b) section shape, (c) bulb shape descriptors, forming the design vector $\boldsymbol{c}$.

The complete set of design variables is written as

$$\mathbf{c} = [\mathrm{c}_1, \mathrm{c}_2, \dots, \mathrm{c}_N]^\mathsf{T} \in \mathcal{C} \subseteq \mathbb{R}^N \tag{2}$$

where each component corresponds to a specific geometric parameter (Fig. 1) and the components jointly span the design space $\mathcal{C}$ within which the optimization is carried out.

The goal of the optimization is to determine the design vector c that minimizes a selected performance measure while satisfying the imposed constraints. The problem is stated as

$$\mathbf{c}^\star = \underset{\mathbf{c}\in\mathcal{C}}{\operatorname{argmin}}\, f(\mathbf{c}) \quad \text{subject to} \quad \begin{cases} g_i(\mathbf{c}) \le 0, & i = 1, \dots, p, \\ h_j(\mathbf{c}) = 0, & j = 1, \dots, q, \end{cases} \tag{3}$$

where f denotes the objective function, for instance the calm-water resistance or another relevant hydrodynamic performance metric and g_i and h_j are the inequality and equality constraints that delimit the feasible region of the design space.

For practical ship-design optimization, dimensionality reduction alone is not sufficient. The reduced representation should also provide a degree of controllability and, where possible, a physically meaningful interpretation of the resulting design variables. In other words, the latent representation should not only capture geometric variability, but should also allow selected hull characteristics to be prescribed directly during design-space exploration. The present formulation therefore introduces the design vector $\mathbf{c}$ as a conditioning variable in the encoder and decoder [32], and the latent prior. The approximate posterior distribution is therefore defined as $q_\phi(\mathbf{z} \mid \mathbf{s}, \mathbf{c})$, where $\mathbf{s}$ represents the input hull geometry, while the conditional prior is given by $p_\psi(\mathbf{z} \mid \mathbf{c})$. The model is trained using

$$\mathcal{L}_{\beta\text{-VAE}} = -\,\mathbb{E}_{q_\phi(\mathbf{z}|\mathbf{s},\mathbf{c})}[\log p_\theta(\mathbf{s} \mid \mathbf{z}, \mathbf{c})] + \beta\, D_{\mathrm{KL}}\left(q_\phi(\mathbf{z} \mid \mathbf{s}, \mathbf{c}) \parallel p_\psi(\mathbf{z} \mid \mathbf{c})\right) \tag{4}$$

Here, the reconstruction term preserves the geometric information required to reproduce the input hull, while the KL-divergence term regularizes the geometry-dependent posterior towards the condition-dependent prior. The conditioning variables therefore provide explicit control over selected hull characteristics, while the latent variables capture the remaining geometric variation not explicitly represented by the conditioning vector. After training, a hull can be generated by sampling $\mathbf{z}$ from the conditional prior and decoding it together with a prescribed $\mathbf{c}$. The resulting representation therefore enables controlled generation while retaining additional geometric flexibility beyond the original parametric description.

For design-space exploration, the latent representation $\mathbf{z}$ is further reduced to a compact set of coordinates $\mathbf{t}$. The final data-driven design vector is defined as $\mathbf{d} = (\mathbf{c}, \mathbf{t})$, where $\mathbf{c}$ controls the prescribed design characteristics and $\mathbf{t}$ describes the dominant residual geometric variations. The decoder then provides a nonlinear mapping from $\mathbf{d}$ to the corresponding hull geometry. The optimization problem can consequently be formulated directly in the reduced design space,

$$\mathbf{d}^\star = \underset{\mathbf{d}\in\mathcal{C}\times\mathcal{T}}{\operatorname{argmin}}\, R(\mathcal{S}_\mathbf{d}; V_s) \quad \text{s.t.} \quad g_k(\mathbf{d}) \le 0, \qquad k = 1, \dots, K \tag{5}$$

subject to the prescribed geometric constraints g_k.

3. Dataset Generation and Geometric Representation

The dataset was constructed to represent geometric diversity within a container-ship hull family, including variations in global hull form and bow configuration. 20 realistic parent hulls were modified using the parametric

functions of Kim et al. [2] and variations in principal dimensions L, B and D. Latin hypercube sampling of the combined parameter space produced approximately 2120 hull forms.

The STL meshes were converted to a common sparse signed-distance (SDF) representation. Each hull was normalized by translating the bounding-box centre to the origin and scaling by the bounding-box diagonal; only one symmetric half-hull was retained during training. A common anisotropic 256×64×64 lattice was used, with a narrow SDF band connected by six-neighbour adjacency. Additional interior and exterior samples constrained the distance field away from the surface.

The resulting representation provides spatially aligned graph nodes across the dataset and preserves the continuous SDF information needed for surface reconstruction.

The resulting 2120 hull representations were divided into 90% training and 10% validation data, with an independent test set of 3 hull meshes reserved for final evaluation.

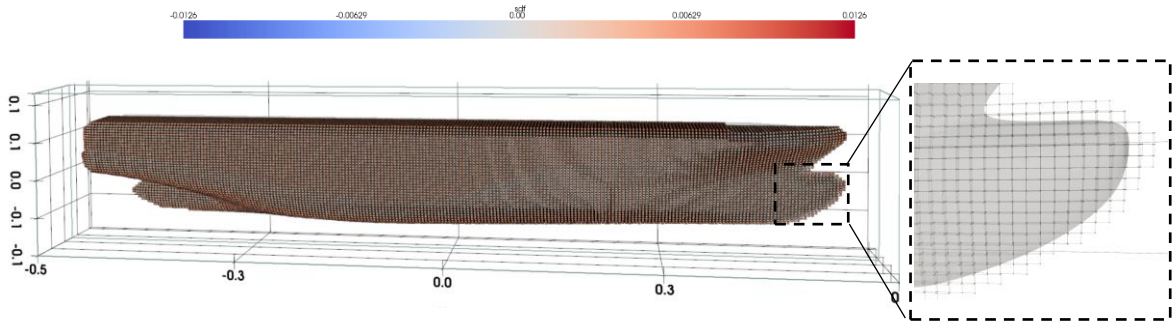


Figure 2: Graph-based sparse signed-distance representation

4. Model Architecture and Training

The conditional β-VAE operates directly on the sparse hull graph and consists of a graph-based encoder, a spatial latent representation with a conditional prior, and a coordinate-query decoder.

Graph encoder: The graph encoder processes the active lattice nodes and their six-neighbour connectivity to extract local geometric features from the hull surface. Each node is described by its spatial coordinates and signed-distance value. The spatial coordinates $p \in \mathbb{R}^3$ is augmented using Fourier positional encodings [33], $\gamma(p) \in \mathbb{R}^{3+6L}$, to capture high-frequency details:

$$\gamma(p) = (p, sin(2^0\pi p), cos(2^0\pi p), \dots, sin(2^{L-1}\pi p), cos(2^{L-1}\pi p)) \in \mathbb{R}^{3+6L} \quad (6)$$

where L is the number of frequency bands. The augmented features are processed using the MeshGraphNet-style message-passing network [34]. A stack of message-passing layers then updates edges and nodes with residual MLP ϕ_e, ϕ_v and mean aggregation,

The design parameters are injected into the encoder by feature-wise linear modulation (**FiLM**) [35] enabling condition-dependent feature extraction.

Spatial latent grid: Conditioned node features are aggregated onto a coarse three-dimensional grid defined by the spatial stride. Within each cell, a query derived from the Fourier-encoded cell-centre position attends to the member-node features, producing a position-dependent latent summary through local cross-attention. A compact 3D convolutional block then refines the grid and predicts the per-cell posterior mean and log-variance.

Conditional prior: A learned conditional prior $p_\psi(z \mid c)$ predicts a latent distribution at each grid cell directly from the design vector. The conditioning embedding is broadcast across the grid and mapped to the prior parameters.

Coordinate-queried decoder: The decoder predicts the continuous SDF at arbitrary query locations by trilinearly sampling the spatial latent grid and combining the sampled latent vector with Fourier-encoded coordinates and c. The zero-level set of the predicted SDF is reconstructed using MISE [36] followed by marching-cubes surface extraction.

The model is trained using a β-weighted reconstruction and KL-regularization objective. The reconstruction loss is evaluated on sampled signed-distance points, with increased weighting near the hull surface to prioritize geometric fidelity. Interior and exterior samples are also included so that the decoder learns the distance field beyond the surface band. A free-bits strategy and gradual β warm-up are employed to reduce posterior collapse

during training. Optimization uses AdamW with a cosine-annealed learning rate, and data-parallel training. Further architectural and training details are provided in Appendix A.

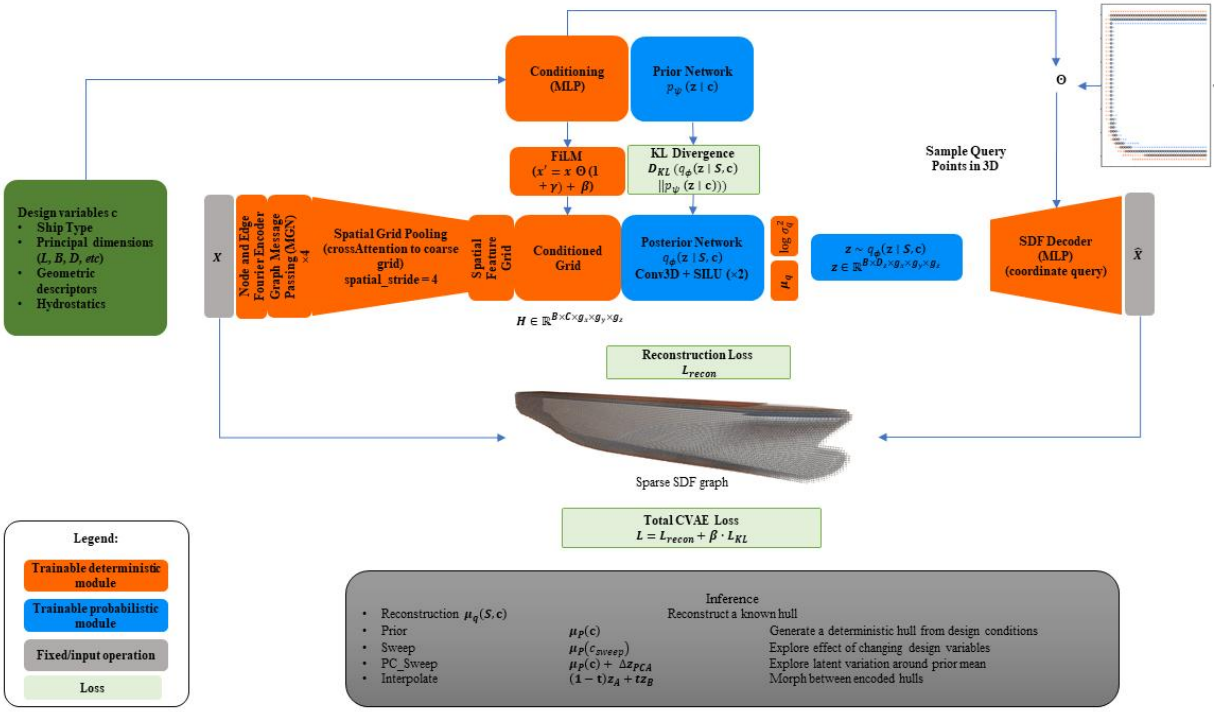


Figure 3: Model architecture of the conditional *β-VAE* with a spatial latent grid for 3D ship hull representation and generation

5. Results and Discussion

5.1. Evaluation metrics for dimensionality reduction

In this study, the learned representation is evaluated from two perspectives: reconstruction fidelity and preservation of geometric relationships. Reconstruction fidelity is assessed using Chamfer Distance (CD) and Hausdorff Distance (HD), which quantify the overall and maximum geometric deviations between the original and reconstructed hull surfaces, respectively.

$$CD(S,\hat{S}) = \frac{1}{|S|}\sum_{x\in S}\min_{\hat{x}\in\hat{S}}|x-\hat{x}|_2^2 + \frac{1}{|\hat{S}|}\sum_{\hat{x}\in\hat{S}}\min_{x\in S}|\hat{x}-x|_2^2 \tag{7}$$

$$HD(S,\hat{S}) = \max\left\{\sup_{x\in S}\min_{\hat{x}\in\hat{S}}|x-\hat{x}|_2, \sup_{\hat{x}\in\hat{S}}\min_{x\in S}|\hat{x}-x|_2\right\} \tag{8}$$

To access the preservation of geometric relationship between hulls i and j, the distance is defined as

$$d_\kappa(i,j) = \frac{1}{N_x}\sum_{x=1}^{N_x}|\boldsymbol{\kappa_i}(x) - \boldsymbol{\kappa_j}(x)|_2 \tag{9}$$

here $\boldsymbol{\kappa_i}(x)$ and $\boldsymbol{\kappa_j}(x)$ denote the mean sectional curvature at longitudinal station x of hulls i and j, respectively, and N_x is the number of stations. The resulting $d_\kappa(i,j)$ is subsequently compared with the corresponding latent-space distance

$$d_z(i,j) = |z_i - z_j|_2 \tag{10}$$

using the Spearman rank correlation coefficient

$$\rho_{\kappa,z} = Spearman\big(d_\kappa(i,j), d_z(i,j)\big) \tag{11}$$

5.2. *Effect of hyperparameters: spatial coarsening f, latent space dimensionality (D_L) and β-coefficient*

A sensitivity study was conducted to investigate the influence of three key hyperparameters of the proposed conditional β-VAE: the **spatial coarsening factor f**, the **latent-space dimensionality D_L**, and the **maximum KL-divergence weighting coefficient β_{max}**. The spatial coarsening factor determines the resolution of the coarse three-dimensional latent grid onto which the conditioned graph features are aggregated, while D_L controls the number of latent channels available to represent the hull geometry. The β_{max}. coefficient regulates the relative contribution of the latent regularisation term to the reconstruction objective. The tested configurations considered includes, spatial coarsening factor $f \in \{4, 8\ 16\}$ latent dimensions $D_L \in \{4, 8\ 16\}$. and $\beta_{\max} \in \{10^{-3}, 5 \times 10^{-3}, 10^{-2}\}$. The sensitivity of the parameters are measured with the evaluation metric in section 5.1 and presented in Appendix A. All other architectural and training parameters were kept fixed to isolate the effect of these three variables.

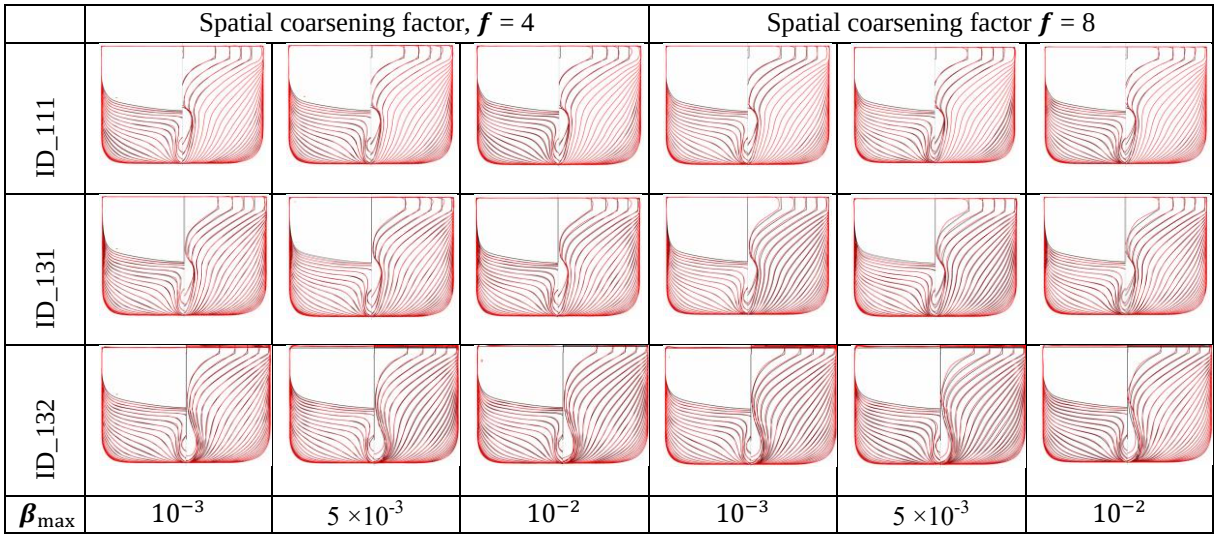


Figure 4: Comparison of original and reconstructed hull forms for different spatial coarsening factors f and β_{max} values (black: true, red: reconstructed, $D_L = 16$)

The reconstructions show that spatial coarsening and latent dimensionality influence the preservation of local hull-form features, particularly in regions with strong geometric curvature. Increasing the KL weighting also changes the balance between reconstruction fidelity and latent regularization. The results therefore indicate that the choice of latent-grid resolution and regularization strength is important for maintaining geometric fidelity while obtaining a compact representation.

5.3. *Visualization and interpretation of the latent space*

To investigate the organization and interpretability of the learned latent representation, the posterior mean μ_q of each hull was extracted from the spatial latent grid and flattened into a single latent representation. The resulting latent representations were centered and projected into a lower-dimensional space using PCA. PCA was then used to identify the dominant directions of variation in the learned latent space.

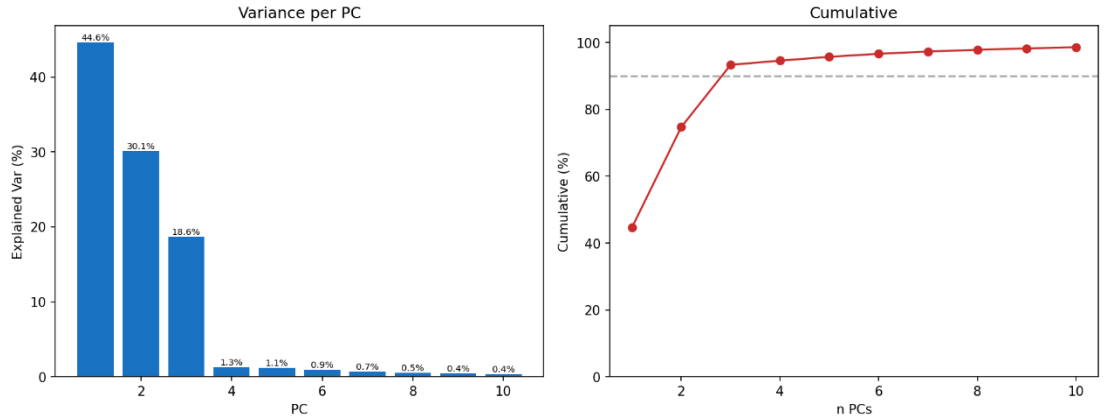


Figure 5: PCA of spatial-grid (PCA 1-10, f = 16, D_L= 8, β_{max}= 10^{-3})

Figure 5 presents the variance captured by the first ten principal components (PC). The first four principal components together account for 94.6% of the variance, while the first ten components capture approximately 98.6%. The pairwise PCA projections in Figure 6 show structured, non-uniform distributions, indicating that the latent representation is organized along dominant directions of variation.

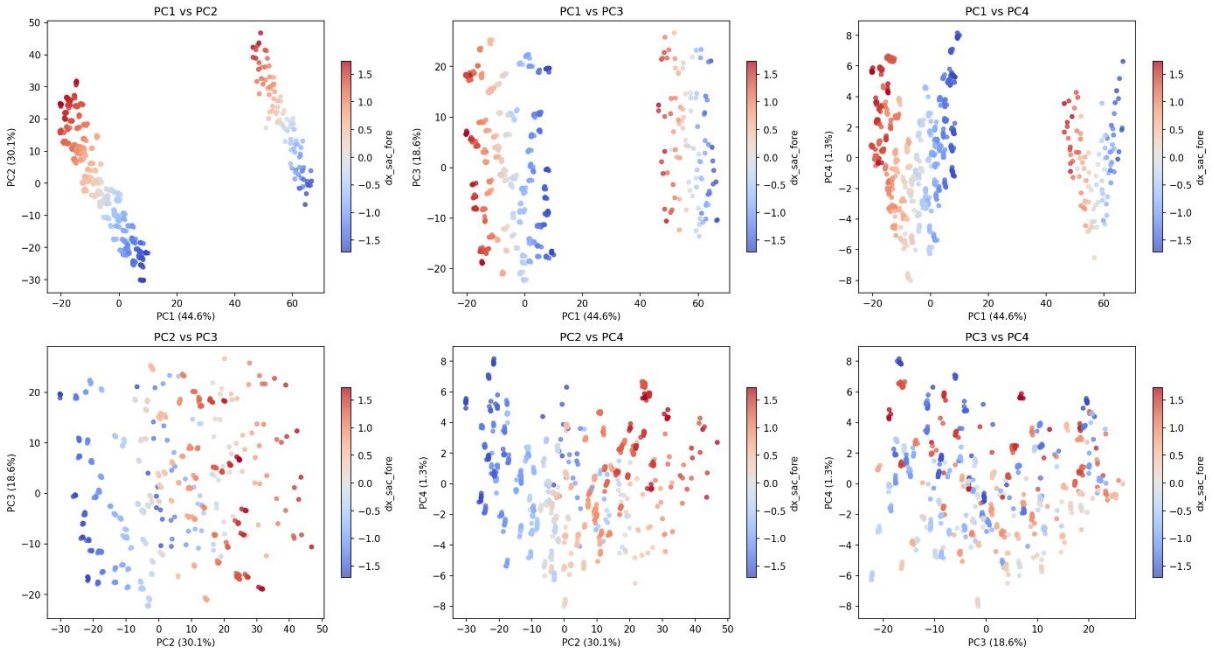


Figure 6: Pairwise projections of the first four principal components of the spatial latent representation, coloured by the normalized $dx_{sac\text{-}fore}$ parameter based on [2]

Figure 7 shows identifiable associations between several design variables and individual PCs, while also demonstrating that parameter influence is distributed across multiple components. The absolute Pearson correlations between the design variables and PC scores quantify pairwise statistical associations rather than one-to-one physical mappings. A single principal component may therefore be correlated with multiple coupled design variables. This distributed structure is consistent with coupled hull geometry, where variation in one design variable can influence several geometric characteristics. The PCA representation therefore provides a compact basis for subsequent latent-space exploration.

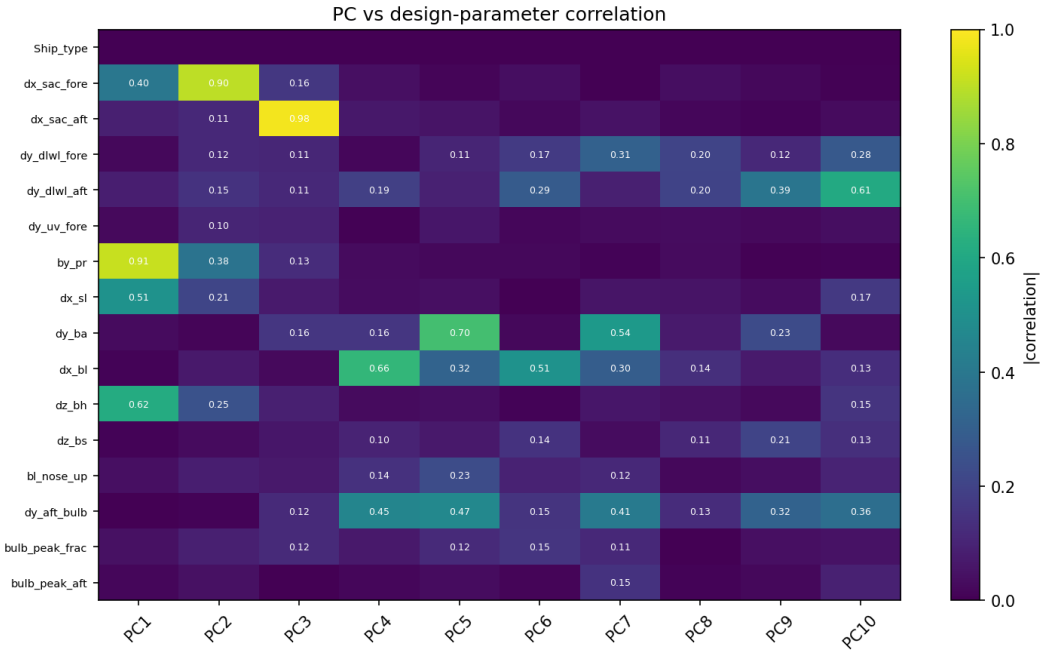


Figure 7: PC vs design-parameter correlation

5.4. Latent vector optimization

As formulated in Eq. (7), the reduced latent representation constitutes the design space to be navigated. Rather than optimizing the full high-dimensional spatial latent field directly, which would be computationally intractable and may lead to geometries outside the dominant learned latent subspace, the latent representation is parameterized by its leading principal-component directions. A candidate latent vector z is generated by perturbing a reference latent z_0 along these directions:

$$z = z_0 + \sum_{i=1}^{k} t_i \, (\sigma_i \, v_i) \tag{12}$$

where t_i is the dimensionless optimization coefficient associated with the *i*-th principal component, v_i is the corresponding unit PCA direction, and $\sigma_i = \sqrt{\lambda}_i$ is the standard deviation associated with that principal component, obtained from its eigenvalue λ_i. Scaling each principal direction by σ_i expresses the latent perturbation in units of the observed variation along that direction; consequently, t_i corresponds to a displacement of one standard deviation along the *i*-th principal direction.

The k coefficients,

$$t = (t_i, \dots, t_k) \tag{13}$$

therefore, define a compact, low-dimensional search space that captures the dominant modes of geometric variation learned from the training data while restricting the optimization to the principal subspace of the latent distribution. The number of retained components k is selected to capture the majority of the observed latent variance while reducing the dimensionality of the optimization problem. In the present case, the leading $k \approx 10$ components account for 98.6% of the total.

5.5. Model Properties at Inference

At inference, the conditional latent representation supports several modes of geometric exploration. Reconstruction evaluates the ability of the model to reproduce a known hull by decoding the posterior mean conditioned on its associated design vector. Prior generation instead uses the conditional prior mean to obtain a deterministic hull corresponding to prescribed design characteristics. Systematic variation of the conditioning vector enables direct investigation of the effect of individual design variables on the generated geometry. In addition, perturbations of the conditional prior mean along the principal directions of latent variation obtained through PCA enable exploration of residual geometric variability not explicitly controlled by the conditioning variables. Finally, interpolation between latent representations of two hulls provides a continuous path through the learned design space and allows the geometric transition between the corresponding hull forms to be examined.

Inference mode	Formulation	Purpose
Reconstruction	$\hat{\mathbf{s}} = g_\theta\big(\mu_q(\mathbf{s}, \mathbf{c}), \mathbf{c}\big)$	Reconstruct a known hull from its encoded posterior mean
Prior generation	$\hat{\mathbf{s}} = g_\theta\big(\mu_p(\mathbf{c}), \mathbf{c}\big)$	Generate a deterministic hull corresponding to prescribed design conditions
Condition sweep	$\hat{\boldsymbol{s}} = g_\theta\big(\mu_p\big(\boldsymbol{c}_{\text{sweep}}\big), \boldsymbol{c}_{\text{sweep}}\big)$	Explore the effect of systematically varying selected design parameters
PCA latent sweep	$\hat{\mathbf{s}} = \big(g_\theta \mu_p(\mathbf{c}) + \Delta \mathbf{z}_{\text{PCA}}, \mathbf{c}\big)$	Explore residual geometric variation around the conditional-prior mean
Interpolation	$\boldsymbol{z}(t) = (1-t)\boldsymbol{z_A} + t\boldsymbol{z_B}$	Morph continuously between two encoded hull representations

6. Conclusions

This study presented a geometry-conditioned representation-learning framework for reducing and exploring ship hull design spaces. A conditional β-VAE was formulated to operate on a sparse signed-distance graph representation of container-ship hull forms, combining graph-based feature extraction, a spatial latent grid with local cross-attention, a learned conditional prior, and a coordinate-queried SDF decoder. This formulation separates prescribed design characteristics from residual geometric variation while retaining a spatially structured latent representation.

The results demonstrate that the learned representation can reproduce the principal geometric characteristics of the investigated hull forms, while the PCA analysis shows that a substantial portion of the latent variation can be described by a relatively small number of principal directions. The observed associations between principal components and hull-design parameters further indicate that the latent space retains identifiable relationships with the original design variables, although these relationships remain distributed across multiple latent directions because of the coupled nature of hull geometry.

The resulting reduced latent representation provides a compact design space in which residual geometric variation can be explored independently of the prescribed design characteristics. PCA-based latent parameterization therefore provides a practical link between representation learning and subsequent design-space exploration and optimization. The proposed framework establishes a basis for incorporating data-driven geometric variation into simulation-based ship design workflows, with future work focusing on quantitative optimization studies, hydrodynamic performance evaluation, and validation across broader ship-form families.

References

[1] C. Yang and F. Huang, 'An overview of simulation-based hydrodynamic design of ship hull forms', *J Hydrodyn*, vol. 28, no. 6, pp. 947–960, Dec. 2016, doi: 10.1016/S1001-6058(16)60696-0.

[2] H.-J. Kim, J.-E. Choi, and H.-H. Chun, 'Hull-form optimization using parametric modification functions and particle swarm optimization', *J Mar Sci Technol*, vol. 21, no. 1, pp. 129–144, Mar. 2016, doi: 10.1007/s00773-015-0337-y.

[3] S. Han, Y.-S. Lee, and Y. B. Choi, 'Hydrodynamic hull form optimization using parametric models', *J Mar Sci Technol*, vol. 17, no. 1, pp. 1–17, Mar. 2012, doi: 10.1007/s00773-011-0148-8.

[4] Y. Feng, O. El Moctar, and T. E. Schellin, 'Parametric Hull Form Optimization of Containerships for Minimum Resistance in Calm Water and in Waves', *J. Marine. Sci. Appl.*, vol. 20, no. 4, pp. 670–693, Dec. 2021, doi: 10.1007/s11804-021-00243-w.

[5] X. Cheng *et al.*, 'Ship Optimization Based on Fully-Parametric Models for Hull, Propeller and Rudder', *JMSE*, vol. 12, no. 9, p. 1635, Sep. 2024, doi: 10.3390/jmse12091635.

[6] K.-L. Jeong and S.-M. Jeong, 'A Mesh Deformation Method for CFD-Based Hull form Optimization'.

[7] D. Wei, L. Wang, J. Yang, X. Sun, X. Ji, and X. Liu, 'Hull form optimization with a new three-dimensional deformation strategy', *Sci Rep*, vol. 15, no. 1, p. 41804, Nov. 2025, doi: 10.1038/s41598-025-25709-7.

[8] J. Wu, X. Liu, and D. Wan, 'Multi-Objective Hydrodynamic Optimization of Ship Hull Based on Approximation Model'.

[9] D. Yu and L. Wang, 'Hull Form Optimization with Principal Component Analysis and Deep Neural Network', Oct. 27, 2018, *arXiv*: arXiv:1810.11701. doi: 10.48550/arXiv.1810.11701.

[10] Y. Zhang, N. Ma, X. Gu, and Q. Shi, 'A Dimensionality Reduction Method Based on Principal Component Analysis for Ship Hull Form Optimization'.

[11] X. Liu, W. Zhao, and D. Wan, 'Linear reduced order method for design-space dimensionality reduction and flow-field learning in hull form optimization', *Ocean Engineering*, vol. 237, p. 109680, Oct. 2021, doi: 10.1016/j.oceaneng.2021.109680.

[12] S. Harries and S. Uharek, 'Application of Radial Basis Functions for Partially-Parametric Modeling and Principal Component Analysis for Faster Hydrodynamic Optimization of a Catamaran', *JMSE*, vol. 9, no. 10, p. 1069, Sep. 2021, doi: 10.3390/jmse9101069.

[13] D. D'Agostino, A. Serani, and M. Diez, 'Design-space assessment and dimensionality reduction: An off-line method for shape reparameterization in simulation-based optimization', *Ocean Engineering*, vol. 197, p. 106852, Feb. 2020, doi: 10.1016/j.oceaneng.2019.106852.

[14] M. Diez, E. F. Campana, and F. Stern, 'Design-space dimensionality reduction in shape optimization by Karhunen–Loève expansion', *Computer Methods in Applied Mechanics and Engineering*, vol. 283, pp. 1525–1544, Jan. 2015, doi: 10.1016/j.cma.2014.10.042.

[15] H. Chang, C. Wang, Z. Liu, B. Feng, C. Zhan, and X. Cheng, 'Research on the Karhunen–Loève Transform Method and Its Application to Hull Form Optimization', *JMSE*, vol. 11, no. 1, p. 230, Jan. 2023, doi: 10.3390/jmse11010230.

[16] Z. Liu, D. Wan, X. Zhang, J. Chen, S. Wang, and Y. Wang, 'Design space nonlinear dimensionality reduction based on deep neural networks in ship hull form optimization', *Ocean Engineering*, vol. 348, p. 124112, Mar. 2026, doi: 10.1016/j.oceaneng.2025.124112.
[17] J. Seo, D. Kim, and I. Lee, 'A study on ship hull form transformation using convolutional autoencoder', *Journal of Computational Design and Engineering*, vol. 11, no. 1, pp. 34–48, Dec. 2023, doi: 10.1093/jcde/qwad111.
[18] Y. Wang, J. Joseph, T. P. Aniruddhan Unni, S. Yamakawa, A. Barati Farimani, and K. Shimada, 'Three-Dimensional Ship Hull Encoding and Optimization via Deep Neural Networks', *J. Mech. Des*, vol. 144, no. 101701, Jun. 2022, doi: 10.1115/1.4054494.
[19] D. D'Agostino, A. Serani, E. F. Campana, and M. Diez, 'Nonlinear Methods for Design-Space Dimensionality Reduction in Shape Optimization', in *Machine Learning, Optimization, and Big Data*, G. Nicosia, P. Pardalos, G. Giuffrida, and R. Umeton, Eds, Cham: Springer International Publishing, 2018, pp. 121–132. doi: 10.1007/978-3-319-72926-8_11.
[20] S. Khan, P. Kaklis, A. Serani, M. Diez, and K. Kostas, 'Shape-supervised Dimension Reduction: Extracting Geometry and Physics Associated Features with Geometric Moments', *Computer-Aided Design*, vol. 150, p. 103327, Sep. 2022, doi: 10.1016/j.cad.2022.103327.
[21] A. Serani and M. Diez, 'Parametric model embedding', *Computer Methods in Applied Mechanics and Engineering*, vol. 404, p. 115776, Feb. 2023, doi: 10.1016/j.cma.2022.115776.
[22] A. Serani, G. Palma, and M. Diez, 'A nonlinear extension of parametric model embedding for dimensionality reduction in parametric shape design', May 12, 2026, *arXiv*: arXiv:2605.11759. doi: 10.48550/arXiv.2605.11759.
[23] S. Khan, K. Goucher-Lambert, K. Kostas, and P. Kaklis, 'ShipHullGAN: A generic parametric modeller for ship hull design using deep convolutional generative model', *Computer Methods in Applied Mechanics and Engineering*, vol. 411, p. 116051, Jun. 2023, doi: 10.1016/j.cma.2023.116051.
[24] K. Yonekura, K. Omori, X. Qi, and K. Suzuki, 'Designing Ship Hull Forms Using Generative Adversarial Networks', *AI*, vol. 6, no. 6, p. 129, Jun. 2025, doi: 10.3390/ai6060129.
[25] G. Anagnostopoulos and P. Kaklis, 'Enhancing Shape-Encoding of a GAN-Based Parametric Modeller for Ship Design'.
[26] L. T. Trinh, T. Hamagami, and N. Okamoto, '3D Ship Hull Design Direct Optimization Using Generative Adversarial Network', *JACIII*, vol. 28, no. 3, pp. 693–703, May 2024, doi: 10.20965/jaciii.2024.p0693.
[27] N. J. Bagazinski and F. Ahmed, 'C-ShipGen: A Conditional Guided Diffusion Model for Parametric Ship Hull Design', May 10, 2024, *arXiv*: arXiv:2407.03333. doi: 10.48550/arXiv.2407.03333.
[28] N. M. Htein, P. Louvros, E. Stefanou, N. Hifi, and E. Boulougouris, 'Representation-Aware Generative Modeling for Early-Stage Ship Design', *JMSE*, vol. 14, no. 7, p. 642, Mar. 2026, doi: 10.3390/jmse14070642.
[29] D. P. Kingma and M. Welling, 'Auto-Encoding Variational Bayes', Dec. 10, 2022, *arXiv*: arXiv:1312.6114. doi: 10.48550/arXiv.1312.6114.
[30] C. P. Burgess *et al.*, 'Understanding disentangling in $β$-VAE', Apr. 10, 2018, *arXiv*: arXiv:1804.03599. doi: 10.48550/arXiv.1804.03599.
[31] I. Higgins *et al.*, 'β-VAE: LEARNING BASIC VISUAL CONCEPTS WITH A CONSTRAINED VARIATIONAL FRAMEWORK', 2017.
[32] A. Pagnoni, K. Liu, and S. Li, 'Conditional Variational Autoencoder for Neural Machine Translation', Dec. 11, 2018, *arXiv*: arXiv:1812.04405. doi: 10.48550/arXiv.1812.04405.
[33] M. Tancik *et al.*, 'Fourier Features Let Networks Learn High Frequency Functions in Low Dimensional Domains', Jun. 18, 2020, *arXiv*: arXiv:2006.10739. doi: 10.48550/arXiv.2006.10739.
[34] T. Pfaff, M. Fortunato, A. Sanchez-Gonzalez, and P. W. Battaglia, 'Learning Mesh-Based Simulation with Graph Networks', Jun. 18, 2021, *arXiv*: arXiv:2010.03409. doi: 10.48550/arXiv.2010.03409.
[35] E. Perez, F. Strub, H. de Vries, V. Dumoulin, and A. Courville, 'FiLM: Visual Reasoning with a General Conditioning Layer', Dec. 18, 2017, *arXiv*: arXiv:1709.07871. doi: 10.48550/arXiv.1709.07871.
[36] L. Mescheder, M. Oechsle, M. Niemeyer, S. Nowozin, and A. Geiger, 'Occupancy Networks: Learning 3D Reconstruction in Function Space', Apr. 30, 2019, *arXiv*: arXiv:1812.03828. doi: 10.48550/arXiv.1812.03828.

Appendix A:

1. Hyperparameter Specifications

This section provides the specific hyperparameter values used for the model architecture and training process, as referenced in the main text. Table I summarizes the parameters used to preprocess the geometric data for model input, including the construction of the canonical graph from the mesh surfaces and the generation of the semi-occupancy field used for training the SDF decoder. Table I presents the architectural hyperparameters of the proposed conditional β-VAE, including the graph-based encoder, spatial latent grid, local cross-attention aggregation, latent-space dimensionality, conditional prior, and SDF decoder. These parameters define the structure and representational capacity of the proposed model. Finally, Table II lists the hyperparameters used during model training, including the optimizer, learning-rate schedule, reconstruction and KL-loss settings, warm-up strategy, and regularization parameters. Table III presents the configurations and corresponding reconstruction metrics from the sensitivity study described in Section 5.2,

Table I: Key Model Architecture Hyperparameters

Component / Category	Parameter	Value
General Model	Hidden Feature Dimension	128
	Conditioning Dimension	16
	Number of MGN Layers	4
Spatial Latent Grid	Canonical Grid Resolution	256 × 64 × 64
	Spatial Coarsening Factor f	4,8, 16
	Latent Grid Resolution ($G_x \times G_y \times Gz$)	16 × 4 × 4
	Latent Dimension (D_L)	4, 8, 16
	Grid Aggregation	Local cross-attention
	Attention Heads	8
Graph/Point Encoder	Node Input Features	SDF + Fourier-encoded (x, y, z)
	Node Encoder MLP	[37, 128, 128]
	Edge Input Features	Fourier-encoded relative position
	Edge Encoder MLP	[36, 128, 128]
	Conditioning Mechanism	FiLM
Spatial Cross-Attention	Cell Query Features	Fourier-encoded cell-centre position
	Cell Query MLP	[36, 128, 128]
	Node Key Input Dimension	164
	Attention Head Dimension	16
	FFN Dimension	128 → 256 → 128
Latent Distribution	Prior Type	Conditional p(z|c)
	Posterior Parameters	μ_q, $\log \mu_q{}^2$
	Prior Parameters	μ_p, $\log \mu_p{}^2$
SDF Decoder	Latent Projection MLP	[8, 128, 128]
	Query Input Features	Raw x, y, z → Fourier encoded (x, y, z)
	Query Encoder MLP	[39, 128, 128]
	Decoder Head MLP	[384, 128, 128, 128, 1]

Table II: Key Training Hyperparameters

Parameter	Value
Optimizer	AdamW
Learning Rate	10^{-3}
Weight Decay	10^{-5}
Learning-Rate Scheduler	Cosine Annealing
Scheduler T	120 epochs
Minimum Learning Rate	10^{-5}
Number of Epochs	120
Batch Size	4
Reconstruction Loss	Weighted L_1 SDF Loss
Deterministic Warm-up	20 epochs
KL Warm-up	50 epochs
Free-Bits Threshold	10^{-4}
Automatic Mixed Precision	Enabled
Number of Query Points	4096

Table III: Sensitivity study

f	D_L	β_{max}	CD	HD
4	4	1.00E-03	1.41E-05	9.03E-03
4	4	5.00E-03	1.41E-05	1.01E-02
4	4	1.00E-02	1.41E-05	1.07E-02
4	8	1.00E-03	1.40E-05	9.10E-03
4	8	5.00E-03	1.41E-05	9.53E-03
4	8	1.00E-02	1.41E-05	9.58E-03
4	16	1.00E-03	1.40E-05	8.53E-03
4	16	5.00E-03	1.41E-05	8.63E-03
4	16	1.00E-02	1.41E-05	8.96E-03
8	4	1.00E-03	1.41E-05	1.02E-02
8	4	5.00E-03	1.41E-05	1.09E-02
8	4	1.00E-02	1.42E-05	1.08E-02
8	8	1.00E-03	1.40E-05	9.83E-03
8	8	5.00E-03	1.41E-05	1.08E-02
8	8	1.00E-02	1.41E-05	1.16E-02
8	16	1.00E-03	1.41E-05	9.34E-03
8	16	5.00E-03	1.42E-05	1.31E-02
8	16	1.00E-02	1.42E-05	1.21E-02
16	4	1.00E-03	1.41E-05	1.04E-02
16	4	5.00E-03	1.42E-05	1.03E-02
16	4	1.00E-02	1.42E-05	1.05E-02
16	8	1.00E-03	1.42E-05	1.05E-02
16	8	5.00E-03	1.41E-05	1.18E-02
16	8	1.00E-02	1.43E-05	1.25E-02
16	16	1.00E-03	1.41E-05	1.05E-02
16	16	5.00E-03	1.41E-05	1.10E-02
16	16	1.00E-02	1.42E-05	1.21E-02

High-Fidelity Optimization of Generic Hull Forms and Energy Saving Devices

Ivan Zeman[1], Luuk Halsema[1], Perry van Oossanen[1]
[1]Van Oossanen Naval Architects
i.zeman@oossanen.nl, l.halsema@oossanen.nl, perry.vanoossanen@oossanen.nl

1 Introduction

While driven by de-carbonization targets, the pursuit of hull efficiency proves to be also a strategic advantage next to a regulatory necessity. A high-performance hull form enhances operational capabilities, offering extended range and higher top speeds for installed power. The research goal of this study is to investigate the effect of incorporating energy saving devices (ESD's) design into an holistic hull-appendage parametric optimization, with the goal of maximizing ship efficiency gains.

This study presents a multi-objective optimization framework for the combined optimization of local and global hull parameters combined with an ESD. The framework is built around POSEIDON[1], an in-house developed platform coupling parametric CAD modeling with high-fidelity Computational Fluid Dynamics (CFD) to evaluate the complex interactions between hull forms and ESD's.

To quantify the effect of applying an ESD, an optimization is performed with and without it. For this paper, three parent hulls were selected as case studies, ranging from 100 to 300 meters of length over all. Six optimization studies were conducted, evaluating each vessel with and without an ESD at three sailing speeds of interest representing the operational profile. To optimize the hull, wave damping aft body (WDA) design principles are applied, as presented by Tsai et al. [1]. In the combined aft ship and ESD optimization, Hull Vane® is selected as an ESD. Application of the Hull Vane® is presented by Hofman et al. [2].

The objective of the optimization is to minimize engine brake power over the operational profile, derived by using state-of-the-art performance prediction from total vessel resistance calculated via CFD, while realistic displacement and stability constraints were enforced to maintain alignment with the parent hulls. This automated approach explores the full design space to identify global minima, delivering significant performance gains through optimized hydrodynamic synergy. Section 2 presents the methodology of the POSEIDON platform, section 3 shows the results of the study and results are discussed and conclusions are drawn in section 4.

2 Methodology

This study utilizes an in-house developed platform, POSEIDON, which couples several tools to perform automatic multi-objective high-fidelity parametric optimizations. The optimization procedure consists of several steps: a parametric modeler, meshing, CFD solver and optimization. A parametric modeler generates an initial sample base which is meshed and analyzed by the CFD solver. A surrogate model is built from the initial sample base and the algorithm finds an optimal solution from it. To ensure that the optimal solution is aligned with the project requirements, displacement (∇), longitudinal center of buoyancy (LCB) and metacentric height constraints (KM_t) are imposed. Finally, the objective of the optimization is to reduce the required brake engine power (P_b) across the operational profile. To obtain the required P_b, a power calculation is performed based on the hull resistance obtained via CFD. Further information on each step is provided in later sections.

2.1 Parametric Modeler

A parametric modeler is developed in Rhinoceros 3D. Important hull and Hull Vane® parameters are identified and implemented. Three parent hulls were selected for this study, resembling the main parameters and characteristics of a 100 m offshore patrol vessel, a 200 m passenger ferry and a 300 m cruise ship. Waterline length (L_{WL}), waterline beam (B_{WL}) and draught are constant, while displacement, LCB and KM_t are constrained to a set range.

[1]Parametrized Optimization for Ship Efficiency via Intelligent Design of Naval Form

The parametric modeler is set up for each hull with and without Hull Vane®, as a WDA and Hull Vane® case. The transverse span and angle of attack (AoA) of the Hull Vane® are constant in the optimization. The parent hulls are shown on Figure 1 and their general particulars are provided in Table 1.

Table 1: General particulars

	Vessel						*Hull Vane®*	
Geometry	L_{WL}, *m*	B_{WL}, *m*	*Draught, m*	∇, m^3	*LCB, m*	KM_t, *m*	*Span, m*	*AoA, deg*
Offshore Patrol Vessel	95.00	16.40	4.60	3902.00	46.44	8.89	13.20	0.00
Passenger Ferry	190.00	26.83	6.30	19513.00	93.32	15.22	21.60	0.00
Cruise Ship	283.00	36.67	7.70	51221.00	138.53	21.28	29.60	0.00

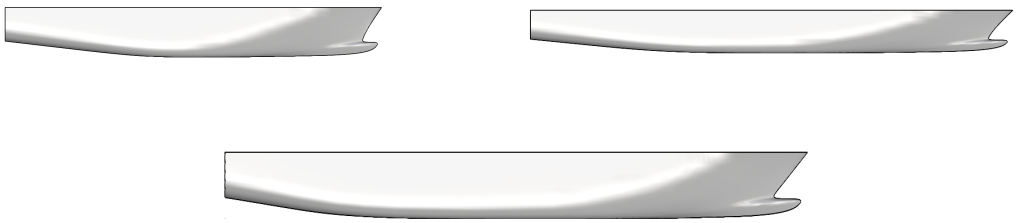


Figure 1: Parent hulls, top left - offshore patrol vessel, top right - passenger ferry, bottom - cruise ship

Five parameters were selected for the hull aft ship geometry optimization: transom immersion, transom beam, buttock shape, deadrise angle and propeller tunnel depth. For the Hull Vane®, three parameters were defined: longitudinal position, vertical position and chord length. Figure 2 shows an example from the offshore patrol vessel. Light blue lines with markers corresponds to a minimum value for all parameters and dark blue lines correspond to maximum value. Two example Hull Vane® geometries are shown as well, with varying longitudinal and vertical position and chord length.

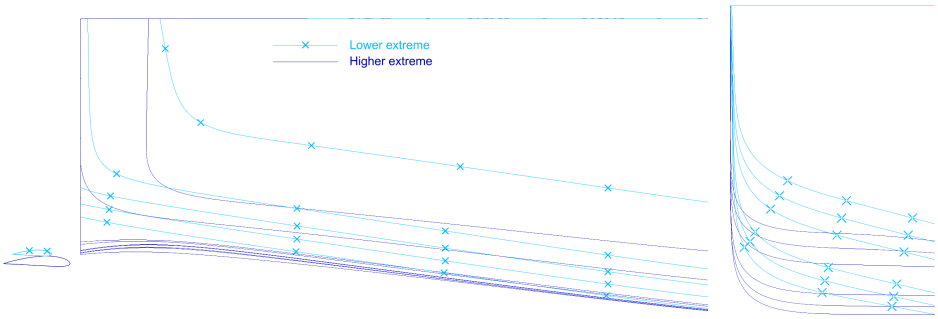


Figure 2: Visualized design variable extremes on offshore patrol vessel case study

2.2 Mesh

Geometries are meshed in Hexpress which is a part of the FINE Marine software package. Computational domain is defined in such a way that the boundaries are far enough from the vessel so as not to influence the results. All hull surfaces have a wall boundary condition. Using the symmetry boundary condition along the centre-line, only half of the vessel is meshed. Prescribed pressure boundary condition is applied to the top and bottom domain boundary. All other domain faces are set to the far field boundary condition. Within the POSEIDON framework, meshing is automated and is a function of reference length and velocity. Figure 3 shows the mesh on the hull surface of the cruise ship geometry.

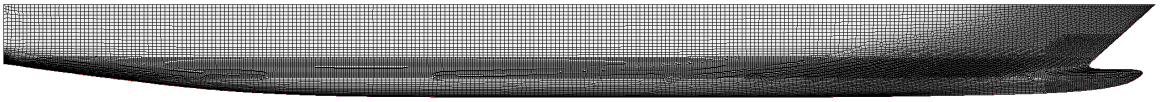


Figure 3: Cruise ship parent hull mesh on the surface of the hull

2.3 Solver

To conduct the CFD analysis, the FINE Marine solver is used. The solver uses Unsteady Reynolds Averaged Navier Stokes (URANS) equations to describe the flow. As the equations require a closure model, two equations k-Omega SST Menter turbulence model is applied. To define the free surface, 'volume of fluid' (VoF) method is used. Both water and air flow are solved, their properties are defined as per ITTC [3] for 15 degrees Celsius. Free stream turbulence quantities were initialised using the reference length and velocity. To resolve the flow in the regions near solid walls, wall functions are used. Heave and trim of the vessel are solved, while the velocity is imposed. The vessel is gradually accelerated from zero to the imposed velocity. The timestep magnitude is defined as per ITTC [4] recommendations.

2.4 Optimization

Initial samples or design points are generated using a Halton sequence. This method ensures that the sample space is well covered by providing a diverse yet uniformly distributed set of points. The number of points is defined by the number of parameters and constraints. Ten points are added for each parameter or constraint. After the CFD analysis of the initial sample base, a multi-objective optimization is performed. It is performed using a Multi-Objective Genetic Algorithm (MOGA), which simulates natural evolution. MOGA begins with a population of candidate designs and iteratively improves them through selection, crossover and mutation. The primary goal is to optimize multiple conflicting objectives simultaneously. Over several generations, MOGA produces a set of non-dominated solutions that formed the Pareto front, representing designs that offer a balance between objectives. The Pareto front from MOGA represented the optimal solutions where no single objective could be improved without compromising another. Each Pareto point is considered equally valid based on the optimization criteria.

2.5 Constraints

Besides the geometry, the parametric modeler outputs main dimensions of each hull, hull coefficients and hydrostatic properties. In the initial sample base, constraints are not considered and samples are generated to cover the design space set by boundary values of each parameter. During the optimization step, constraints are respected. In this study, selected constraints are volume displacement, longitudinal center of buoyancy and transversal metacentric to keel height. Displacement is constrained to ±0.5% of parent hull value, LCB is constrained to ±1.0% and KM_t has a minimum value equal of that to the parent hull.

2.6 Objectives

The objective of the optimization is to minimize engine brake power (P_b) over the operational profile. Therefore, all simulations are conducted at three sailing speeds of interest, which represent the operational profile. To calculate the P_b, first the total resistance of the vessel is to be obtained. Starting with the barehull resistance obtained through CFD, additional resistance components are added in the form of allowances (roughness, correlation, air resistance and additional appendages). These additional resistance components are calculated through an internal resistance prediction tool. Added resistance due to waves or shallow water is not taken into consideration. As a next step, open water characteristics (K_T, K_Q and open water efficiency) of a propeller are obtained from Wageningen B-Series, [5], while wake fraction, thrust deduction and relative rotative efficiency are obtained as per Holtrop [6]. Losses in the driveshaft are assumed constant at 96%. With total propulsive efficiency and total resistance known, required power can be calculated. Fuel consumption can be determined using the vessels' brake specific fuel consumption and be directly correlated to emissions and cost reduction with obtained required power, however that is not a part of this study.

3 Results

Six optimizations were conducted, one for each hull without and with Hull Vane® at three sailing speeds representing the operational profile. This results in hundreds of conducted simulations. Results are shown on Figure 4, Figure 5 and Figure 6. Light blue circles represent the initial sample base or design of experiment (DoE), used to build the surrogate model.

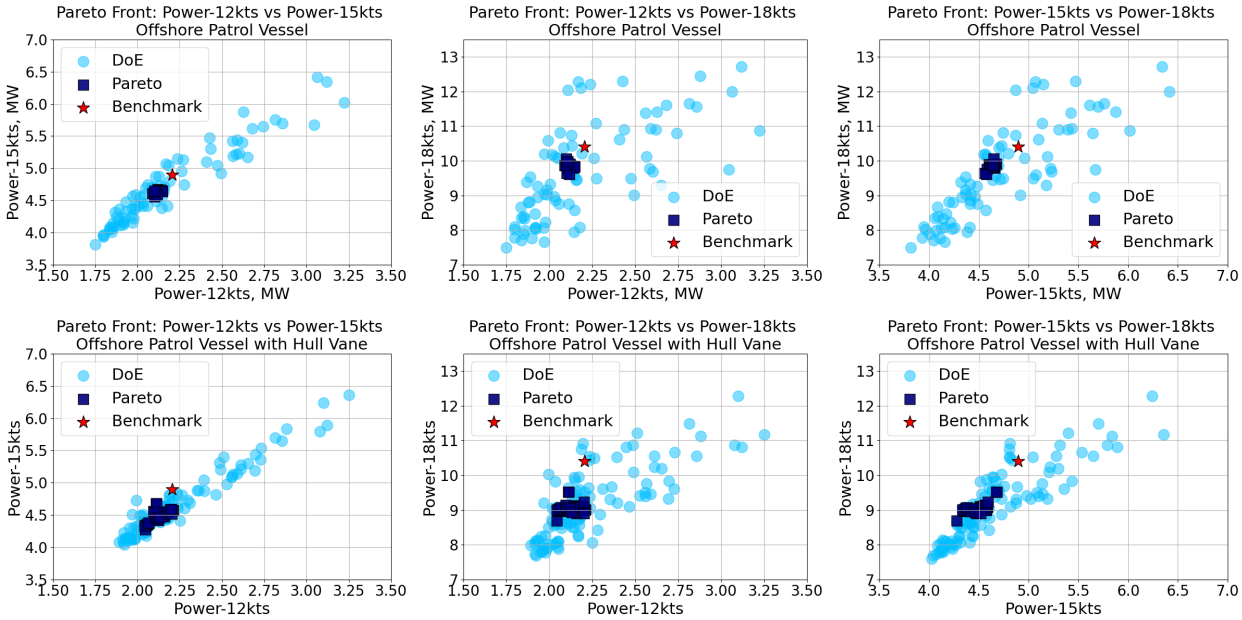


Figure 4: Optimization results of case study on offshore patrol vessel

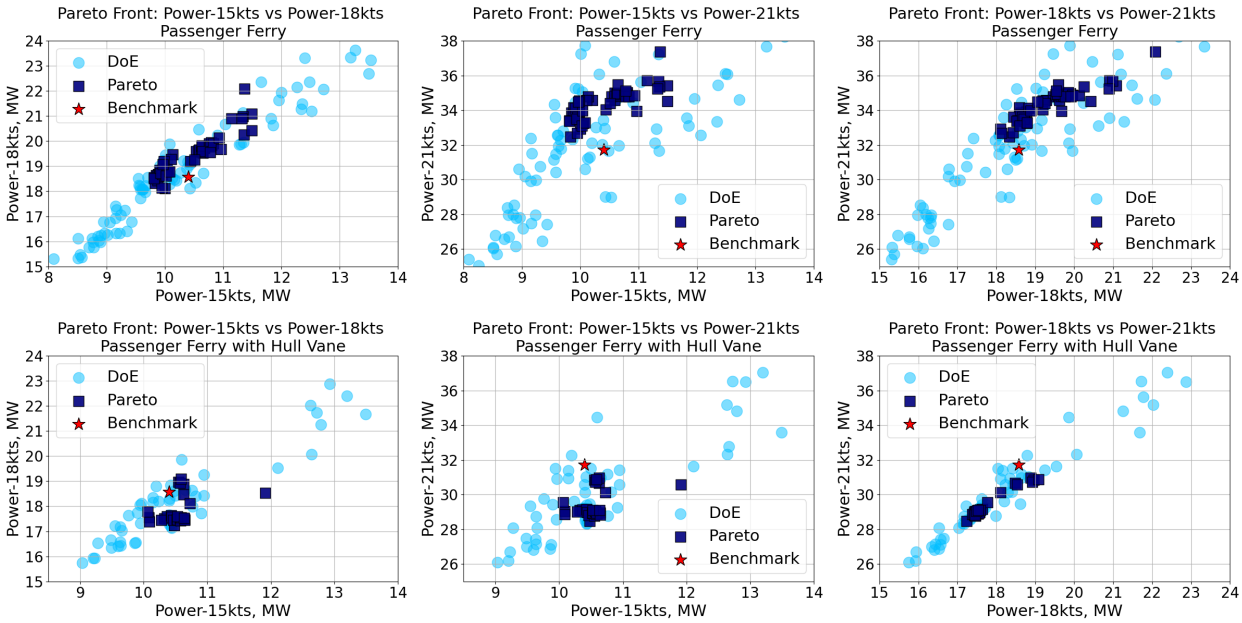


Figure 5: Optimization results of case study on passenger ferry

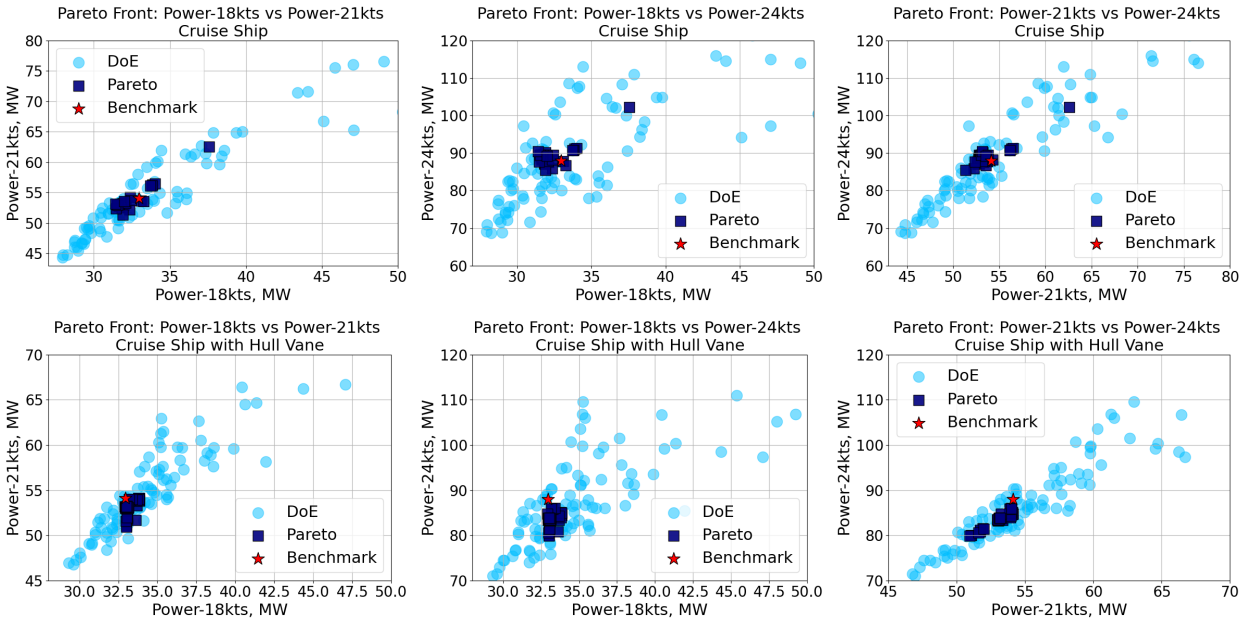


Figure 6: Optimization results of case study on cruise ship

DoE points do not respect the imposed constraints and are allowed to explore and build the design space. The dark blue squares show the optimal solutions or the Pareto front within the design constraints. Additionally, the red star is the benchmark case. The benchmark case is the parent hull without Hull Vane®. The offshore patrol vessel was analyzed at 12, 15 and 18 knots, the passenger ferry at 15, 18 and 21 knots and the cruise ship at 18, 21 and 24 knots. Maximum power reduction obtained in the optimization at each sailing speed for each hull is shown in Table 2.

Table 2: Maximum obtained power reduction for each hull at each sailing speed

Offshore Patrol Vessel			Passenger Ferry			Cruise Ship		
	No Hull Vane®	Hull Vane®		No Hull Vane®	Hull Vane®		No Hull Vane®	Hull Vane®
12kts	-5.31%	-7.36%	15kts	-5.71%	-3.28%	18kts	-4.69%	-0.08%
15kts	-6.88%	-12.59%	18kts	-2.54%	-7.77%	21kts	-5.15%	-5.89%
18kts	-7.60%	-16.45%	21kts	2.39%	-10.63%	24kts	-2.93%	-9.20%

As this is a multi-dimensional optimization it can be difficult to determine relations between parameters, constraints and objectives. They are better visualized in Figure 7 for the offshore patrol vessel with Hull Vane® case. Light blue lines with triangle marker represent DoE geometries, while dark blue lines with square marker represent optimized Pareto geometries.

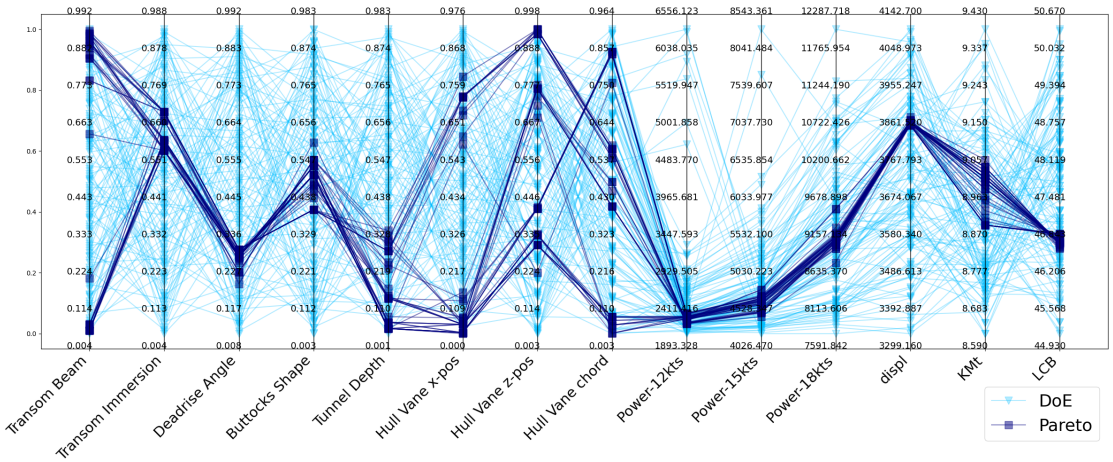


Figure 7: Relation between parameters, objectives and constraints - Offshore Patrol Vessel with Hull Vane®

4 Discussion and Conclusions

This study has shown the POSEIDON framework's ability to successfully co-optimize hull forms and Energy Saving Devices (ESD's). Results show that significant engine power savings can be obtained, particularly when hull geometries are optimized in conjunction with and ESD, in this case study a Hull Vane®, at higher sailing speeds. A trend visible among all case studies shows that as the vessel size increases relative power savings decrease, with maximum power savings obtained in the offshore patrol vessel Hull Vane® study. However, as the vessel size increases, absolute power requirements increase exponentially for which a couple percent of power reduction can lead to significantly greater energy savings.

When comparing the WDA studies, larger savings are found for lower sailing speeds in the passenger ferry and cruise ship studies, while in the offshore patrol vessel study the opposite trend can be seen. When outfitted with the Hull Vane®, largest power savings are obtained at top speed in all cases. Furthermore, when comparing the WDA and Hull Vane® studies results show that the integration of Hull Vane® in the optimization yielded larger energy savings compared to only optimizing the hull.

While the algorithm identified hull and Hull Vane® geometries with reduced required power in nearly all scenarios, it was unsuccessful in the top speed speed passenger ferry WDA case. It is likely that by increasing the constraint range, POSEIDON would find larger savings across all conducted studies. Even though this is an academic study, the constraints were set to a narrow range as there would be design limitations for a commercial project in which the main particulars are already defined in the concept phase.

When optimizing a multi-dimensional problem such as this, it can be difficult to correlate individual parameters to the obtained result. Nevertheless, some trends can be derived from Figure 7. In the offshore patrol vessel with Hull Vane® study, some parameters such as deadrise angle and Hull Vane® x-position are clustered around a single value, which implies that is the most favorable choice for those parameters. However, other parameters are clustered around multiple values, such as transom beam and Hull Vane® z-position. With multiple designs of similar performance, it allows one to select the most suitable solution based on other criteria, such as weight or cost.

To conclude, the POSEIDON framework demonstrates its modularity by being able to optimize different hull types with and without an ESD. This combined optimization is essential to meet strict environmental standards while providing ship operators with the clear advantage of enhanced operational capabilities through increased range and top speed. The goal of future studies will be to expand the framework with different ESD's, hull parameters and design constraints.

References

[1] Jing-Fa Tsai et al. *Wave-Making Resistance Reduction of a Container Ship*. 2008.

[2] J. Hofman and N. Moerke. "Full-Scale Application of Hull Vane® on a 108m Holland-Class OPV of the Royal Netherlands Navy: Confirming Predictions and Tactical Benefits". In: (2025).

[3] W. Chen et al. *Fresh Water and Seawater Properties*. ITTC Recommended Procedures and Guidelines 7.5-02-01-03. International Towing Tank Conference (ITTC), 2024. URL: https://www.ittc.info/media/11764/75-02-01-03.pdf.

[4] K. Maki et al. *Practical Guidelines for Ship CFD Applications*. ITTC Recommended Procedures and Guidelines 7.5-03-02-03. International Towing Tank Conference (ITTC), 2024.

[5] Michael M Bernitsas, D Ray, and P Kinley. "KT, KQ and efficiency curves for the Wageningen B-series propellers". In: (1981).

[6] J. Holtrop and G.G.J. Mennen. "An approximate power prediction method". In: *International shipbuilding progress* 29.335 (1982), pp. 166–170.

Use of a Computationally Lightweight Analysis Approach for Early Stage AUV Hull Form Optimisation

Henry Hallam, Joseph Banks, Stephen Turnock

Maritime Engineering, School of Engineering, University of Southampton
h.hallam@soton.ac.uk

1. Introduction

Research scale autonomous underwater vehicles (AUVs) are required to operate at deep submergence for extended periods. With limited energy storage space available, designing the hull form for minimum resistance is important to improve endurance over the research mission. This work demonstrates the development, validation and deployment of a computationally lightweight analysis approach for optimising a bare-hull AUV for minimum resistance at low Reynolds numbers (1.1E7), whilst maintaining a defined internal pressure vessel volume.

Computational fluid dynamics (CFD) modelling approaches are widely used for the performance prediction of AUVs (Vasudev et al. 2025). However, optimisation studies require the evaluation of potentially hundreds or thousands of candidate geometries, making large-scale deployment of three-dimensional CFD computationally expensive. Existing approaches are also constrained by the geometric parameterisations used to represent the bare hull shape. A computationally lightweight method is therefore required to rapidly explore a high-dimensional design space whilst retaining sufficient accuracy to capture the effect of hull geometry on the flow.

An axisymmetric CFD approach is utilised using Simcenter STAR-CCM+, with validation performed against reference towing-tank data for SUBOFF (Liu & Huang. 1998) and three-dimensional steady RANS simulations. The method is coupled with a Bézier-Spline hull parameterisation and demonstrated through the optimisation of the research AUV Autosub. A total of 700 candidate hull forms are evaluated, demonstrating both the computational efficiency of the approach and its ability to identify improved hull geometries.

2. Autosub Optimisation Framework

2.1 Hull Parameterisation

The optimisation framework was demonstrated using the Autosub research AUV, which is 7 m in length and operates at 2 m/s, corresponding to a Reynolds Number of 1.07E7. The bare hull geometry is based on the dimensions reported by Philips et al. (2007).

The hull was parameterised using separate Bézier splines for the bow and stern, controlled by eight design variables. Tangency conditions were enforced at the join to the parallel midbody, with vertical gradient constraints at the bow and stern tips. The splines were constrained to remain outside a fixed internal pressure vessel, thereby maintaining the required enclosed volume. The resulting parameterisation provides a flexible design space whilst retaining a smooth hull surface. The range of geometries generated is shown in Figure 1. This work is intended as a design exercise to demonstrate the capabilities of lightweight analysis tools; consequently, the geometric variations investigated do not account for the spatial requirements of internal equipment outside the pressure vessel.

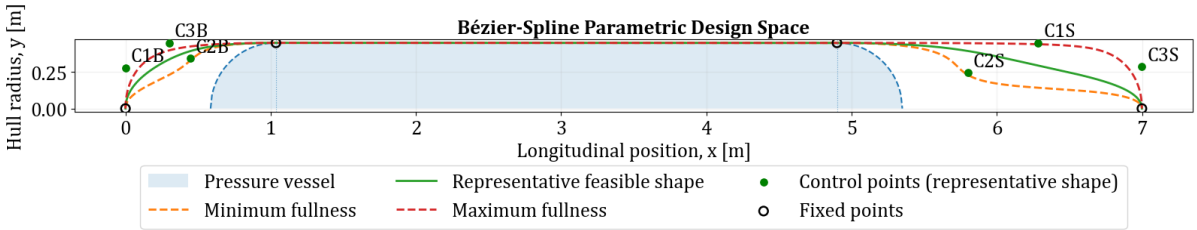


Figure 1 – Demonstration of the Bézier Spline Parametric Design Space (bow left, stern right). Coefficients C1B & C3S are free to move along the y-axis, enforcing vertical tangency at the bow and stern. Coefficients C3B & C1S are free to move along the x-axis, enforcing tangency at the parallel mid-body.

Coefficients C2B and C2S are free to move along the x and y axes, controlling the fullness of the shape generated.

2.2 Candidate Analysis Methods

An Integral Boundary Layer (IBL) method was initially implemented to provide rapid estimates of skin-friction and viscous pressure drag. The method works by solving the Von Karman integral momentum equation over a 2D surface discretised into panels, using Thwaites' method, as detailed by Katz and Plotkin in Low-Speed Aerodynamics (2012). The method required only a few seconds to analyse each candidate geometry and demonstrated excellent agreement with experimental data for conventional streamlined geometries, with an error of approximately 1.5% across the tested speed range. However, the IBL method is not suitable for analysis of separating flows, unable to solve flow around candidate hulls exhibiting large adverse pressure gradients. Since such geometries are naturally generated during optimisation, the IBL approach was not considered sufficiently reliable as the primary optimisation tool.

Axisymmetric CFD was therefore adopted as the principal analysis method. Simcenter STAR-CCM+ solves the two-dimensional form of the Navier–Stokes equations in cylindrical coordinates for a meridional cross-section of the body of revolution. The formulation considers the flow through an annular control volume and assumes axisymmetry, such that no circumferential velocity or variation in the circumferential direction exists, i.e. $v_\theta = 0$and $\partial/\,\partial\theta = 0$. The integral conservation of momentum is expressed as (Siemens. 2020):

$$\frac{\partial}{\partial t}\int_A \rho\mathbf{v}\, r\, dA + \oint_{\partial A} \rho\mathbf{v}\otimes\mathbf{v}\cdot r\, ds = -\oint_{\partial A} p\mathbf{I}\cdot r\, ds + \oint_{\partial A}\mathbf{T}\cdot r\, ds + \int_A \frac{1}{r}\begin{bmatrix} 0 \\ p-\tau_{\theta\theta} \\ 0 \end{bmatrix} r\, dA + \int_A \mathbf{f}_b\, dA + \int_A \mathbf{s}_u\, dA,$$

$$\mathbf{v} = (v_z v_r v_\theta)^{\boldsymbol{T}},\ v_\theta, \frac{d}{d\theta} = 0,$$

$$\boldsymbol{T} = \mu\begin{pmatrix} \frac{2\partial v_z}{\partial z} - \frac{2}{3}\nabla\cdot v & \frac{\partial v_z}{\partial r} + \frac{\partial v_r}{\partial z} & 0 \\ \frac{\partial v_z}{\partial r} + \frac{\partial v_r}{\partial z} & \frac{2\partial v_r}{\partial r} - \frac{2}{3}\nabla\cdot v & 0 \\ 0 & 0 & \frac{2v_r}{r} - \frac{2}{3}\nabla\cdot v \end{pmatrix},$$

where r is the radial coordinate, A is the area, $\boldsymbol{I}$ is the identity matrix, $\mathbf{T}$ is the viscous stress tensor, $\mathbf{f}_b$ represents body forces and $\mathbf{s}_u$ represents additional momentum source terms. The r-weighting accounts for the annular geometry of the axisymmetric control volume. The resulting formulation provides substantially lower computational cost than three-dimensional CFD while allowing high mesh resolution around the hull, including a low wall $y^+$and a fully resolved boundary layer through the use of prism layers. Furthermore, the axisymmetric formulation can resolve flow around hull geometries exhibiting slight to moderate flow separation. The approach is therefore well suited to the automated analysis of large numbers of candidate geometries.

2.3 Optimisation Workflow

A Latin Hypercube sample of the feasible Bézier-spline design space was generated and analysed using the axisymmetric CFD methodology. Candidate hull geometries were generated by sampling the Bézier coefficients within constrained parameter ranges. Each geometry was then assessed for feasibility by checking that the bow and stern splines did not intersect the pressure vessel or extend beyond the region bounded by the parallel midbody, central axis, and bow and stern ends. Geometries violating these constraints were rejected. The sampling process was repeated, increasing the initial sample size as required, until 700 feasible candidate hull forms were obtained. The coefficient ranges were constrained to provide a practical sampling efficiency while retaining sufficient variation within the design space. Approximately 23% of the generated parameter combinations satisfied the geometric feasibility constraints.

Of the 700 design variants, approximately 50 of the lowest-drag candidates exhibited large negative pressure-drag values associated with blunt-ended stern shapes and extensive flow separation. To prevent these spurious predictions from dominating the optimisation, the 100 highest-performing candidates were subsequently analysed using three-dimensional steady RANS. This provided an independent check of the resistance predictions for the more streamlined candidate geometries and identified the limitations of the axisymmetric approach for separated flows.

3. Validation of the Lightweight Analysis Framework

3.1 Axisymmetric CFD Settings Sensitivity and Validation

A settings sensitivity study was performed to establish an axisymmetric CFD setup that balanced resistance prediction accuracy with computational efficiency. The main findings are consolidated in Table 1. Mesh resolution, prism-layer resolution and solver type were found to have significant effects on the predicted resistance and computational time. In particular, reducing the mesh resolution by a factor of ten reduced solver time by 93%. Increasing the first cell height into the high-y+ regime increased solver time by approximately 600%. Fully resolving the boundary layer and increasing the number of prism layers improved the resistance prediction, with 120 prism layers selected for the final setup. Although the segregated solver produced a lower resistance error, the coupled solver was selected for the optimisation due to its substantially lower computational time.

The final axisymmetric setup was validated against experimental resistance data for the bare-hull SUBOFF geometry over a range of speeds using towing-tank data from Liu & Huang (1998). The optimum setup produced a resistance prediction error of -0.39% at the sensitivity-study condition. The results demonstrate that the axisymmetric methodology can provide accurate resistance predictions while retaining the computational efficiency required for large-scale optimisation. The mesh set up for the SUBOFF validation study can be seen in Figure 3.

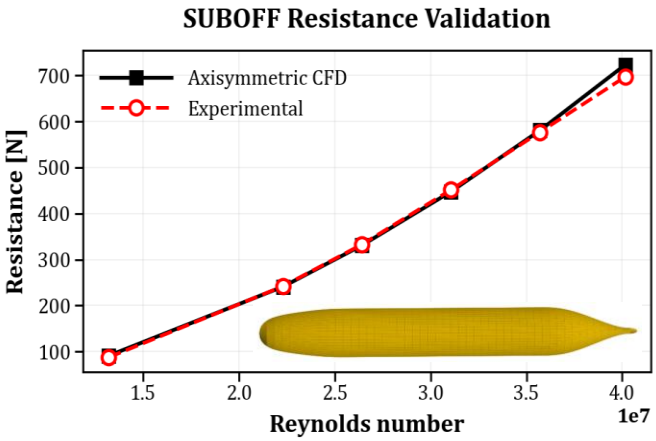


Figure 2 – SUBOFF Resistance Validation: axisymmetric CFD versus experimental data (Liu & Huang. 1998), with the SUBOFF geometry lower right.

An additional turbulence-model sensitivity study found that the k-ω SST model provided the most accurate and robust resistance prediction of the tested models. The k-ε model gave an error of -3.92%, compared with -0.39% for k-ω SST, while the Spalart-Allmaras model gave -1.33%. The k-ω SST model was therefore retained for subsequent simulations.

Table 1 - Axisymmetric CFD Settings Sensitivity Study Findings

Parameter	Sensitivity finding	Computational impact	Selected setup
Mesh resolution	Resolution must capture hull curvature without introducing unnecessary numerical error.	10× reduction in resolution reduced solver time by 93%.	TSS = 0.01 m; Min SS = 0.001 m
Prism-layer first cell	Lowest error obtained with wall y+ significantly below 1.	Increasing first cell height to high y+ increased solver time by ~600%.	First cell height = 1.0E-7 m
Prism-layer thickness	Fully resolving the boundary layer improved accuracy; partially resolved BL gave >10% error.	No significant solver-time impact.	Overall thickness = 0.03 m
Number of prism layers	Increasing layers improved solution accuracy; 30→120 layers improved error by >4%.	30→120 layers increased solver time by 75%.	120 layers
Solver type	Segregated solver produced lower resistance error than coupled solver.	Segregated solver increased solver time by 286%.	Coupled solver

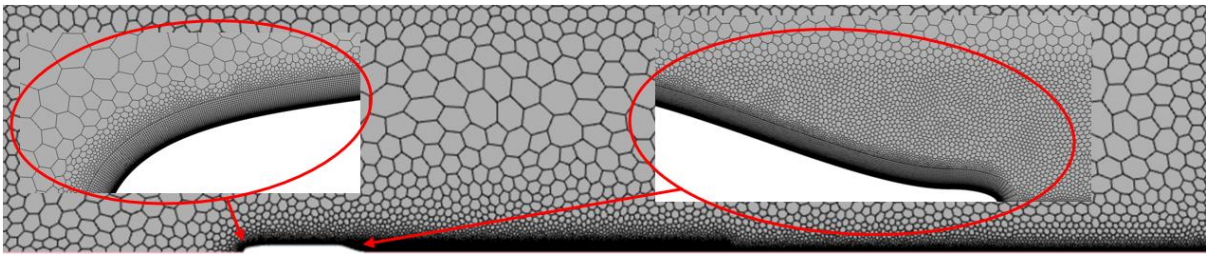


Figure 3 – Axisymmetric CFD mesh example detailing fine surface sizes for curvature resolution and 120 prism layers.

3.2 Comparison with Three-Dimensional CFD

To assess whether the automated axisymmetric CFD approach was appropriate for candidate hull geometries, the top 100 designs from the optimisation study were also analysed using a three-dimensional steady RANS solver. A settings sensitivity study was first performed for the SUBOFF bare hull at 3.046 m/s to establish the three-dimensional setup, with the optimum settings detailed in Table 2. The refined setup predicted the bare hull resistance of 88.2 N compared with the experimental value of 87.4 N, corresponding to an error of 0.9%. A slice of the three-dimensional mesh can be seen in Figure 4.

Table 2 - 3D Steady RANS Optimum Setup for SUBOFF

No. Prism Layers	20	**Min Wall Y+**	22
First Cell Height	8.0E-4 m	**Max Wall Y+**	72
Overall Thickness	0.05 m	**Shear Drag**	76.4 N
TSS	0.021 m	**Pressure Drag**	11.8 N
Min SS	0.009 m	**Resistance**	88.2 N
Refined Region Size	0.04 m	**% Error vs. Exp. (87.4N)**	0.9 %
Total Cell Count	2.36E6	**Solver Time**	1115 s (running on one node, allocated 48 cores)

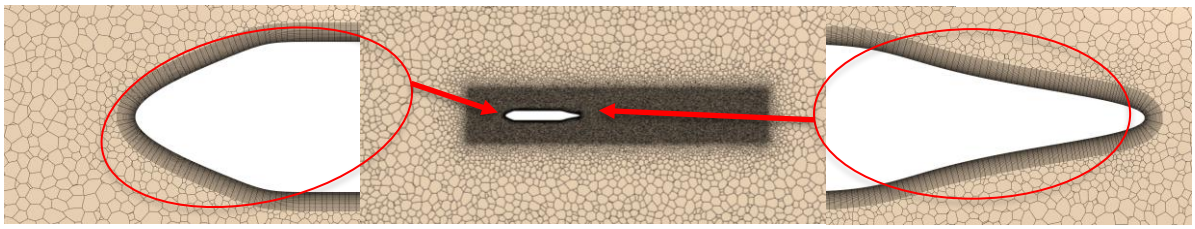


Figure 4 – A 3D CFD mesh slice showing prism layer and cell spacing around the bow and stern.

For use on the longer Autosub geometry (7 metres versus 4.35 metres), the optimum settings (no. prism layers, first cell height, overall thickness, TSS, Min SS and refined region size) for three-dimensional CFD of the SUBOFF were scaled according to hull length and flow speed to create an equivalent mesh with the same resolution and *y+* values. For streamlined candidate hull shapes, the resistance predictions from the axisymmetric and three-dimensional approaches agreed closely, with most predictions differing by approximately 0.5%. Figure 5 shows that the strongest correlation was obtained for shear drag, with an R^2 value of 0.988, while the correlation for total drag was $R^2 = 0.817$. The weaker correlation in pressure drag ($R^2 = 0.526$) indicates that the remaining differences in total resistance are primarily associated with prediction of pressure recovery at the stern rather than boundary-layer shear drag.

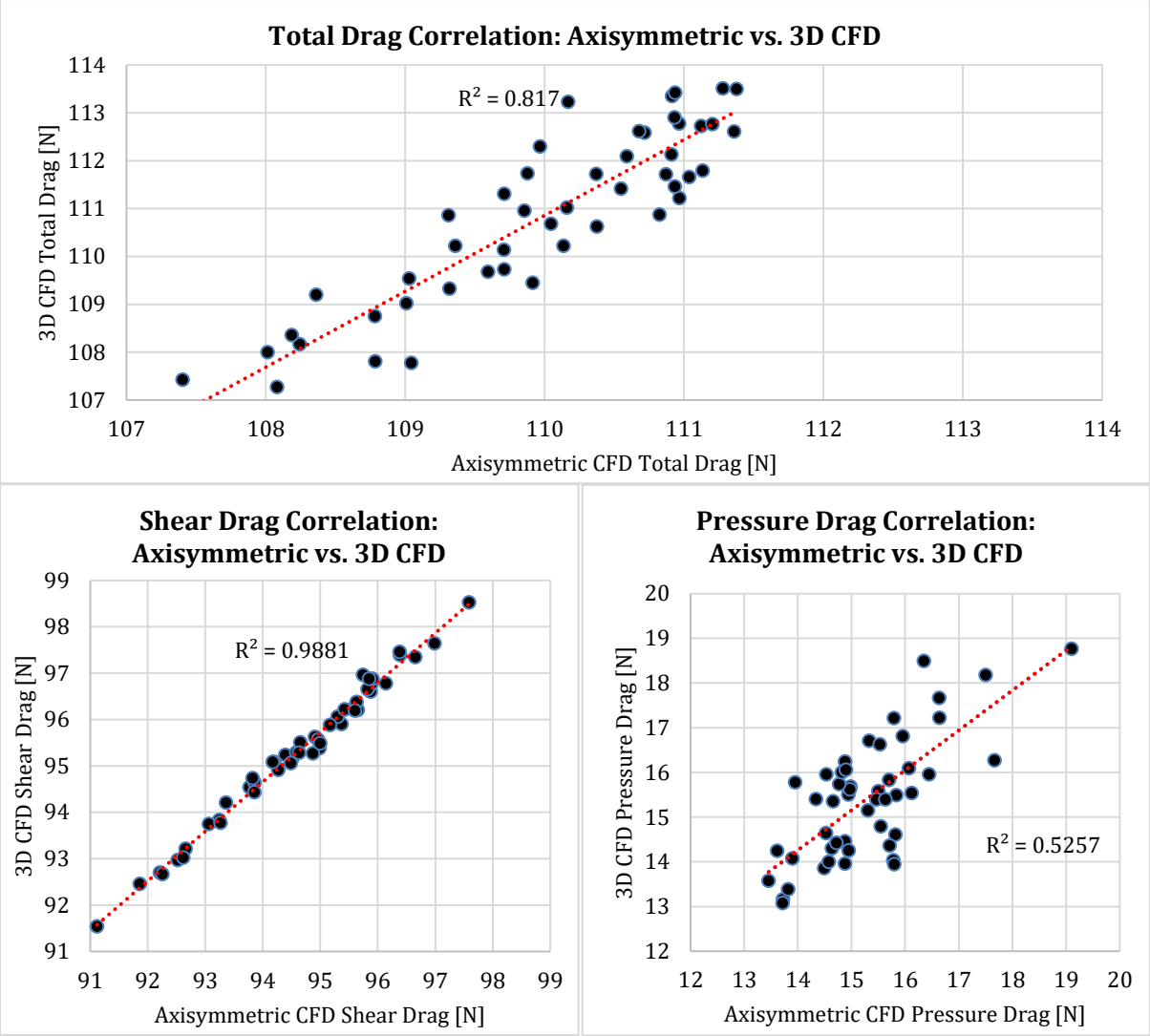


Figure 5 – The correlation between drag predictions for streamlined hull shapes with the axisymmetric and 3D CFD methodologies.

The axisymmetric methodology was less reliable for low-Reynolds-number flows over blunt stern shapes. Approximately 50 of the 100 lowest-drag candidates produced large negative pressure drag estimates in the axisymmetric simulations, caused by the treatment of the separated flow as homogeneous about the central axis. These predictions were not observed in the three-dimensional simulations, where the blunt-ended geometries were correctly ranked as high-drag designs. Since a hull shape producing extensive separation would not be expected to be optimal, an automated screening step based on the identification of separation, such as regions where wall shear stress approaches zero, could be incorporated to identify such geometries before accepting their axisymmetric resistance predictions. Furthermore, a three-dimensional mesh with an equivalent spatial resolution would be expected to contain approximately 700 million cells, further demonstrating the substantial computational savings offered by the axisymmetric formulation.

4. Autosub Hull Optimisation Demonstration

The validated axisymmetric methodology, coupled with the Bézier-Spline geometry model, was applied to 700 Autosub hull variants. The resulting design space is shown in Figure 6, demonstrating the trade-off between internal volume and total drag. A hull form with a 4% reduction in predicted bare-hull resistance relative to the baseline Autosub geometry was identified, while maintaining the same internal pressure-vessel volume. A total of 25 candidate hulls outperformed the original geometry.

The Bézier coefficients of the ten lowest-resistance designs showed strong convergence for the parameters controlling stern fullness in the x and y directions. This indicates that resistance is primarily driven by the fullness of the stern, with greater variation in the bow coefficients producing a comparatively smaller effect on drag. The baseline and lowest-resistance geometries are compared in Figure 7. The 700 design evaluations required approximately 11 hours of computational time when run in parallel across two nodes on Iridis 6 (the University of Southampton's high-performance computer), demonstrating the suitability of the approach for large-scale early-stage design exploration.

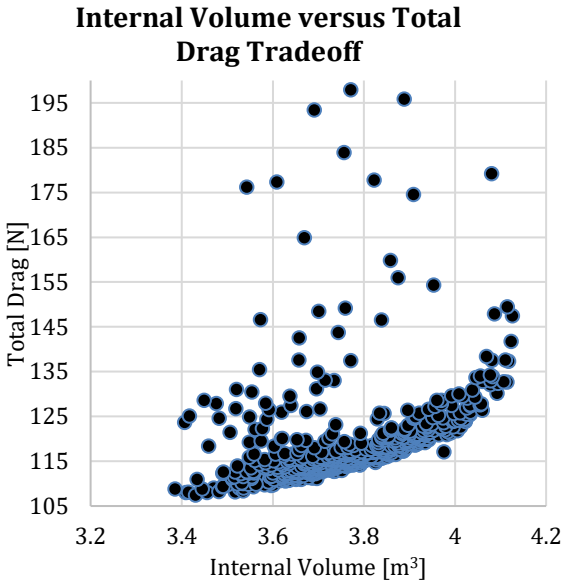


Figure 6 - The trade-off between increasing internal volume of AUV, and the associated increase in drag force incurred.

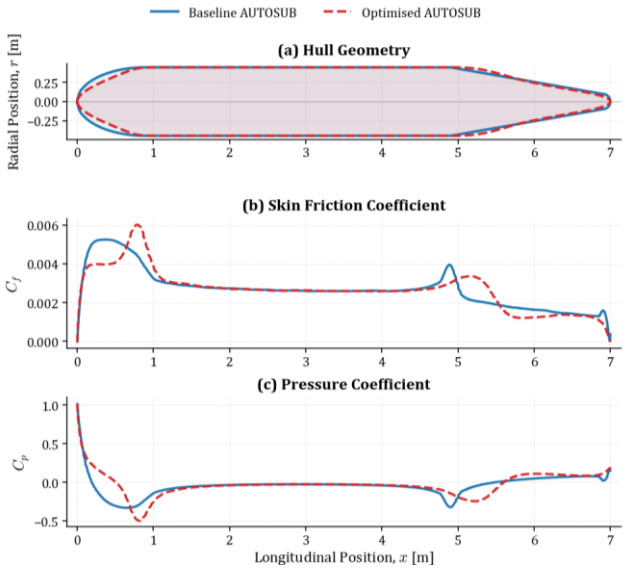


Figure 7 – Comparison of the baseline and optimised Autosub geometries with C_f and C_p plots.

5. Conclusions

A computationally lightweight framework for the automated optimisation of bare-hull AUV forms was developed, validated and demonstrated. An integral boundary layer approach provided rapid and accurate predictions for streamlined geometries, but was not sufficiently robust for candidate hulls with large adverse pressure gradients or flow separation. An axisymmetric CFD methodology was therefore developed and validated against experimental SUBOFF resistance data, obtaining an error of -0.39%.

The axisymmetric predictions for streamlined optimisation candidates showed strong agreement with three-dimensional steady RANS, while reducing computational time by approximately 89%. The main limitation was identified for blunt stern geometries exhibiting extensive separation, where the axisymmetric assumption produced spurious negative pressure drag predictions. Incorporating an automated separation-screening step would provide a means of excluding such geometries before accepting their resistance predictions.

Application of the framework to 700 Autosub hull variants identified a design with a 4% reduction in predicted bare-hull resistance at fixed pressure-vessel volume, with 25 candidate geometries outperforming the baseline. The convergence of the stern design variables also indicates that stern fullness is a dominant driver of resistance within the investigated design space. The proposed framework therefore provides a computationally efficient method for exploring large AUV hull-form design spaces at the early design stage.

References

Abidin, N., Grondin, F., Muller, P., & Sigrist, J. (2025). Comprehensive Numerical Hydrodynamic Analysis of Submarine in a Straight Course Simulation Using Wall-Resolved RANS Models. Proceedings of the 26th French Congress of Mechanics.

Katz, J., & Plotkin, A. (2001). Enhancement of the Potential Flow Model. In Low-Speed Aerodynamics (pp. 483–536). Cambridge University Press. https://doi.org/10.1017/CBO9780511810329.017

Liu, H.-L., & Huang, T. (1998). Summary of DARPA Suboff Experimental Programme. Report for DTIC Hydromechanics Directorate.

Philips, A., Furlong, M., & Turnock, S. (2007). The use of computational fluid dynamics to assess the hull resistance of concept autonomous underwater vehicles. 10th Numerical Towing Tank Symposium.

Katz, J., & Plotkin, A. (2001). The Laminar Boundary Layer. In Low-Speed Aerodynamics (pp. 448–482). Cambridge University Press. https://doi.org/10.1017/CBO9780511810329.016

Siemens. (2020). Simcenter STAR-CCM+ Documentation.

Suman, K., Nageswara Rao, D., Das, H., & Bhanu Kiran, G. (2010). Hydrodynamic Performance Evaluation of an Ellipsoidal Nose for a High Speed under Water Vehicle. Jordan Journal of Mechanical and Industrial Engineering, 4(5), 641–652.

Vasudev, K., Pandey, M., & Pu, J. H. (2025). A Comparative Study on Hydrodynamic Optimization Approaches for AUV Design Using CFD. Fluid Dynamics & Materials Processing, 21(7), 1545–1569. https://doi.org/10.32604/fdmp.2025.065289